School of Physics and Astronomy

Investigating the High Redshift Universe with H-ATLAS

Elizabeth Pearson

Submitted for the degree of Doctor of Philosophy
School of Physics and Astronomy
Cardiff University
March 2013

Abstract

Upon its completion the *Herschel* ATLAS (H-ATLAS) will be the largest submillimetre survey to date, detecting close to half-a-million sources. It will only be possible to measure spectroscopic redshifts for a small fraction of these sources. However, if the rest-frame spectral energy distribution (SED) of a typical H-ATLAS source is known, this SED and the observed *Herschel* fluxes can be used to estimate the redshifts of the H-ATLAS sources without spectroscopic redshifts.

In this thesis, I use a subset of 40 H-ATLAS sources with previously measured redshifts in the range $0.5 < z < 4.2$ to derive a suitable average template for high redshift H-ATLAS sources. I find that a template with two dust components ($T_{\rm c} = 23.9$ K, $T_{\rm h} = 46.9$ K and ratio of mass of cold dust to mass of warm dust of 30.1) provides a good fit to the rest-frame fluxes of the sources in our calibration sample. I use a jackknife technique to estimate the accuracy of the redshifts estimated with this template, finding a root mean square of $\Delta z/(1+z) = 0.26$. For sources for which there is prior information that they lie at $z > 1$ we estimate that the rms of $\Delta z/(1+z) = 0.12$. I have used this template to estimate the redshift distribution for the sources detected in the H-ATLAS equatorial fields, finding a bimodal distribution with a mean redshift of 1.2, 1.9 and 2.5 for 250, 350 and 500 μm selected sources respectively.

Using these redshifts I have estimated luminosity functions for the Phase 1 field. This has shown evidence of strong evolution out to a redshift of $z \sim 2$. At which point luminosity evolution begins to slow until $z \sim 3$, where it appears to stop altogether. Estimations of the angular correlation function showed strong clustering across most wavelengths and redshifts.

Declaration of authorship

- DECLARATION:
  This work has not previously been accepted in substance for any degree and is not concurrently submitted in candidature for any degree.

  Signed: .... (candidate) Date: ....

- STATEMENT 1:
  This thesis is being submitted in partial fulfillment of the requirements for the degree of Doctor of Philosophy (PhD).

  Signed: .... (candidate) Date: ....

- STATEMENT 2:
  This thesis is the result of my own independent work/investigation, except where otherwise stated. Other sources are acknowledged by explicit references.

  Signed: .... (candidate) Date: ....

- STATEMENT 3
  I hereby give consent for my thesis, if accepted, to be available for photocopying and for inter-library loan, and for the title and summary to be made available to outside organisations.

  Signed: .... (candidate) Date: ....

Contents

List of Figures

List of Tables

Space... is big. Really big. You just won't believe how vastly hugely mindbogglingly big it is...

Douglas Adams

Chapter 1

Introduction

> Space... is big. Really big. You just won't believe how vastly hugely mind-bogglingly big it is...
>
> *Douglas Adams*

1.1 The History of Extragalactic Astronomy

In 1750 it was speculated that the universe consisted of a flat disc of stars and that the band of stars seen across the night's sky as the Milky Way was our view through this disc (Wright, 1750). Wright also suggested that there may be 'cloudy spots' that existed outside the local starry region. Immanuel Kant, building on the observations of nebulae and star clusters by William Herschel and Charles Messier, put forward the idea of 'island universes', that there were many collections of stars floating in space separate from each other.

For many years there was great contention about whether the Milky Way was the limit of the universe or whether these fuzzy blobs were independent island universes. The limitations of observational technology meant that it was impossible to make a determination one way or the other. In 1920 the Great Debate was held between Harlow Shapely and Heber Curtis about whether these diffuse objects were from within the Milky Way or from without it. Inspired by the talk, Edwin Hubble measured the distance to variable stars (Hubble, 1925) and found that the distance measurements put them well outside the accepted limits of the Milky Way. From then on it was widely accepted that the Milky Way was just one of many galaxies.

The great distances involved bring many challenges to the task of observing galaxies from a practical standpoint and the greater the distance involved, the greater the challenge. However it is important to observe to the very limits of what is possible if we wish to understand the evolution and history of how galaxies grow and evolve. When observing light from a very distant object we are observing that object as it was when that light was emitted. If the galaxy is very far away then due to the travel time of the light we are looking at the galaxy as it was when the light left. This allows us to observe galaxies as they were billions of years ago at various stages throughout their formation and lets us piece together how they were formed.

The currently accepted model for the cosmic history of the universe is the Λ-CDM model. The Λ-CDM model states that the universe is dominated by cold dark matter (CDM), a substance whose only strong interaction is gravitational, meaning that it does not affect photons traveling through it but it will keep a system gravitationally bound when there does not appear to be enough mass to do so. There is also a second component, dark energy, that drives the acceleration of the universe's expansion resulting in a positive cosmological constant (Λ). The model states large scale structure of the universe grew from quantum fluctuations in the primordial universe causing peaks in the density of the universe which then attracted matter towards them to form gravitationally bound dark matter halos. Gas poured into these halos and cooled to the point where they could form galaxies and stars. Over time small galaxies collided and merged together to form a single larger galaxy (see Figure 1.1), these interactions causing huge bursts of star formation. These interactions changed the galaxy population to what we see today. This model of galaxy formation is known as the *hierarchical model*.

1.2 Galaxy Type

Astronomers have always always felt the need to classify objects and galaxies were no exception. Edwin Hubble created the first classification system, using the the morphology of galaxies to differentiate between them. He created three groups of galaxies: spiral, elliptical and irregular.

Spiral galaxies (or late type galaxies, see Figure 1.2a for a typical example) are rotating disk shaped galaxies with a bright bulge at the centre. It was hypothesised that the Milky Way was most likely this galaxy type before the concept of galaxies was even thought of (Wright, 1750). The stellar population of these galaxies is fairly young, making their colours bluer. Spirals are rich in gas and dust. The central bulge contains a densely packed group of stars, often the oldest in the galaxy. The disk is arranged into a spiral structure and the finer points of this structure, such as the tightness of the arms and whether or not there are bars present, are used to classify them more precisely (see the tuning fork diagram in Figure 1.3).

Elliptical galaxies (early type, see Figure 1.2b for a typical example) are what they sound like: elliptically spheroidal in shape. They have little free gas or dust as this has

Figure 1.1: The Antennae Galaxies are two spiral galaxies in the middle of a collision and in the process of merging together. This interaction has caused a huge burst of star formation within the galaxy. Provided by NASA/ESA.

been used up to make stars. There is little on-going star formation meaning that all the stars within them are old and red in colour. Ellipticals tend to be found in clusters whereas spirals were more likely to be field galaxies.

Hubble organised these further by using the tuning fork diagram (see Figure 1.3). He noticed that there appeared to be a smooth continuum of morphology, rather than well defined groups, so created subcategories dependent on how tightly wound the spiral arms were and how elliptical the galaxies appeared.

The third subset, irregular galaxies, are the most varied. These show no regular shape and are thought to be galaxies that were once elliptical or spirals but that have been disturbed by some interaction. Many are thought to be two galaxies that have collided (such as the Antennae galaxy in Figure 1.1) or a galaxy that has had a near miss with another, the intense gravitational pull causing the two to become disturbed.

1.3 Sub-mm astronomy

The infrared was discovered by William Herschel in 1800. Attempting to measure the temperature of different parts of the spectrum he realised his control thermometer, set somewhere beyond the red end of the visible spectrum, registered distinctly higher than those in the direct sunlight. This was the first experiment to show that the electromagnetic spectrum extended beyond what could be seen with the eye, a discovery that would revolutionise the field of astronomy.

Different wavelengths of light correspond to different processes and objects within a stellar system. It is only by observing them all that it is possible to gain a full picture of what is going on. Broadly speaking different wavelengths of light correspond to different temperatures. The longer the wavelength, the cooler the object being observed. The infrared (IR) covers wavelengths from around $1\,\mu$m to 1mm and corresponds to temperatures of between 10 - 1000 K. The IR is separated further into the near IR (0.7 - 5 μm), the mid infrared (MIR, 5 - 30 μm) and the far infrared and sub-millimeter (30 - 1000 μm).

For many years it was known that there was a strong infrared background to the universe (Puget et al., 1996), known as the Cosmic Infrared Background (CIB). This CIB is thought to have as much energy as both the UV and optical output of the universe combined, meaning it makes up for 50% of all energy output in the universe. This was believed to be the accumulation of the IR emission of all the galaxies in the universe but it has not been until relatively recently that it was possible to resolve it into discreet sources.

(a) Spiral

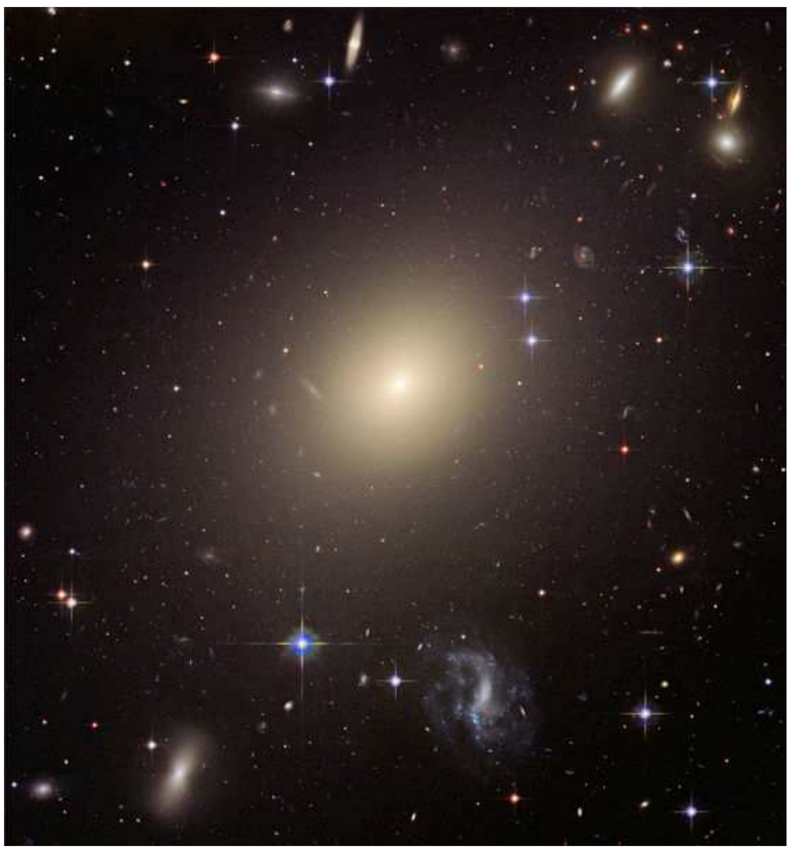

(b) Elliptical

Figure 1.2: A typical galaxy for each of the two main types of galaxy. 1.2a is provided by ESA/Hubble and 1.2b by NASA.

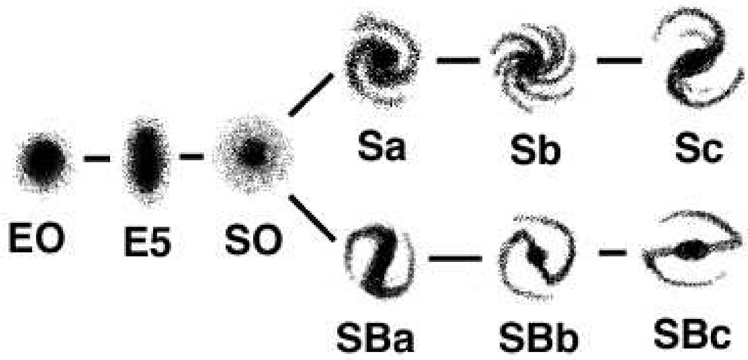

Figure 1.3: The tuning fork diagram of galaxy type created by Edwin Hubble. Ellipticals lie to the left and are subcategorised depending on their ellipticity. Spirals on the right are split into those which are barred and those which are not, then by how tightly the spiral arms are wound.

1.3.1 Problems with Observations

There are many issues that must be overcome when dealing with IR emission. One of the biggest issues is extinction due to the Earth's atmosphere. Water vapor in the Earth's atmosphere absorbs a large portion of the IR radiation traveling through it. In order to overcome this barrier it is necessary to build observatories above most of the water vapor in the atmosphere, either by building observatories high up on mountains or by placing satellites in space. The former is still not ideal. While this reduces the amount of radiation absorbed, much still is absorbed. Figure 1.4 shows the atmospheric transmission at the JCMT observatory on top of Mauna Kea, $\sim$4000 m above sea level. There are atmospheric windows above 800 μm and the region of $450 - 300\,\mu$m where observations are possible. However observing between $20 - 300\,\mu$m is impossible from ground based observatories and in order to access these wavelengths it is necessary to use space based observations.

Another huge problem with infrared observations is poor angular resolution. The maximum possible angular resolution of a telescope is set by the diffraction limit of the mirror and is given by the Rayleigh criterion

$$\theta = \frac{\lambda}{1.22D} \tag{1.1}$$

where θ is the angular resolution limit, D is the diameter of the receiver and λ is the observed wavelength. As sub-mm wavelengths are long when compared to those of optical the angular resolution is much coarser. It is possible to combat this by building bigger dishes but the larger a mirrors the greater the engineering issues when building them. For instance a space based telescope is limited in size by what will fit into the back end

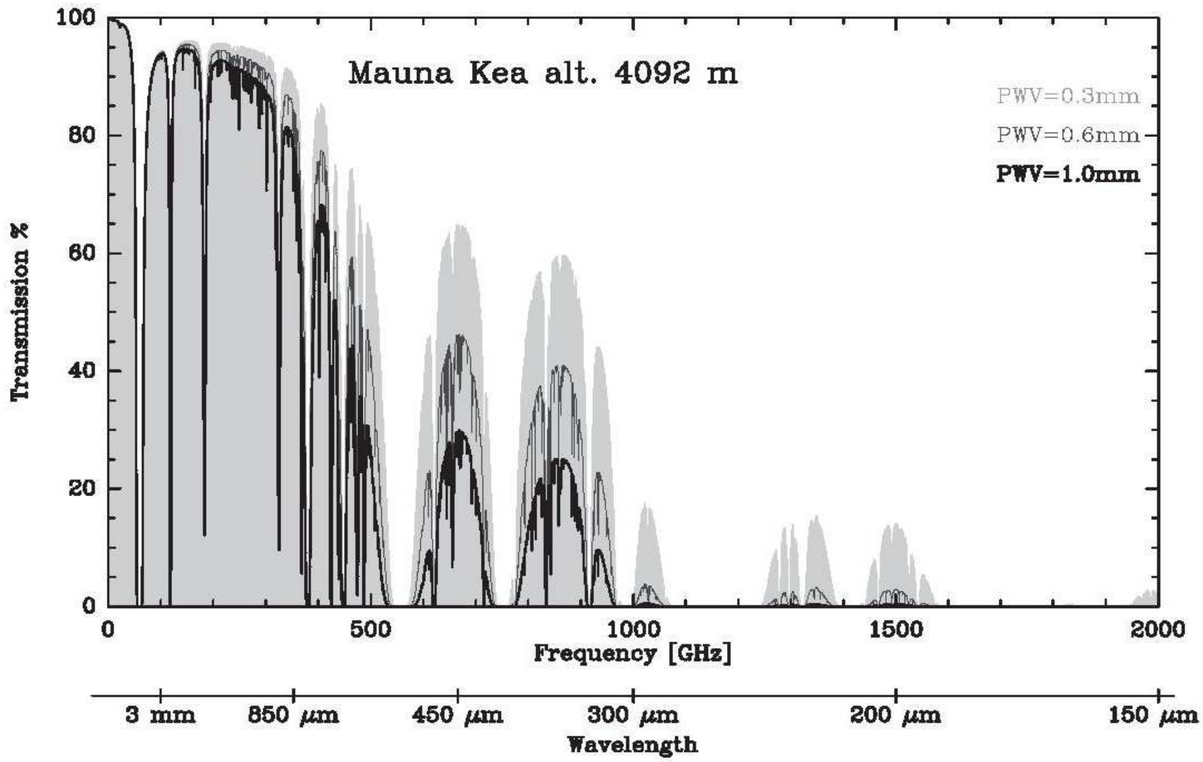

Figure 1.4: Figure taken from Schneider et al. (2009). The infrared transmission through the earth's atmosphere for different precipital water vapor (PWV) levels on top of Mauna Kea.

of a rocket.

This coarseness in angular resolution leads to a problem known as confusion. If two sources are separated by less than the angular resolution then distinguishing between them is difficult, if not impossible and the sources are 'confused'. The longer the wavelength, the greater this problem becomes. It is a common practice to attempt to match sources at one wavelength to those previously observed at another wavelength in order to gain a good range of data. A single sub-mm source will have its signal spread out due to poor angular resolution. This means a single sub-mm source can cover the same area as multiple optical sources and sophisticated matching techniques are required to match them.

1.3.2 Infrared Observatories

It took many years from the initial discovery of IR radiation to develop IR cameras due to the technical difficulties involved in observing at these wavelengths even once you find a wavelength window. Infrared observatories have to be cryogenically cooled as otherwise all the radiation detected from space will be swamped by the thermal emission of the detector itself. An uncooled IR telescope would be the equivalent of an optical telescope made out of fluorescent light tubes. Cooling the detector to cryogenic temperatures is necessary to have any hope of observing emissions from space.

Though other smaller observatories had been imaging sources in the infrared the *Infrared Astronomical Satellite* (IRAS, Neugebauer et al., 1984) was the first observatory to observe a large portion of the sky (96%) at 12, 25, 60 and 100 μm. IRAS detected 350,000 sources in the infrared, several times that which had been observed up until that point. These bands were not sensitive to dust temperatures less than 30K and 90% of the dust mass was expected to emit at longer wavelengths Devereux & Young (1990).

The *Infrared Space Observatory* (ISO, Kessler et al., 1996) followed in 1995, an ESA led satellite imaging in the range of 2.5 - 240 μm as well as spectroscopy. ISO had improved sensitivity and resolution compared to its predecessor but despite its wider bandwidth was still not sensitive enough to observe the coldest dust within galaxies.

The *Spitzer Space Telescope* (Werner et al., 2004) was a NASA project launched in 2003. The instruments on board were once again not sensitive to cold dust but were much more sensitive than that of either ISO or IRAS. The various instruments imaged from 3.6 to 160 μm and Spitzer was the first instrument to detect light from extrasolar planets directly. The small dish (0.6 m), however, meant that the observations suffer from poor angular resolution.

SCUBA at the JCMT was a ground based instrument and the first multipixel camera to image at wavelengths long enough to probe the cold dust content of the universe. This

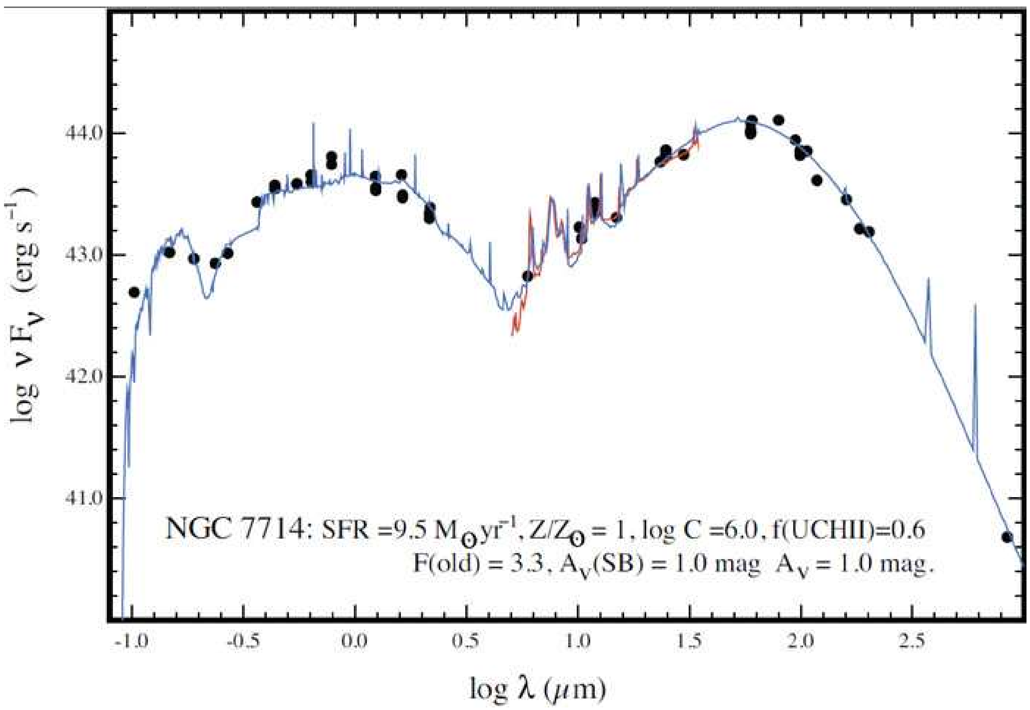

Figure 1.5: Taken from Groves et al. (2008). A model SED (blue curve) is fit to the starburst galaxy NGC 7714. The black points are flux measurements taken of the galaxy and the red curve is the mid-IR spectra [Courtesy M. Dopita].

utilised the observational windows at 450 and 850 μm to be able to make observations from the ground. Due to observational constrains it was still very time consuming to take images and surveys would typically detect only a few tens of sources.

1.4 Spectral Energy Distributions

The spectral energy distribution (SED) is how the flux of a galaxy changes with respect to the wavelength of light being observed. The brightness of a galaxy at a certain wavelength depends on the mechanics and processes taking place within that galaxy. Study of the SED can tell us much about what is going on within a galaxy.

A typical SED that spans both optical and sub-mm wavelengths is shown in Figure 1.5. There are two main peaks within this SED. The lower wavelength peak is in the optical range. This is the emission that comes from the the visible starlight within the galaxy, the sum of all the black body spectra for all the individual stars which emit mainly in the optical and UV. At longer wavelengths in the sub-mm there is a secondary peak. This is from the absorption and re-emission of stellar light by dust within the galaxy which will be covered in detail in Section 1.4.1.

Over the top of these two peaks there is a series of peaks and troughs, absorption and emission lines of elements within the galaxy. These can be used to determine the metalicity of the galaxy which is strongly related to its age and can give key clues to how star formation evolves over time.

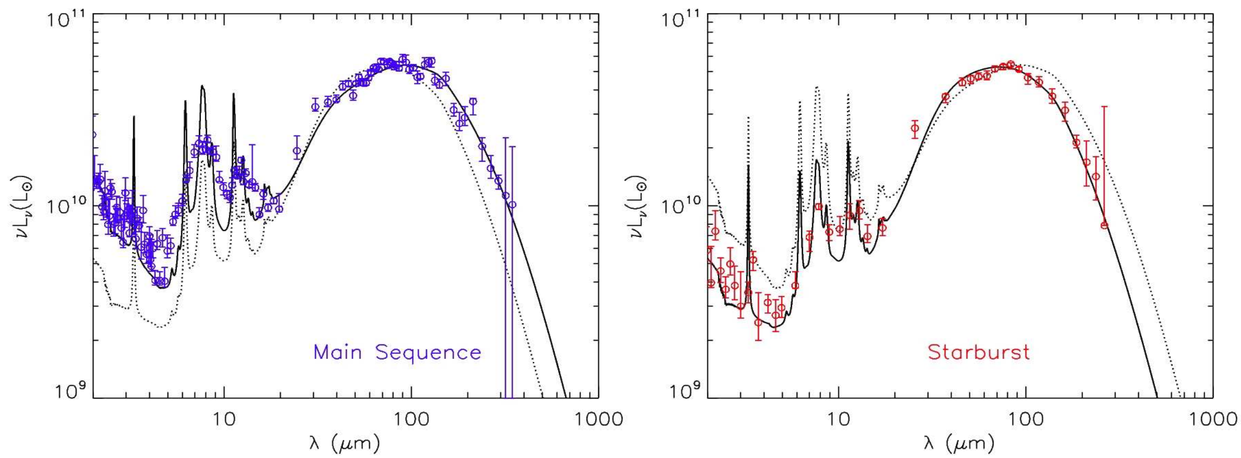

Figure 1.6: A typical infrared SED for a main sequence (left) and a starburst (right) galaxy at infrared wavelengths. To the left there are a great many spectral lines from the gas within the galaxy, but to the right from 30 μm is the secondary peak caused by re-emission of the dust. David Elbaz, CEA Saclay, Service d'Astrophysique.

Figure 1.6 shows the sub-mm SEDs for a normal galaxy with a moderate amount of star formation (labeled as Main Sequence) and a starburst galaxy with a period of intense star formation. There are certain common features between the two but there are also key differences that can be used to differentiate between them. The main grey body peak for the starburst galaxy is slightly narrower. At the lowest wavelength end of both SEDs is a region of strong emission lines. These stem from polycyclic aromatic hydrocarbons (PAHs), a group of molecules based around benzene rings which emit in the mid-IR, from 1-10 μm. In this region the continuum is much higher for main sequence galaxies compared to starburst galaxies and all of these features can be used to best determine the type of galaxy being considered. If more of the SED can be observed then other features can also be used such as the 4000 Åbreak where calcium lines in spiral galaxies appear to create a sudden jump in the SED at 4000 Å.

In Figure 1.5 a model SED, created from many detailed observations and modeling, is fit to flux observations of a galaxy. This method of SED fitting requires a huge amount of data about a certain galaxy with as many observations as possible to ensure the best fit.

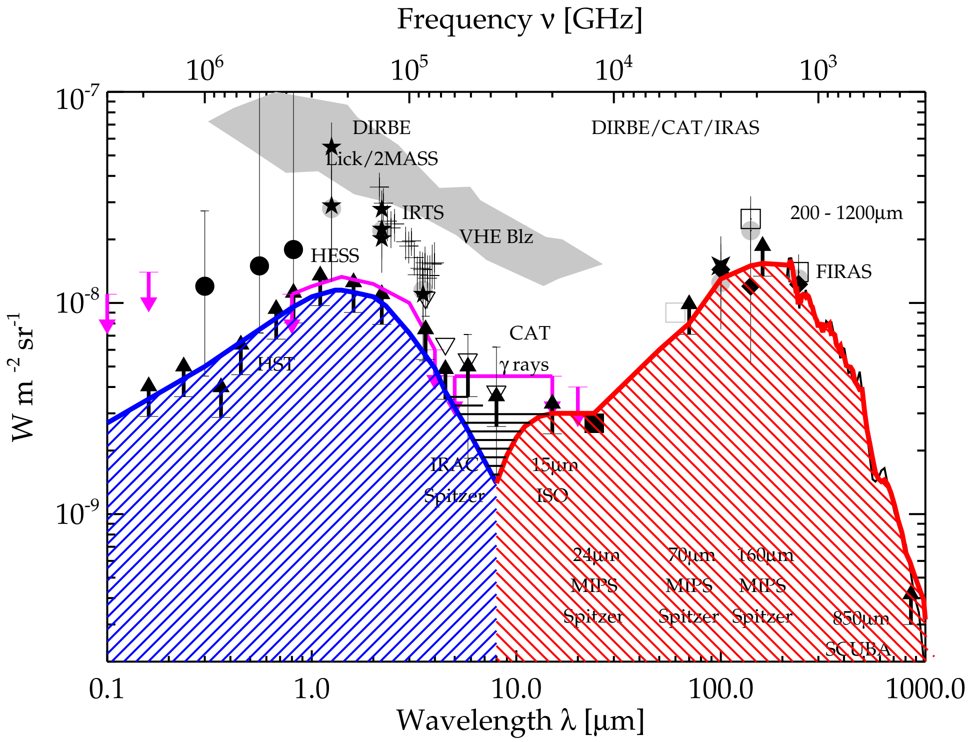

Figure 1.7: Figure taken from Dole et al. (2006). An estimate of the CIB (red) and optical (blue) background in the Universe.

1.4.1 Dust and the infrared

Within a galaxy dust absorbs a huge amount of starlight and then re-emits this light in the form of infrared radiation, so by studying dust it is possible to ascertain information about the underlying stellar population that lies hidden within the cloud.

The Cosmic Infrared Background (CIB) is the accumulation of all infrared sources in the sky. The CIB is thought to have as much energy as both the UV and optical output combined (see Figure 1.7), suggesting that half of all energy output by stars is absorbed by dust clouds and then re-radiated in the sub-mm, peaking at around $\sim 140\,\mu$m (Elbaz et al., 2002). Studies of the local universe (Soifer & Neugebauer, 1991), however, found that IR output of galaxies is only about one third of the output of optical galaxies. To account for this discrepancy galaxies must have evolved greatly between now and early cosmic time.

It was relatively recently that astronomers were able to resolve the CIB into individual galaxies, known as sub-mm galaxies (SMGs). These are very distant galaxies observable only in the sub-mm and infrared. They are believed to be a group of very dusty galaxies undergoing a period of high star formation. The limits on the observable windows means that attempts to resolve the CIB have been restricted to these windows. This meant that the peak of emission has yet to be resolved into individual sources.

To astronomers at optical wavelengths dust is a huge nuisance, as dust clouds within our own galaxy blocks out the light from stars behind it by both scattering and absorption. Preferential absorption of certain wavelengths can also led to reddening of the galaxy.

The exact composition of dust is still uncertain. Grains trapped in meteorites give us some physical evidence but for the main part we must rely on observations of dust. Observations of absorption and emission features in the infrared region suggest that the bulk of dust is made up of silicates and carbonaceous materials. The precise size of grains is unknown but it is thought that there is a wide distribution of sizes.

There have been efforts to recreate interstellar dust grains in the lab (Jones, 2002) as there are many attributes of such grains it would be useful to know but which are difficult to test from observation, such as the dust emissivity index which relates how well a gas emits radiation. It is difficult to measure this quantity from observations of galaxies as it is degenerate with temperature, meaning that changes in the dust emissivity are easily confused with changes in the temperature.

Dust is thought mainly to originate from the outer layers of post main-sequence stars such as giants, super giants and asymptotic giant branch stars which are then blown off by interstellar winds. These conditions are just right to allow grains to grow (Salpeter, 1974). It was recently discovered that dust grains can also grown in supernovae (Gomez et al., 2012). It was previously thought that the intense environments of supernovae would destroy dust grains but it appears that after the initial shock wave dust grains are able to condense. However the relative importance of these two is as yet unknown.

1.4.2 Why study dust?

In terms of mass, dust only makes a small contribution to the galaxy as it is only 1% of the interstellar medium (ISM) (Whittet, 2003), which in turn only comprises 15-20% of the mass contained within the galactic disk (Yin et al., 2009). In terms of its contribution to the mechanics and evolution of the galaxy, though, it is very important.

Dust is a key driver of star formation within galaxies. Dust absorbs the UV radiation that would cause molecules to dissociate and provides a formation site for H_2 allows the dense hydrogen clouds necessary for star formation to form. Studying dust is important to understanding the evolution of galaxies. The role and abundance of dust within an individual galaxy changes over cosmic time as different stages of star formation change and tracking dust helps to track changes in the galaxy population as a whole. It is also important to understanding the underlying stellar population that is heating the gas. This star light isn't lost, merely reprocessed and by considering dust it is possible to obtain a full picture of the stellar population.

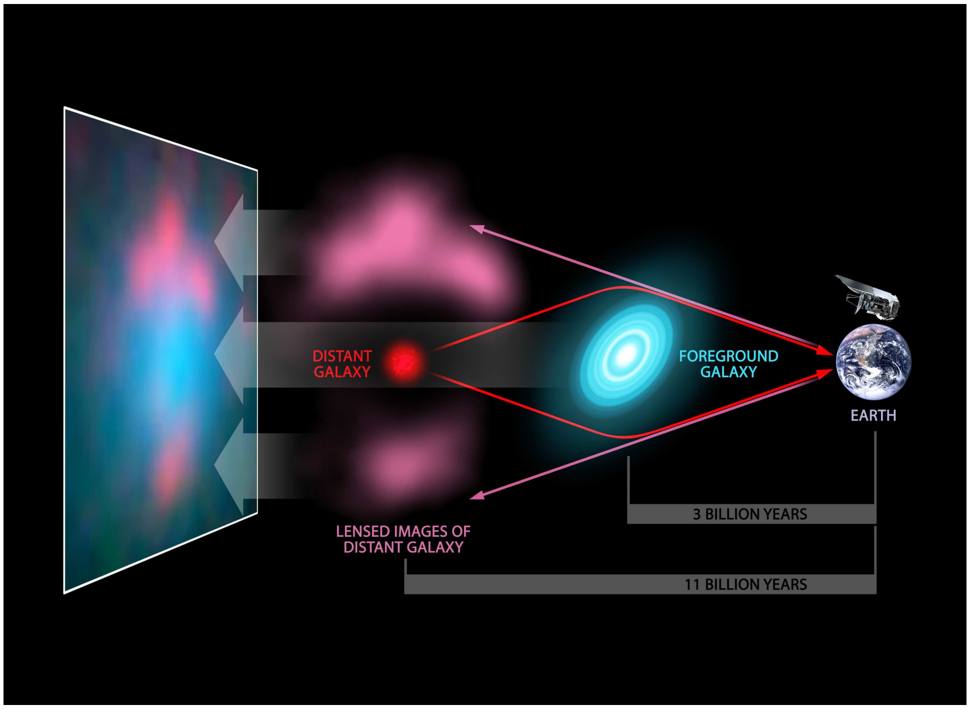

Figure 1.8: A schematic of gravitational lensing. The foreground galaxy acts as a giant lens, bending the light of the distant galaxy, resulting in a distorted image.

1.5 Gravitational Lensing

The principal of gravitational lensing arose from the Theory of Relativity, stating that if two objects lie along the same line of sight then the light from the background object would be bent by the gravitational well of the foreground object. The foreground object would act like a lens, magnifying the background object. This was confirmed to be the case by observing the bending of light from stars around the sun (Dyson et al., 1920). Einstein (1936) put forward that lensing could happen with lens stars other than the sun but that "there is no hope of observing this phenomenon directly". However the same principal applies when whole galaxies are considered and such lenses are much easier to observe and were detected by Walsh et al. (1979).

A statistical study of lens populations is a good way to test cosmological constants and probe models of galaxy formation (Blandford et al., 1989; Turner, 1990; Fukugita & Peebles, 1993; Cooray & Huterer, 1999; Cooray, 1999) as it is a direct study of the mass distribution of the universe. The magnification effect means that it is possible to probe high redshift sources that would other wise being too dim to be observed. This is particularly beneficial in the sub-mm where poor angular resolution and high source confusion make studying high redshift objects difficult. However the detection of gravitational lenses is slow, time consuming and unreliable as the best method is to survey by eye. Though lensing happens throughout the galaxy on a small scale, in order to be strongly lensed the lens must be very massive and the alignment very precise so the chances of this occurring is relatively low and strong lenses are quite rare. When strong lensing occurs there is obvious distortion of the background galaxy, the image forming arcs and possibly even a ring on the sky around the foreground lens. The most common method of detection is looking for disturbed morphology and multiple images due to lensing but is only obvious in the most extreme cases. If the lensing is not extreme enough to distort the background galaxy into the tell-tale arcs and rings then it is difficult to tell whether or not the source is simply a funny shape. The handful of previously detected lenses showed that lens galaxies are dominated by large early type galaxies (Fukugita & Turner, 1991).

A more rigorous method for finding lenses needed to be found if there was any hope of using these lenses as a statistical sample. It was proposed (Blain, 1996; Perrotta et al., 2002, 2003; Negrello et al., 2007) that sub-mm galaxies could be very useful in the search as a simple cut in flux density would greatly increase the proportion of lensed sources in a sample. The number counts of sub-mm galaxies is very steep, meaning that if a sub-mm sources is very bright at 500 μm it has a large likelihood of being a lensed source (see Figure 1.9). So far this has proved very successful (Negrello et al., 2010). As the lenses lie at significantly lower redshifts they are likely to have been previously observed and so are easily found. If a high redshift sub-mm galaxy is strongly associated with or found near a low redshift optical galaxy then there is a good chance that the two might be related.

As the surface density of sources at such flux limits is very low previous surveys have been unable to take full advantage of this effect due to high levels of confusion (Devlin et al., 2009) and small survey area size (Coppin et al., 2006; Weiß et al., 2009a). With the advent of the *Herschel Space Observatory* (Pilbratt et al., 2010) such large surveys are now being conducted and this method can be fully exploited.

1.6 High Redshift Galaxies

Studying the history and evolution of galaxies can be done in one of two ways: studying nearby galaxies as they are at the current epoch and trying to trace back their growth; or observing high redshift objects. The former is easier from an observational stand point but analysing the data is difficult and many assumptions have to be made. When observing distant objects, however, we are observing them as they were in the past, so we do not need to extrapolate what they used to be like. Such distant observations are very challenging though. There are many observational biases and problems, such as dust

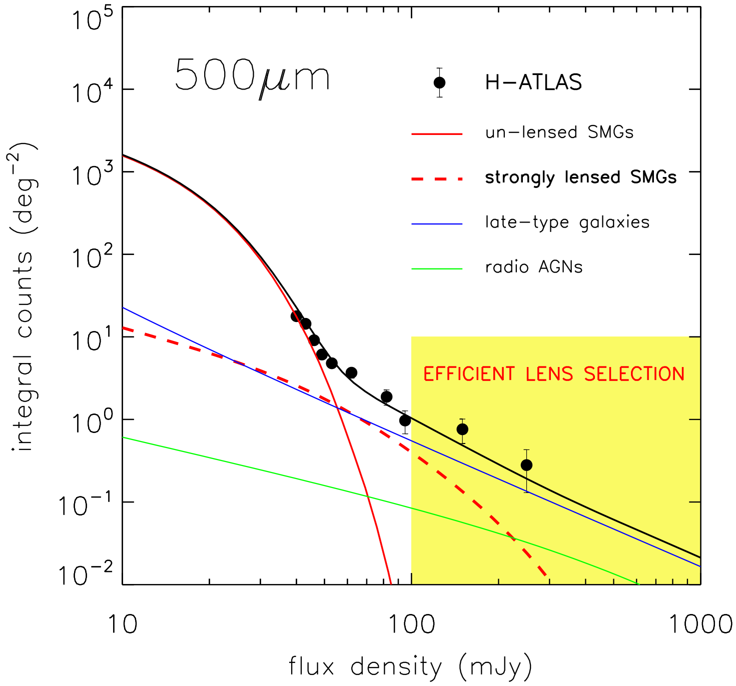

Figure 1.9: Source counts at 500 μm of different populations. At very bright fluxes the lensed SMGs dominated over the unlensed SMGs. Taken from Negrello et al. (2010).

extinction and that SMGs are very faint.

When performing studies which examine changes over redshift it is important make sure that the redshift of the objects in the study are known accurately. Redshifts can be determined in one of two ways: spectroscopically or photometrically.

1.6.1 Spectroscopic

Spectroscopic methods of redshift determination require looking for a feature, most often an emission line of an element. These occur at a specific wavelength and so by determining what wavelength they have been shifted to it is possible to determine what redshift the source is at. Most often this is done at optical and near-IR wavelengths using a spectrograph. These use diffraction gratings to split the light into a spectrum which can then be analysed. Until recently most spectrographs could only split one beam at a time and required large array CCDs to image however new developments have made spectroscopy much more efficient.

Obtaining spectroscopy of sources, particularly those at high redshifts, is difficult and time consuming. As distance increases the spectral lines become less clear and the changes in redshift can mean that the observed lines are redshifted beyond the limits of the spectrograph.

It is possible to determine the redshifts of distant sources using CO line spectroscopy. CO is the second most abundant molecule after H_2 found in most galaxies and is often used as an H_2 tracer. As it is a diatomic molecule it has a rotational quantum state, determined by the quantum number J. The rotational energy level, $E(J)$ is found using

$$E(J) = B\ J(J+1) \qquad J = 0, 1, 2, ... \tag{1.2}$$

where B is a rotational constant. The ground state (J = 0 - 1) transition produces a line at 2.6 mm. Higher energy transitions are usually observed as well, and these occur at shorter wavelengths. However CO observations are not always possible for every galaxy. Higher energy transition lines are needed to determine redshift and sometimes these are not present or too weak. This can happen if the gas is not warm enough to excite to higher energy states. CO spectroscopy is particularly useful for sub-mm sources as CO lines arise from molecular gas and if there is dust it is likely there will be molecular gas as well (Weiß et al., 2009a). Until recently such observations were time consuming and difficult to produce as receivers were very narrow band meaning it was difficult to pin point the lines needed unless there was already a fairly good knowledge of the redshift.

1.6.2 Photometric

Photometric methods use flux measurements at a range of wavelengths to determine how much the SED has been shifted. This method is a lot less precise than the spectroscopic method. No two galaxies are the same. Even using a very well defined model SED and taking account of differing galaxy types there will be differences between the model and the actual galaxy. Errors on the flux measurements of the galaxy will propagate into the redshift as well.

1.7 *Herschel*

The *Herschel Space Observatory* (Pilbratt et al., 2010) was launched on 19th May 2009 and was a huge advancement in the field of sub-mm/infrared astronomy. Previous to *Herschel*'s creation the observations were limited to small areas, poor angular resolutions and limitations on the wavelengths available for study. *Herschel*, however, with a 3.5m primary mirror, was capable of observing very distant objects. The wavelength range covered by *Herschel* (60 - 680 μm) covers most of the dust emission of a typical galactic SED. The satellite was positioned at the second Lagrangian point 1.5 million km from the Earth, meaning that the Sun and Earth were always within close proximity to each other, increasing the field of view available.

The detectors of the telescope were cooled with liquid helium to temperatures of 0.3 K while much of the rest was cooled to 4 - 10 K. This coolant boiled away over time and, while precautions were set in place to make the cooling as efficient as possible, it set the life time of *Herschel* at roughly 3 years. The helium dropped too low to maintain operation on 29th April 2009 and the last of the satellites fuel used to knock it into a solar orbit.

The telescope had three main instruments.

1.7.1 SPIRE

The Spectral and Photometric Imaging Receiver (SPIRE) was capable of observing at 250, 350 and 500 μm bands simultaneously. Each band was detected by an array of 139, 88 and 43 bolometers respectively. The instrument also contained a low-resolution spectrometer covering 194-672 μm. SPIRE performed very well, with 1σ sensitivities of 5.8, 6.3 and 6.8 mJy/beam. This meant that the maps were so sensitive that the survey was often limited by confusion as much as by their signal to noise ratio.

This region of the sub-mm is the least examined by previous instruments due to its absorption by the Earth's atmosphere and allowed new insight into the cold, dusty universe. The spectrograph was used to gain a new understanding of the chemistry of the ISM, observing carbon monoxide and water lines as well as many others.

1.7.2 PACS

The Photodetecting Array Camera and Spectrometer (PACS) had three potential bands at 70, 100 and 160 μm though only either the 70 or 100 μm band could be observed along side the 160 μm at any time. It too contained a spectrometer covering the wavelengths 55 - 210 μm. The instrument was capable of imaging along side SPIRE in 'parallel' mode.

The main scientific drive of PACS was to answer questions on topics such as the origin of stars, planetary systems, galaxies and the evolution of the universe.

1.7.3 HI-FI

The *Herschel* Heterodyne Instrument for the Far Infrared (HI-FI) was a high resolution spectrometer between 157 - 625 μm. The instrument only had a single pixel but maps could be built up from several observations. The main goal of the instrument was investigate the ISM and its interaction with stars in galaxies by searching for molecular rotational lines.

1.8 H-ATLAS

The *Herschel* Astrophysical Terahertz Large Area Survey (H-ATLAS, Eales et al., 2010) was the largest open time project using the *Herschel* satellite. Over 600 hours of observing time the survey covered 550 square degrees with both SPIRE at (250, 350 and 500 μm) and PACS (at 100 and 160 μm), operating in parallel mode so both instruments could operate at once. The size of the survey is of more importance than the sensitivity and so only two scans were taken, in near orthogonal directions, and using the fastest scan rate (60 arcsec s^{-1}).

H-ATLAS is an extragalactic survey and so the fields were chosen to have minimal amounts of Galactic dust. Fields were chosen along the celestial equator (GAMA fields) and at both the northern (NGP) and southern galactic pole (SGP) to ensure a good spread across the sky (see Figures 1.10 and 1.11). The three GAMA fields make up Phase 1 of the survey. In addition the fields were chosen depending of the amount of complimentary data available from surveys at many different wavelengths:

- Spectroscopy is covered by the Galaxy and Mass Assembly Survey(GAMA, Driver et al., 2011), Sloan Digital Sky Survey (SDSS, York et al., 2000) and 2dF Galaxy Redshift Survey (2dFGRS, Colless et al., 2001).

- Much of the survey area has been covered in the ultraviolet by GALEX.

- At optical wavelengths the SDSS has also covered the GAMA and NGP fields in five bands. GAMA and the SGP fields have been covered by the Kilo Degree Survey (KIDS) on the VLT Survey Telescope (VST) and in six bands by SkyMapper (Keller et al., 2007). Pan-STARRS1 will also cover the NGP and GAMA fields in five bands. The SGP field will eventually be covered by the Dark Energy Survey.

- In the near infrared the GAMA and NGP have been covered by the Large Area Survey (LAS) in four bands as part of UKIRT Infrared Deep Sky Survey (Warren et al., 2007). The VISTA Kilo-Degree Infrared Infrared Galaxy Survey (VIKING) will cover GAMA and SGP fields in five bands.

- NRAO VLA Sky Survey has covered all fields at 1.4 GHz but not with enough sensitivity to detect a significant proportion of H-ATLAS sources. To compensate for this the GAMA fields were covered with the Giant Meter-wave Radio Telescope (GMRT) with a 5σ sensitivity of 1mJy at 325 MHz (Mauch et al., 2013). The NGP will be covered with the Low Frequency Array for Astronomy (LOFAR).

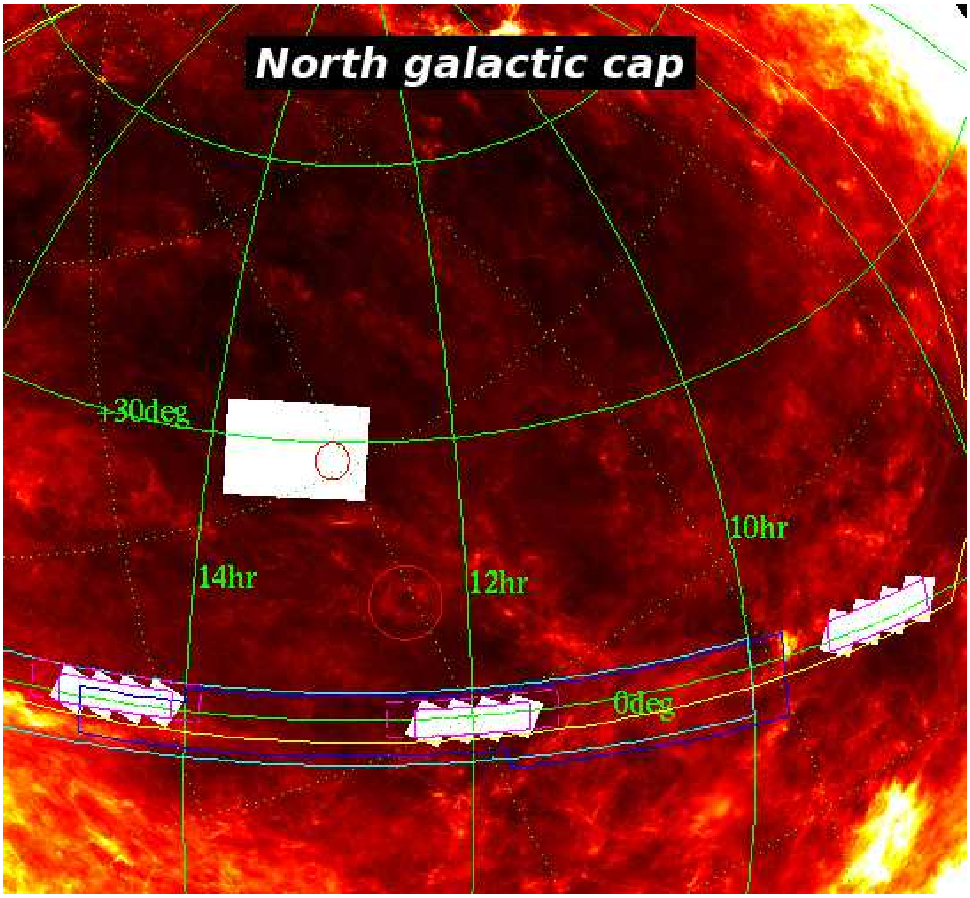

Figure 1.10: The H-ATLAS fields shown in white superimposed upon the IRAS 100 μm map tracing the galactic dust. Ra and dec are shown with solid green lines, green dotted lines show the ecliptic latitude and longitude. KIDS/VIKING is highlighted in cyan, yellow shows the SDSS area, blue the 2dFGRS fields, magenta the Dark Energy Survey, magenta/ blue dashed are the areas covered by the South Pole Telescope (Eales et al., 2010).

The expected magnitude limits of the various fields are given in Table 1.1. For this work only the Phase 1 data is considered, covering the three GAMA equatorial fields at 9, 12 and 15 hr.

1.8.1 Aims of H-ATLAS

H-ATLAS has several projects of interest. H-ATLAS is a relatively shallow survey so there is a large focus on the local universe. Making accurate estimates of the local sub-mm luminosity and dust mass function will help to understand the structure and composition of the local universe within the last three billion years. Using existing redshift surveys it is possible to investigate the star formation in galaxies that are obscured at optical wavelengths by dust.

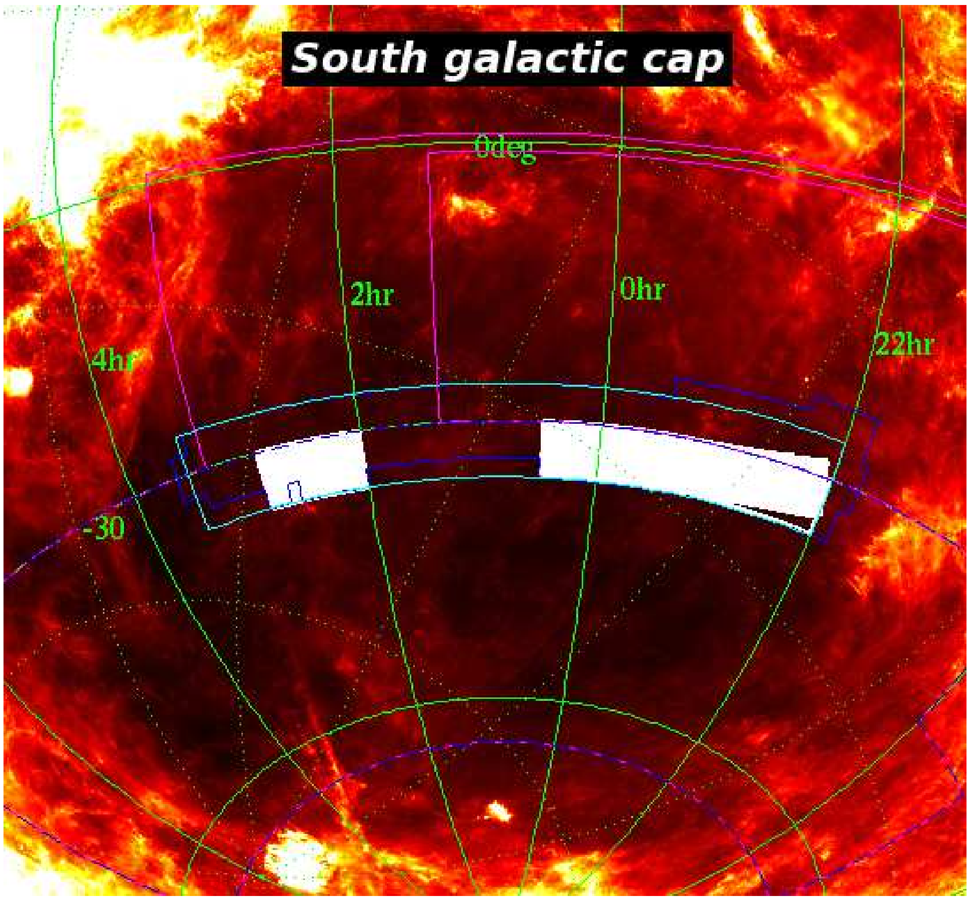

Figure 1.11: As Figure 1.10 for the south fields

Table 1.1: The sensitivity limits of various ancillary surveys in AB magnitudes (Eales et al., 2010).

H-ATLAS field	Datasets	u	v	g	r	i	z	Z	y	Y	J	H	K
NGP	SDSS	22.0	...	22.2	22.2	21.3	20.5	...	...	...	...	...	...
NGP	Pan-STARRS1[a]	...	...	24.1	23.5	23.4	22.4	...	21.2	...	...	...	...
NGP	LAS	...	...	...	...	...	...	...	...	20.87	20.55	20.28	20.13
GAMA	SDSS	22.0	...	22.2	22.2	21.3	20.5	...	...	...	...	...	...
GAMA	KIDS	24.0	...	24.6	24.4	23.4	...	...	...	...	...	...	...
GAMA	Pan-STARRS1[a]	...	...	24.1	23.5	23.4	22.4	...	21.2	...	...	...	...
GAMA	SkyMapper[b]	22.9	22.7	22.9	22.6	22.0	21.5	...	...	...	...	...	...
GAMA	LAS	...	...	...	...	...	...	...	...	20.87	20.55	20.28	20.13
GAMA	VIKING	...	...	...	...	...	...	23.1	...	22.4	22.2	21.6	21.3
SGP	KIDS	24.0	...	24.6	24.4	23.4	...	...	...	...	...	...	...
SGP	SkyMapper[b]	22.9	22.7	22.9	22.6	22.0	21.5	...	...	...	...	...	...
SGP	VIKING	...	...	...	...	...	...	23.1	...	22.4	22.2	21.6	21.3

A large number of objects are observed that are not in the local universe. Even with only two scans *Herschel* is capable of resolving the CIB into discreet sources meaning it is possible to examine the large scale structure of the sub-mm universe.

The H-ATLAS fields provide a new way of searching for rare gravitational lenses. Several different methods of finding such lenses are currently being investigated. From these lensed systems we can investigate the evolution profile of such lenses and study the structures of high redshift dusty sources.

Active galactic nuclei (AGN) are galaxies with a compact region of abnormally high luminosity at their centre. This is believed to come from the accretion of mass by the galaxy's central supermassive black hole. By studying these AGN it is possible to investigate the relationship between the formation of black holes and the formation of stars.

H-ATLAS covers a huge area, is estimated to show around 200,000 individual sources that reach to very high redshifts. Measurements, such as angular correlation functions, will allow us to test various models of galaxy formation. The unresolved background data (H-ATLAS will only resolve $\sim 10\%$ of the extragalactic background radiation) holds a wealth of data on the clustering of dust in the universe.

Though care has been taken to avoid dust within the Galaxy, there will be some dust from stars which can be studied, particularly the dust and debris disks around stars on the asymptotic giant branch. It may also be possible to look for prestellar cores and protostars.

1.9 Thesis outline

This thesis is organised as follows:

- In Chapter 2 I will introduce a sample of well known and well measured sources for the H-ATLAS field. These are all bright sources with very precisely measured redshifts. They are chosen to be a representative sample of all the H-ATLAS sources however many potential sources of bias are possible, which will be discussed here.

- Chapter 3 discusses creating a template SED from the sample of sources in Chapter 2. From this template the redshifts of every source in the H-ATLAS sample shall be estimated. These estimates are then examined for their viability and accuracy.

- Chapter 4 uses the redshift distributions from Chapter 3 to determine the luminosity function of the Phase 1 field, examining how the luminosity of SMG changes with redshift.

- Chapter 5 uses the redshift distributions to determine the angular correlation function in the Phase 1 field. This investigates the clustering of the field and how it changes with redshift.

- Chapter 6 summarises the thesis and talks about possible future work.

Chapter 2

The High Redshift Sample

This history of astronomy is the history of receeding horizons.

Edwin Hubble

2.1 Introduction

The H-ATLAS survey observed a huge number of sub-mm galaxies (SMGs) to deep redshifts. While the fields were chosen for their wealth of complimentary data, finding the multi-wavelength counterparts for all of the sources is difficult. Those at high redshifts are the most difficult to find. In Phase 1 of the survey, covering the GAMA 9, 12 and 15 hr fields, over 78,000 sub-mm sources were detected (Maddox et al., 2010; Rigby et al., 2011). Many of these were matched to counterparts at optical wavelengths (Smith et al., 2011) from the SDSS catalogues (York et al., 2000). This involved using a likelihood technique to match sources by taking the sub-mm positions and searching for optical sources within a $10''$ radius.

The likelihood ratio is the ratio of the probability of the ID being correct and the probability of the source being a random back ground source. As there was often more than one source within the search radius, a reliability for each source was found, i.e. the reliability that the counterpart found was the correct one from the other sources in the search radius. If this reliability factor was greater than 80%, the source was considered a match. This means that sources with two potential counterparts were often removed. This found counterparts to 30% of all sources in the catalogue, most of which had either a spectroscopic or a photometric redshift. Nearly all of these were at $z < 1$ and 77% are at $z < 0.5$. For this reason a great many previous in depth studies have been targeted at low redshift sources (Dunne & Eales, 2001; Farrah et al., 2003; Yang et al., 2007; Clements et al., 2010) as these were the only sources with a redshift.

When observing SMGs at high redshift, Malmquist bias begins to effect the results:

in order to observe objects at high redshifts they must be the most luminous objects if they are to be detected above the flux limit of the survey. This means that sources that are observed at high redshifts will be bright.

Ultra luminous infrared galaxies (ULIRGs) are galaxies where the infrared luminosity between (1-1000 μm) is in excess of $L_{\mathrm{FIR}} \geq 10^{12}\mathrm{L}_{\odot}$ and the bulk of the luminosity emitted in the infrared (Wright et al., 1984; Sanders et al., 1988). In the local universe these are considered to be galaxies undergoing a starburst phase, resulting from the merger of two gas and dust rich spirals as they blend together to form a single massive elliptical (Barnes & Hernquist, 1991).

Locally these are intense starburst galaxies resulting for mergers and AGN activity and are thought to be the precursor to elliptical galaxies in the local universe. In the local universe such IR bright galaxies are relatively rare but as look back time increases ($z \geq 1$), IR bright sources become much more common (Blain et al., 2002; Fox et al., 2002; Scott et al., 2002; Floch et al., 2005). What is not known is whether these high redshift ULIRGs arise from mergers as with their low redshift counterparts or whether they are caused by a different mechanism entirely. While the properties of low redshift ULIRGs have been studied in depth at a multitude of wavelengths this is much more difficult for the high redshift IR bright galaxies.

This Chapter will take a sample of well catagorised high redshift sources in order to compare them to the properties of low redshift ULIRGs.

2.2 Source selection

In order to examine high redshift IR bright SMGs I first needed to create a selection of well defined sources with highly accurate flux measurements at high redshift, which I define here to be sources with $z > 0.5$. I created two separate subsets for this sample: one for sources with $0.5 < z < 1$ and a second with $z > 1$.

The first subset were sources with spectroscopic redshifts from the SDSS counterparts in the range $0.5 < z < 1$. I wanted to create a sample of sources with good flux measurements and so only considered sources with $S_{250} > 50\,\mathrm{mJy}$. This insured that the sources were bright, so had a good signal to noise ratio, but were not so bright that they were likely to be a subset of unusual galaxies. From these cuts 25 sources were selected at random (see Table 2.1). Only 25 were chosen so as to not overwhelm the sources at $z > 1.0$ (see below) and these are discussed in further depth in Section 2.3.

There is a chance that the sources we select in this way are in fact gravitationally lensed pairs, so that the optical and sub-mm source are actually separate galaxies with the SMG being lensed by the low redshift optical counterpart. This would mean that the redshift of the optical galaxy was not the same as the redshift of the SMG. Using a $S_{250} > 50\,\mathrm{mJy}$ increases the likelihood of this being the case (Negrello et al., 2010). However all of these sources have bright optical counterparts and the SPIRE fluxes suggest that the spectroscopic redshift is correct.

For the high redshift end, $z > 1$, I did not use the SDSS survey to provide optical redshifts in order to make the selection. Galaxies observed with an optical redshift of $z > 1$ by the SDSS tend to be atypical objects such as quasars. I wanted this sample to be as typical of all H-ATLAS high redshift galaxies as possible so only sources where the redshift had been verified by other means were used, in this case using observations of the CO transition lines to perform spectroscopy on the sources. This work concerns itself with Phase 1 of the H-ATLAS survey. At the time of this work 17 sources had had follow up CO observations for a variety of instruments. Of these 17 only 15 are used in this work (see Table 2.2). Two were removed due to uncertainties. These sources will be discussed in greater depth in Section 2.4.

I call this sample the High Redshift sample (HS). Figure 2.1 shows the colour relation between S_{350}/S_{250} and S_{500}/S_{350}. Sources without spectroscopic redshifts are slightly skewed towards redder colours. This is expected as high redshift sources are more likely to not have an optical counterpart and so not be spectroscopically detected. The spectroscopically selected high redshift sources is within the most highly populated region of the colour-colour diagram, and seem to be typical of many other sources both with and without spectroscopic IDs. The colours of the CO sources, meanwhile, are much redder and exhibit much less scatter. For the CO sources the correlation between S_{350}/S_{250} and S_{500}/S_{350} is very linear.

In order to examine the HS more closely I created a rough SED template for each source individually. It is important to note that these fits are intended to get 'a feel' for the data, and are no means meant to be a scientifically rigourous explanation of the sources in question. I did this by shifting the fluxes of each source to their rest frame wavelength. To this I then fit a two temperature SED according to a modified black body spectrum:

$$F_\nu = A[B_\nu(T_h)\nu^\beta + aB_\nu(T_c)\nu^\beta] \tag{2.1}$$

where F_ν is the flux at a rest-frame frequency ν, A is a normalisation factor, B_ν is the Planck function, β is the dust emissivity index, T_h and T_c are the temperatures of the hot and cold dust components, and a is the ratio of the mass of cold dust to the mass of hot dust . In accordance with the literature (see Chapter 3) the dust emissivity index has been set to $\beta = 2$. This was not left as a free parameter due to the lack of data points

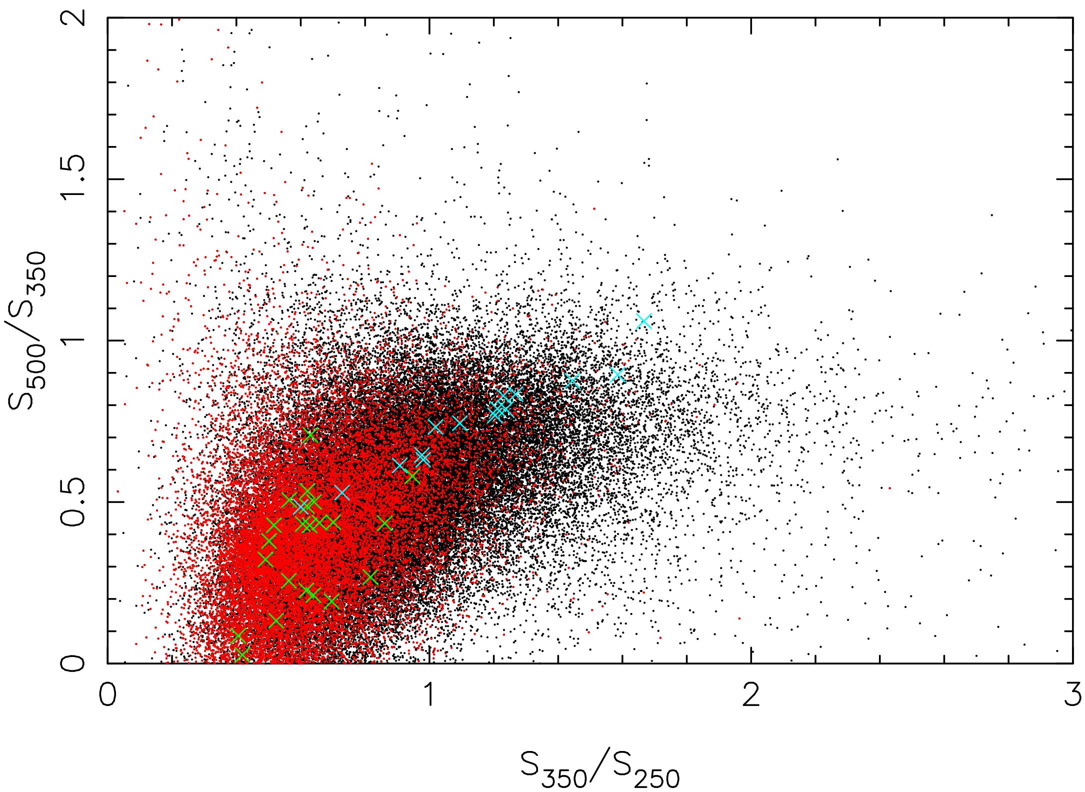

Figure 2.1: The colours of the high redshift sample, spectroscopic sources are shown in green, CO observed sources are shown in cyan. These are compared with the entire H-ATLAS sample (black) and those sources with optical redshifts (red).

Table 2.1: All spectroscopic sources with redshifts $0.5 < z < 1.0$ used to make up the high redshift sample. Redshifts were obtained from the Sloan Digital Sky Survey (SDSS) Data Release 7 (DR7) (York et al., 2000).

No.	H-ATLAS Name	S_{100}	S_{160}	S_{250}	S_{350}	S_{500}	$z_{\rm spec}$	Reference
1	HATLAS J143845.8+013504	-25 ± 30	25 ± 31	74 ± 7	70 ± 8	41 ± 9	0.501	SDSS DR7
2	HATLAS J140746.5-010629	59 ± 41	112 ± 66	81 ± 7	42 ± 8	18 ± 9	0.507	SDSS DR7
3	HATLAS J090758.2-001448	91 ± 38	135 ± 45	63 ± 7	27 ± 8	1 ± 9	0.516	SDSS DR7
4	HATLAS J142534.0+023712	26 ± 45	75 ± 47	70 ± 7	43 ± 8	18 ± 9	0.518	SDSS DR7
5	HATLAS J143703.8+014128	197 ± 44	122 ± 48	115 ± 7	58 ± 8	22 ± 9	0.522	SDSS DR7
6	HATLAS J141815.6+010247	26 ± 43	107 ± 44	58 ± 6	37 ± 7	8 ± 8	0.524	SDSS DR7
7	HATLAS J083713.3+000035	-28 ± 42	84 ± 64	56 ± 7	37 ± 8	16 ± 9	0.534	SDSS DR7
8	HATLAS J090359.6-004555	102 ± 32	178 ± 39	141 ± 7	91 ± 8	45 ± 9	0.538	SDSS DR7
9	HATLAS J140640.0-005951	28 ± 44	53 ± 44	51 ± 7	32 ± 8	23 ± 9	0.539	SDSS DR7
10	HATLAS J140930.6-013805	58 ± 49	46 ± 65	62 ± 7	51 ± 8	14 ± 9	0.539	SDSS DR7
11	HATLAS J141343.4+004041	125 ± 29	105 ± 48	63 ± 7	39 ± 8	19 ± 9	0.546	SDSS DR7
12	HATLAS J121353.8-024317	44 ± 70	144 ± 100	57 ± 7	27 ± 8	-1 ± 9	0.557	SDSS DR7
13	HATLAS J092340.2+005736	25 ± 45	71 ± 49	56 ± 7	23 ± 8	2 ± 9	0.560	SDSS DR7
14	HATLAS J120248.3-022944	13 ± 40	3 ± 69	54 ± 7	28 ± 8	4 ± 9	0.563	SDSS DR7
15	HATLAS J114619.8-014356	73 ± 40	86 ± 67	57 ± 6	40 ± 8	18 ± 8	0.571	SDSS DR7
16	HATLAS J141429.0-000900	45 ± 45	74 ± 47	58 ± 7	50 ± 8	22 ± 9	0.574	SDSS DR7
17	HATLAS J085230.1+002844	165 ± 46	137 ± 48	57 ± 7	27 ± 8	-2 ± 9	0.584	SDSS DR7
18	HATLAS J143858.1-010540	86 ± 41	183 ± 47	79 ± 7	39 ± 8	12 ± 9	0.615	SDSS DR7
19	HATLAS J084846.2+022032	- ± -	- ± -	79 ± 7	49 ± 8	26 ± 9	0.627	SDSS DR7
20	HATLAS J120246.0-005221	47 ± 45	9 ± 49	55 ± 7	31 ± 8	8 ± 9	0.653	SDSS DR7
21	HATLAS J113859.3-002934	-6 ± 48	80 ± 69	52 ± 7	37 ± 8	7 ± 9	0.684	SDSS DR7
22	HATLAS J084217.0+010920	61 ± 38	159 ± 45	55 ± 7	34 ± 8	15 ± 9	0.761	SDSS DR7
23	HATLAS J090420.9+013038	111 ± 43	81 ± 50	62 ± 7	25 ± 8	-10 ± 9	0.792	SDSS DR7
24	HATLAS J114023.0-001043	29 ± 40	56 ± 69	72 ± 7	41 ± 8	21 ± 9	0.844	SDSS DR7
25	HATLAS J141148.9-011439	58 ± 49	79 ± 44	64 ± 7	39 ± 8	9 ± 9	0.857	SDSS DR7

Table 2.2: As Table 2.1 for all the CO observed sources with $z > 1$. Follow up observations were taken using the Caltech Submillimeter Observatory (CSO) with Z-Spec, IRAM Plateau de Bure Interferometer (PBI), Green Bank Telescope (GB) with Zpectrometer, Combined Array for Research in Millimeter-wave Astronomy (CMA), Atacama Pathfinder Experiment (APEX), Sub Millimeter Array (SMA). CO redshifts are listed after the linebreak where H is Harris et al. (2012), F is Frayer et al. (2011), L is Lupu et al. (2012) and C is Cox et al. (2011).

No.	H-ATLAS Name	S_{100}	S_{160}	S_{250}	S_{350}	S_{500}	z_{spec}	Reference	Observations
26	HATLAS J142935.3-002836	821 ± 28	1164 ± 32	778 ± 6	467 ± 7	227 ± 8	1.026	-	ZSpec, CMA
27	HATLAS J090740.0-004200	202 ± 46	385 ± 49	471 ± 7	343 ± 8	181 ± 9	1.577	L	CSO
28	HATLAS J091043.1-000321	141 ± 41	353 ± 47	417 ± 6	378 ± 7	232 ± 8	1.784	L	CSO
29	HATLAS J085358.9+015537	59 ± 40	197 ± 48	389 ± 7	381 ± 8	241 ± 9	2.091	-	ZSpec, PBI
30	HATLAS J115820.2-013753	35 ± 32	162 ± 55	131 ± 6	143 ± 8	106 ± 8	2.191	H	GT
31	HATLAS J090302.9-014127	74 ± 42	202 ± 48	347 ± 7	339 ± 8	219 ± 9	2.305	L	CSO, CMA, GB, PBI
32	HATLAS J084933.4+021443	0 ± 39	169 ± 46	242 ± 7	293 ± 8	231 ± 9	2.410	H	CMA, GB
33	HATLAS J141351.9-000026	29 ± 53	105 ± 69	190 ± 7	240 ± 8	200 ± 9	2.478	H	GB
34	HATLAS J113243.1-005108	-	-	76 ± 7	120 ± 8	108 ± 9	2.578	H	GB
35	HATLAS J091840.8+023047	12 ± 46	118 ± 68	142 ± 7	175 ± 8	138 ± 9	2.581	H	GB
36	HATLAS J091305.0-005343	-14 ± 66	81 ± 86	116 ± 6	140 ± 7	108 ± 8	2.626	L, F, H	CSO, GT, PBI
37	HATLAS J090311.6+003906	75 ± 50	111 ± 50	138 ± 7	199 ± 8	174 ± 9	3.042	L, F, H	CSO, PBI, GT
38	HATLAS J113526.3-014605	30 ± 45	98 ± 45	290 ± 7	295 ± 8	216 ± 9	3.127	H	GB
39	HATLAS J114637.9-001132	92 ± 34	223 ± 35	290 ± 6	356 ± 7	295 ± 8	3.259	H	GB
40	HATLAS J142413.9+022303	-51 ± 50	-73 ± 70	115 ± 7	192 ± 8	203 ± 9	4.243	C	APEX, PBI, SMA

available as well as the fact that there is a strong degeneracy between temperature and dust emissivity. By fixing β we remove ambiguity as to whether changes are caused by differences in β or in temperature.

Two temperature SEDs have been consistently shown to describe SMGs and ULIRGs far better than a single temperature template (Dunne & Eales, 2001; Vlahakis et al., 2005; Clements et al., 2010). However lack of data means that this is not always possible. I varied T_h, T_c, a and A such that

$$\chi^2 = \sum^{\lambda} \left[\frac{S_{\mathrm{model}} - S_{\mathrm{meas}}}{\sigma_{\mathrm{meas}}} \right]^2 \tag{2.2}$$

is a minimum, where S_{model} is the flux as predicted by Equation 2.3, S_{meas} is the observed flux and σ_{meas} is the observed uncertainty.

If the restframe wavelength of all the bands was greater than $50\,\mu$m then the SED was fit to all five flux bands. If the rest frame of any wavelength used was less than $50\,\mu$m then the PACS data was not used, as PACS fluxes begin to leave the regime described by Equation 2.3 and begin to flatten out beyond this wavelength. T_h and T_c were allowed to vary in the range $10\,\mathrm{K} < T < 60\,\mathrm{K}$, a varied over $10^{-5} < a < 10^5$ and A over $10^{-2} < A < 10^2$.

The resulting temperatures and ratios are given in Table 2.3 and the SEDs shown in Figure 2.2. It is worth noting that these results are not intended to be rigorous values for dust temperatures and mass ratios, but are meant to give a rough idea of the galaxies being looked at in this and subsequent Chapters.

It is apparent from the higher redshift sources that our stipulation that the restframe wavelength must be greater than $50\,\mu$m in order to use the PACS bands is warranted, as these wavebands begin to pull away from the regime described by Equation 2.3. In most cases it is the SPIRE fluxes that govern the fit, as the high signal to noise ratio of the PACS fluxes means that they contribute little to the χ^2 value.

However, at this stage four parameters are being fit to only three data points, meaning they are being overfitted. Even though their χ^2s are relatively low, this is merely due to the high number of parameters available and is not representative of a good fit. In order to compensate for this I also performed a single temperature fit using the same procedure but instead of Equation 2.3, I used

$$F_\nu = A B_\nu(T) \nu^\beta. \tag{2.3}$$

The results from this are shown in Table 2.4 and the fits shown in green in Figure 2.2.

The temperatures and dust ratios are shown in Figure 2.3 are compared to the temperatures in Clements et al. (2010) and Dunne & Eales (2001). Dunne & Eales (2001) had 32 sources in the luminosity range $L \sim 10^{10} - 10^{11} \mathrm{L}_{\odot}$, making them luminous infrared galaxies (LIRGs) while falling short of being LIRGs. Clements et al. (2010), however, had 15 sources in the range $L \sim 10^{11} - 10^{12} \mathrm{L}_{\odot}$ pushing them into ULIRG territory.

Several sources were fit with a $\chi^2 > 2$, but are included in the Tables and Figures for completeness. The reasons for these high values of χ^2 is most likely because it is unlikely that high-redshift galaxies will have SEDS that can be explained by the same dust model.

In the single temperature models there are more fits which fail to meet the required χ^2 cut off. This is most likely indicative that a single temperature SED is not sufficient to model these sources. In (Dunne & Eales, 2001) it was also shown that constraining β to higher values (such as $\beta = 2$) forced the SEDs towards a two temperature model, so it could be discrepancies in β that caused the high values of χ^2. However, without more data, I could not investigate this further.

It is also apparent that even when a two temperature fit was used several of the sources tended towards a single temperature. It is again difficult to say whether this is a result of overfitting and lack of data points, or whether this is an indication that these individual sources would be best described by a single temperature fit.

The lower redshift sources have a slightly warmer T_w, with the ULIRGs edging towards the warmer end. T_c appears to be relatively equal between local LIRGs and the HS, though the ULIRGS are slightly warmer. The dust mass ratios are fairly consistent between the different survey. From Figure 2.3 (d) there is a slight upward trend in both temperatures with redshift. However this appears to come from the fact that at $z < 1$ there is a greater spread of temperatures and a few low temperatures drag down the line. At higher redshifts the temperature is fairly evenly scattered. This increase in temperature may be due to an increase in luminosity rather than the increase in redshift, as these sources are likely to be intrinsically brighter.

When a single temperature fit is applied the temperatures obtained seem follow the values obtained for T_w at higher redshifts.

Table 2.3: The SED parameters for all the sources in the Template sample. S ources with $0.5 < z < 1.0$ used the PACS data where available and the spectroscopic redshifts. Sources with $z > 1.0$ used only the SPIRE data and the redshifts obtained from CO follow up observations.

Redshift	T_w	T_c	a	χ^2	Redshift	T_w	T_c	a	χ^2
0.5007	15.29	15.27	36.69	0.762	0.6843	24.57	24.45	4.41	1.144
0.5074	26.27	26.23	2.54	0.079	0.7614	38.49	15.64	10.29	2.318
0.5159	32.44	32.44	0.76	1.143	0.7919	39.15	10.00	0.00	4.884
0.5183	27.69	20.22	6.62	0.001	0.8439	31.93	23.87	3.40	0.201
0.5225	35.13	17.51	5.35	2.396	0.8570	35.87	23.10	2.54	0.715
0.5238	25.70	25.66	3.04	1.296	1.026	34.12	23.27	3.08	6.987
0.5343	20.64	20.64	8.21	1.104	1.577	32.97	32.97	1.32	1.908
0.5375	30.44	15.60	10.14	0.034	1.784	34.47	22.44	4.28	1.623
0.5386	31.30	15.37	20.36	0.414	2.091	33.84	33.84	1.43	0.058
0.5394	31.48	16.35	16.40	1.737	2.191	31.56	27.88	4.11	5.754
0.5460	37.29	13.12	24.81	0.063	2.305	38.28	25.49	3.87	0.000
0.5567	31.32	31.30	1.09	1.569	2.410	29.17	29.08	5.70	0.540
0.5598	28.34	28.30	1.64	1.275	2.478	28.80	28.80	4.05	0.724
0.5629	24.64	24.62	3.48	1.632	2.578	34.41	25.14	14.08	0.000
0.5708	35.09	14.85	19.91	0.144	2.581	30.38	30.37	4.40	0.304
0.5742	32.52	14.63	29.52	0.526	2.626	31.27	31.27	3.61	0.248
0.5837	39.94	10.00	0.00	1.437	3.042	31.73	31.73	3.88	0.293
0.6152	32.29	32.28	0.94	0.920	3.127	40.18	12.93	100.0	0.017
0.6274	22.39	21.68	7.08	2.321	3.259	39.92	22.08	6.34	0.000
0.6528	25.35	25.17	3.40	1.816	4.243	40.19	18.72	22.6	0.000

Table 2.4: As Table 2.3 but using a single temperature fit model.

Redshift	Temp	χ^2	Redshift	Temp	χ^2
0.5007	15.27	0.76	0.6843	24.47	1.14
0.5074	25.28	0.17	0.7614	34.64	2.86
0.5159	32.44	1.14	0.7919	39.04	4.89
0.5183	22.36	0.04	0.8439	26.99	0.24
0.5225	30.69	4.62	0.8570	31.29	0.87
0.5238	25.67	1.30	1.026	32.55	8.51
0.5343	20.64	1.10	1.577	32.22	1.76
0.5375	24.39	4.14	1.784	30.69	9.40
0.5386	20.18	0.94	2.091	31.01	1.36
0.5394	19.87	2.30	2.191	29.14	5.75
0.5460	33.39	3.01	2.305	32.31	0.20
0.5567	31.31	1.57	2.410	28.35	1.14
0.5598	28.31	1.27	2.478	28.79	0.72
0.5629	24.63	1.63	2.578	27.18	0.05
0.5708	25.30	2.57	2.581	30.37	0.30
0.5742	18.83	1.80	2.626	31.27	0.25
0.5837	39.83	1.44	3.042	31.73	0.29
0.6152	32.29	0.92	3.127	38.21	1.10
0.6274	21.82	2.32	3.259	35.65	1.03
0.6528	25.21	1.82	4.243	37.61	1.09

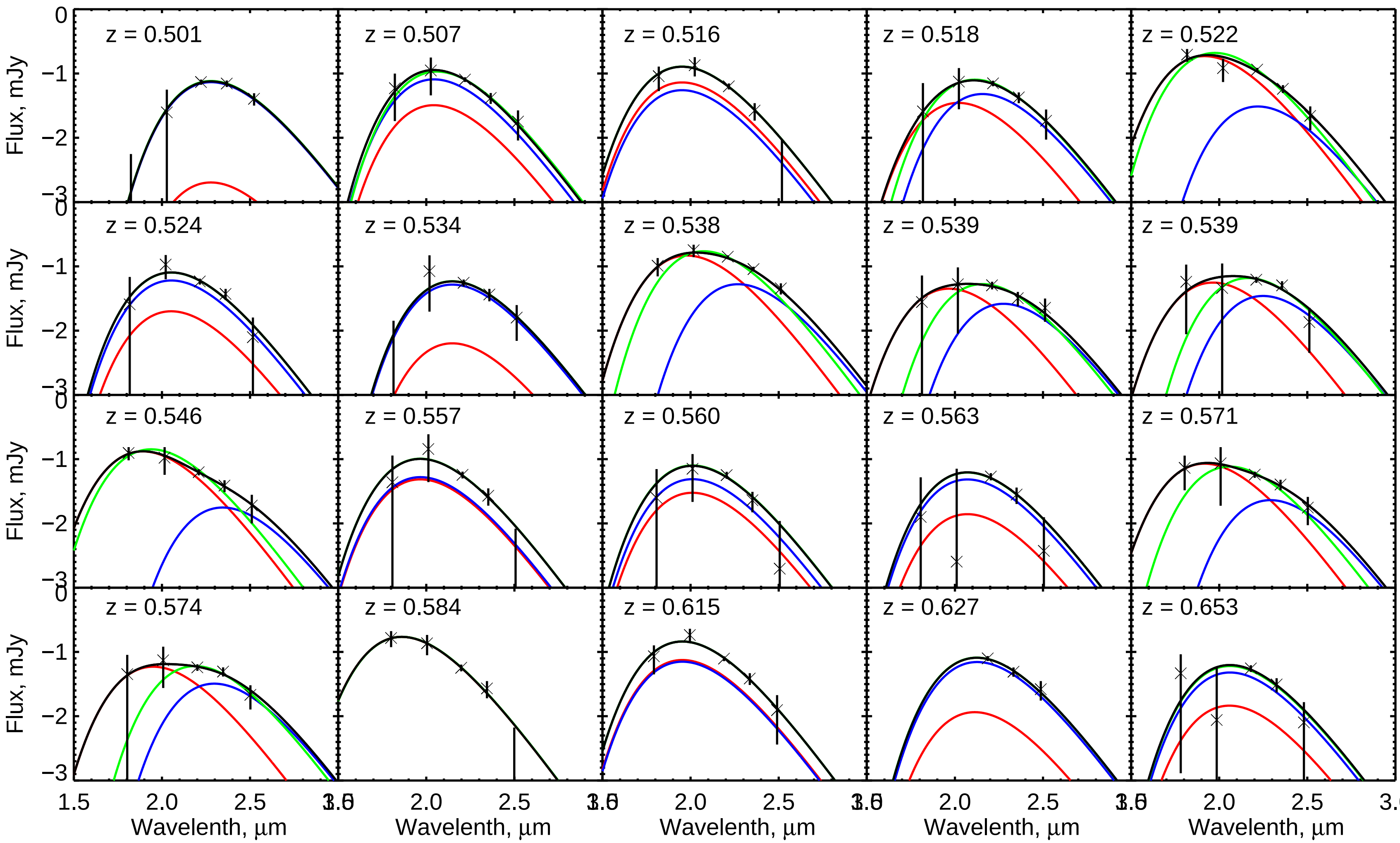

Figure 2.2: SED fits to all of the Template Sample sources. Sources have been adjusted to their restframe wavelength and then fitted with a two temperature SED (black), a single temperature SED (green). The cold (blue) and hot (red) components of the two temperature SED are also shown.

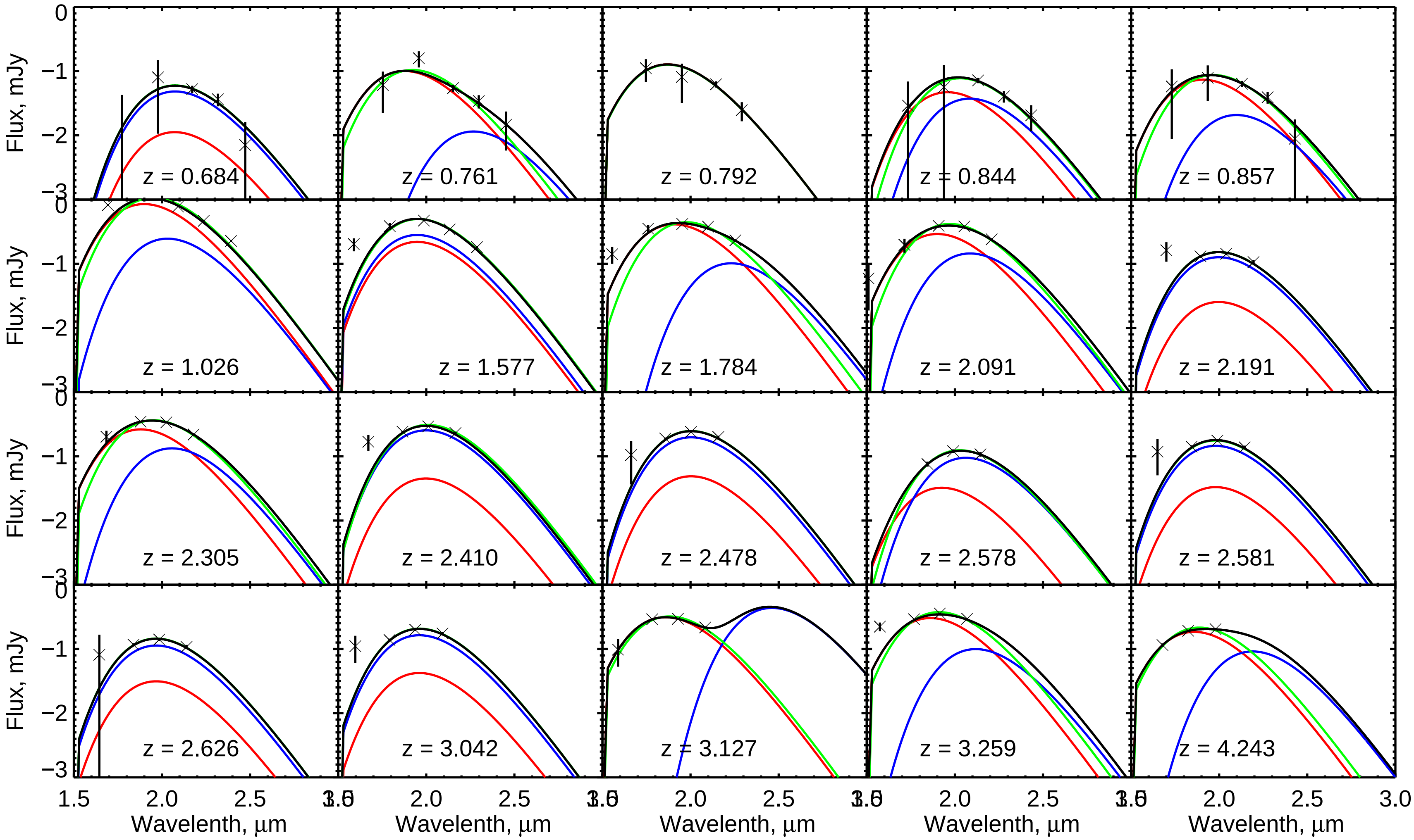

Figure 2.2: cont. Sources with $z > 1.0$ had redshifts obtained from CO follow up observations of interesting H-ATLAS sources.

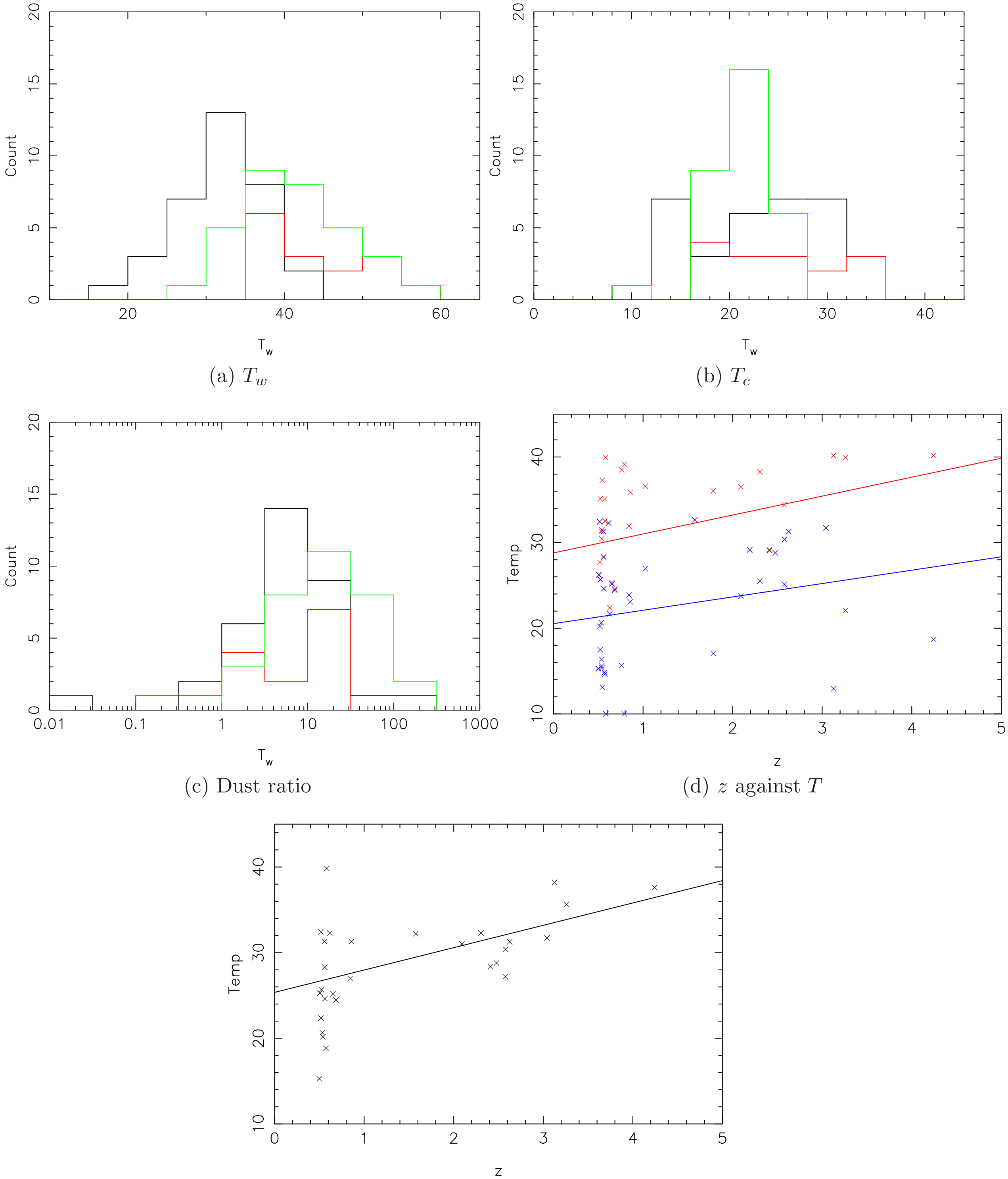

(a) T_w

(b) T_c

(c) Dust ratio

(d) z against T

(e) z against single T

Figure 2.3: Histograms of the dust temperatures and ratios of the high redshift sample (black) and the low redshift ULIRGs from Clements et al. (2010) (red) and LIRGs from Dunne & Eales (2001) (green). Figures d and e shows the temperatures of the high redshift sample as a function of redshift. The lines show the best fit to the temperatures, showing there is an apparent increase in temperature with redshift both in the single and double temperature models.

2.3 Spectroscopic Sources

Figures 2.4 - 2.28 show thumbnails of all the sources in the HS in the redshift range $0.5 < z < 1.0$ with counterparts in the SDSS survey. Shown here are the five *Herschel* bands (where available, shown in heat scale) alongside an R-band image (in black and white) for comparison.

In most cases the galaxy is clearly in the centre of the r-band image as the source must be optically bright as well as bright in the sub-mm in order to have been observed spectroscopically. As suggested before there is a chance that these optical sources might be a gravitational lens, magnifying the background sub-mm source, but inspection of the *Herschel* fluxes suggest that this is unlikely. It is worth noting that in a few cases the bright central object is a star. This is noted on the captions of the relevant cutouts.

There are also several sources that clearly have more than one sub-mm source overlapping, meaning they are confused at longer wavelengths. The fluxes were calculated according to the method laid out in Rigby et al. (2011), whereby sources were sorted in order of significance and then a Gaussian fitted to provide an estimate for the source position in the 250 μm band. Though neighbouring sources can influence this positioning the effect was deemed to be minimal. The flux was then estimated using a bi-cubic interpolation and a scaled PSF then subtracted from the map to prevent the flux from contaminating fainter sources. This method of ordering and PSF subtraction reduced the effects of confusion, but in future the fluxes will be calculated using a multi-source fitting to blended sources. As the sources used here are very bright at sub-mm wavelengths, it is unlikely that flux boosting will be an issue.

From the images shown here is does appear that several of the sub-mm sources are offset from the optical. As wavelength increases, the sources appear to drift from the centre. The drift is too large to simply be an error in centring due to increased pixel size. Confusion might explain the shift in position, as longer wavelengths will be worse effected and so as wavelength increases, the offset will increase as well.

It is possible that a selection bias was introduced, as any confusion that was not accounted for in the method descibed by Rigby et al. (2011) would make the sources appear brighter, potentially pushing them above the flux cut off of this selection. As the sources chosen were exceptionally bright at 250 μm rather than longer wavelengths, this should keep any selection bias to a minimum. Any flux boosting will most prominently effect the 500 μm fluxes.

Figure 2.29 shows a close up of the r-band images. The K-band (centred at 2.2 μm) images from the VISTA VIKING survey are shown in Figure 2.30. Cutouts at this wavelength were not available for every source, only those that had been identified in the

K-bands at the position of the SMG.

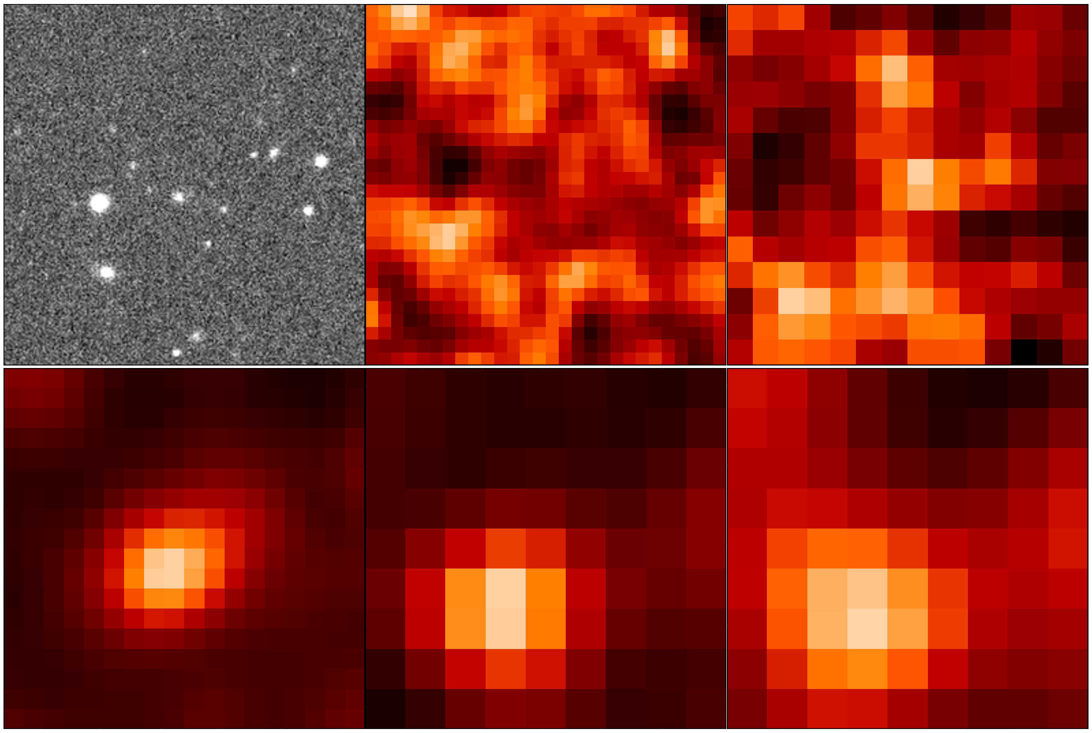

Figure 2.4: A thumbnail for HATLAS J143845.8+013504, hereafter source S1, at $z = 0.501$. Top row, left to right - R band image, the PACS bands: 100 and 160 μm. Bottom row, left to right - all three SPIRE wavelengths: 250, 350 and 500 μm. The images are $90'' \times 90''$. The separation between optical counterpart from the SDSS and 250 μm position is $3.20''$.

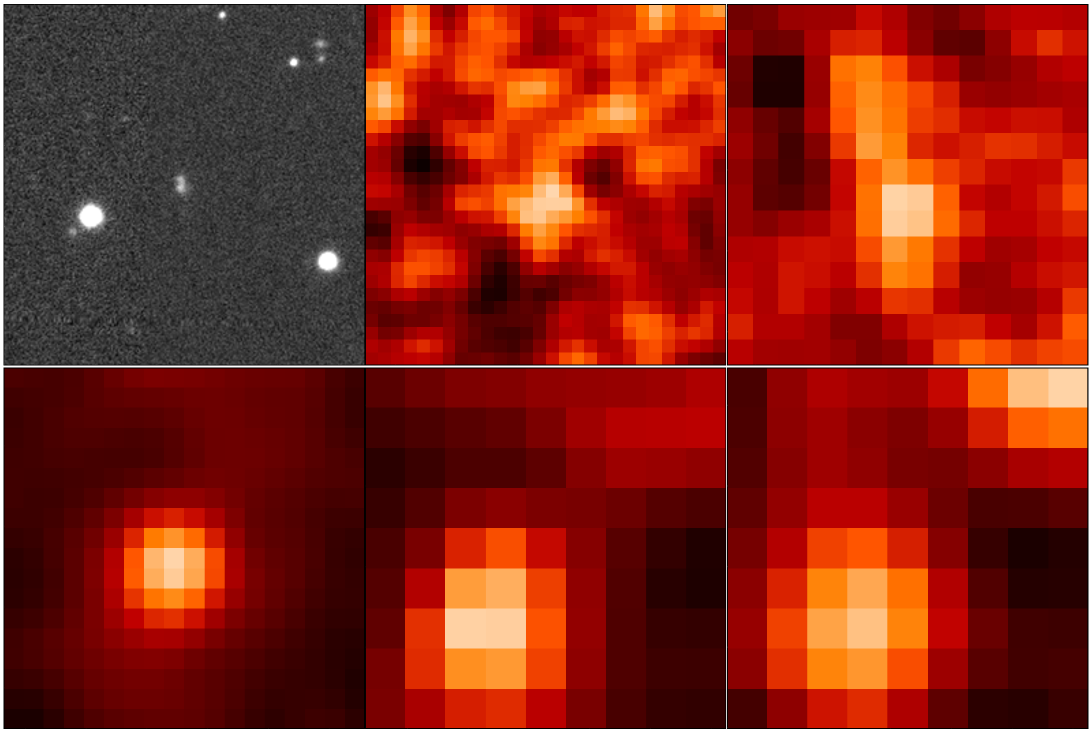

Figure 2.5: As previous for HATLAS J140746.5-010629, S2, at $z = 0.507$. The separation between optical counterpart from the SDSS and 250 μm position is 0.59″.

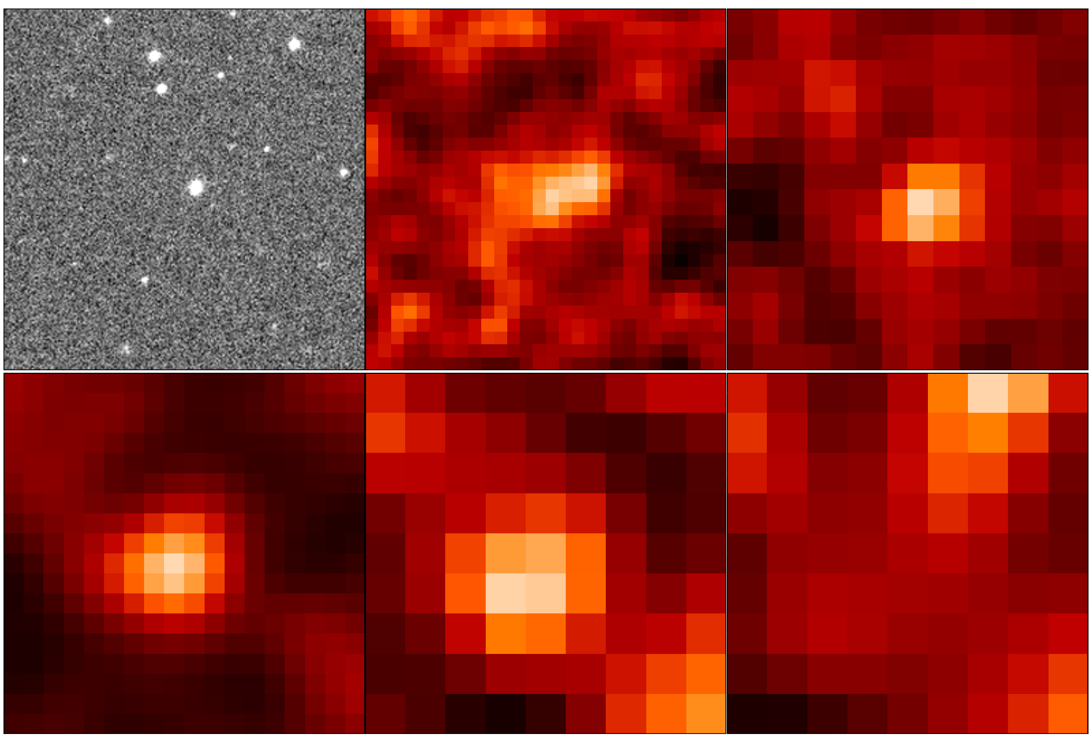

Figure 2.6: As previous for HATLAS J090758.2-001448, S3, at $z = 0.516$.The separation between optical counterpart from the SDSS and 250 μm position is 3.24″. A K-band image of this source is shown in Figure 2.30.

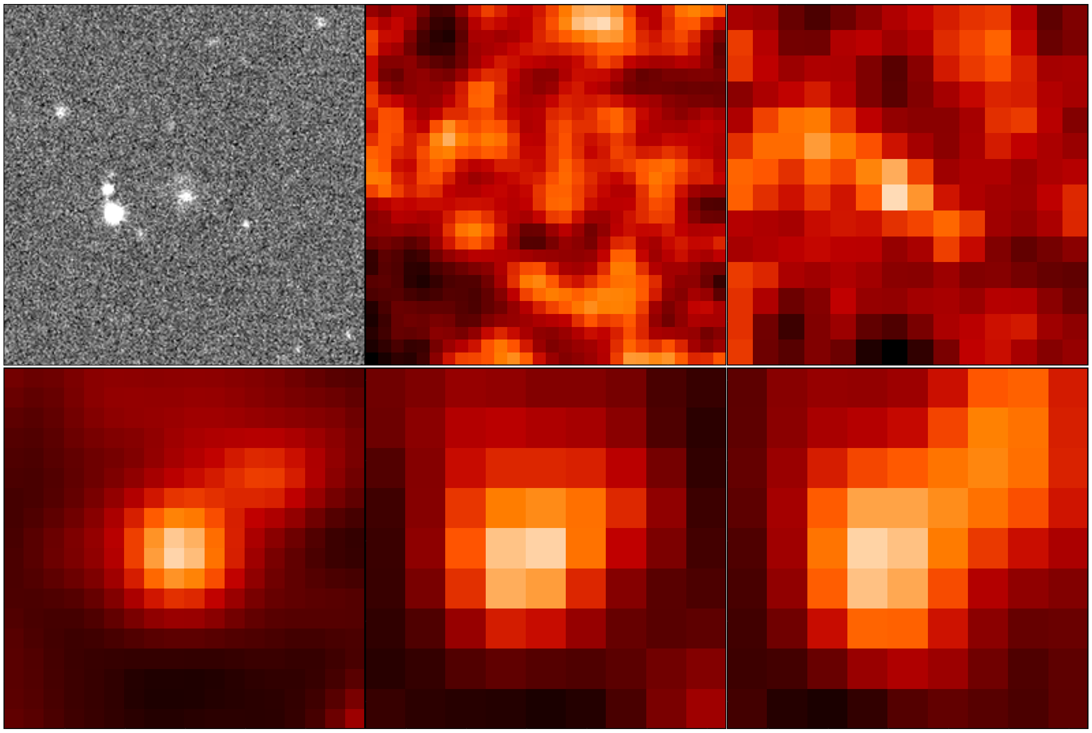

Figure 2.7: As previous for HATLAS J142534.0+023712, S4, at $z = 0.518$. The separation between optical counterpart from the SDSS and 250 μm position is $2.73''$.

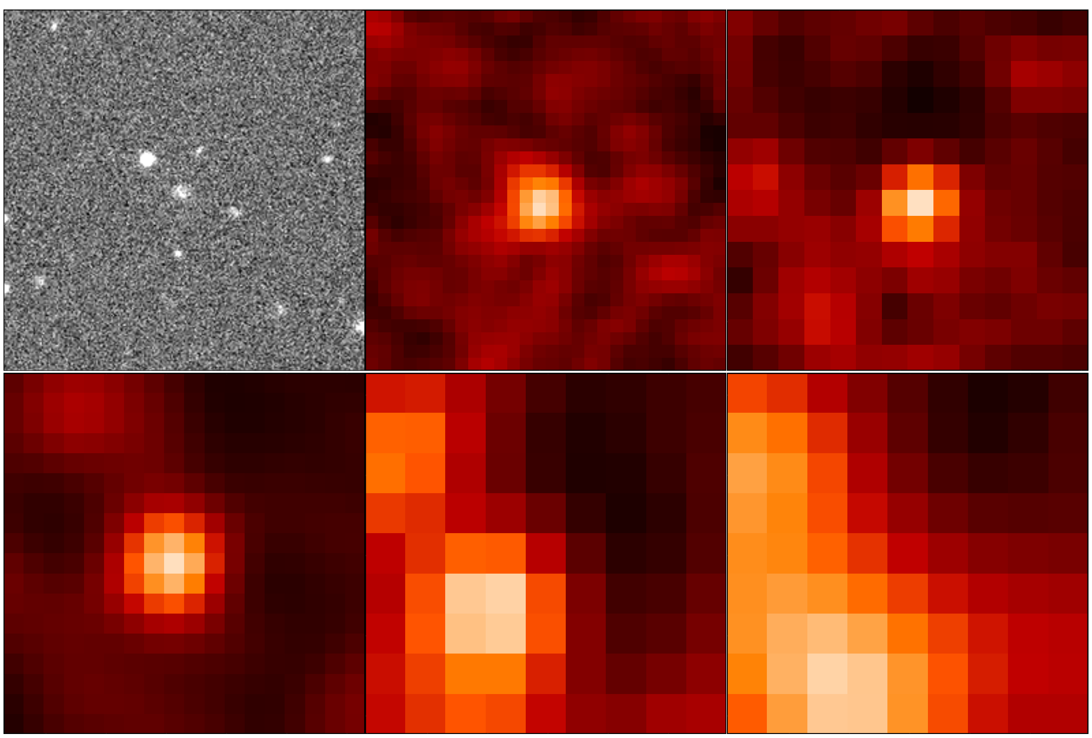

Figure 2.8: As previous for HATLAS J143703.8+014128, S5, at $z = 0.522$. The separation between optical counterpart from the SDSS and 250 μm position is $0.79''$.

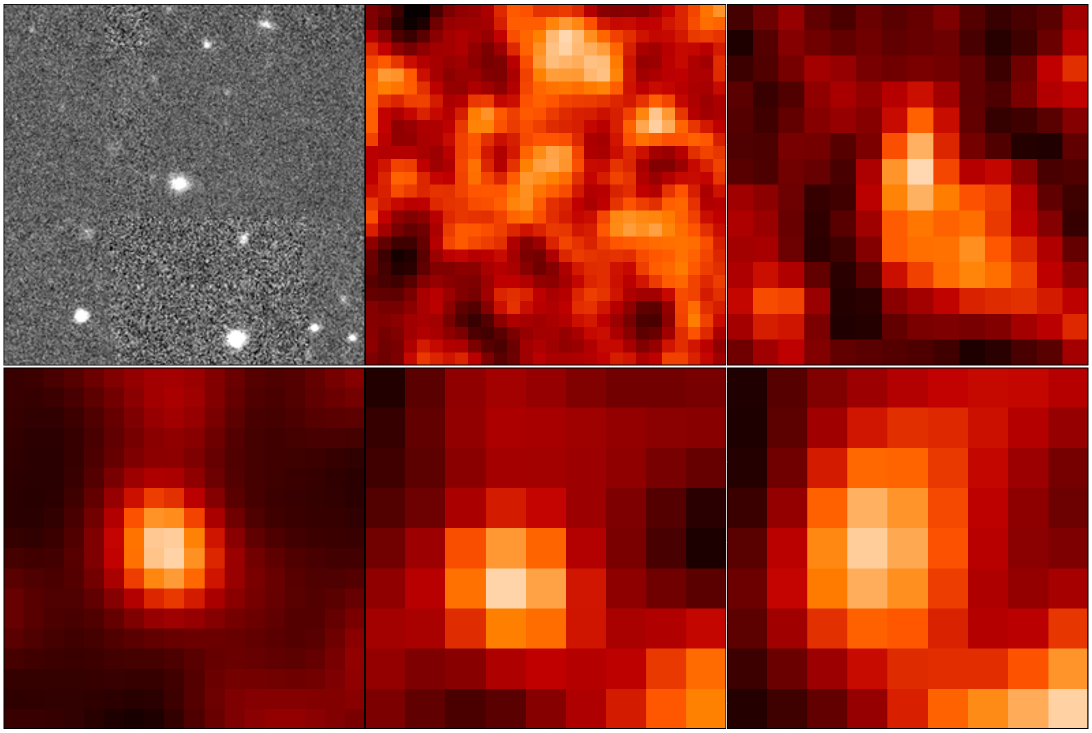

Figure 2.9: As previous for HATLAS J141815.6+010247, S6, at $z = 0.524$. The separation between optical counterpart from the SDSS and 250 μm position is $1.14''$.

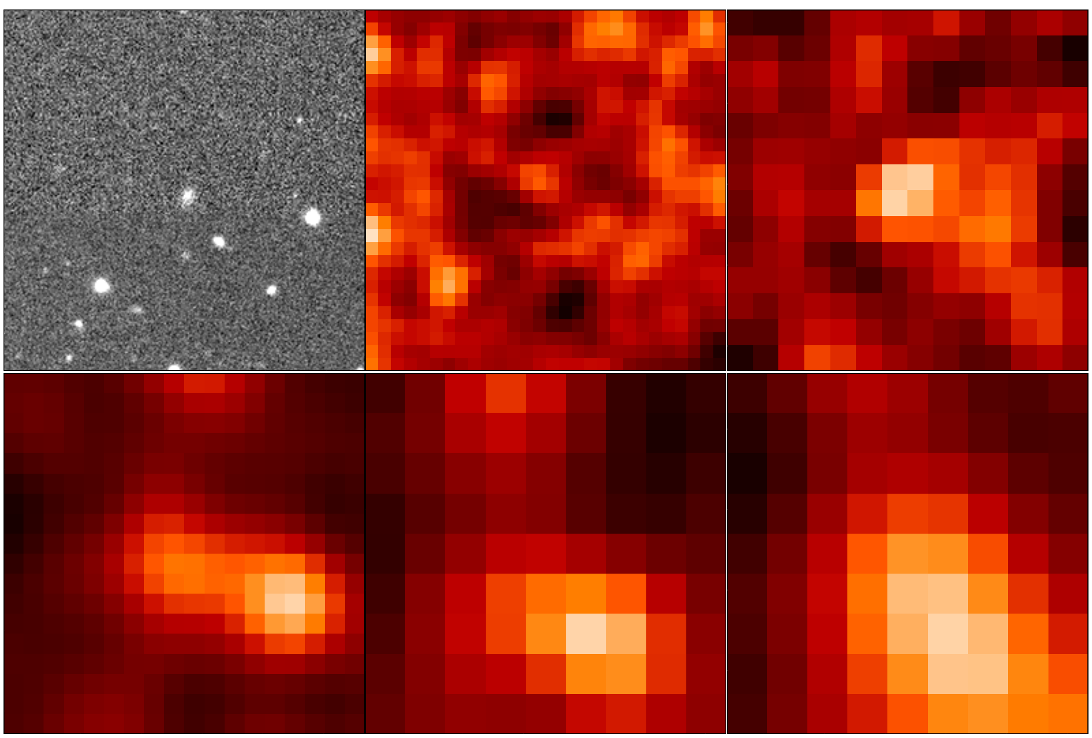

Figure 2.10: As previous for HATLAS J083713.3+000035, S7, at $z = 0.534$. The separation between optical counterpart from the SDSS and 250 μm position is $1.47''$. A K-band image of this source is shown in Figure 2.30.

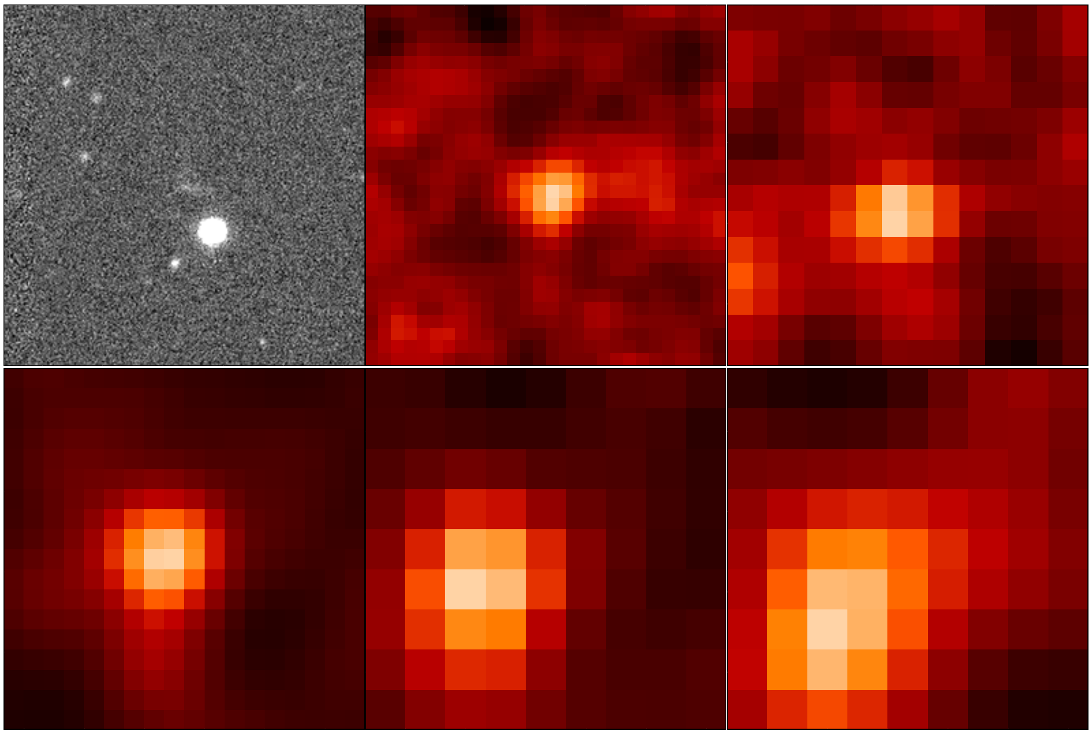

Figure 2.11: As previous for HATLAS J090359.6-004555, S8, at $z = 0.538$. The separation between optical counterpart from the SDSS and $250\,\mu$m position is $0.72''$. Due to the bright star in the low right of the r-band image it is difficult to see the galaxy even in the closeup 2.29. A K-band image of this source is shown in Figure 2.30 in which the galaxy is clearly visible.

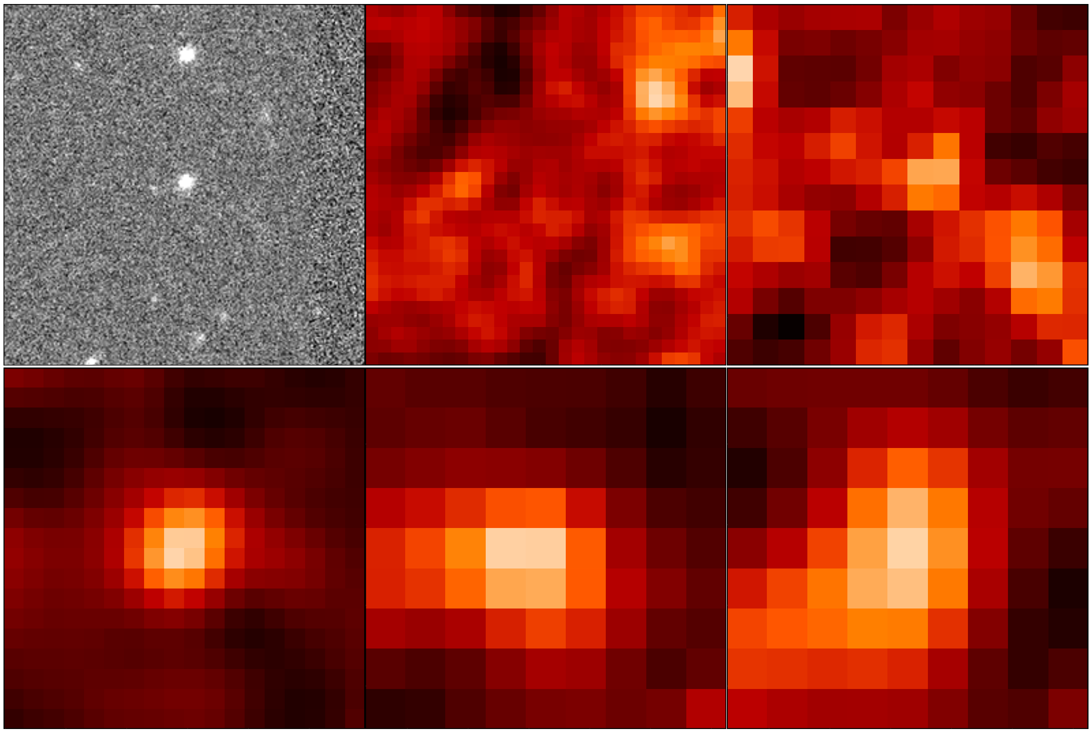

Figure 2.12: As previous for HATLAS J140640.0-005951, S9, at $z = 0.539$. The separation between optical counterpart from the SDSS and 250 μm position is $1.22''$.

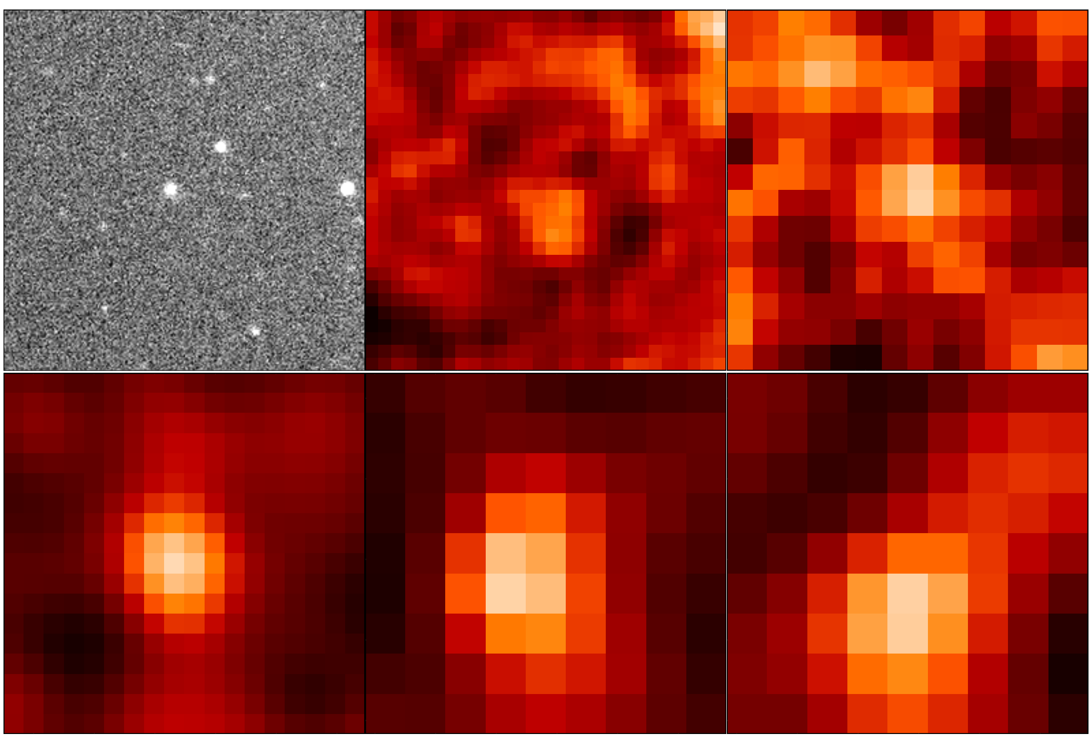

Figure 2.13: As previous for HATLAS J140930.6-013805, S10, at $z = 0.539$. The separation between optical counterpart from the SDSS and 250 μm position is $2.77''$.

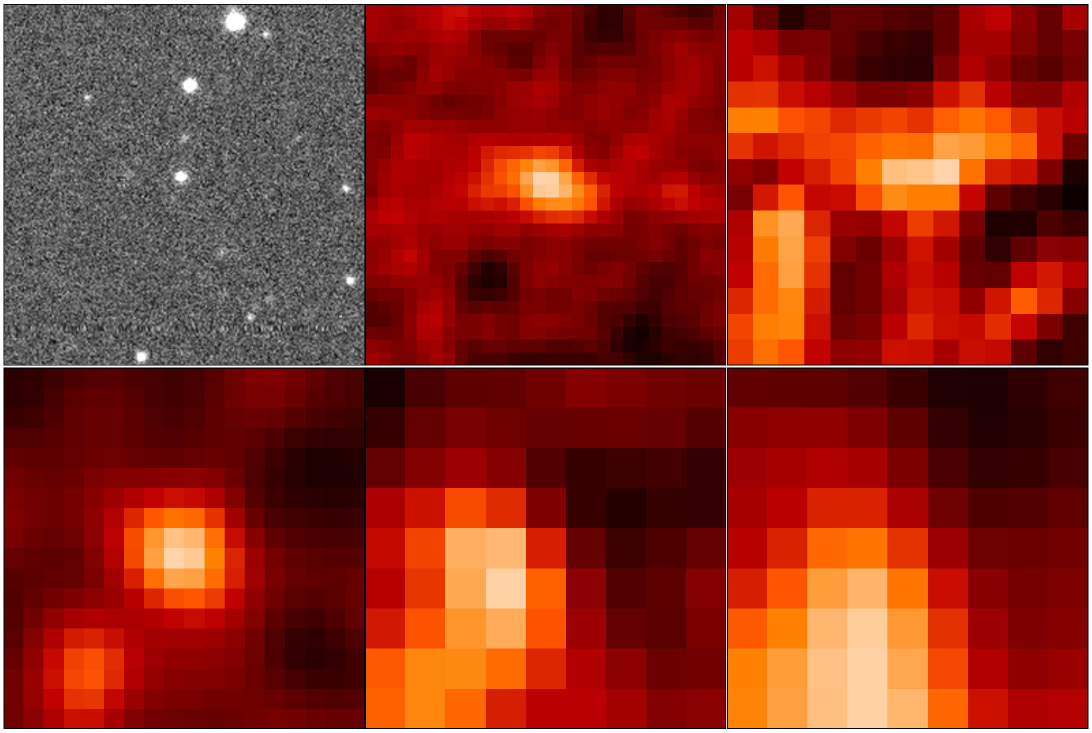

Figure 2.14: As previous for HATLAS J141343.4+004041, S11, at $z = 0.546$. The separation between optical counterpart from the SDSS and $250\,\mu$m position is $2.31''$.

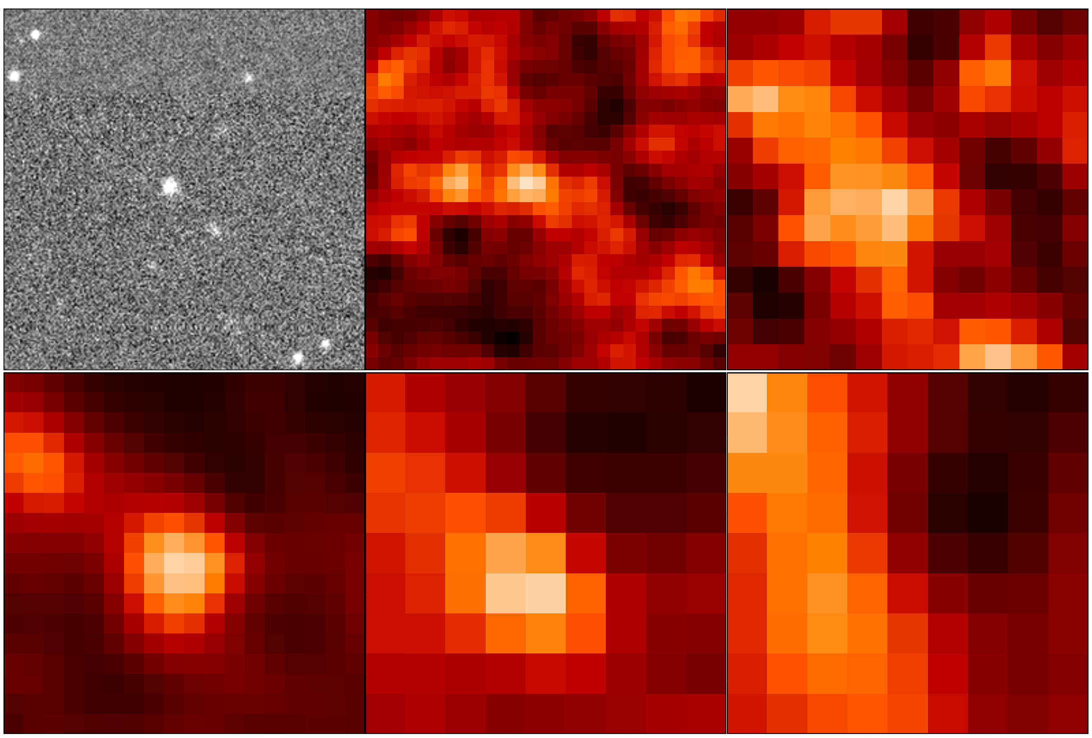

Figure 2.15: As previous for HATLAS J121353.8-024317, S12, at $z = 0.557$. The separation between optical counterpart from the SDSS and $250\,\mu$m position is $3.47''$.

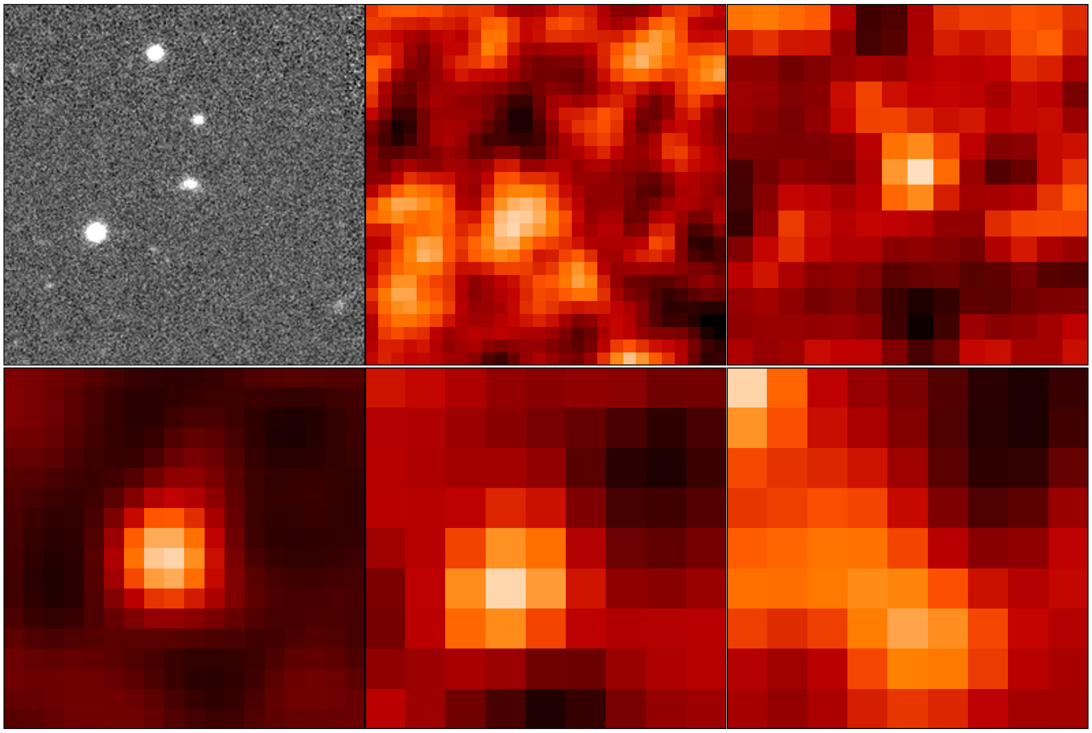

Figure 2.16: As previous for HATLAS J092340.2+005736, S13, at $z = 0.560$. The separation between optical counterpart from the SDSS and 250 μm position is 2.17″. A K-band image of this source is shown in Figure 2.30.

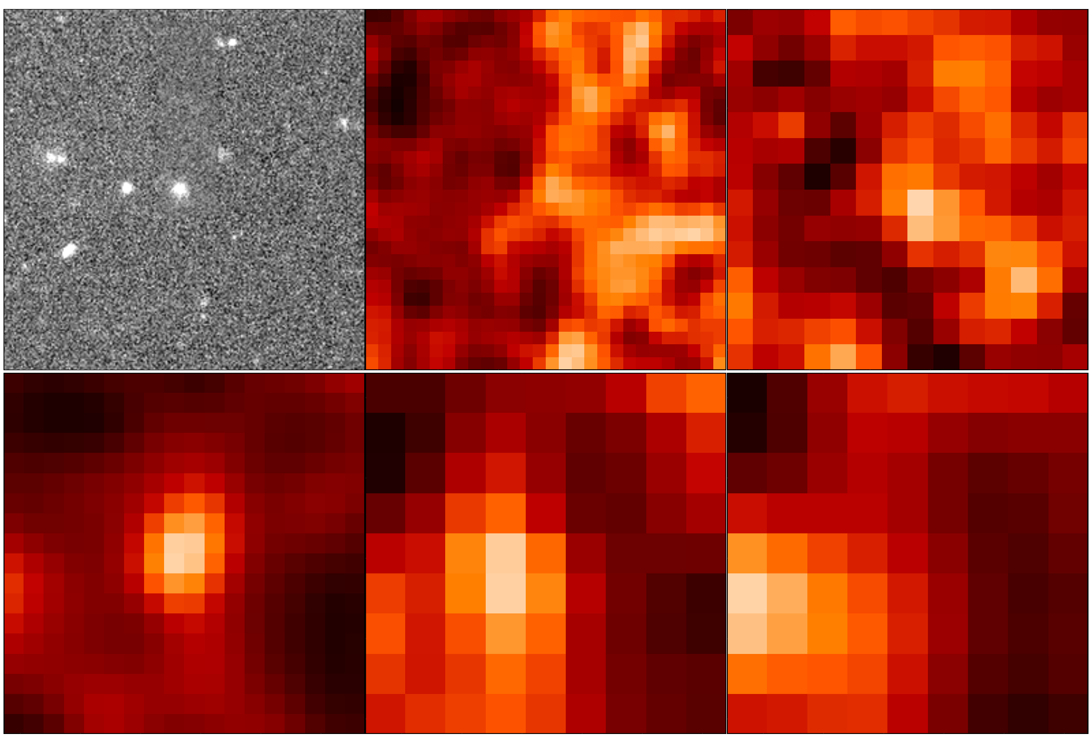

Figure 2.17: As previous for HATLAS J120248.3-022944, S14, at $z = 0.563$. The separation between optical counterpart from the SDSS and 250 μm position is 0.95″.

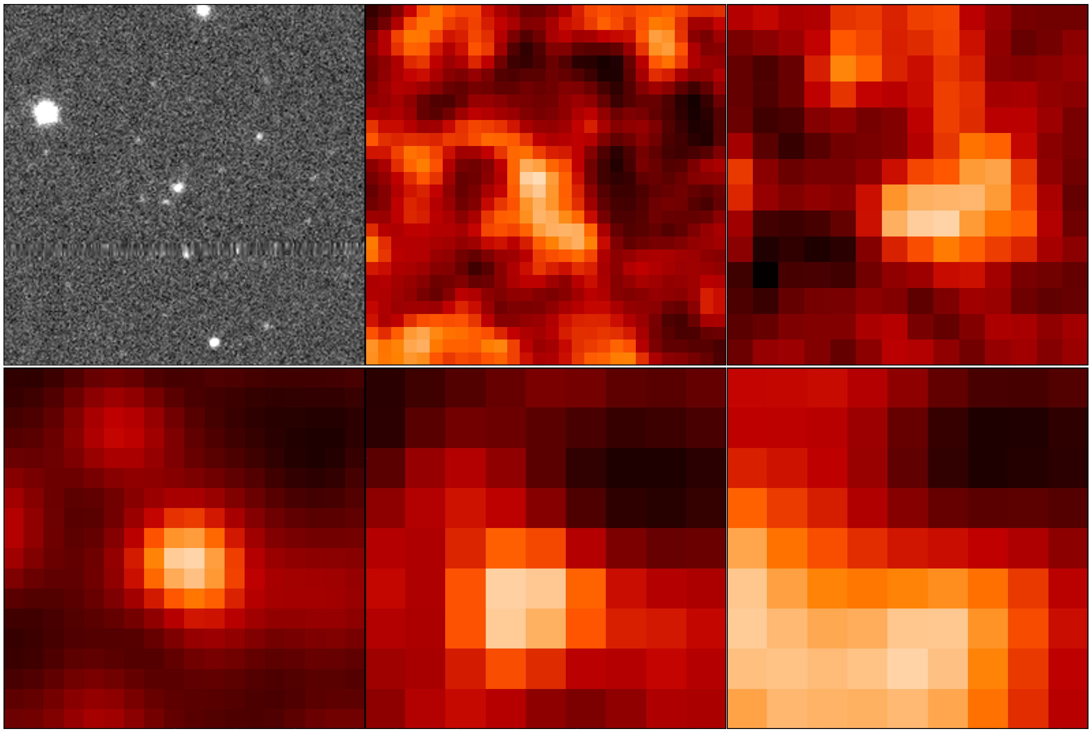

Figure 2.18: As previous for HATLAS J114619.8-014356, S15, at $z = 0.571$. The separation between optical counterpart from the SDSS and 250 μm position is 1.26″.

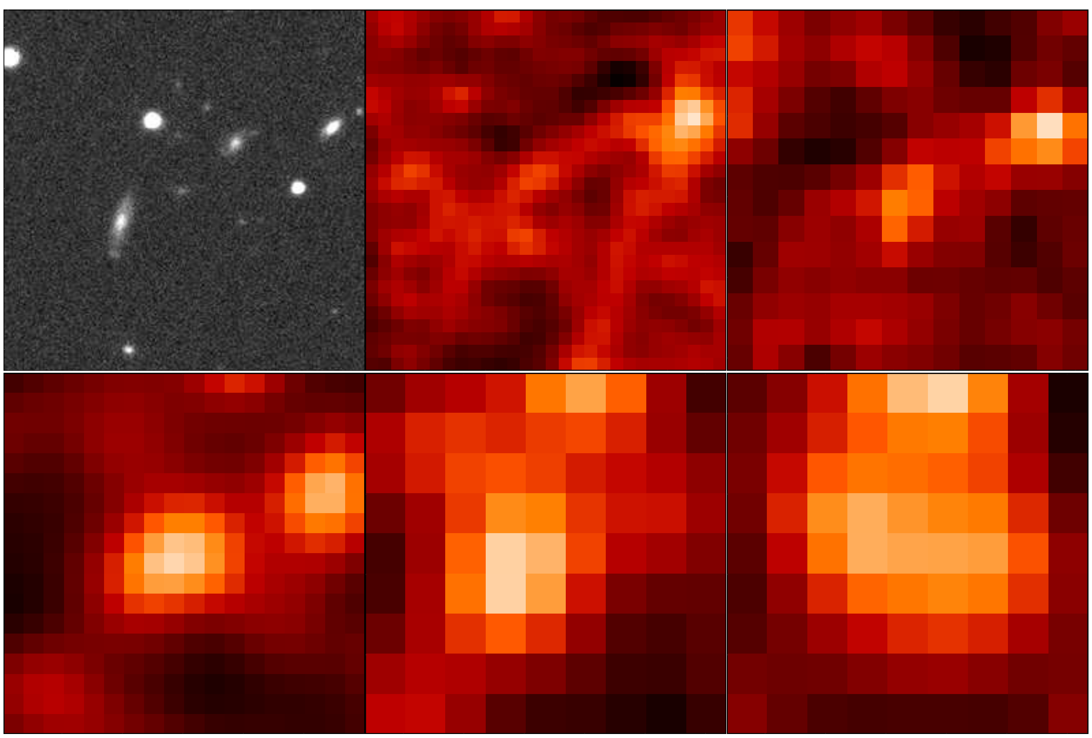

Figure 2.19: As previous for HATLAS J141429.0-000900, S16, at $z = 0.574$. The separation between optical counterpart from the SDSS and 250 μm position is 0.44″.

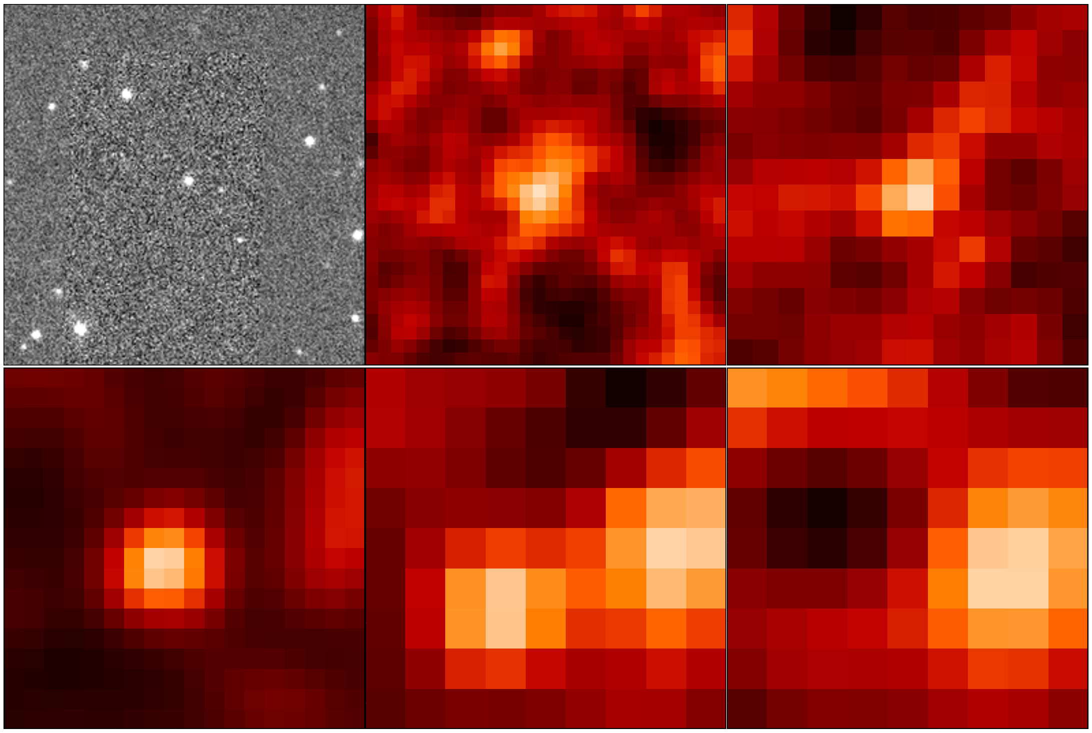

Figure 2.20: As previous for HATLAS J085230.1+002844, S17, at $z = 0.584$. The separation between optical counterpart from the SDSS and 250 μm position is 1.81″. A K-band image of this source is shown in Figure 2.30.

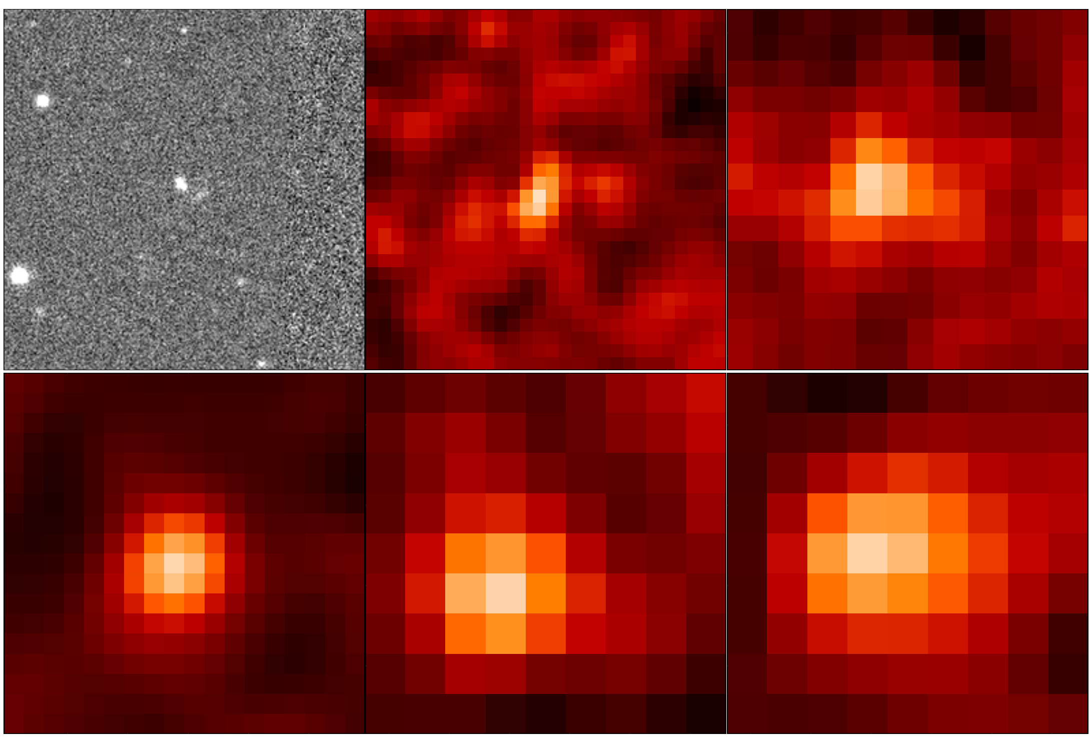

Figure 2.21: As previous for HATLAS J143858.1-010540, S18, at $z = 0.615$. The separation between optical counterpart from the SDSS and 250 μm position is 1.38″.

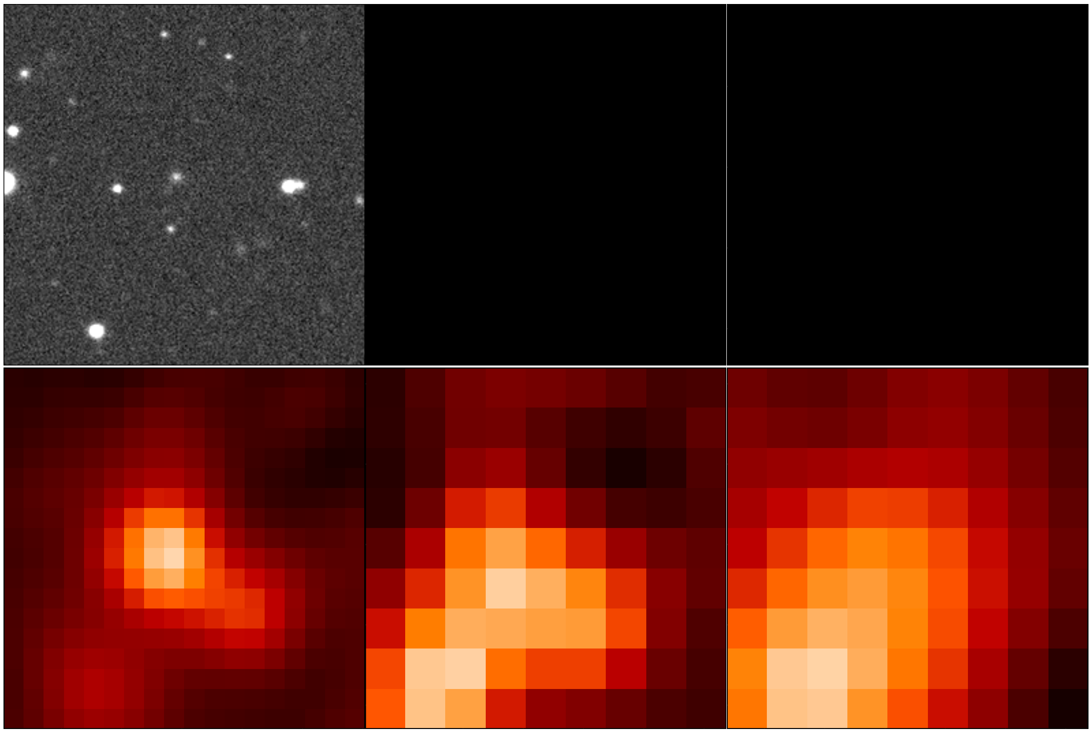

Figure 2.22: As previous for HATLAS J084846.2+022032, S19, at $z = 0.627$. The separation between optical counterpart from the SDSS and 250 μm position is 2.51″. A K-band image of this source is shown in Figure 2.30.

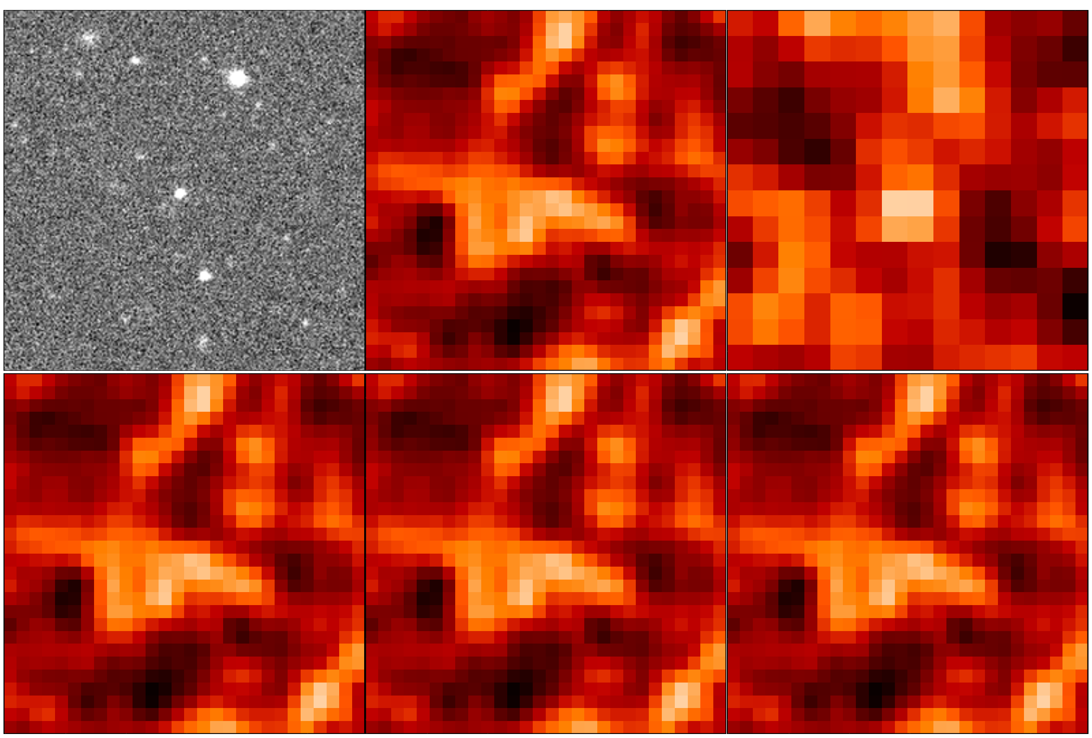

Figure 2.23: As previous for HATLAS J120246.0-005221, S20, at $z = 0.653$. The separation between optical counterpart from the SDSS and 250 μm position is 0.73″.

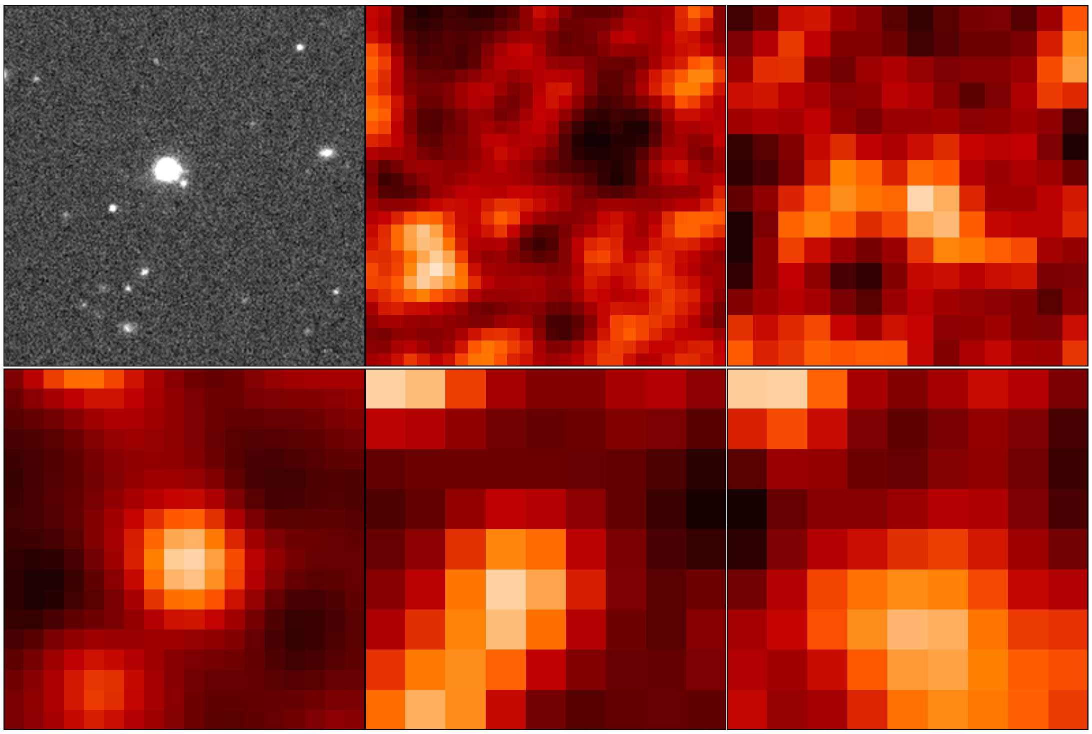

Figure 2.24: As previous for HATLAS J113859.3-002934, S21, at $z = 0.684$. The separation between optical counterpart from the SDSS and 250 μm position is $0.97''$. In the r-band image the optical counter part is the faint source in the centre of the image, masked slightly by the bright star on the upper left. For a clearer image see Fig 2.29.

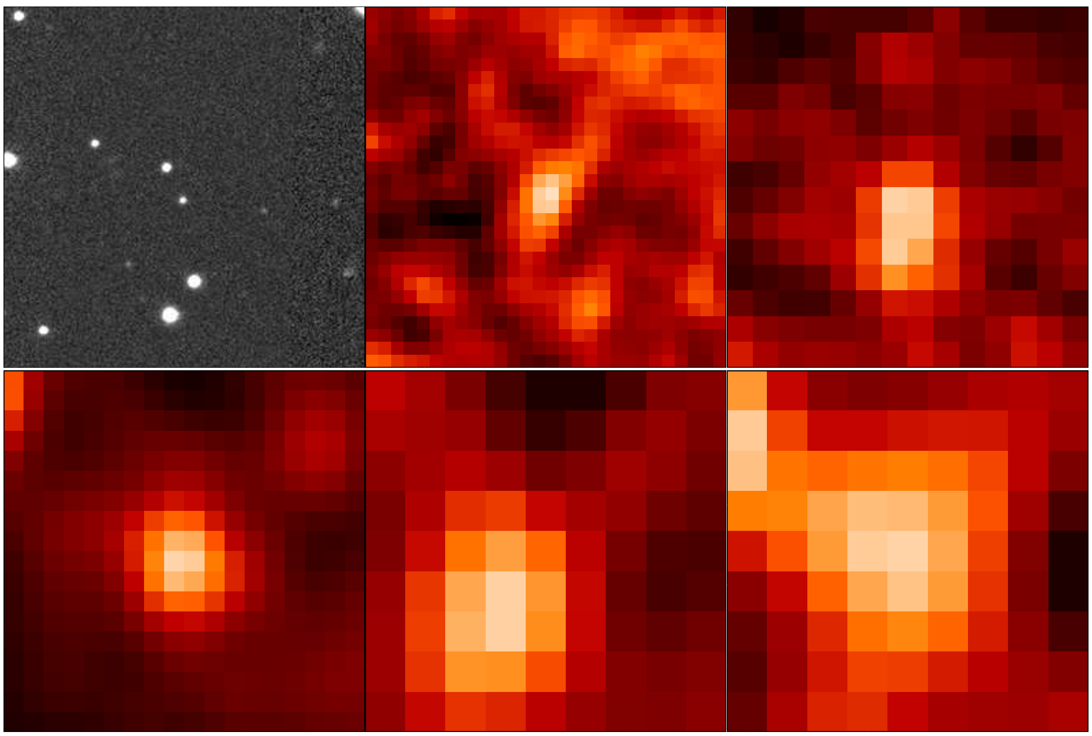

Figure 2.25: As previous for HATLAS J084217.0+010920, S22, at $z = 0.761$. The separation between optical counterpart from the SDSS and 250 μm position is $2.85''$. A K-band image of this source is shown in Figure 2.30.

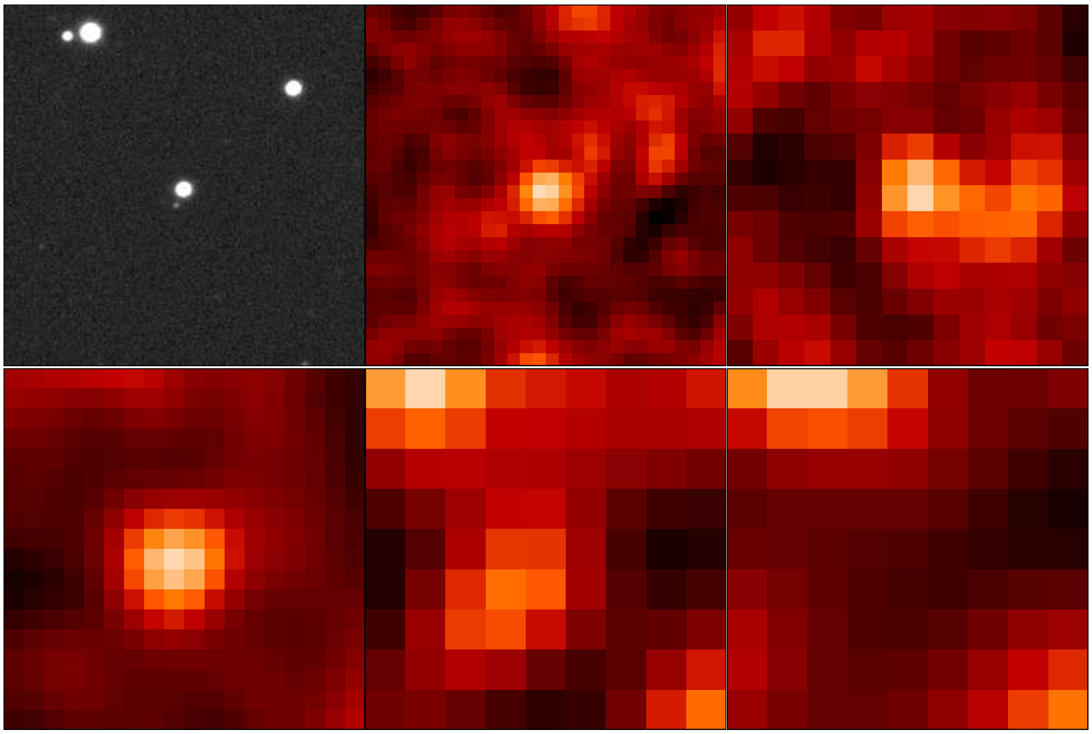

Figure 2.26: As previous for HATLAS J090420.9+013038, S23, at $z = 0.792$. The separation between optical counterpart from the SDSS and 250 μm position is $0.68''$. In the r-band image the central bright object is a star. The optical counterpart lies to the bottom left. For a clearer image see Fig 2.29. A K-band image of this source is shown in Figure 2.30.

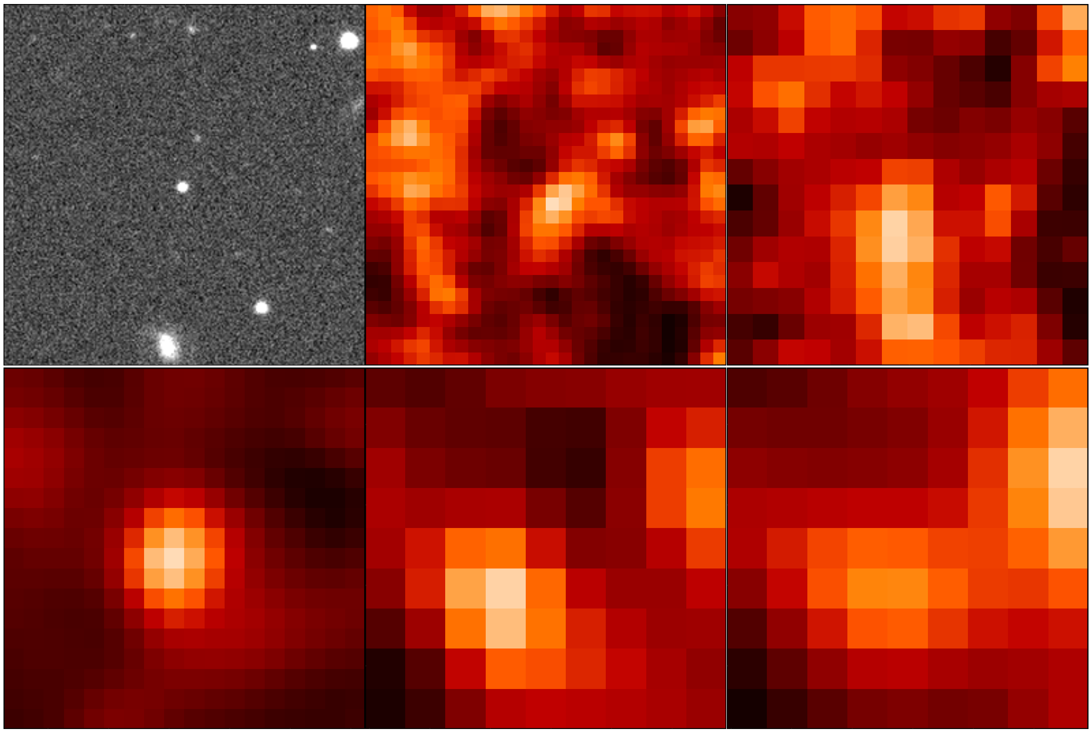

Figure 2.27: As previous for HATLAS J114023.0-001043, S24, at $z = 0.844$. The separation between optical counterpart from the SDSS and 250 μm position is $0.47''$.

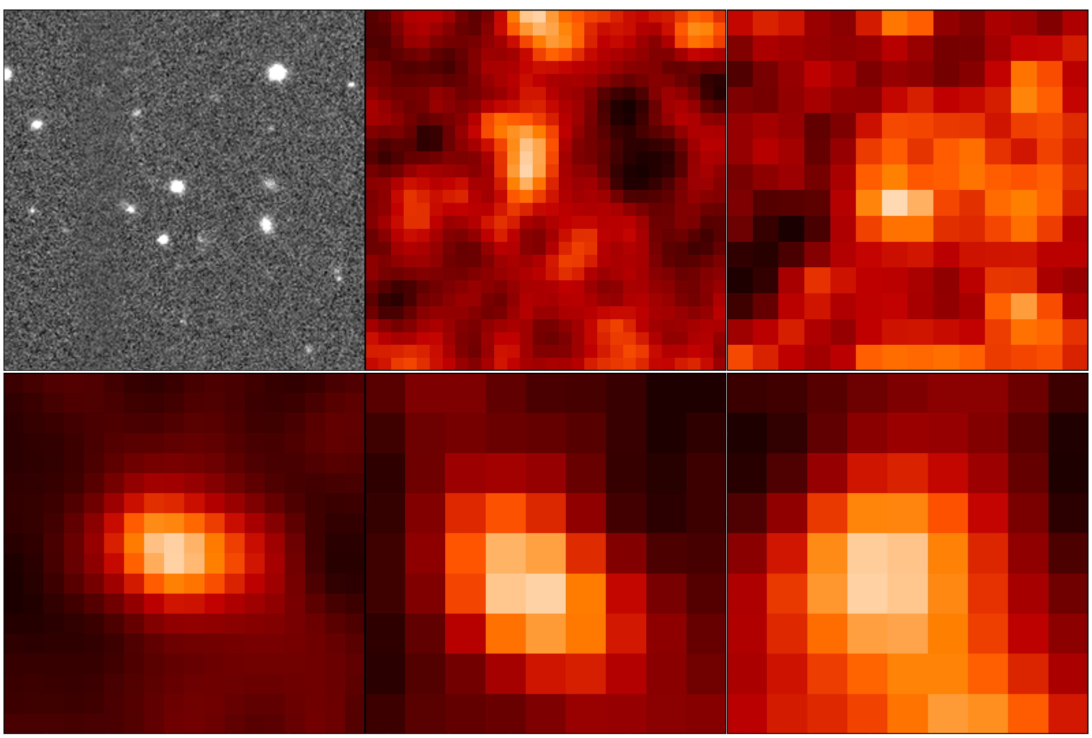

Figure 2.28: As previous for HATLAS J141148.9-011439, S25, at $z = 0.857$. The separation between optical counterpart from the SDSS and 250 μm position is $1.63''$.

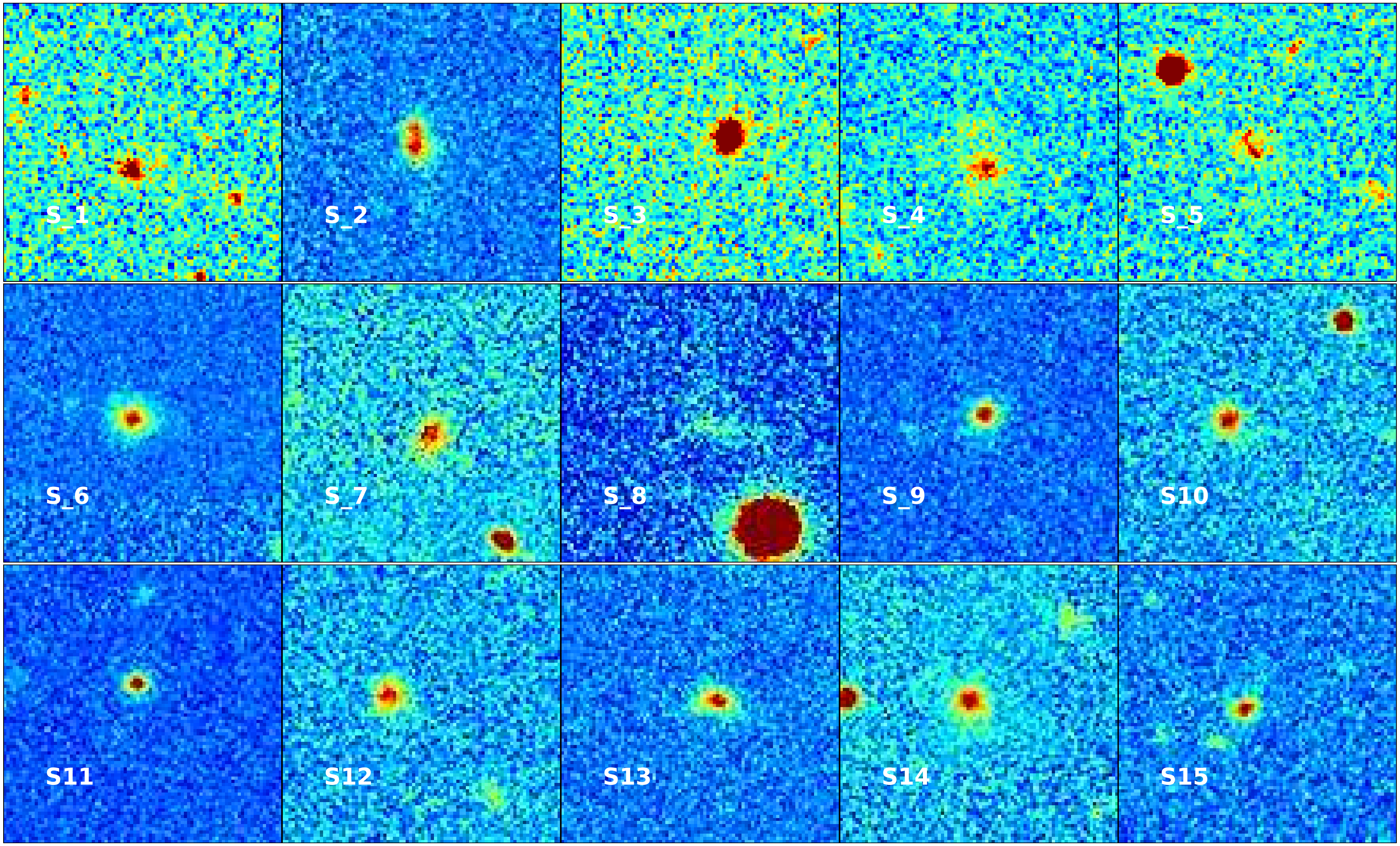

Figure 2.29: Closeup of r-band images showing optical counterparts from the SDSS for the spectroscopically selected sources. Images are $30'' \times 30''$.

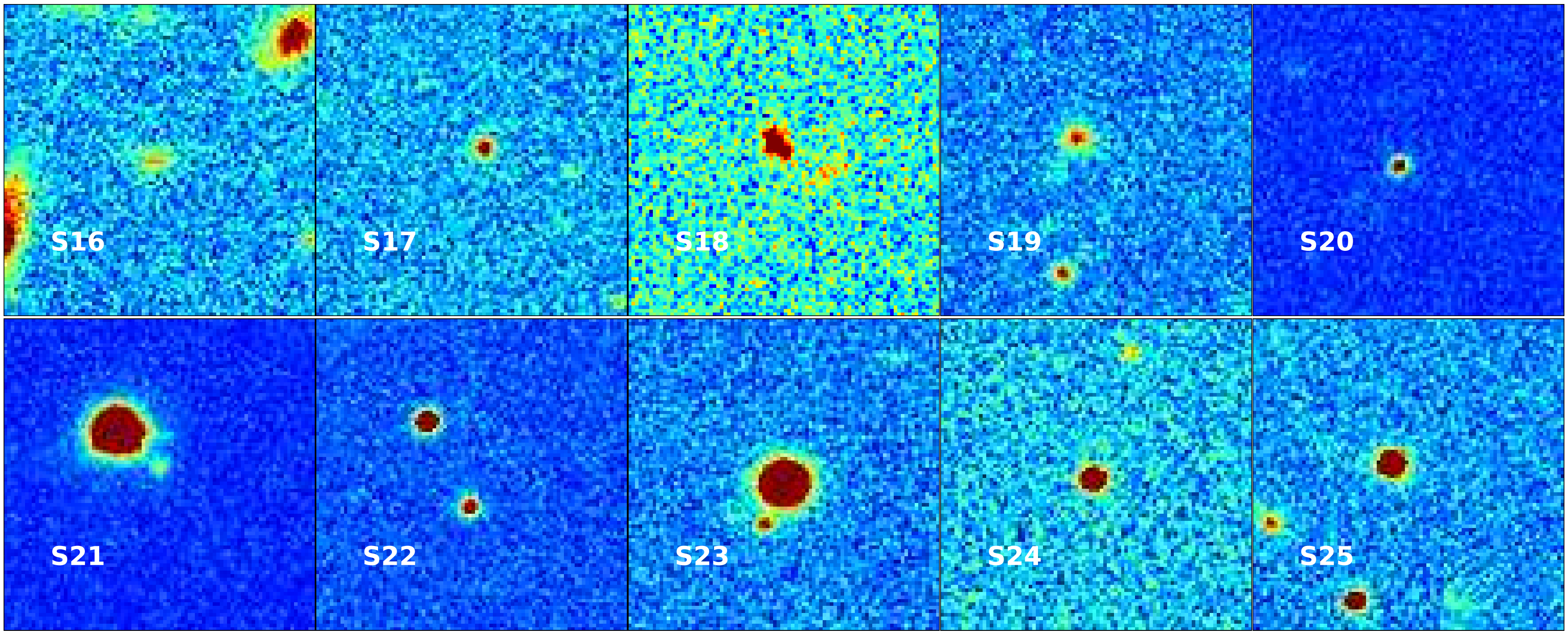

Figure 2.29: cont.

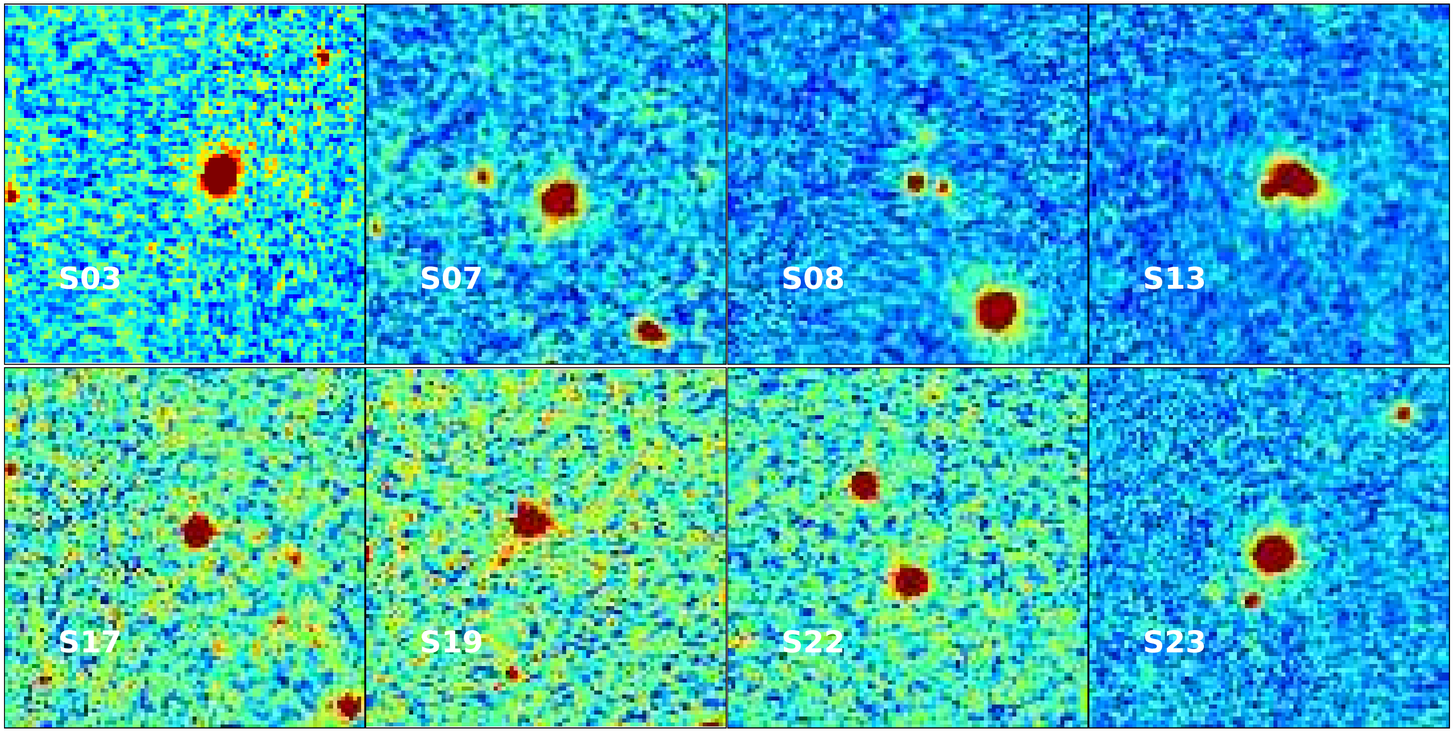

Figure 2.30: Closeup of K-band images showing optical counterparts from the VIKING survey for spectroscopically selected sources. Images are $30'' \times 30''$.

2.4 CO Sources

Figures 2.32 - 2.46 show thumbnails of all the sources used in the HS with $z > 1.0$ as determined from CO observations. The sources were observed in several different publications, which will be discussed here. These surveys selected their targets for followup observations for a variety of different reasons but all were bright sub-mm galaxies that were suspected of lying at high redshift.

Several of the CO followup observations were documented in by Harris et al. (2012) (hereafter as H12). These were chosen from the early H-ATLAS catalogues (Collaboration, 2010) as they were "350 μm peakers". Each of the H12 sources had flux densities of $S_{350} \geq 115$mJy with the peak of sub-mm emission occurring in the 350 μm band, suggesting that the galaxy must be at a redshift of $z \approx 2$ - 3 in order to redshift the peak of emission into this band. The targets were observed with Zpectrometer on the Green Bank Telescope (Harris et al., 2012).

The survey targeted 24 sources, only making clear detections on 11 of the targets. The missed sources may be bright SMGs but are either lacking in CO or are at a vastly different redshift to what was expected. There may be a potential bias from selecting galaxies in this manner. This selection might bias towards warmer galaxies where these CO transitions are visible but by observing for multiple CO transitions they should have opened up to a range of temperatures.

Lupu et al. (2012) (hereafter as L10) was searching for potential gravitational lenses and selected sources with reliable optical counterparts at much lower redshifts than suggested by their sub-mm colours. These sources were observed in L10 by the Caltech Submillimeter Observatory (CSO) using ZSpec to measure their CO lines.

Cox et al. (2011) (hereafter as C11) investigated a single source, the highest redshift source of the HS and one of the brightest *Herschel* sources detected in any survey. Further details can be found in Section 2.4.1.

Fu et al. (2012) did an in depth study of a single source that was found to be lensed by multiple sources. Further details can be found in Section 2.4.1

Many of these sources are lensed and so in these cases the optical galaxy associated by the likelihood ratio technique is not the same galaxy as the SMG. Instead the optical source is the galaxy acting as the gravitational lens, a lower redshift galaxy that the light from the background SMG is being bent by. The lenses were frequently identified using the matching technique used to find the sources in the spectroscopic selection. However this method required a single optical source to be associated with the SMG to be considered reliable. This was not a perfect method to find lenses though, as there is often more than one galaxy lensing a background source. Sometimes even a whole cluster can be responsible.

These lenses tend to be large elliptical galaxies which are relatively free of dust and so even though we are imaging two galaxies along the line of sight we can assume that the lens is not contributing to the SPIRE fluxes and no adjustment for lensed galaxies needs to be taken. However there is a few cases where the lens may contaminate the background source which will be discussed more below.

H12 was able to determine whether or not certain sources were lensed due to the difference between the CO luminosity and the line width of the emission (see Figure 2.31). The relationship between these two quantities is very closely related, similar to the Tully-Fischer relation (Tully & Fisher, 1977). If a source is lensed then the galaxies appear much brighter than you would expect, given their line width, as the luminosity has been magnified but not broadened. This can be used as a rough guide of how much the source has been magnified by.

Lensing increases the brightness of the source galaxy allowing relatively dim sources that would be well below the flux limit of the survey to be seen. This means that we can see what we believe are typical starburst galaxies at a much higher redshift than we would normally be able to and can see sources much further back in their evolutionary history. These lensed galaxies are thought to be fairly typical of most SMGs at this redshift and the magnification is equal across all wavelengths, meaning that their ratios remain the same.

Not all of our sources are lensed, however. In order to be detected by these surveys, and to meet the high flux cut off that these publications looked for, unlensed sources must for some reason be undergoing a period of extreme brightness. This means that they might not be typical of galaxies at this redshift. However any galaxy that would be picked up by H-ATLAS at these extremely high redshifts would still have to be very bright.

2.4.1 The CO sources in detail

HATLAS J142935.3-002836

HATLAS J142935.3-002836 (S26, Fig 2.32) is an as yet unpublished result. It was chosen for followup observation as it was the brightest high redshift source at 160 μm in the whole of the H-ATLAS field, as well as being the brightest in the near-IR (Fu, 2010). The source is lensed to an Einstein ring, $2''$ in diameter. The faint object in the R-band image here is the edge on spiral acting as a lens at a redshift of $z = 0.218$. As the lens is a spiral rather than than elliptical there is a chance that the sub-mm fluxes might be contaminated by the lens but we were unable to test this at this time. The sub-mm fluxes

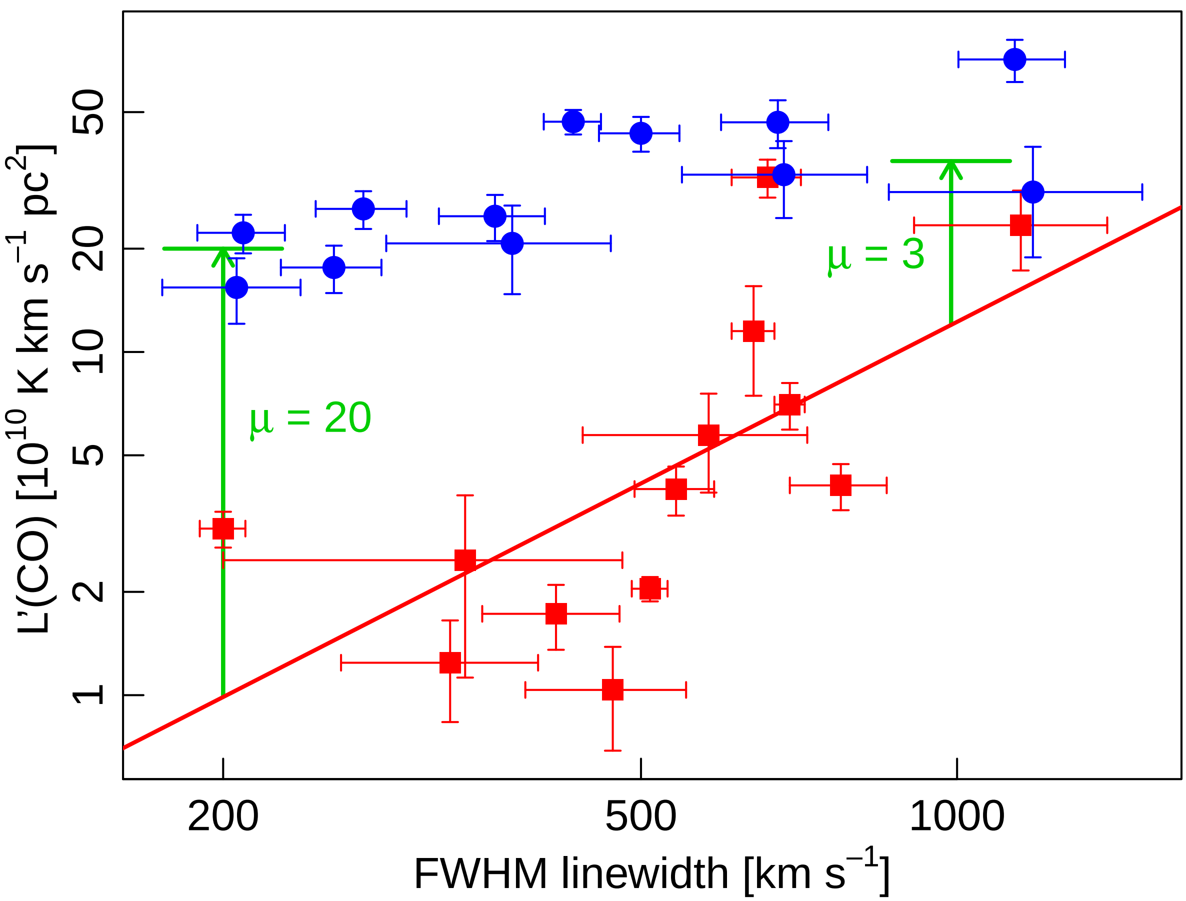

Figure 2.31: Line luminosities of L_{CO} against FWHM linewidths for the CO $J = 1$ - 0 line. The square points are taken from Harris et al. (2010); Carilli et al. (2010); Ivison et al. (2011); Riechers et al. (2011) and have been adjusted for magnification etc. (Smail et al., 2002) and appear to follow a power law. The blue points are from Harris et al. (2012) and show the 11 sources used here. It is clear that these are disparate from each other. In increase in line width for a given luminosity suggests that they have been magnified. (Harris et al., 2012) attempted to estimate the magnification of these sources using this relation.

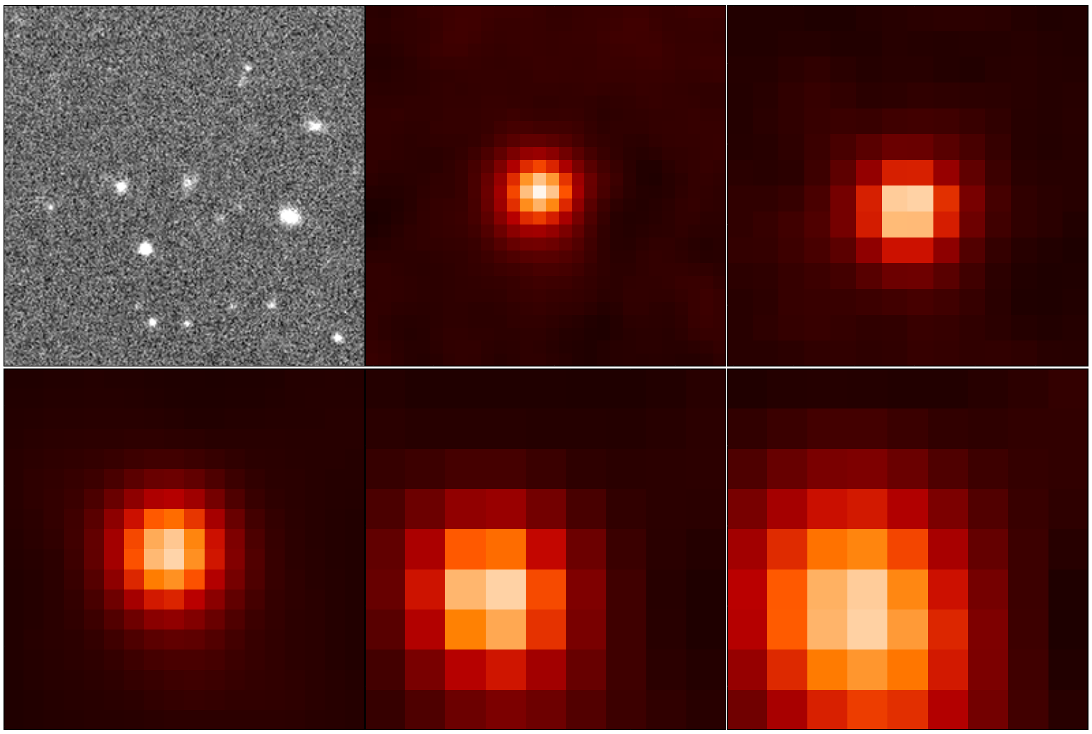

Figure 2.32: A thumbnail for HATLAS J142935.3-002836, hereafter source S1, at $z = 1.026$. Top row, left to right - R band image, the PACS bands: 100 and 160 μm. Bottom row, left to right - all three SPIRE wavelengths: 250, 350 and 500 μm. The images are $90'' \times 90''$.

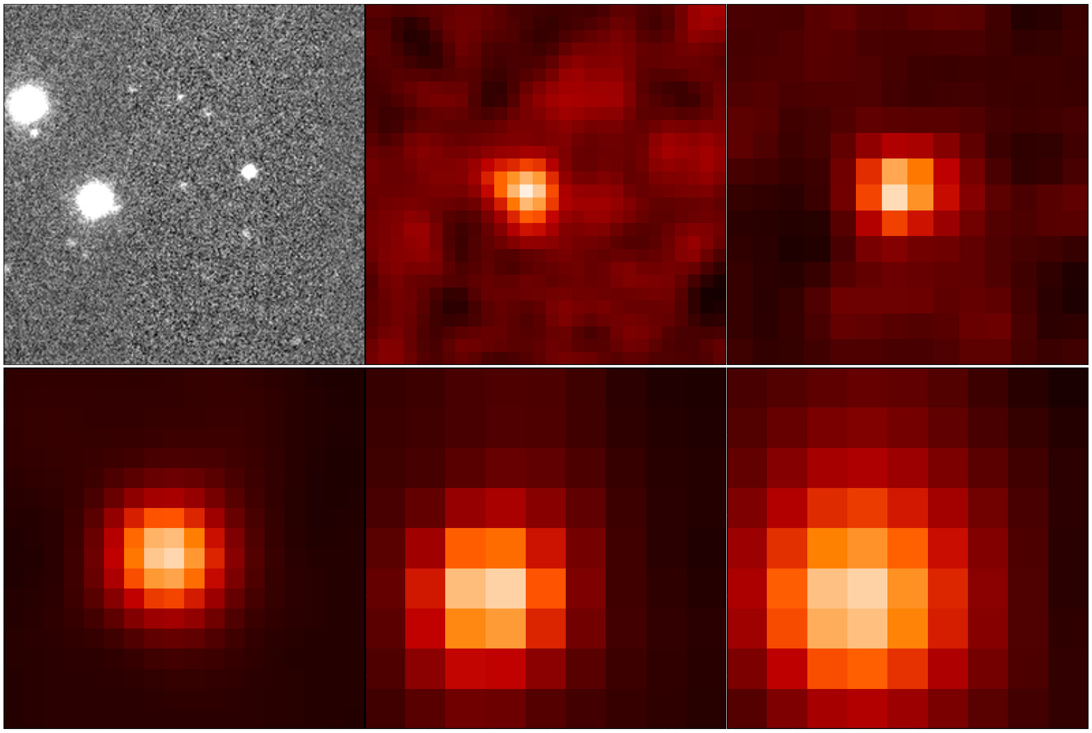

Figure 2.33: As previous for HATLAS J090740.0-004200, S27, at $z = 1.577$. A K-band image of this source is shown in Figure 2.30.

used in subsequent Chapters remain as they were observed. The CO observation give a redshift of $z = 1.026$. The separation between optical SDSS counterpart and $250\,\mu$m position is $1.62''$.

HATLAS J090740.0-004200

HATLAS J090740.0-004200 (S27, Fig 2.33) was observed in L10 as a potential lens, the optical lens galaxy found to have a redshift of $z = 0.68$. The CO observation give a redshift of $z = 1.577$ for the sub-mm source. The separation between optical SDSS counterpart and $250\,\mu$m position is $0.11''$. A K-band image of this source is shown in Figure 2.48, where the counterpart seems much brighter than in the optical.

HATLAS J091043.1-000321

HATLAS J091043.1-000321 (S28, Fig 2.34) was observed in L10 as a potential lens, the optical lens galaxy found at a redshift of $z_{\text{photo}} = 0.46$ but with a reliability below our threshold of $R > 80\%$. Closer examination of the SDSS catalogue shows that there are two galaxies very close to the position of the SMG, the closest with a separation of $4.26''$ between optical counterpart and $250\,\mu$m position. Either or both of these could be lensing the source. In the case of lensing the sub-mm and optical source are simply

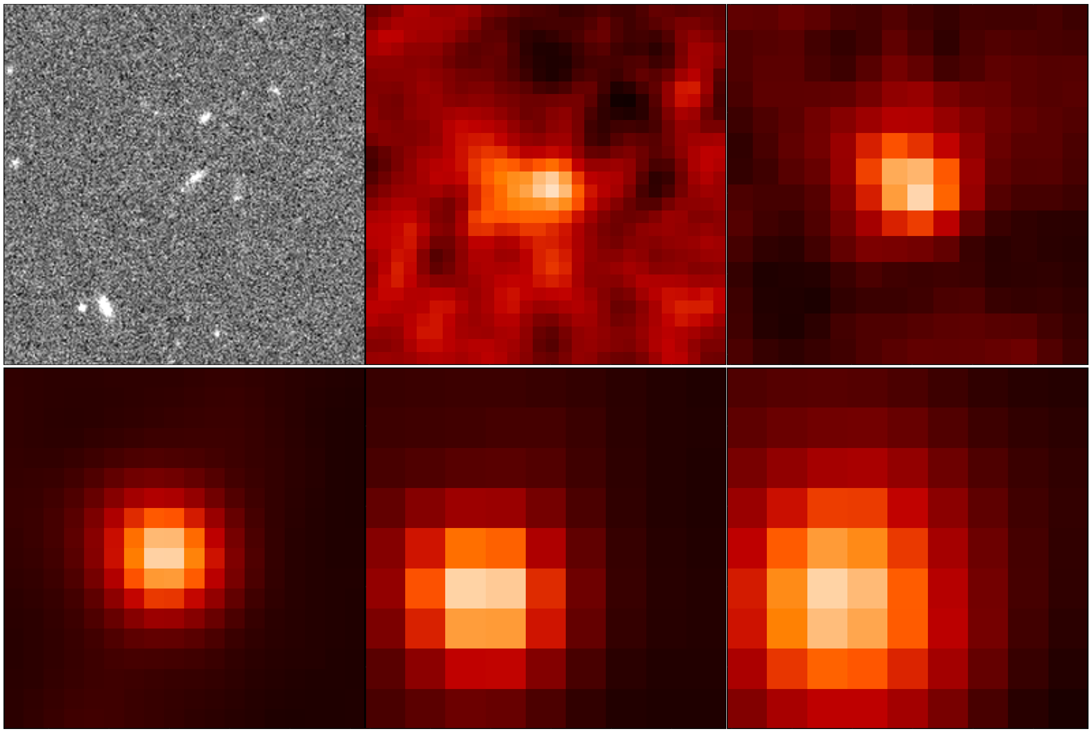

Figure 2.34: As previous for HATLAS J091043.1-000321, S28, at $z = 1.784$. A K-band image of this source is shown in Figure 2.30.

associated, they are not the same source and so it is possible to have two or more optical sources. The CO observations give a redshift of $z = 1.784$. A K-band image of this source is shown in Figure 2.48 showing the second, central source much more clearly.

HATLAS J085358.9+015537

HATLAS J085358.9+015537 (S29, Fig 2.35) is an as yet unpublished result. The bright point source with a separation of $4.38''$ in the centre of the r-band image is a foreground star. The CO observation give a redshift of $z = 2.091$. A K-band image of this source is shown in Figure 2.48. A central source is clearly seen in the K-band image that is only weakly observed in the optical, as well as the bright star.

HATLAS J115820.2-013753

HATLAS J115820.2-013753 (S30, Fig 2.36) was detected in H12. The CO observation give a redshift of $z = 2.191$.

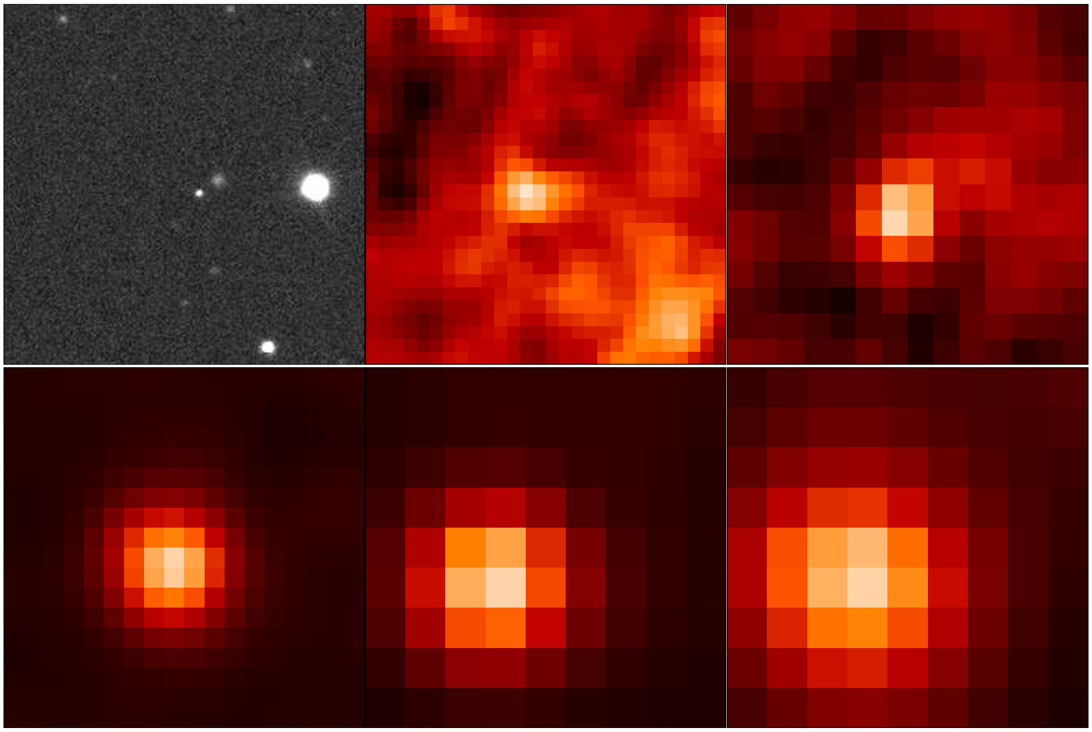

Figure 2.35: As previous for HATLAS J085358.9+015537, S29, at $z = 2.091$. A K-band image of this source is shown in Figure 2.30.

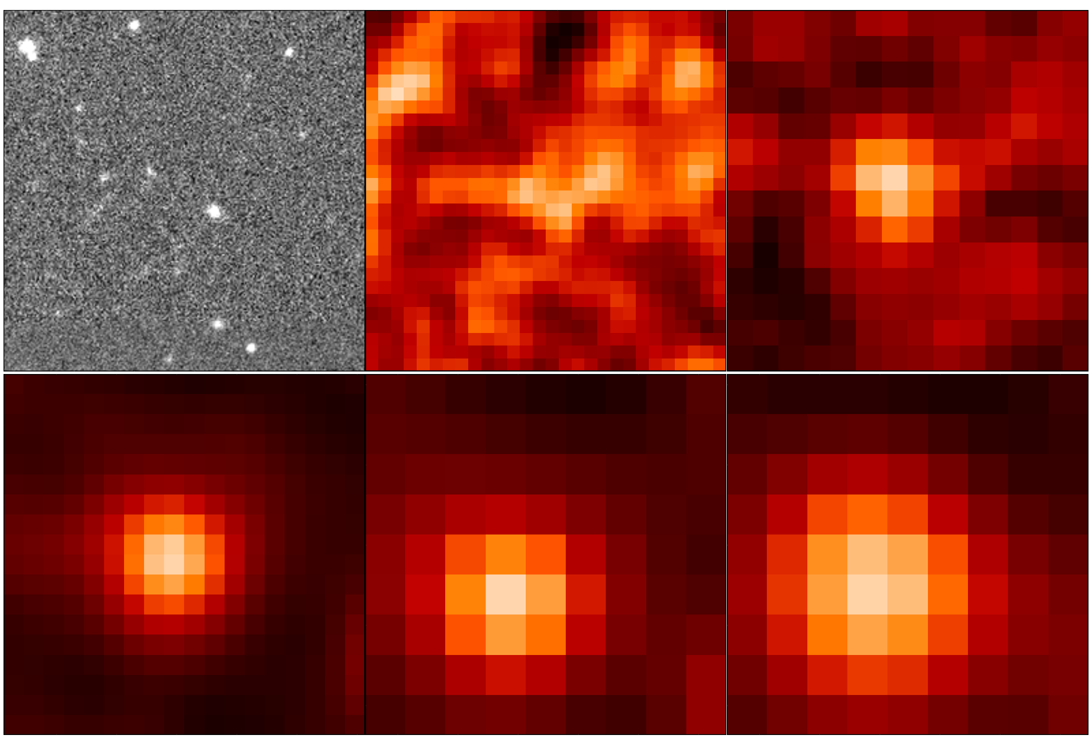

Figure 2.36: As previous for HATLAS J115820.2-013753, S30, at $z = 2.191$.

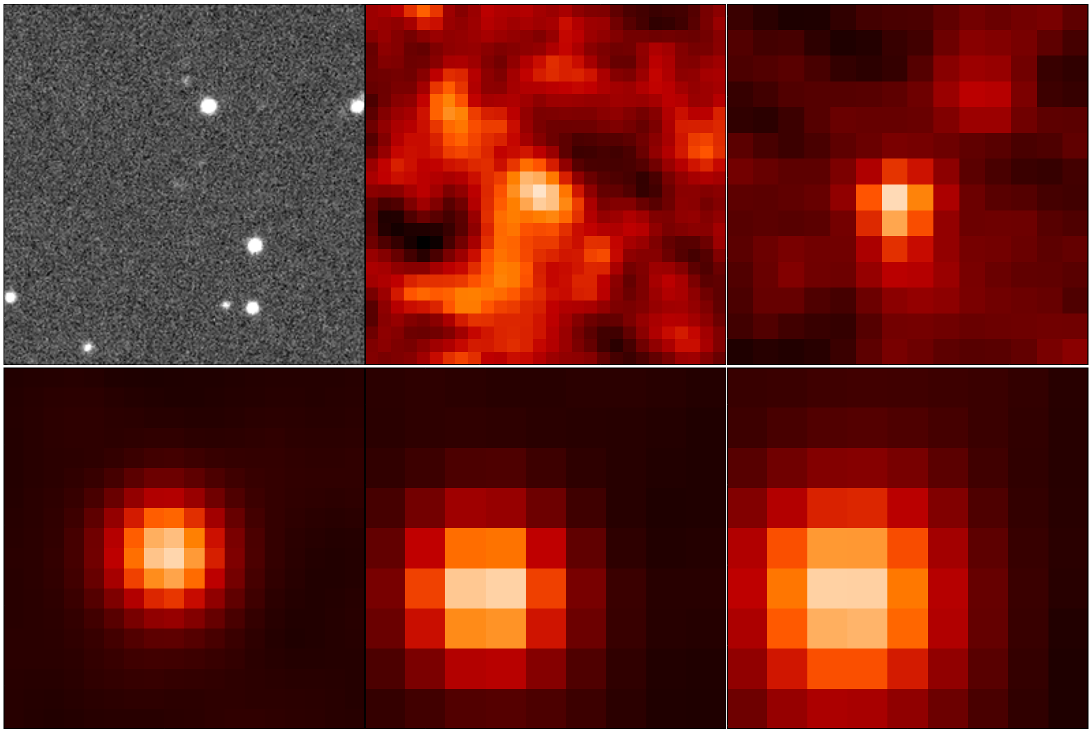

Figure 2.37: As previous for HATLAS J090302.9-014127, S31, at $z = 2.308$.

HATLAS J090302.9-014127

HATLAS J090302.9-014127 (S31, Fig 2.37) was imaged in L10. During CO observations S31 was found to lie at $z = 2.308$ while a second source was detected at $z = 0.942$. The optical photometric redshift placed the optical source at $z = 0.77$. Either the optical and the low-z CO source are in fact the same object, as the error limits on photometric redshifts allow for this, or they are two separate galaxies at low redshift, both potentially lensing the background object. In either case there is a foreground object in front of the SMG, rich in CO and thus molecular gas. It is possible that the lens contains dust and is thus emitting in the SPIRE bands but we were unable to test this. The fluxes used for this source were as observed. The separation between optical SDSS counterpart and 250 μm position is $1.39''$. Even in the close up of the r-band image the optical galaxy is nearly invisible.

HATLAS J084933.4+021443

HATLAS J084933.4+021443 (S32, Fig 2.38) was detected in H12. In the r-band image there are several nearby objects but these are mostly stars. A reliable, but faint optical galaxy at redshift $z_{\mathrm{photo}} = 0.33$ was found at a separation of $1.81''$. The CO observation give a redshift of $z = 2.410$. A K-band image of this source is shown in Figure 2.48.

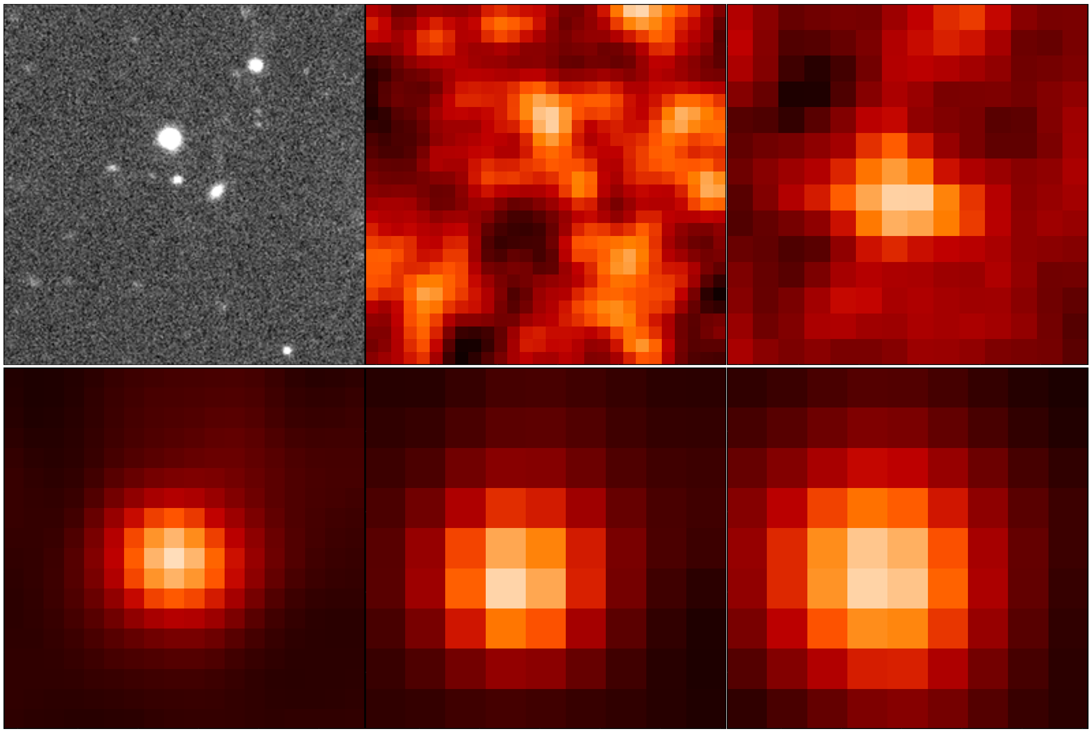

Figure 2.38: As previous for HATLAS J084933.4+021443, S32, at $z = 2.410$. A K-band image of this source is shown in Figure 2.30.

HATLAS J141351.9-000026

HATLAS J141351.9-000026 (S33, Fig 2.39) was detected in H12. In the r band image there are several faint galaxies around the position of the SMG. The SDSS catalogue puts most of these at a redshift of $z_{\mathrm{photo}} \sim 0.5 - 0.6$ which could imply that there is a cluster of galaxies lensing the source, as with S30, but investigating this was beyond the scope of this work. The closest optical counterpart was at $1.19''$ separation from the $250\,\mu$m position. The CO observation give a redshift of $z = 2.478$.

HATLAS J113243.1-005108

HATLAS HATLAS J113243.1-005108 (S34, Fig 2.40) was detected in H12. No match to an optical target was found and no source was seen in the r-band or SDSS images. The CO observation give a redshift of $z = 2.578$.

HATLAS J091840.8+023047

HATLAS J091840.8+023047 (S35, Fig 2.41) detected in H12. No match to an optical target was found and no source was seen in the r-band or SDSS images. The CO observation give a redshift of $z = 2.581$. A K-band image of this source is shown in Figure

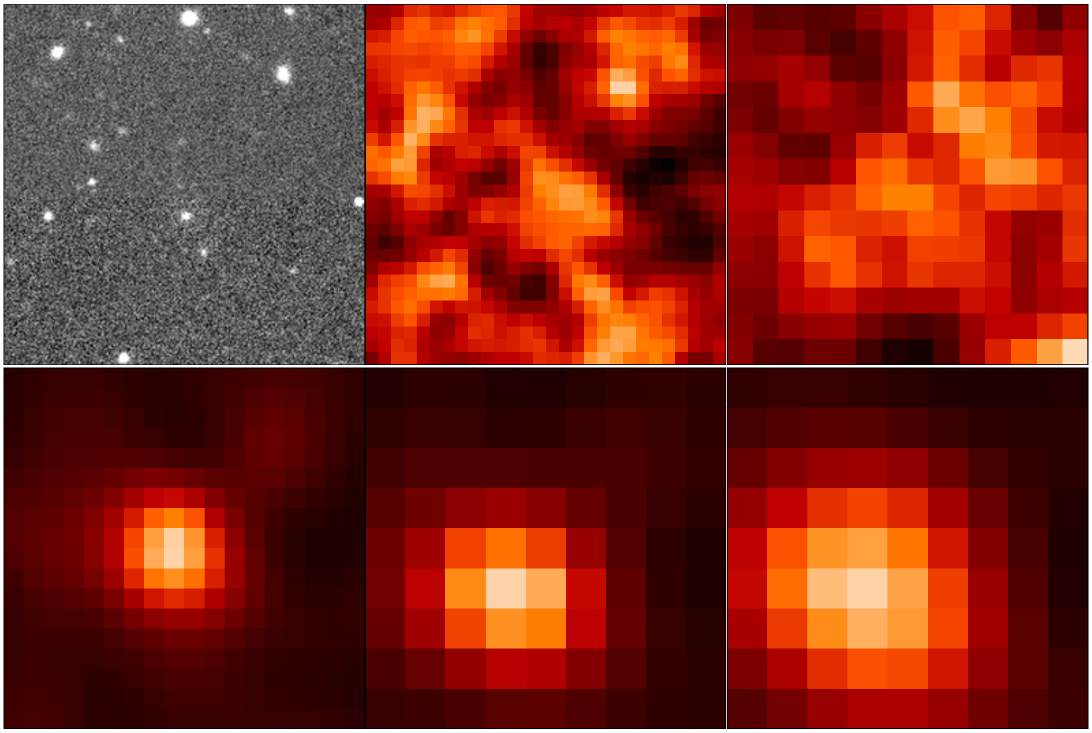

Figure 2.39: As previous for HATLAS J141351.9-000026, S33, at $z = 2.478$.

2.48. The K-band images weakly show some sources in the vicinity of the SMG but no relation has been verified.

HATLAS J091305.0-005343

HATLAS J091305.0-005343 (S36, Fig 2.42) was imaged in L10 and H12. L10 measured three CO transition lines, all of relatively low order (i.e. low energy). The lack of higher transition detections suggests a low gas temperature (< 50K) (Lupu et al., 2012). A reliable optical source with $z = 0.24$ was matched to this source and it was established that S36 is lensed (Negrello et al., 2010). The CO observation give a redshift of $z = 2.626$. The separation between optical SDSS counterpart and 250 μm position is 2.22″. A K-band image of this source is shown in Figure 2.48.

HATLAS J090311.6+003906

HATLAS J090311.6+003906 (S37, Fig 2.43) was imaged in L10 and later confirmed with the IRAM Plateau de Bure Interferometer. The separation between optical SDSS counterpart and 250 μm position is 1.18″. Current estimates put the magnification of the sub-mm source at a factor of 25 (Negrello et al., 2010). The CO observation give a redshift of $z = 3.037$. A K-band image of this source is shown in Figure 2.48.

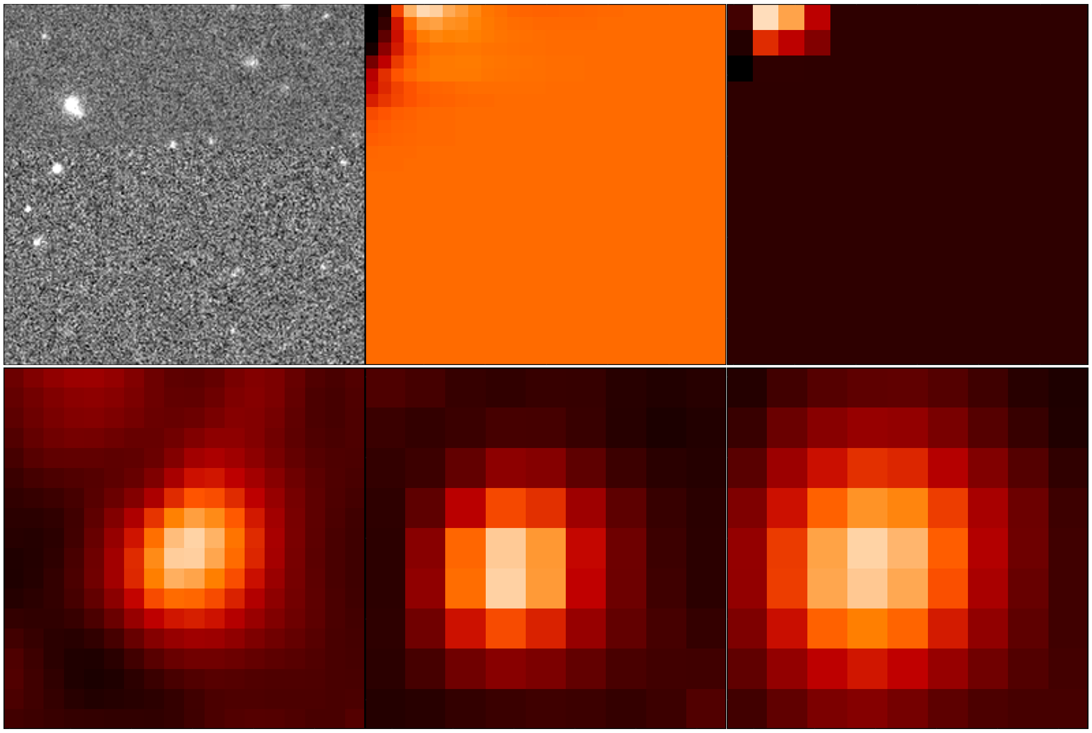

Figure 2.40: As previous for HATLAS J113243.1-005108, S34, at $z = 2.578$.

HATLAS J113526.3-014605

HATLAS J113526.3-014605 (S38, Fig 2.44) was detected in H12. No match to an optical target was found and no source was seen in the r-band or SDSS images. The CO observation give a redshift of $z = 3.128$.

HATLAS J114637.9-001132

HATLAS J114637.9-001132 (S39, Fig 2.45) was detected in H12. This source was investigated by Fu et al. (2012) as a potential lens. The optical image did not find a singular reliable source but, as can be seen in the r-band image, there are several faint optical galaxies in the vicinity. Their SDSS photometric redshifts put all of these sources at $z \sim 1$, considerably lower than suggested by the SPIRE fluxes and the $z = 3.259$ observed for the sub-mm source during followup CO line observations (Harris et al., 2012; Fu et al., 2012). Fu et al. (2012) found that the source was being lensed by all four of these objects, making interpretations of the original galaxy difficult. They estimated that the source was being magnified by approximately a factor of ten. It is believed that the background galaxy is a in the process of a major merger, the same mechanism that is thought to drive starburst activities in SMGs at $z > 2$. It is believed that the galaxy is a gas-rich starburst system similar to most SMGs and local ULIRGs. The separation

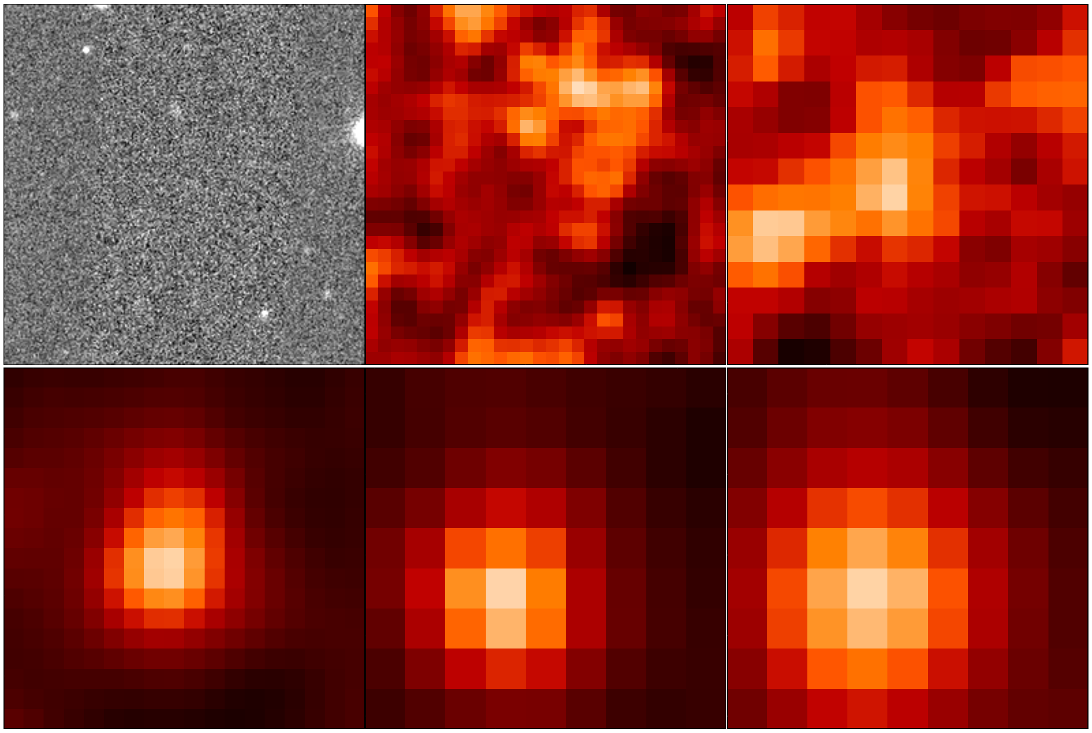

Figure 2.41: As previous for HATLAS J091840.8+023047, S35, at $z = 2.581$. A K-band image of this source is shown in Figure 2.30.

between optical counterpart from the SDSS and 250 μm position is $0.80''$.

HATLAS J142413.9+022303

HATLAS J142413.9+022303 (S40, Fig 2.46) was detected in C11. This source was selected for followup as it was one of the brightest SMGs detected in any *Herschel* surveys and is the brightest source with a peak of emission lying at 500 μm imaged in Phase 1. Such a high peak of emission indicates that the source lies at a redshift $z > 3$. As all SPIRE fluxes are in excess of 100 mJy this indicates that the source is likely lensed (Negrello et al., 2010).

The source was imaged with a variety of telescopes such as the IRAM 30m Telescope, the Plateau de Bure Interferometer, the Submillimeter Array and the APEX 12m telescope confirming the source to be at a redshift of $z = 4.243$. The galaxy appears to be a luminous ($L_{\mathrm{FIR}} \approx 3 - 8 \times 10^{12}$ L$_{\odot}$), dense ($n \approx 10^4\mathrm{cm}^{-3}$) and warm ($T_{\mathrm{kin}} \approx 40$K) galaxy, undergoing a period of starburst activity. Evidence was found to suggest a disc galaxy or a galaxy undergoing a merger but the source was unresolved.

When correlating with the SDSS survey we find that there is an optical source at $z_{photo} = 0.70$, though no spectroscopy was available for this source. The separation between optical counterpart from the SDSS and 250 μm position is $0.40''$. This would

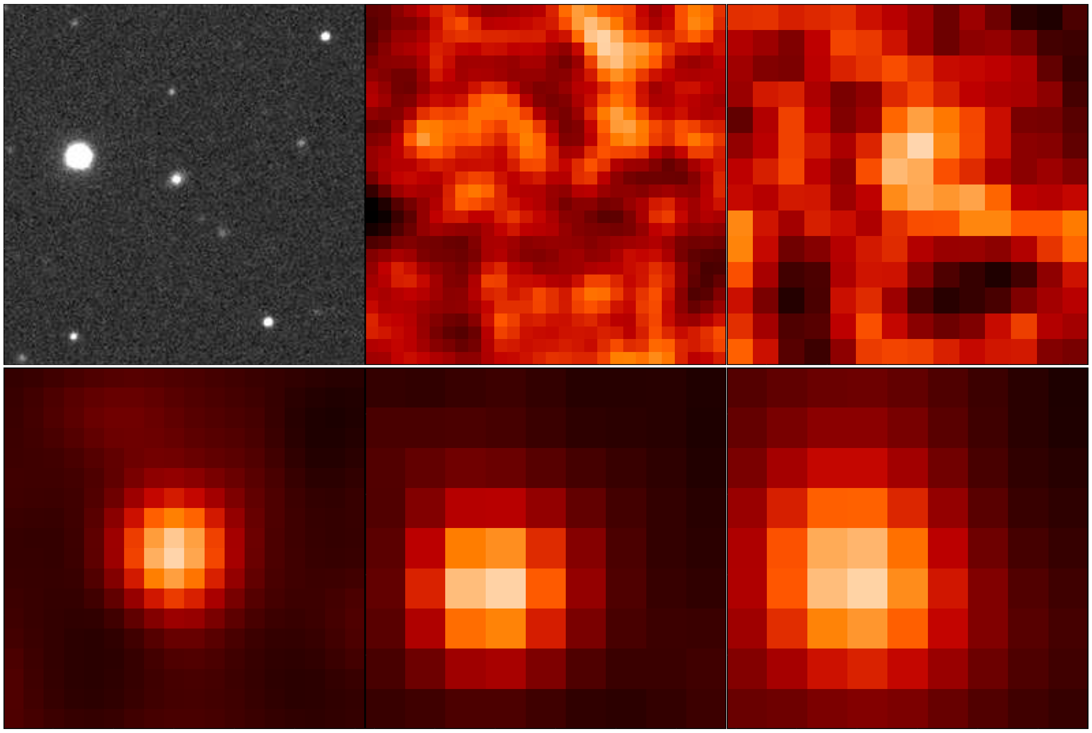

Figure 2.42: As previous for HATLAS J091305.0-005343, S36, at $z = 2.626$. A K-band image of this source is shown in Figure 2.30.

suggest that the source is lensed but this was not taken into account for the above calculations.

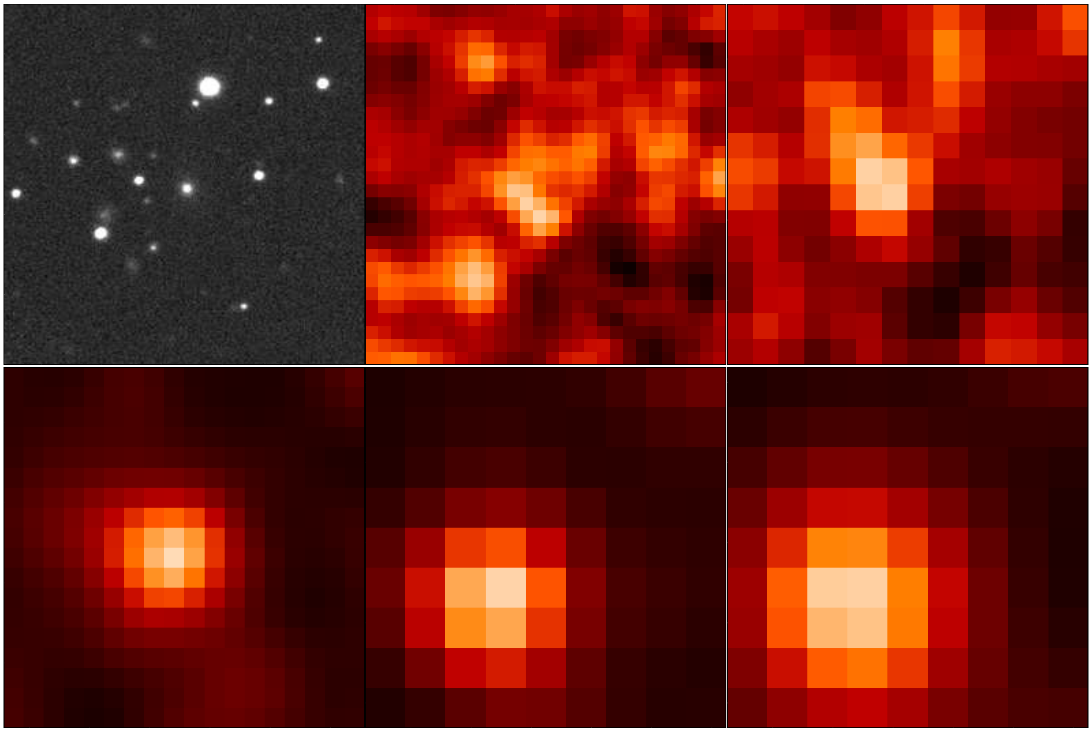

Figure 2.43: As for HATLAS J090311.6+003906, S37, at $z = 3.037$. A K-band image of this source is shown in Figure 2.30.

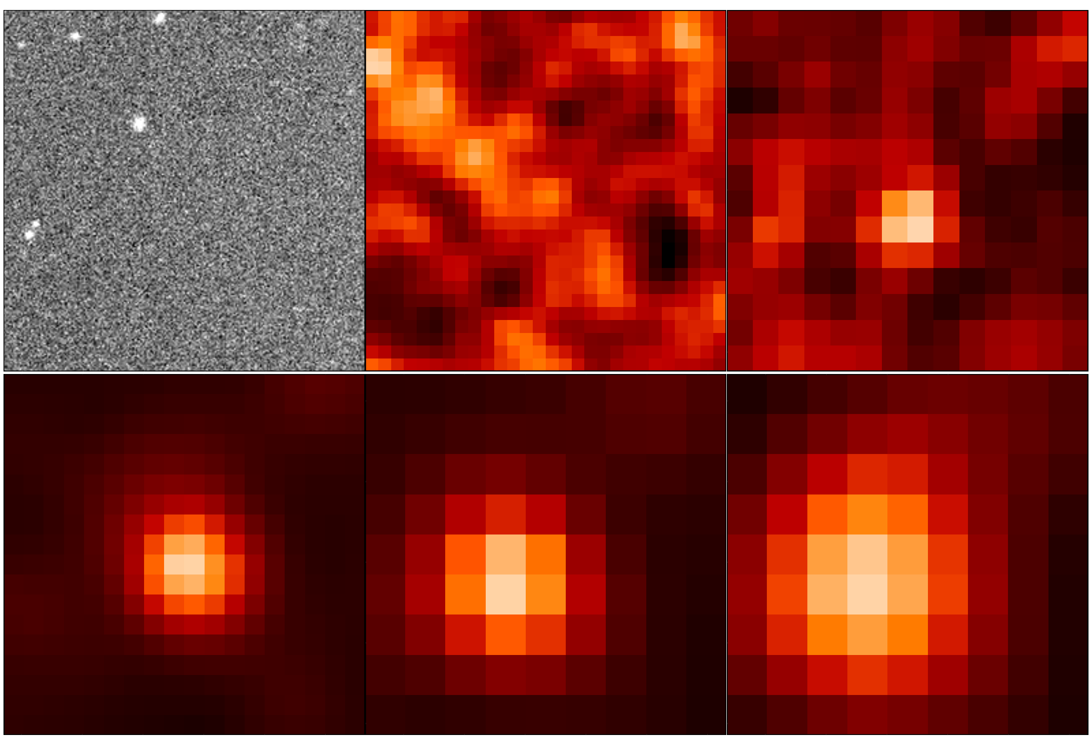

Figure 2.44: As previous for HATLAS J113526.3-014605, S38, at $z = 3.128$.

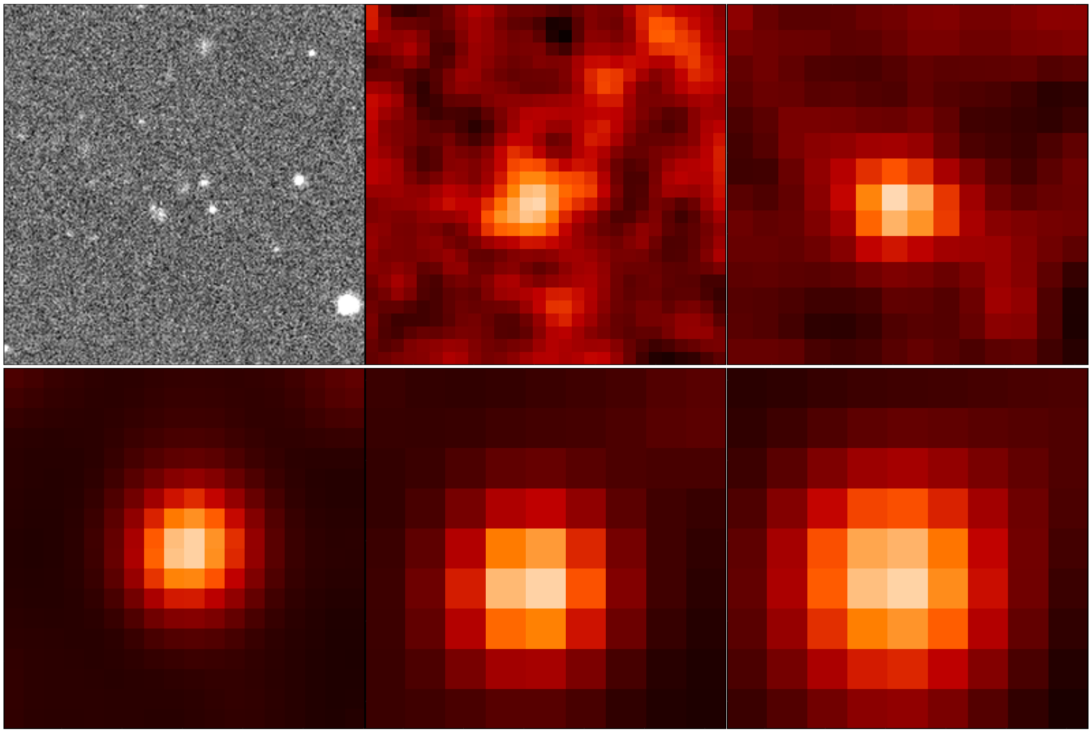

Figure 2.45: As previous for HATLAS J114637.9-001132, S39, at $z = 3.259$.

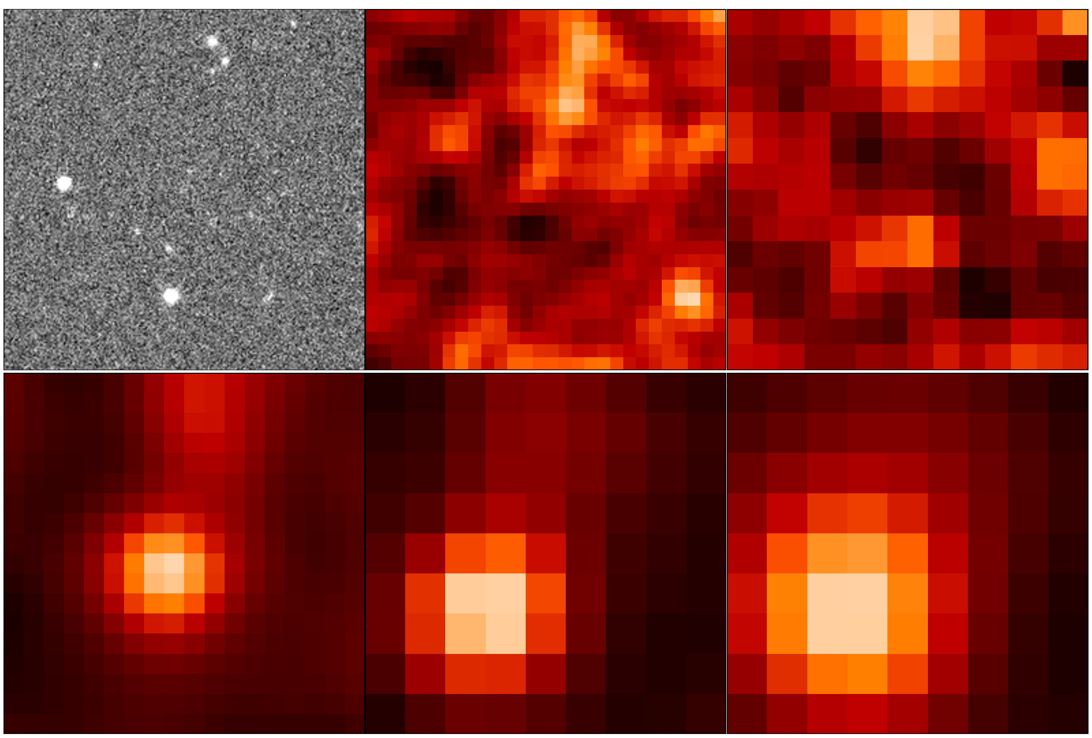

Figure 2.46: As previous for HATLAS J142413.9+022303, S40, at $z = 4.243$.

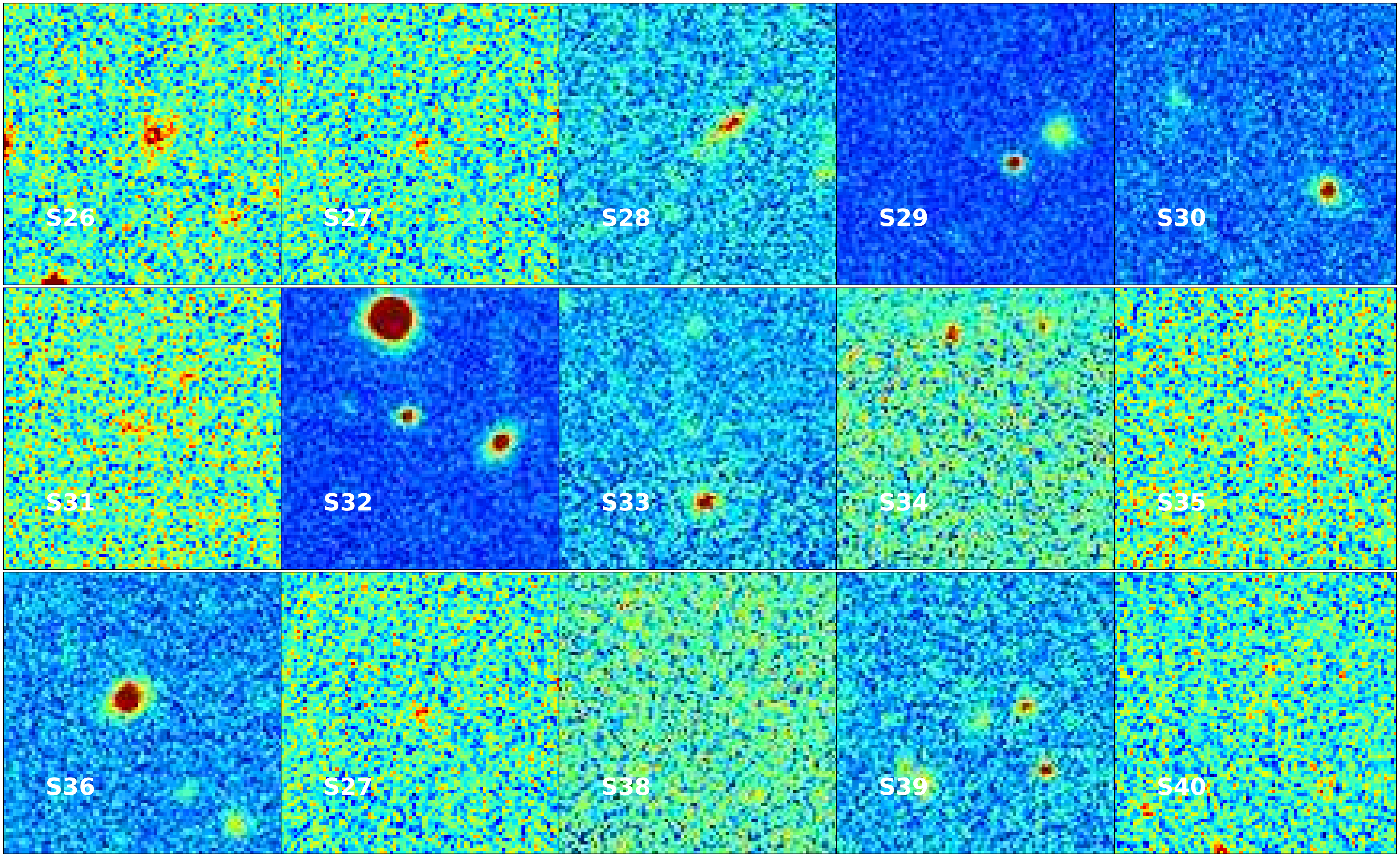

Figure 2.47: Closeup of r-band images showing optical counterparts from the SDSS for the CO selected sources. Images are $30'' \times 30''$.

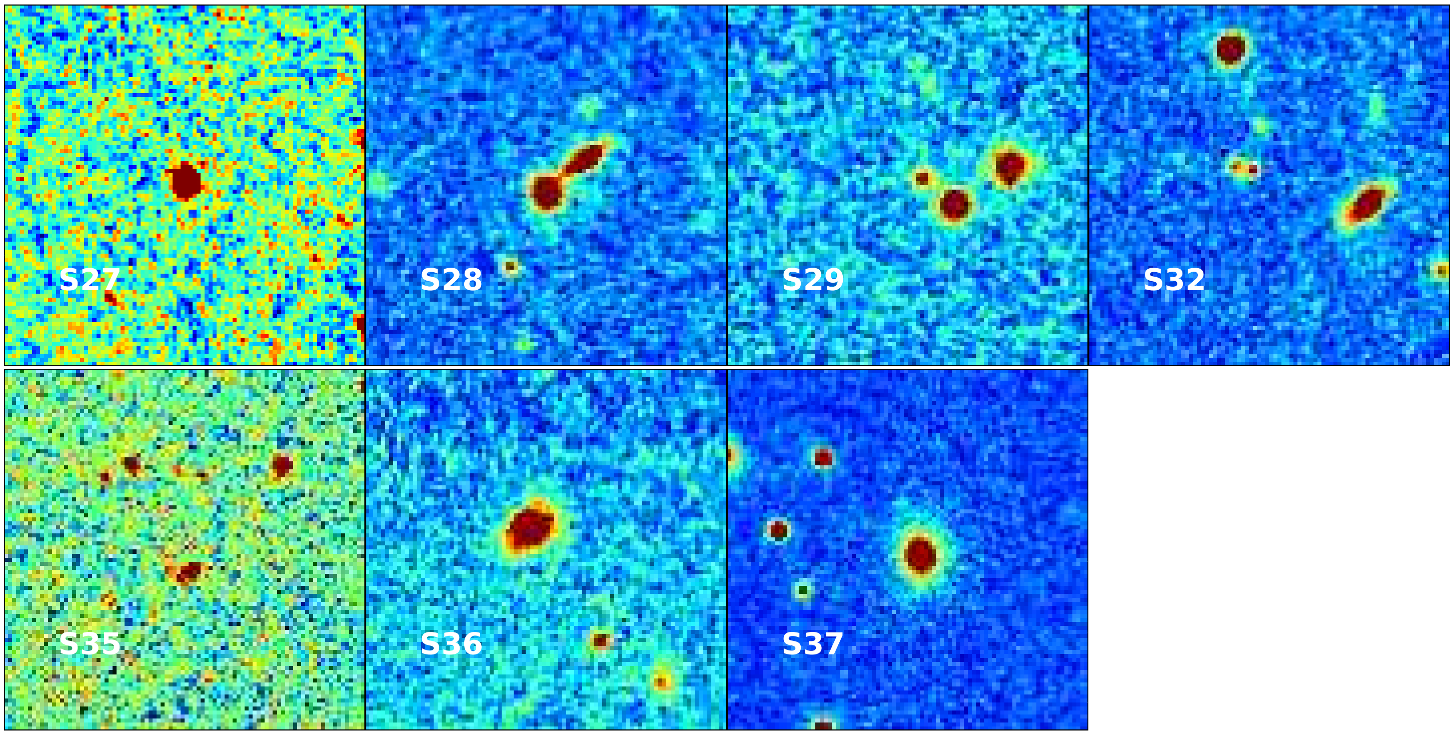

Figure 2.48: Closeup of K-band images showing optical counterparts from the SDSS for the CO selected sources. Images are $30'' \times 30''$.

2.5 Discussion of bias

There are many potential biases in this source selection. The sources I selected were all chosen to be bright in the sub-mm. This was done to ensure that the fluxes were as accurate as possible in as many *Herschel* bands as possible, as only the brightest sources had reliable PACS measurements. However, by selecting the brightest sources we may be selecting a subset of sources that does not accurately represent the sample. More luminous galaxies could be at a different temperature or contain more dust than a typical H-ATLAS galaxy.

There appears to be an increase in temperature with redshift both from our own roughly fitted temperatures and comparison with H12, C11 and L10. There is a well known problem with $T - z$ degeneracy within SED fitting. Increases in temperature shifts the peak of emission to shorter wavelengths. A source at a higher redshift will appear to peak at longer wavelengths and these two effects are easily confused. As we know the redshift to a high degree of accuracy for these sources, this effect will not be so great when fitting temperatures.

Comparison with previous work has shown how changing the dust emissivity index can cause huge differences in the resulting temperature. A lower value of β results in higher temperatures. However the actual shape of the SED remains relatively unchanged. In subsequent sections $\beta = 2$ was used based on evidence from Eales et al. (2012).

Several of the galaxies at $z > 1$ are lensed meaning that another galaxy lies directly along the line of sight. In most cases gravitational lenses are elliptical galaxies which are usually relatively free of dust. However the lens might still be emitting in the sub-mm and contributing to the SPIRE fluxes measured. This would mean that the sources that are lensed might appear to have an SED indicative of a lower redshift, or a lower temperature. Though the sample is too small to make any significant conclusions when predicting the dust temperature of the SEDs in Table 2.3 it does appear that there is no particular bias in temperature for those sources that are confirmed lenses and those that are not.

2.6 Summary

The High Redshift Sample is made up of a selection of spectroscopic sources in the range $0.5 > z > 1.0$ and sources with CO observations at $z > 1.0$. These sources were chosen to be bright in order to have a low signal to noise ratio.

Due to these criteria there is an increased likelihood of choosing a gravitationally lensed pair. For several we know that this is the case, meaning that the sources is not necessarily intrinsically bright but has been magnified. In these cases there is a chance that the lens may contaminate the *Herschel* fluxes. However the lens is often a massive, and relatively dustless, elliptical galaxy. In a few cases this is known not to be the case but the fluxes were left as they were measured.

We are certain that all redshifts are accurate. We believe that this selection of sources is representative of the H-ATLAS sample as a whole, although some bias may come from the selection process of the sources. Sources were chosen to be exceptionally bright. Sources chosen for CO follow up were chosen due to either being exceptionally bright or having colours that suggested they lied at high redshift. While they all do in fact lie at high redshift, there is still a chance that they are intrinsically redder sources as well. Whether lensed or not, the higher redshifts sources suffer from Malmquist bias, as only the brightest sources are observable above the survey threshold. This means that we cannot tell if these are typical of the galaxies at higher redshift, though previous evidence shows that there is a higher number density of sources at higher redshifts than in the local universe.

The sources with CO redshifts will be biased towards sources that are warm enough and contain enough CO to emit detectable transition lines. Not all sources that were pursued for CO follow up had CO lines detected. H12 detected CO lines in less than half of the sources they observed.

From fitting two temperature SEDs to the *Herschel* fluxes it appeared that there was a subtle trend of increasing warm dust temperature with increasing redshift for the HS. However comparison with values for low-z ULIRGs and LIRGs suggested that local sub-mm bright galaxies are warmer than those of the HS. A subtle temperature increase was seen with redshift but this could be due to increases in luminosity or due to a larger range of galaxy temperatures at $z < 1$.

A higher proportion of the CO galaxies had K-band images than those selected via their SSDS counterparts. This is most likely a selection effect. Sources selected for CO followup were significantly brighter than those from the SDSS survey. It would be expected that the K-band would also be brighter for these sources and so they would be more likely to be detected. However it is clear that not all sources are bright in the K-band.

Chapter 3

Estimating redshifts with the H-ATLAS sample

> Now, concentrate this time, Dougal. These are very small. Those are far away.
>
> *Father Ted Crilly*

3.1 Introduction

Much of the optical emission from distant galaxies is absorbed by dust and re-radiated at sub-millimeter (sub-mm) wavelengths (Fixsen et al., 1998). Sub-mm observations have revealed a population of dusty galaxies at $z > 2$, previously hidden at optical wavelengths (see review by Blain et al. (2002)). The inferred star formation rates for these galaxies are huge, averaging at $\simeq 400\mathrm{M}_{\odot}\,\mathrm{yr}^{-1}$ (Coppin et al., 2008). Observations of sub-mm galaxies (SMGs) allow us to examine star formation in the early universe and the strong cosmic evolution in the star formation rate (Gispert et al., 2000). Ground based surveys have managed to identify and study individual sub-mm sources (Barger et al., 1998; Hughes et al., 1998; Blain et al., 1999). Such surveys however covered small areas of sky and only found a few tens of SMGs and suffered from biases in their selections. The BLAST survey (Devlin et al., 2009) covered $\sim 9\,\mathrm{deg}^2$ of sky and found a few hundred SMGs (Eales et al., 2009) but to really probe the evolution of the SMGs with redshift much larger blind surveys are needed.

In order to investigate the SMGs, particularly the evolution of the star formation rate and the luminosity function, we need to know the redshifts of all sources being considered. Ideally this is done by matching a source to an optical counterpart and then measuring the redshift of this counterpart spectroscopically. However the poor angular resolution of sub-mm telescopes and high confusion between sources means that finding optical counterparts in this way is difficult. One method to find counterparts is to first match the sub-mm source to a mid-IR or radio source, then match the mid-IR/radio source to its corresponding optical counterpart. This can lead to a bias, however, as cold or high redshift objects are more likely to be undetected at mid-infrared and radio wavelengths (Chapman et al., 2005; Younger et al., 2007).

Fully exploiting the potential of sub-mm wavelengths on a large scale was impossible until the advent of the *Herschel Space Observatory* (Pilbratt et al., 2010)[1]. The infrared emission of galaxies peaks between $70 - 500\,\mu$m, the wavebands that are covered by *Herschel*'s two instruments: the Spectral and Photometric Imaging Receiver, SPIRE (Griffin et al., 2010), and the Photodetector Array Camera and Spectrometer, PACS (Poglitsch et al., 2010). The *Herschel* Astrophysics Terahertz Large Area Survey, H-ATLAS (Eales et al., 2010), covers 550 deg^2 of sky and is the largest sub-mm blind survey to date.

The H-ATLAS fields were chosen partly due to the high quantity of complementary data at other wavelengths. However, less than 10% of the H-ATLAS sources in the 15h field are detected by *WISE* at $22\,\mu$m (Bond et al., 2012) and current large-area radio surveys only detect a tiny fraction of H-ATLAS sources. Nevertheless, Smith et al. (2011) and Fleuren et al. (2012) have shown that it is possible, using a sophisticated Baysian technique, to match the H-ATLAS sources to optically-detected galaxies directly. However, only approximately a third of the H-ATLAS sources have single reliable optical counterparts on images from the Sloan Digital Sky Survey (SDSS) (Smith et al., 2011) which has limited subsequent investigations into the luminosity (Dye et al., 2010) or dust mass (Dunne et al., 2011) functions. Matching to the near infrared images from the VIKING survey produces a higher proportion of counterparts, 51% opposed to the 36% provided by the optical (Fleuren et al., 2012), but there are still a large number of sources without counterparts.

CO line spectroscopy, using wide band instruments, can be used to accurately measure the redshift of sub-mm sources without the need for accurate optical positions (Lupu et al., 2012; Frayer et al., 2011; Harris et al., 2012). However, CO observations are time consuming and even with ALMA it will only be possible to measure redshifts for a tiny fraction of the H-ATLAS sources.

The only feasible method currently for estimating redshifts for such a large number of *Herschel* sources is to estimate the redshifts from the sub-mm fluxes themselves. Previous attempts to estimate redshifts for *Herschel* sources from the sub-mm fluxes have used as templates the spectral energy distributions (SEDs) of individual galaxies e.g. Lapi

[1] *Herschel* is an ESA space observatory with science instruments provided by European-led Principal Investigator consortia and with important participation from NASA.

et al. (2011); González-Nuevo et al. (2012). Many of these template galaxies are at low redshift and their SEDs may not be representative of the SEDs of the high-redshift *Herschel* sources and even if a high-redshift galaxy is used it may not be representative of the high-redshift population as a whole. For these reasons, we describe in this paper a method for creating a template directly from the sub-mm fluxes of all the high-z H-ATLAS sources for which there are spectroscopic redshifts. The SEDs are also important for increasing our understanding of the population of high-redshift dusty galaxies and investigating the SEDs at the range of wavelengths in which the dust emission is at its peak. The average SED that we derive in this paper, although obviously telling us nothing about the diversity of the population, is still useful for comparing this population with dusty galaxies of low redshift (Dunne & Eales, 2001; Blain et al., 2003).

Section 3.2 describes the observations on which the method is based. We describe the method of template determination in Section 3.3 and present the estimated redshift distributions in Section 3.4. We summarise our results in Section 3.5. We assume $\Omega_{\mathrm{m}} = 0.3$, $\Omega_{\lambda} = 0.7$, $H_0 = 70$ km s^{-1} Mpc^{-1}.

3.2 Data

3.2.1 FIR images and catalogues

Phase 1 of the H-ATLAS survey covers around 160 deg^2 of sky with both PACS observations at 100 and 160 μm and SPIRE observations at 250, 350 and 500 μm. However only a few percent of the H-ATLAS sources were detected at PACS wavelengths at greater than 5σ, so we have developed a method of estimating redshifts using only the SPIRE fluxes. Phase 1 coincides with the three equatorial fields of the Galaxy and Mass Assembly, GAMA (Driver et al., 2011), spectroscopic survey.

The FWHM beam sizes of the SPIRE observations are 18″, 25″ and 35″ for 250, 350 and 500 μm respectively. Pascale et al. (2011) describes the map-making procedure for the SPIRE observations. To find the sources, the MADX algorithm (Maddox et al., 2010; Rigby et al., 2011) was used on the maps that had been passed through a point spread function filter. The algorithm initially used the 250 μm map to find the positions of sources detected above 2.5σ. The corresponding fluxes from the 350 and 500 μm maps were then measured at these positions. If a source was detected at greater than 5σ in any of the three wavebands then it was listed as a detection, with 78,014 sources extracted in total. The 5σ sensitivities of the catalogues are 32, 36 and 45 mJy for 250, 350 and 500 μm, respectively. The error on the flux, σ_{meas}, is the combined instrumental and confusion noise with an additional 7% calibration error added in quadrature. The Phase

1 *Herschel* maps and catalogues will be described fully in Valiante et al. (in prep.).

3.2.2 Optical Counterparts

The fields were chosen due to their lack of galactic cirrus (though G09 does still contain a large amount of cirrus) and large amount of complementary multi-wavelength data. However the lack of radio and mid-IR data meant counterparts were found directly by applying a likelihood ratio technique (Smith et al., 2011) to objects in the SDSS (York et al., 2000) DR7 catalogue with a search radius of 10″. Only optical objects matched with a reliability factor R≥80% were considered as reliable matches.

23,312 sources have reliable optical counterparts. For these there is photometry in *ugriz* and *YJHK* from the SDSS and UKIDS Large Area Survey (Lawrence et al., 2007), respectively, and FUV and NUV data from GALEX (Martin et al., 2005). 12,136 sources also have spectroscopic redshifts available from the SDSS, 6dFGS (Jones et al., 2009) and 2SLAQ-QSO/LRG (Croom et al., 2009; Cannon et al., 2006) surveys and from the GAMA catalogues (Driver et al., 2011). A further 10,972 photometric redshifts have been estimated from optical and near-IR photometry using the artificial neural network code (ANNz) (Smith et al., 2011). These redshift distributions are shown in Fig 3.1. In Fig 3.2 sources without optical counterparts are shown to have slightly redder sub-mm colours, suggesting that they lie at higher redshifts than those with counterparts.

3.2.3 CO Observations

We used fifteen H-ATLAS sources with redshifts from CO observations to construct our template. These sources are examined in detail in Chapter 2. Five of these are from Lupu et al. (2012), who measured CO redshifts for sources with $S_{500} > 100$mJy; seven are from Harris et al. (2012), who observed galaxies whose sub-mm emission peaked at 350 μm, indicating a high redshift; one is from Cox et al. (2011), who studied one of the brightest sources in the GAMA 15hr field, which has the peak of its emission at 500 μm; and the remaining two are as yet unpublished redshifts from the H-ATLAS team.

The selection criteria for these follow-up observations picked out bright galaxies that were likely to be at high redshift and so only represent the most luminous high-z galaxies. The *Herschel* colours of these galaxies are very red, which might introduce a bias towards colder objects. There is also a bias towards galaxies that are rich in CO gas, since not all sources observed in the CO programme were detected. Many of these sources are likely to have been strongly lensed (Negrello et al., 2010; Harris et al., 2012). As the gravitational magnification is likely to vary over a source it is possible that an unusually warm section of a galaxy might be magnified more strongly, boosting the flux at short

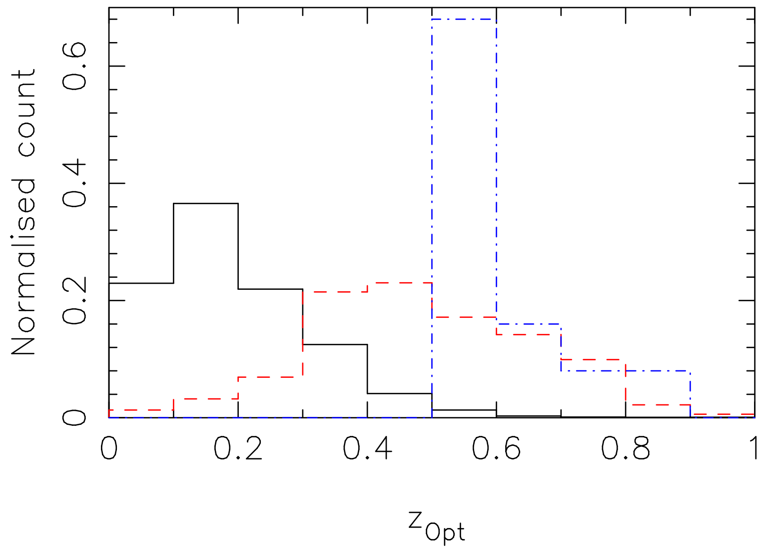

Figure 3.1: Redshift distributions of the H-ATLAS galaxies as determined from their SDSS counterparts. The solid black line shows those with measured spectroscopic redshifts and the dashed red line those with photometrically estimated redshifts only. The dot-dashed blue line shows the redshift distribution of the objects in the sample used to derive the template (Section 3.3): 25 spectroscopically observed sources with $0.5 < z < 1.0$ and $S_{250} > 50$mJy.

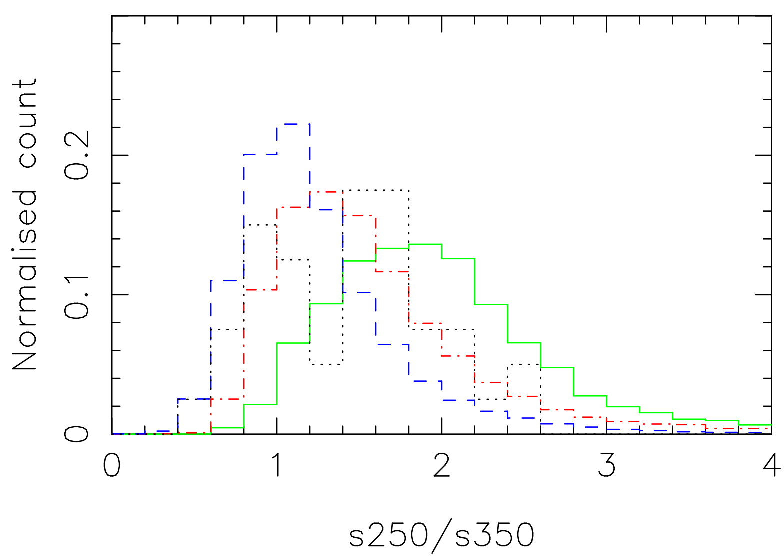

Figure 3.2: Histograms of the ratio of $250\,\mu$m to $350\,\mu$m fluxes. The solid green line represents those with spectroscopically measured optical counterparts. The dot-dashed red line shows sources with only photometric redshifts. The blue dashed line shows sources without any optical counterpart. The black dotted line shows the sample of 40 sources in the sample used to derive the template (Section 3.3). Sources without counterparts are redder in colour, indicating a higher redshift population.

wavelengths. However the dust detected at SPIRE wavelengths is likely to be cool and evenly distributed throughout the galaxy and so the *Herschel* colours are likely to remain reasonably unaffected and resulting temperatures can be taken as safe upper limits.

3.3 The Template

3.3.1 Sample selection

To create the template we formed a sample of bright sources with accurately known redshifts. To do this we selected sources with either a redshift determined from the CO observations, $z_{\rm CO}$, or an optically determined redshift, $z_{\rm spec}$, with $0.5 \leq z_{\rm spec} < 1$. In addition the flux must be greater than 50 mJy in at least one of the SPIRE wavelengths. Optically selected sources with $z_{\rm spec} > 1$ are more likely to be quasars or atypical galaxies and so we did not use sources with optically determined redshifts above this reshift. The flux and redshift limits ensure we have a selection of high-z sources for which we have accurate measurements of the SEDs.

We excluded sources at $z < 0.5$ for two reasons. First, these sources do not actually provide much extra information about the rest-frame *Herschel* SEDs, because for low-redshift galaxies the SPIRE colours depend very weakly on dust temperature. Second, there is evidence from studies that combine the PACS and SPIRE data for individual sources (Lapi et al., 2011; Smith et al., 2012) and from stacking analyses (Eales et al. in prep.) that the SEDs of low-redshift and high-redshift Herschel sources are quite different.

These selection criteria produced a sample of 40 sources with known redshifts from Chapter 2: 15 sources with CO redshifts and 25 sources with optical redshifts. There are actually many more sources in the redshift range $0.5 < z < 1.0$ with optical redshifts, but 25 were randomly chosen in order to prevent them from overwhelming the CO sources. We assume that this sample is representative of the whole survey; their redshifts and *Herschel* colours are shown for comparison in Figs 3.1 and 3.2. The colours of this sample seem to be similar to those of sources with no optical counterpart. However, a possible bias may arise from the fact that all these sources are chosen to be bright and so will be among the most luminous H-ATLAS sources at their respective redshifts and so may not be representative of less luminous sources (Casey et al., 2012). We will use PACS data to test the dependence of dust temperature on luminosity in a later paper (Eales et al. in prep.).

3.3.2 Creating the Template

We then transform these sources to their rest-frame wavelengths as determined by their $z_{\rm spec}$ or $z_{\rm CO}$, thus giving a range of flux measurements from $\sim 50-350\,\mu$m. We then fit our model, based upon a modified black body spectrum, consisting of two dust components each with a different temperature:

$$S_\nu = A[B_\nu(T_{\rm h})\nu^\beta + aB_\nu(T_{\rm c})\nu^\beta] \tag{3.1}$$

where S_ν is the flux at a rest-frame frequency ν, A is a normalisation factor, B_ν is the Planck function, β is the dust emissivity index, $T_{\rm h}$ and $T_{\rm c}$ are the temperatures of the hot and cold dust components, and a is the ratio of the mass of cold dust to the mass of hot dust.

A two temperature model is important because galaxies with high far-infrared luminosities are known to contain a cold dust component (Dunne & Eales, 2001). We used $\beta = 2$ because recent *Herschel* observations of nearby galaxies suggest this is a typical value (Eales et al., 2012). The SPIRE fluxes for the H-ATLAS sources do not give useful constraints on β as they do not lie in the Rayleigh-Jeans region of the SED, where β has the greatest effect.

For a given set of $T_{\rm c}$, $T_{\rm h}$ and a the template was then fitted to the fluxes at their rest-frame wavelengths of all the sources within our sample. Different intrinsic brightnesses and distances caused a large variation in flux between sources and so we introduced an additional normalisation factor, N_i, for each source such that

$$\chi^2 = \sum_{i=1}^{n} \left[\sum^{\lambda} \frac{S_{{\rm model},i} - N_i S_{{\rm meas},i}}{N_i \sigma_{{\rm meas},i}} \right]^2, \tag{3.2}$$

where $S_{{\rm model},i}$ is the predicted flux of the $i^{\rm th}$ source according to Equation 3.1 for the set of values being considered and $S_{{\rm meas},i}$ is the measured flux and $\sigma_{{\rm meas},i}$ is the total error. For the $i^{\rm th}$ source the measured fluxes and errors at all wavelengths are multiplied by N_i, and then the difference from the flux predicted by the model is found. Since the sources in our calibration sample are very bright, there are PACS measurements for many of them. In fitting the template, we used the PACS measurements for the sources as long as the rest-frame wavelength of the flux measurement was at $>50\,\mu$m; at shorter wavelengths there is likely to be significant emission from dust that is not in thermal equilibrium. χ^2 is a sum over all 40 sources in the sample and over all available wavelengths.

For each combination of $T_{\rm c}$, $T_{\rm h}$ and a we found the values of N_i that gave the minimum value of χ^2. Our best-fit model was the set of $T_{\rm c}$, $T_{\rm h}$ and a that gave the lowest value of

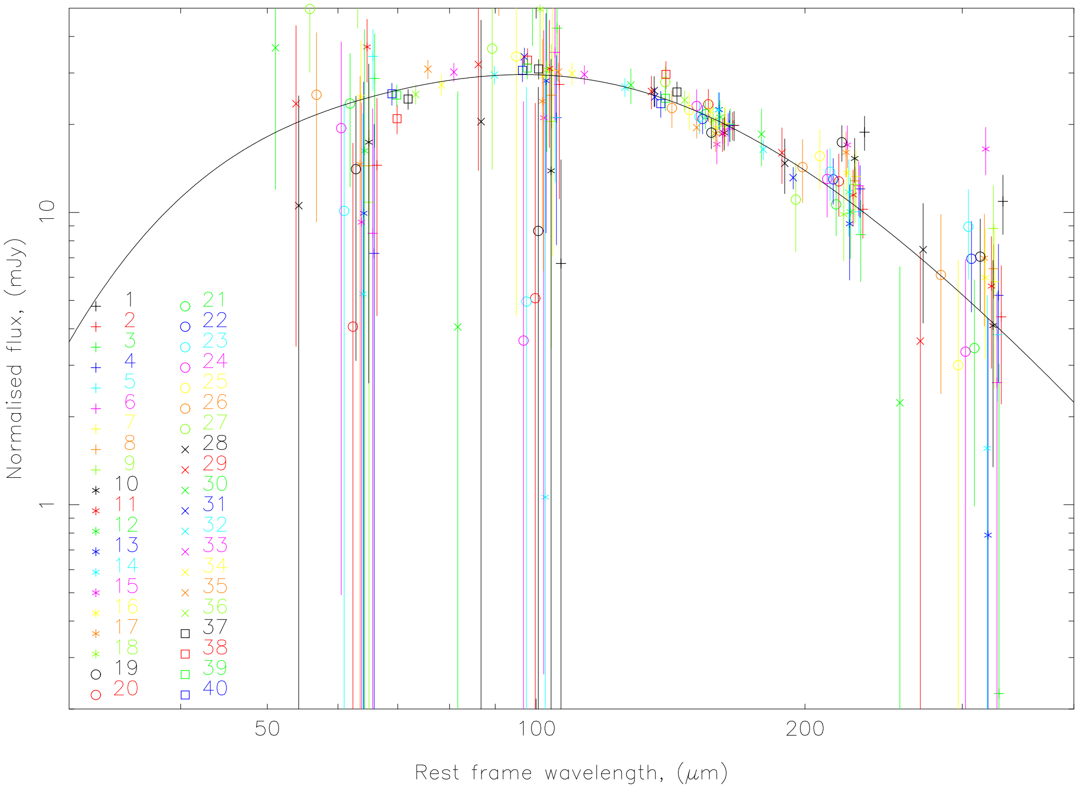

Figure 3.3: Best-fit model with the rest frame fluxes for all 40 of the sources in Chapter 2 adjusted by their best normalisation factors, N_i. The red and blue lines show the SEDs for the individual dust components of our template. All fluxes from a given source are shown with the same plot points, the key of which is given in Chapter 2.

χ^2 overall, resulting in the template shown in Figure 3.3 and the values given in Table 3.1. Our best-fit model gives $T_{\rm c} = 23.9$K, $T_{\rm h} = 46.9$K with a ratio of cold to hot dust mass being 30.1. For comparison we have also shown the SEDs of SMM J2135-0102 ($z = 2.3$) and G15.141 ($z = 4.2$) in Figure 3.4, as used in Lapi et al. (2011) for estimating the redshifts of the sources in the H-ATLAS field observed during the *Herschel* Science Demonstation Phase (SDP). All SEDs are normalised to the best values of N_i given by our template as seen in Figure 3.3. The template we find from the sample peaks at a slightly higher wavelength than that of those found in Lapi et al. (2011) though the Rayleigh-Jeans region has very similar slope, most likely as both use $\beta = 2$ for at least one of the dust components. When compared to the SED from Casey et al. (2012), generated from spectroscopically selected HerMES galaxies, the peak lies in a very similar position. The SED dervied by Casey et al. (2012) is controlled by a power law shortward of the peak to cover the mid-IR component, which is why is is so different from the other SEDs. However this region is well below the rest frame wavelength of sampled by our SPIRE observations.

It should be noted that the template is not expected to be a physically real SED but

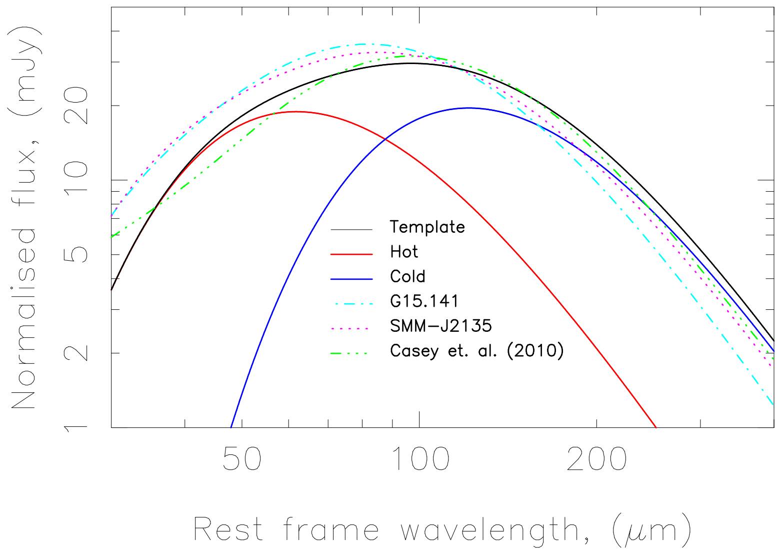

Figure 3.4: Best-fit model as compared with the SEDs from G15.141 (dotted magenta) and SMM J2135-0102 (dot-dashed cyan) used by Lapi et al. (2011) and the best fit SED from Casey et al. (2012) (green triple-dot dash). The comparative SEDs have been normalised to best fit the fluxes as they are shown in Figure 3.3.

simply a statistical tool for estimating redshifts from SPIRE fluxes. The peak of Fig 3.3 will represent the real SED of sources with $z \sim 2-4$, with the SED at longer wavelengths representing the real SED of H-ATLAS galaxies at lower redshift. In a later paper we will make a more detailed comparison of the SEDs of high-redshift H-ATLAS galaxies with low-redshift dusty galaxies. Here we note that the average SED is quite similar to the two-temperature SEDs found by Dunne & Eales (2001) for luminous low-redshift dusty galaxies.

3.3.3 A Jackknife Method for Testing the Template

In order to test the accuracy of the redshifts determined from the template we used a jackknife technique. From the initial selection of 40 sources we created two subsets by listing the sources by redshift and alternately placing them into each subset. This ensured an even spread of redshifts and thus equal wavelength coverage. This was repeated twice more, this time splitting the sources randomly, resulting in three pairs of subsets from the initial data sample. For each subset we created a template as detailed in Section 3.3.2. We then used the template to estimate the redshifts, $z_{\rm temp}$, of the sources in the other sample from the pair. In estimating the redshifts the template was allowed to vary in redshift between $0 \leq z < 20$ with the minimum χ^2 between the fluxes and the template giving the best estimate of $z_{\rm temp}$.

The temperatures and dust ratio values for the templates derived from the jackknife

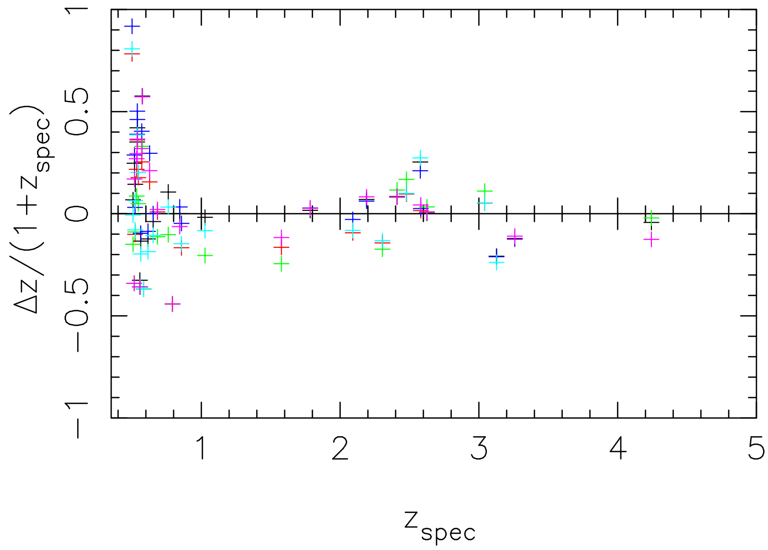

Figure 3.5: The data was split three ways into pairs of subsets. Each of these were used to create a template, then the template used to estimate the redshifts of the other subset in the pair. The resulting redhshift errors are shown here plotted against the spectroscopic redshifts. They key is given in Table 3.1

sets, as well as the values for the whole sample are shown in in Table 3.1. To estimate the accuracy of the template derived from a set of sources, we calculate the value of

$$\frac{\Delta z}{1+z} \equiv \frac{z_{\rm temp} - z_{\rm spec}}{1+z_{\rm spec}} \tag{3.3}$$

for the sources in the other set from the pair (or the whole sample when the template is derived from the whole sample), where $z_{\rm spec}$ is the best optical or CO redshift. Fig 3.5 shows the estimates from all three jackknife pairs. The mean and root mean squared (rms) values for each template are shown in Table 3.1. For comparison we have also used the two SEDs used in Lapi et al. (2011) to estimate the redshifts of the sources in our sample.

As our estimate of the uncertainty in the redshifts estimates $z_{\rm temp}$ from the template obtained from the whole sample, we use the average from all the jackknife tests in Table 3.1 giving a mean rms of $\Delta z/(1+z) = 0.26$. Note that if we only look at sources where $z_{\rm spec} > 1$ then the error is much less. Fig 3.5 clearly shows that there is much higher accuracy above this cut off. If we restrict our error analysis to the sources in the template sample with $z_{\rm spec} > 1$, we obtain a mean $\Delta z/(1+z) = -0.013$ with and rms of 0.12.

Our results are comparable to the error estimates given by Lapi et al. (2011). When the templates from Lapi et al. (2011) (SMM J2135-0102 and G15.141) are used to estimate redshifts for our 40-source sample, there is a larger systematic error than when we use our own template, with the predicted redshifts considerably higher than the actual values.

Table 3.1: Results of the jackknife tests applied to the data. 'Template' indicates the subset used to create the template and the temperatures and dust mass ratios of the template are listed in the following three columns. 'All' is the template resulting from using the whole sample and is the template that will be used in subsequent sections. The next two columns show our estimates of the redshift errors that will be obtained using that template, which were obtained by comparing the redshift estimates and the spectroscopic redshifts for the sources in the other member of the jackknife pair (or all the sources for the template that was obtained from the whole sample). Column 5 shows the mean value of $\Delta z/(1 + z_{spec})$ and column 6 gives the root mean squared (rms) of this. Column 7 gives the key for Fig 3.5. The two rows below the line show the result of testing two of the templates used by Lapi et al. (2011) against our calibration sample.

Template	T_c	T_h	a	$\Delta z/(1+z)$	rms	Key
1	24.8	45.5	22.25	0.06 ± 0.04	0.28 ± 0.03	Black
2	22.2	43.0	22.22	-0.03 ± 0.03	0.24 ± 0.03	Red
3	18.8	39.6	20.97	-0.06 ± 0.03	0.24 ± 0.03	Green
4	26.6	51.1	44.55	0.08 ± 0.04	0.29 ± 0.03	Blue
5	22.9	44.3	24.15	0.01 ± 0.03	0.25 ± 0.03	Cyan
6	18.3	34.3	5.41	0.02 ± 0.04	0.27 ± 0.03	Magenta
All	23.9	46.9	30.10	0.03 ± 0.04	0.26 ± 0.03	-
SMM	-	-	-	0.135	0.332	-
G15.141	32.0	60.0	50.0	0.269	0.431	-

The reason for this can be seen in Fig 3.3, which shows that the templates for SMM and G15.141 peak at lower wavelengths compared to our template.

For the subsequent sections we will use the template created when all sources in the sample were used ('All' in Table 3.1). We have obtained this template from bright sources, whereas the majority of the Phase 1 sources have considerably lower signal to noise ratios, increasing the uncertainty in our redshift estimates. To gauge the total effect of this uncertainty on any particular redshift estimate we have used the template to estimate the redshifts for all the sources in the Phase 1 catalogue. We have then plotted the estimated redshifts against the statistical error, which has been obtained by changing the redshift estimate until there is a change in $\chi^2(\Delta\chi^2)$ of one (one 'interesting' parameter, (Avni, 1976)) (Fig 3.7). This change in χ^2 corresponds to a confidence region of 68%. We can see that the uncertainty on z grows with redshift up to $z = 2$, where it begins to fall again.

The figure suggests that for a source that is detected at the signal-to-noise limit of the catalogue, the error is about 0.8 if the source is at a redshift of 3 but only 0.08 at a redshift of zero. This, however, ignores the important systematic error caused by the difference in dust temperature between low- and high-redshift H-ATLAS sources, which we address in the next section.

3.3.4 Cold Sources at Low Redshift

Fig 3.7 shows that the statistical error, z_{err}, for a redshift estimate for a low-redshift source is fairly small, but in reality there is a large systematic effect caused by the fact that low-redshift *Herschel* sources have much cooler SEDs than the template we have derived from our high-redshift ($z > 0.5$) spectroscopic sample. This is shown dramatically in Fig 3.6, where we have plotted $\Delta z/(1 + z_{\rm spec})$ for all H-ATLAS sources with either CO redshifts or optical counterparts (reliability > 0.8) and spectroscopic redshifts. As expected, at $z > 0.5$ the errors are quite small, but of the thousands of sources at $z < 0.5$ there are a large number with extremely large redshift discrepancies. As we demonstrate below this is likely to be mostly caused by a systematic temperature difference between low and high-z *Herschel* sources, but there will be some discrepancies due to gravitational lensing, in which the *Herschel* source is really at a very high redshift with the apparent optical counterpart at much lower redshift being the graviational lens (Negrello et al., 2010; González-Nuevo et al., 2012). The effect of this will be investigated in a subsequent paper.

We have investigated the possibility of systematic errors caused by temperature diffences by using a Monte-Carlo simulation. In this simulation we start with the Phase 1 H-ATLAS sources with reliable optical counterparts (reliability > 0.8) and redshifts, either spectroscopic or estimates from optical photometry, < 0.4. We then use these sources to generate probability distributions for the redshifts and the 250 μm fluxes. The first step in the simulation is to create an artificial sample of galaxies by randomly drawing 250- μm fluxes and redshifts from these distributions. To produce an SED for each galaxy, we randomly assign one of the five average SEDs for low-redshift H-ATLAS galaxies from Smith et al. (2012). This library of SEDs seems the most appropriate for generating an artificial H-ATLAS sample, although we have also used 74 SEDs found for Virgo galaxies by Davies et al. (2012) and the 11 SEDs found for the KINGFISH sample by Galametz et al. (2012), with very similar results. We use the SEDs and the redshifts to calculate 350 μm and 500 μm fluxes for each galaxy. The next step is to add noise to each galaxy. In order to allow for both instrumental noise and confusion, we add noise to each galaxy by randomly selecting positions on the real SPIRE images. We use the SPIRE images that have been convolved with the point spread function, since these were the ones used to find the sources and measure their fluxes. The final step in the simulation is to estimate the redshifts of the sources using our template.

Fig 3.8 shows that the systematic errors can be very large. Although $\simeq$80% of the sources have estimated redshifts < 1, a significant fraction have higher estimated redshifts, although by $z > 2$ the number of cool low-redshift sources that are spuriously placed at high redshift is very small. The simulation shows very clearly that one should not rely

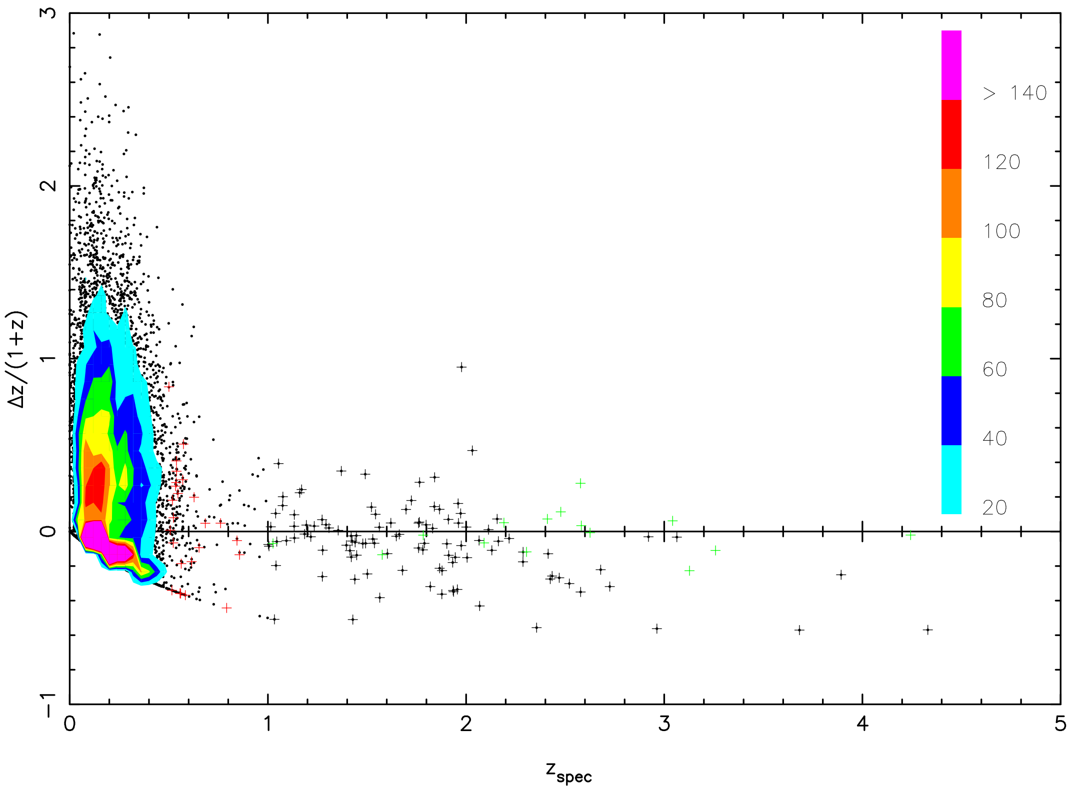

Figure 3.6: Plot of $z_{\rm spec}$ against $\Delta z/(1+z)$ for all sources with measured redshifts, either CO redshifts or optical spectroscopy. Sources with $z_{\rm spec} > 1$ are shown with crosses for clarity. Contours are included to show the density of sources at low redshifts. The key shows the number of sources in a bin where $\Delta z = 0.04$ and $\Delta(\Delta z/(1+z)) = 0.1$. Sources in red are the sources with optical redshifts that were used to create the template and the sources in green are the ones with CO measurements.

on this technique for estimating the redshifts of indvidual sources close to the flux limit of the survey. However, as we show in the next section, we can with care use it to draw some statistical conclusions about the survey.

3.4 Redshift Distribution

We used the following procedure to estimate the redshift distribution of the H-ATLAS sources. The template was used to estimate the redshifts, $z_{\rm temp}$, of all the H-ATLAS Phase 1 sources without an optical counterpart, but where a reliable optical counterpart with a redshift was available we continued to use this value because of the problem described in the previous section. Fig 3.9 shows the redshift distributions for sources with fluxes greater than 5σ in a given band. The mean redshift increases with wavelength: z =1.2, 1.9 and 2.6 for 250, 350 and 500 μm respectively due to the increasingly strong K-correction. A high-z tail extends to $z \sim 5$ for 350 and 500 μm selection and to $z \sim 4$ for 250 μm.

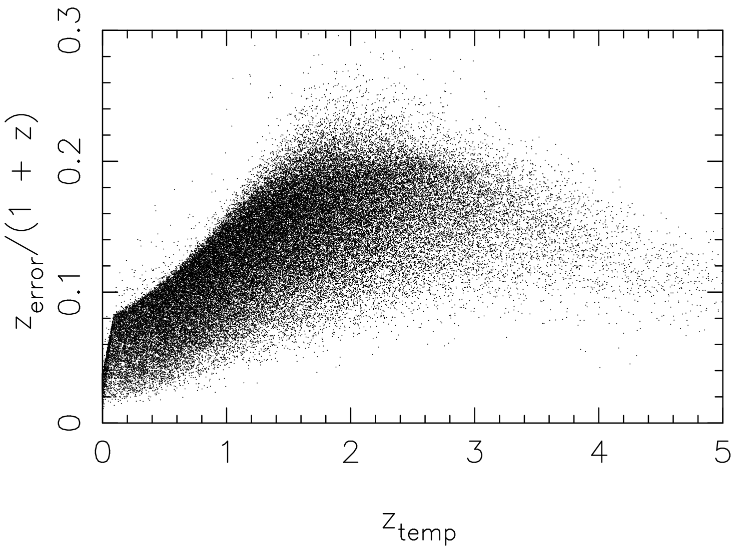

Figure 3.7: Plot of redshift according to our template against the estimated error as predicted from the χ^2 corresponding to a confidence region of 68% (see text). The hard edge at low $z_{\rm temp}$ arises as these sources lie on the Rayleigh Jeans tail and are at the flux limit of the survey.

We see a bimodal distribution with a large number of sources at low-z ($z \leq 0.8$), dominated by those sources with optical counterparts. This is seen in all three wavebands, though is most obvious at 250 μm. By requiring that every source must have $z_{\rm temp} \geq 0$, instrumental scatter may increase the size of the low-z peak. However most of the sources in the low-z peak come from the optical counterparts and few of our estimated redshifts are used, particularly at longer wavelengths. Although there are undoubtedly H-ATLAS sources at low redshift that do not have reliable counterparts and which may be spuriously placed at high redshift, we do not see any way that this could create the bimodal redshift distribution seen for the 250-μm sample. We have also plotted in the figure the redshift distributions we obtain if we do not use the redshifts of the optical counterparts. At 250 μm, but not at the other two wavelengths, there is still clear evidence of a bimodal distribution. The redshift distribution estimated by Dunlop et al. (2010) for the BLAST survey at 250 μm is quite similar to ours and shows a similar bimodal distribution although it only contains a few tens of sources.

Eales et al. (2010) presented predicted H-ATLAS redshift distributions using models based on the SCUBA Local Universe and Galaxy Survey, SLUGS (Dunne et al., 2000), and the model described in Lagache et al. (2004). The results are shown in Figure 3.10 alongside our estimated distributions. The SLUGS model predicts few sources with $z > 2$, in strong disagreement with our results. The Lagache et al. (2004) model predicts a bimodal distribution similar to what we find for the H-ATLAS sources and extends to redshifts similar to our distributions. However our high-z peaks are at a much higher

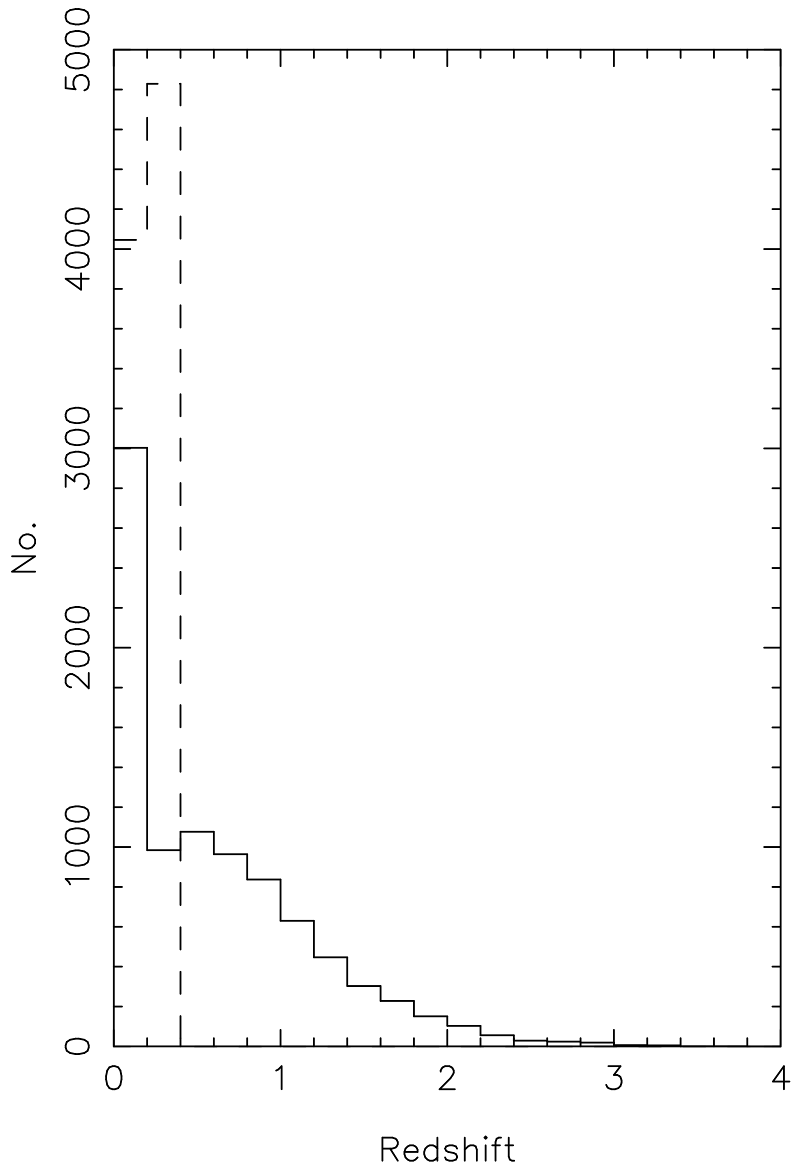

Figure 3.8: Results of Monte-Carlo simulation of our redshift estimation method for sources at low redshift, which are known to have cooler SEDs than our template. The dashed line shows the redshift distribution for sources in the Phase 1 catalogue with reliable identifications which have redshifts (spectroscopic or photometric) < 0.4. The solid line shows the redshift distribution for these sources estimated using our template.

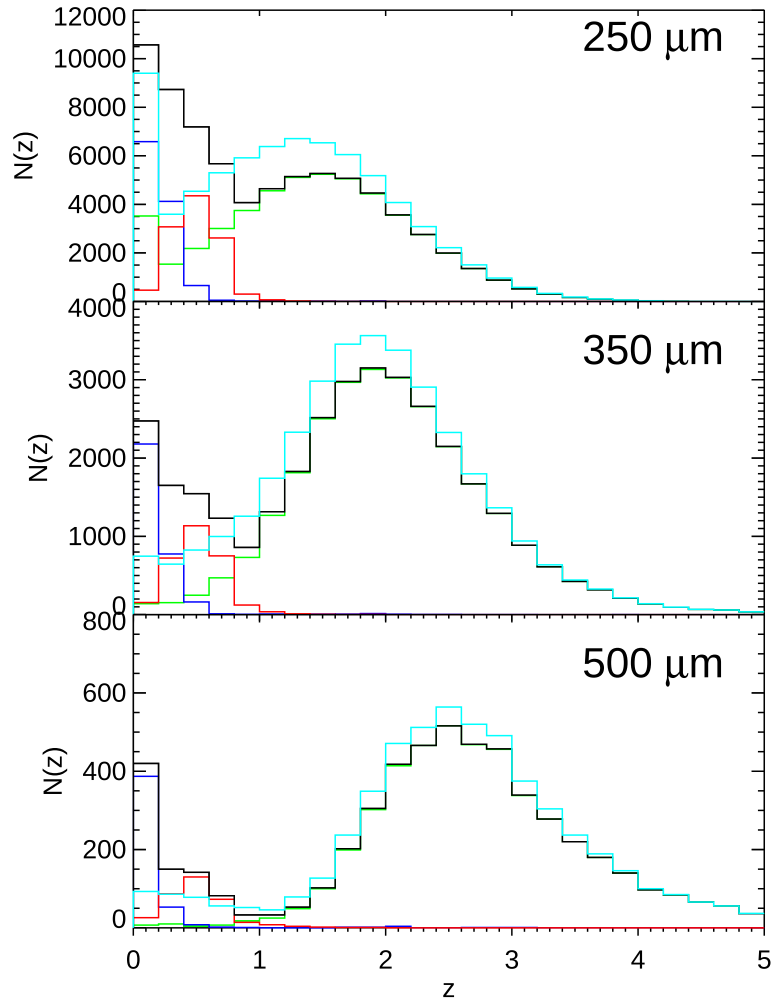

Figure 3.9: Redshift distribution for sources with fluxes greater than 5σ in the stated waveband. The upper plot shows the 250 μm selection, with a median $z = 1.0$, the middle 350 μm with a median $z = 1.8$ and the lower 500 μm with a median $z = 2.5$. All three show a large number of sources with $z < 0.2$ and a second broader distribution of sources at much higher redshifts. The dark blue line shows those sources with spectroscopic redshifts from optical counterparts. The red line shows those sources with optical photometric redshifts. The green line shows the redshifts estimated from the template for those sources with no reliable optical counterpart. The black line shows the sum of all three distributions (the median values stated are for these distributions). The light blue line shows the predicted redshift distributions if we do not use the redshifts of the optical counterparts but instead the redshifts estimated using the template.

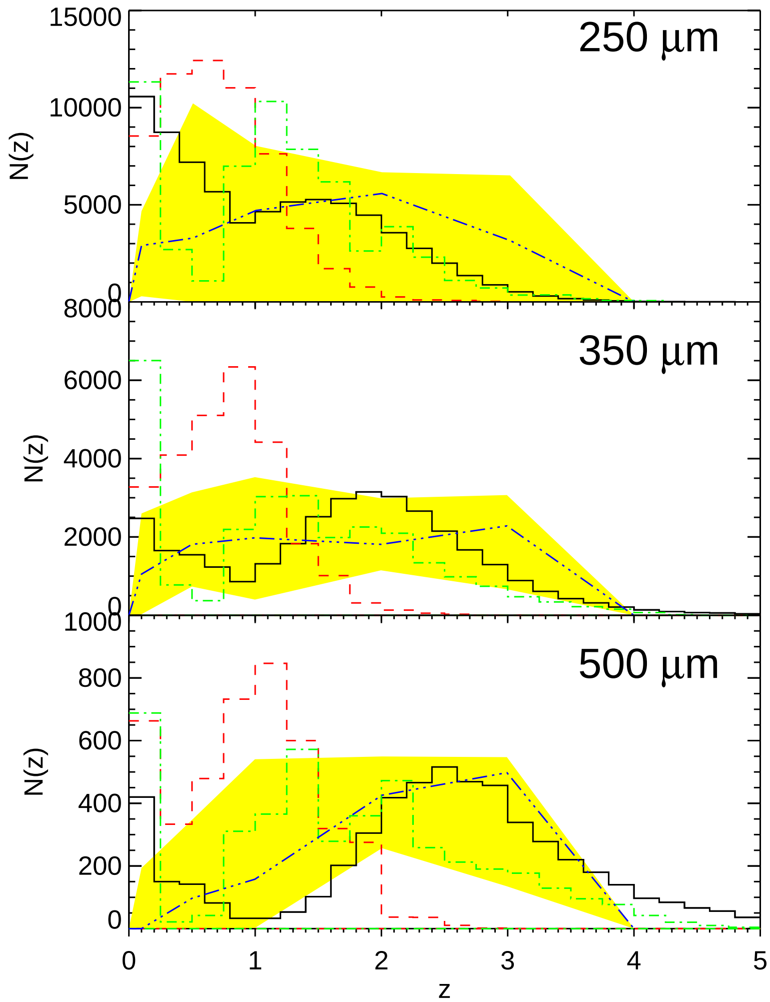

Figure 3.10: Redshift distribution for sources with fluxes greater than 5σ in the stated waveband. Overlaid are the models from Eales et al. (2010). The model from Lagache et al. (2004) is shown by the green dot-dashed line. The red dashed line is the SLUGS model. The blue dash-triple dotted line shows the model from Mitchell-Wynne et al. (2012) with 1σ confidence region in yellow. All models have been normalised to the number of sources detected with H-ATLAS.

redshift than predicted by the model.

Lagache et al. (2004) used both normal and starburst galaxies in their model. The differing cosmological evolution of these two populations causes the bimodal distribution seen in the model. Our redshift distribution also shows this bimodality suggesting that there really is two populations of galaxies, although we cannot exclude the possibility that there is a single population, and the effects of the cosmic evolution of this population and the cosmological model combine to produce the bimodal redshift distrubution (Blain & Longair, 1996). This bimodality provides some support for the conclusions of Lapi et al. (2011) that the high-z H-ATLAS sources represent a different population to the low-z sources: spheroidal galaxies in the process of formation, rather than more normal star-forming galaxies seen at low redshift.

Mitchell-Wynne et al. (2012) created a model by estimating the sub-mm redshift distribution from the strong cross-correlation of *Herschel* sources with galaxy samples at other wavelengths, for which the redshift distribution is known. The initial redshift distributions were obtained by using 24 μm Spitzer MIPS sources to cover the redshift range $0.5 < z < 3.5$ and optical SDSS galaxies to cover $0 < z < 0.7$. The authors estimate redshift distributions for samples of sources brighter than 20 mJy at the three SPIRE wavelengths, $\simeq$1.5-2 times fainter than the H-ATLAS limits. Their distributions agree quite well with the high-redshift peak of the H-ATLAS sources at all three wavelengths, but their distributions do not show the bimodal distribution that we find.

Amblard et al. (2010) and Lapi et al. (2011) have also estimated redshifts for H-ATLAS sources in the SDP field, which only contained ~ 6000 sources. Amblard et al. (2010) used one-temperature modified black bodies with a range of temperature and β to estimate the redshifts for sources from the SDP H-ATLAS field. These sources were selected to be detected at$> 3\sigma$ at 250 and 500 μm and with fluxes greater than 35mJy (5σ) at 350 μm. These cuts bias against sources at lower redshifts, though the sample still includes several sources that were identified optically.

Amblard et al. (2010) estimated a mean redshift of $z = 2.2$. In Fig 3.11, we have used our template to estimate redshifts for Phase 1 sources that satisfy the same flux criteria as used by Amblard et al. (2010). Unlike Amblard et al. (2010), we find a bimodal distribution, but it is worth noting that the majority of sources in the low-z peak are redshifts from optical counterparts. We find many more sources beyond $z > 3$. This is presumably due to our use of a two-component dust model rather than the single-component model used by Amblard et al. (2010). We find a mean redshift of 2.0, slightly lower than that found by Amblard et al. (2010).

We also include in Figure 3.11 our distribution of predicted redshifts if we now ignore the redshifts of any optical counterparts. In this case we see no low redshift peak and a

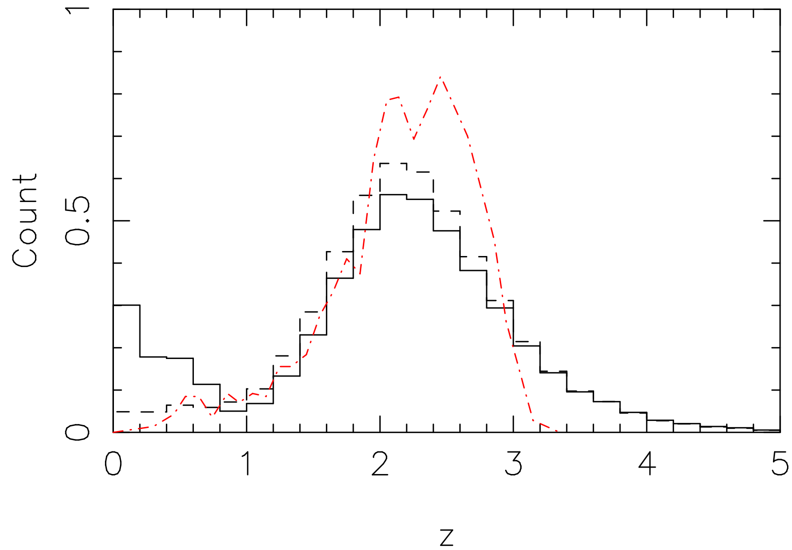

Figure 3.11: The estimated redshift distributions found by using our method and applying the cuts used by Amblard et al. (2010): $S_{350} > 35$mJy, S_{250} and $S_{500} > 3\sigma$. The solid black line shows our predicted redshift distribution if we use the redshifts of the reliable optical counterparts in preference to those estimated from the *Herschel* fluxes. The black dashed line shows the results of using only the redshifts estimated from the *Herschel* fluxes. In the first case we find a mean redshift of $z = 2.0$. The red dot-dashed line shows the redshift distribution obtained by Amblard et al. (2010).

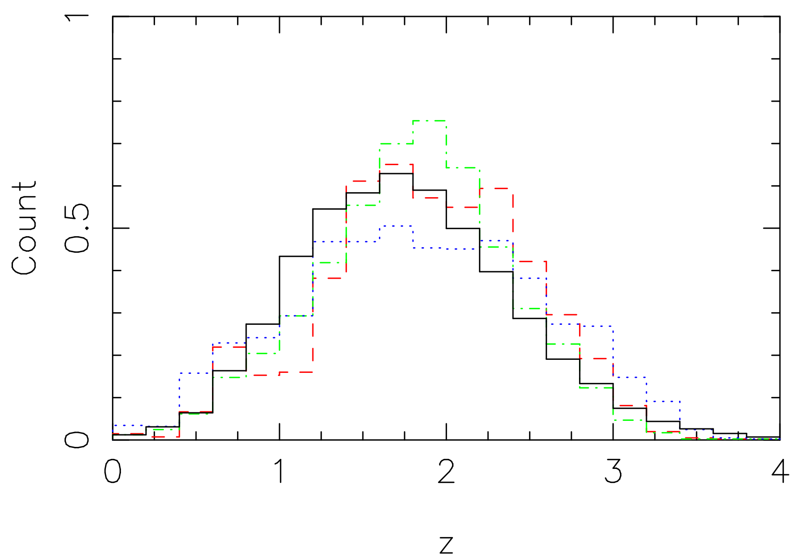

Figure 3.12: The estimated redshift distributions found by using our template and applying the cuts used by Lapi et al. (2011): $S_{250} > 35$mJy, $S_{350} > 3\sigma$, no optical counterpart; solid black. The other lines shows the redshift distributions found by Lapi et al. (2011) for the H-ATLAS SDP field, the red dashed line with SMM J2135-0102 as the template, the green dot-dashed line with G15.141 as the template and the blue dotted line with Arp220 as the template.

mean $z = 2.3$ in good agreement with what Amblard et al. (2010) found. One possible explanation of the disappearance of the low-redshift peak are that these sources are mostly lensed high-redshift *Herschel* sources.

Lapi et al. (2011) used a $S_{250\,\mu m} > 35$mJy, $S_{350\,\mu m} > 3\sigma$ selection on SDP sources without an optical counterpart, again biasing against low-z sources. Three reference SEDs from galaxies at $z = 0.018, 2.3$ and 4.2 were used to estimate redshifts from these fluxes and all produced similar distributions with a broad peak at $1.5 \lesssim z \lesssim 2.5$ and a tail up to $z \approx 3.5$. Using our template and these same cuts, we find a mean of $z = 1.8$ (see Fig 3.12). Our and Lapi's estimates for the $z_{\rm temp}$ distribution are very similar. This also confirms the methods of both Lapi et al. (2011) and González-Nuevo et al. (2012) are reliable for estimating the redshifts of high-z sources. Lapi et al. (2011) present a model for the formation of early-type galaxies that gives much better agreement with the estimated redshift distribution of H-ATLAS galaxies at $z > 1$.

3.5 Conclusions

We generated a template for estimating the redshift of H-ATLAS galaxies using a sample of H-ATLAS galaxies with measured redshifts. Our best-fit template consists of two dust components with $T_{\rm h} = 46.9$K, $T_{\rm c} = 23.9$K, $\beta = 2$ and the ratio of cold dust mass to warm dust mass of 30.1. To estimate the uncertainty in the template we used a jackknife technique and found a mean $\Delta z/(1+z) = 0.03$ with an rms of 0.26. If there is some *a priori* knowledge that the source is at $z > 1$, we estimate a mean $\Delta z/(1+z) = 0.013$ with an rms or 0.12.

This template was then used to estimate the redshifts of the entire H-ATLAS Phase 1 sources, though optical redshifts were used where available. Our redshift distributions show two peaks, suggesting there are two populations of sources experiencing different cosmological evolution. The mean redshifts for sources detected at $> 5\sigma$ at three wavelengths are 1.2, 1.9 and 2.6 for 250, 350 and 500 μm selected sources respectively.

Chapter 4

Luminosity Functions

Light brings us the news of the Universe.

Sir William Bragg

4.1 Introduction

In order to study the evolution of galaxies, from their origins as fluctuations in the initial mass structure of the universe to the present day, we need to study the history of how stars form within galaxies and throughout the universe as a whole. How the stars form in a galaxy is dependent upon the physics and dynamics of the gas within that galaxy (Lapi et al., 2011). Different types of galaxies will form stars in different ways i.e. late types are more active than early type galaxies. By looking at which type of galaxies dominates the formation of stars with cosmic times we are able to determine how galaxies evolve dependent on various factors such as time, environment and mass (Peng et al., 2010).

One of the easiest ways to trace star formation is by studying the luminosity function (LF) of galaxies in the universe. The luminosity function is the number of galaxies with a given luminosity per unit volume. Studying the LF at different wavelengths allows us to probe different aspects of galactic evolution and is one of the prime statistical tools for testing models of galaxy formation. Different wavelengths tell us about different components of galaxies. Visible stars emit mainly in the UV and optical, meaning that the LF at these wavelengths describes these objects (Stefanon & Marchesini, 2013). Due to the relative ease of observing at these wavelengths they have been well covered. The IR LF, however, is from the starlight that has been absorbed and re-radiated by dust clouds (Fixsen et al., 1998). It is only recently that this has been able to be probed in a meaningful way as observations in the sub-mm are difficult and time consuming. Since the first sub-mm surveys (Smail et al., 1997; Hughes et al., 1998; Eales et al., 1999; Bertoldi et al., 2000) much has been learned about high redshift sources that are rich in dust.

Over time, and therefore redshift, the main drivers of star formation change and so the LF evolves. The local luminosity function indicates a large number of normal galaxies with a relatively low star formation rate making up the bulk of star formation in the local universe, (Chary & Elbaz, 2001). Starburst galaxies, which are galaxies undergoing a period where the rate of star formation is very high (<100 $M_\odot$ yr^{-1}) (Sanders & Mirabel, 1996) are relatively rare in the local universe and so contribute very little to the total star formation rate at these times. Such galaxies are usually very bright in the infrared and those with $L_{IR} \geq 10^{11} L_\odot$are known as luminous infrared galaxies (LIRGs). As redshift increases, moving back through cosmic time, the contribution of luminous infrared galaxies to the star formation increases as they become more common and by a redshift of $z \sim 1$ they dominate the star formation rate (Franceschini et al., 2001; Elbaz et al., 2002; Magnelli et al., 2009).

For star forming and AGN galaxies the IR SED peaks at a rest frame wavelength of 60-200 μm. In order to study the LF in great detail at a wide range of redshifts it is necessary to study the sub-mm. The *Herschel* wavelengths are ideal as at high redshifts the wavebands will be directly over the peak of emission.

In Section 4.2 I will go over the theory necessary in estimating the luminosity function from the data as well as building a model estimate. In Section 4.3 I will look at previous work done on the wavelength dependant luminosity function at a range of sub-mm wavelengths, and then compare these to the results obtained from the H-ATLAS Phase 1 field. In Section 4.4 I will examine the bolometric luminosity function. Finally in Section 4.5 I will draw my conclusions.

4.2 Background Theory

The luminosity function is defined as the number of galaxies per unit volume as a function of their luminosity. The luminosity of a certain galaxy depends on many factors of the stellar and gas dynamics within the galaxy, as well as its mass. Here we will be using it to trace the evolution of galaxies over redshift.

4.2.1 Monochromatic Luminosity

The monochromatic luminosity of a galaxy per *Hz* can be estimated from its flux, provided we have a reasonable estimate of its distance, as

$$L_\nu = 4\pi D^2 S_{\nu,meas}(1+z)K, \tag{4.1}$$

where D is the distance, calculated here from the redshift of the source, and $S_{\nu,meas}$ is the flux measured at an observed frequency of ν. As most of the Phase 1 galaxies are at high redshift we must include a K-correction factor to adjust for the changes in flux caused by intrinsic differences in the SED at different wavelengths such that

$$K = \frac{S_\nu}{S_{\nu_{\rm ref}}} \tag{4.2}$$

where S_λ and $S_{\nu_{\rm ref}}$ are the fluxes given by the model SED at the observed and rest-frame frequency respectively. This adjusts the luminosity to what the value of the luminosity should be if the source was observed at the desired wavelength, rather than at it's rest frame wavelength.

It is a convenient quirk of sub-mm astronomy that when studying wavelengths on the Rayleigh-Jeans tail ($\sim 100\,\mu$m upwards) the K-correction is negative up to a redshift of about $z \sim 1$ (when considering the SPIRE bands). This means that as the effect of redshifting increases the waveband is shifted to intrinsically brighter wavelengths. Even though the redshift is increasing, thus dimming the source due to distance, the brightening due to the K-correction counteracts this. This means that often it is easier to observe sub-mm sources at higher redshifts than at lower (Dye et al., 2010).

In order to calculate the distance to the H-ATLAS galaxies we need their redshifts, and here we use those estimated in Chapter 3 for all the H-ATLAS galaxies. There I used a template to estimate the redshifts directly from their SPIRE fluxes. At low redshifts this method was not very reliable so where available an optical redshift was used. Most sources with an optical redshift were at low redshifts and ~75% of sources with $z < 1$ were estimated using an optical counterpart and so I assumed that using optical redshifts would remove most of the spurious estimates.

Redshift can be converted to distance using the Hubble Law:

$$D = \int_0^z \frac{c}{H_0\left(\Omega_m(1+z)^3 + \Omega_\lambda\right)^{\frac{1}{2}}} dz. \tag{4.3}$$

Though $z_{\rm temp}$ was not meant to be used as an absolute guide to an individual sources redshift as the distribution is being used as a whole, $z_{\rm temp}$ can be used in this manner. The luminosity function relies on the sample as a whole, rather than examining individual galaxies meaning that errors will be averaged out over the whole of the luminosity function. Rather than causing a discrepancy at any one particular point, errors within the redshifts will cause the luminosity function to 'smear out', spreading over a wider range of luminosities, but reducing the value of ϕ as it does so, creating a flatter LF.

However, this means that error in the distance will propagate into the luminosity, D

and the K-correction factor. The low-z sources and those close to the flux limit of the survey are the worst effected. There appears to be a large bias upwards in these redshifts. For sources with $z \lesssim 1.5$ this would cause both the K-correction and distance to be over estimated, meaning that the luminosity at low redshifts will be pushed towards the bright end. However, as I use the optical sources for low-z sources the effect of any upwards bias should be greatly reduced.

4.2.2 The Luminosity function

The luminosity function was found via the method laid down in Eales et al. (2009). Once the luminosity of the individual galaxies is known it is possible to calculate the number, n, in a given redshift-luminosity bin, i.e. those within $(L, L + dL)$ and $(z, z + dz)$. The luminosity function, $\phi(L, z)$, is given by

$$\phi\left(L_1 < L < L_2, z_1 < z < z_2\right) \Delta log_{10} L = \frac{n}{V} \tag{4.4}$$

where n is the number of sources with a luminosity between $L_1 < L < L_2$ and a redshift between $z_1 < z < z_2$. V is the accessible co-moving volume, the potential volume a source could occupy and still be both within the bin and detected by the survey. A source at high redshift will need to be intrinsically brighter in order to be seen. A high luminosity source will have a larger range of redshifts over which it can be detected.

Traditionally V_i is used (Avni & Bahcall, 1980), which measures the volume directly from the data, taking each source in the survey individually and then using

$$\phi(L)\Delta\log(L) = \sum_{i}^{n} \frac{1}{V_i}. \tag{4.5}$$

However this is very susceptible to errors in both flux and redshift. Instead V (Page & Carrera, 2000) is used here, the theoretical accessible volume averaged over the luminosity bin, independent of the measured luminosities. As V is independent of the measured luminosity, it is free of the errors and biases (such as flux boosting) that might effect V_i. These can still cause errors in n as flux boosting may push sources into another L bin and errors in redshift will effect both the z bin population and the luminosities found.

V is given by

$$V = \frac{1}{\Delta\log_{10}(L)} \int_{L_d}^{L_u} \int_{\mathrm{sur}} \int_{z_d}^{\min[z_u, z(L, S_{\min(A)})]} \frac{c}{H_0} \frac{D^2}{\sqrt{\Omega_M (1+z)^3 + \Omega_\Lambda}} dz\, dA\, d\log_{10}(L). \tag{4.6}$$

where dA is an element of the survey area, S_{min} is the flux density limit of the survey.

L_d, L_u, z_d and z_u are all the limits of the redshift-luminosity bin.

For the most part the luminosity function is considered in terms of log space. The number of sources within an interval of real space must be the same as the sources in the same interval in log space meaning

$$\phi(L)dL = \phi(\log L)d\log L. \tag{4.7}$$

As

$$\frac{d\log(L)}{dL} = \frac{1}{L} \tag{4.8}$$

this means that

$$\phi(\log L) = \phi(L)L. \tag{4.9}$$

We assume that the sources are distributed uniformly in redshift across each bin. This may not be true as on large scales structure in the universe will begin to effect the luminosity function as galaxies order themselves into clusters. This means that the number of galaxies of a given luminosity found within a certain volume depends upon the structure of the universe as much as it does on $\phi(L)$. We however will be looking in large enough redshift slices that these effects should average out. The uncertainties were calculated from the Poissonian error on the number counts on each bin. Though redshift errors would contribute to the total error as well these effects are not known well enough and so were excluded from error calculations.

The main disadvantage to the Page & Carrera (2000) method is that it does not use the data themselves to calculate the accessible volume. Instead it uses a theoretical model. If reality deviates from this model, i.e. if the galaxies are colder or warmer than the temperatures given in the model, then this will cause the accessible volume to be over or under estimated accordingly. For high-luminosity galaxies the accessible volume is limited by the redshift limits of the bin, rather than by the limits imposed by luminosity that will be effected by changes in temperature etc., meaning that low-luminosity galaxies are more suseptible to problems with the method. The standard technique does not usffer from this problem because it uses the SED of each detected galaxy to calculate the acessible volume.

4.2.3 Parametrising the Luminosity Function

Traditionally luminosity functions are parametrised by using a Schechter function (Press & Schechter, 1974; Schechter, 1976)

$$\phi(L)dL = \phi^\star \left(\frac{L}{L^\star}\right)^\alpha \exp\left(-\frac{L}{L^\star}\right) d\left(\frac{L}{L^\star}\right), \tag{4.10}$$

where $\phi^\star$, $L^\star$ and α are fit parameters. $\phi^\star$ is a normalisation term, $L^\star$ determines the position of the knee where the LF begins to fall sharply and α characterises the slope of the low luminosity LF.

IR LFs are characterised by a large number of high luminosity sources (Floch et al., 2005), meaning the bright end of the luminosity function pulls away from the Schechter function and it is best to use a double-exponential (Saunders et al., 1990), leading to four fit parameters rather than three. This version of the luminosity function acts as a power law for luminosities with $L << L^\star$ and as a Gaussian in $\log(L)$ for $L >> L^\star$. The double-exponential is commonly given as:

$$\begin{aligned}
\phi_\lambda(L) &= \frac{dN(L)}{dV\,d\log_{10}(L)} && (4.11)\\
&= \phi^\star_\lambda \left(\frac{L}{L^\star_\lambda}\right)^{1-\alpha_\lambda} \exp\left\{-\frac{1}{2\sigma^2_\lambda}\log^2_{10}\left[1+\left(\frac{L}{L^\star_\lambda}\right)\right]\right\}, && (4.12)
\end{aligned}$$

where dV is the element of co-moving volume, $dN(L)$ is the number of sources with a luminosity L within that dV per bin of $d\log_{10}(L)$ where σ_λ is an additional fit parameter characterising the slope of the high luminosity leg.

4.3 Luminosity functions for the H-ATLAS fields

The luminosity function has been measured on either side of the peak of emission before *Herschel*. Instruments such as the Infrared Astronomical Satellite (IRAS) covered the shorter wavelengths ($10\,\mu$m $< \lambda <$ $100\,\mu$m), while the Sub-millimeter Common User Bolometer Array (SCUBA, Holland et al. (1999)) on the James Clerk Maxwell Telescope covered the longer end (450 and 850 μm). However these instruments suffered from poor resolution and the wavelength coverage available left a wide blank over the central peak of emission.

Early surveys indicated that there were two distinct populations of galaxies important to the evolution of the LF (Dunne et al., 2000) and that using a single template was an over simplistic method (Floch et al., 2005). There was strong evidence that the relative population of normal and starburst galaxies changed over time. Sargent et al. (2012)

created a model LF using a starburst and normal SED, attempting to separate out the contribution to the total LF from both of these galaxy types separately. These models, and observations used to constrain them, can be seen in Figure 4.1. They found that locally most ULIRGs are starburst galaxies undergoing a merger leading to a period of unusually high star formation rate, while at $z > 0.9$ ULIRGs were dominated by normal galaxies undergoing a particularly bright IR phase.

Many previous attempts to estimate the sub-mm LF have been hampered by completeness issues. Most of the galaxies used have to have their redshifts obtained from complimentary surveys, relying on optical counterparts. While the negative K-correction means that sub-mm galaxies can be seen to deep redshifts, at optical wavelengths the increase in distance makes these galaxies difficult, if not impossible, to observe. This means that large surveys have been limited in the observable redshift range as optical counterparts are rare above $z = 1$. However, the redshift estimates from Chapter 3 reach to far higher redshift than have been previously observed. The template estimates over 45,000 sources with $z > 1$. This means it is now possible to probe the luminosity function to much higher redshifts than ever before.

I created the luminosity functions following the procedure laid out in Section 4.2. If an optical redshift was present, either spectroscopic or photometric, then this was used. Other wise the redshift determined by the template was used. These sources are referred to as $z_{\rm best}$. As stated in Chapter 3 the template method is highly inaccurate for low redshift sources but such low-z sources are likely to have an optical ID. Only $\sim 25\%$ of sources in this catalogue with an estimated redshift of $z < 0.5$ uses a redshift predicted by the template rather than from an optical ID.

If a source was at a low redshift ($z \lesssim 0.5$) then the average SED found in Dye et al. (2010), with a single dust temperature of $T_d = 23$K and $\beta = 2$, was used for obtaining the K-correction and luminosity. This was done because, as previously stated, the template is an average SED and has been found to not be very accurate for low redshift sources. This may cause an artificial 'jump' in the LF if the redshift bin spans the cross over and so caution must be taken when interpreting the results.

If a source has a redshift of $z \geq 0.5$ then the template SED from Chapter 3 was used. Previous work demonstrated that using a single SED over simplified the results. This was mostly due to the change in dominant galaxy type with redshift. By using the template, which is an average SED, as well as the rough redshift cut for a low-z SED, I will be able to use a single SED avoiding the issues of having to determine SED type. This would require using complimentary data at different wavelengths and so would eliminate potential sources not observed in other bands, thus introducing a bias. By using $z_{\rm best}$ we can use all sources meeting the flux cut of the survey.

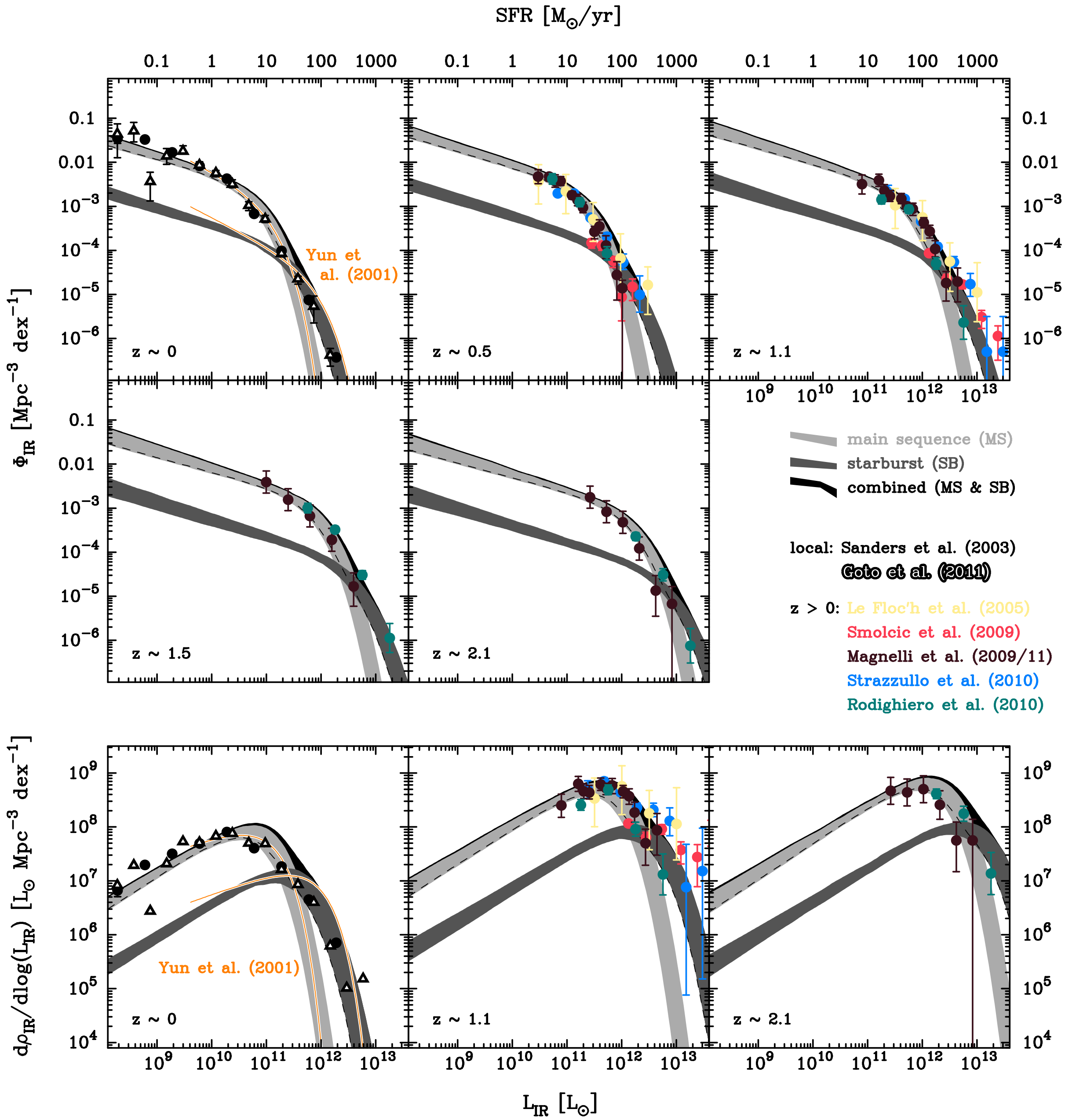

Figure 4.1: Luminosity functions taken from Sargent et al. (2012) up to $z \sim 2.1$. The grey regions are the predicted contributions from starburst and main sequence (normal) galaxies. These are models drawn from the data. The points shown from various publications were used to constrain the model (Sanders et al., 2003; Goto et al., 2011; Floch et al., 2005; Smolčić et al., 2009; Magnelli et al., 2009, 2011; Strazzullo et al., 2010; Rodighiero et al., 2010).

All the luminosity function estimates were then fitted with the double exponential shown in Equation 4.12. First all four parameters were left free and fit to the LF for the lowest redshift bin. The best fit values of α_λ and σ_λ were then used for all subsequent calculations. This was done as the lowest redshift bin is usually the most well defined, with good coverage both before and after the knee. It should be noted that for the LFs in Section 4.3.2 this means that α_λ and σ_λ were fit to the LFs derived using the low redshift SED but were used on all LFs, including those that used the high redshift template SED.

Errors on the fit parameters were then calculated via a bootstrapping technique using 500 LFs, based on the original LF with a Gaussian scatter on ϕ based upon the error values of the points. Each of these new randomised data sets had a double exponential fit to it and the standard deviation of the all 500 fit parameters was taken to be the error of that parameter.

In all the luminosity functions we produce there is a turn off in the LF at low luminosities where the value of ϕ drastically reduces. This is believed to be a completeness issue at low luminosities due to the flux cut of the survey and the problems explained in Section 4.2.2. These points are included in the data but were not used when fitting the double exponential function. Only sources with luminosities brighter than the luminosity with the peak value of $\phi(L)$ were used to fit the function.

4.3.1 Comparison

Several works have previously attempted to estimate the LF of sub-mm galaxies. I shall now study these individually.

The Local Universe

In many previous studies the main focus has been on the high redshift universe, as it is in this work, the local universe has had its sub-mm LF investigated by both (Dye et al., 2010) (hereafter D10) and Vaccari et al. (2010) (hereafter V10). D10 estimated the LF from the H-ATLAS SDP data while V10 took an estimate using HerMES, another *Herschel* survey. Both used optically selected galaxies with either a spectroscopic or photometric redshift. As with many of the higher redshift studies, these were limited by incompleteness but this is less of an issue at lower redshifts where many of the sources have been observed in other wavebands. D10 applied a correction factor, which accounted for the number of sources that would have had a counterpart that was missed due to the finite search radius, however this does not account for sources that are too weak in the optical to be seen. The SEDs used to determine the luminosity and K-correction were found for each source individually by fitting them directly to the data. D10 used only the available Herschel bands while V10 used all available data to accurately constrain the SED down to wavelengths shorter than the sub-mm grey body regime.

The LF in the local universe is observable to much lower luminosities, as these are below the flux limit of the survey at higher redshift. The evolution with respect to redshift seems to most highly effect the high luminosity end of the LF.

As both studies were at $z < 0.5$ it was decided that the template SED generated in Chapter 3 would not be valid. Instead, here I used the average SED from D10 for both of the comparisons. Figures 4.2 and 4.4 show the comparisons to the LF given in D10 and V10 respectively. Figure 4.4 also shows a comparison between the two works and finds them in good agreement.

Comparing to D10 to that obtained from the Phase 1 data we see good agreement in the lowest two redshift bins between our LF. However at higher redshifts the LFs tend to be $\sim$10% lower than that predicted by D10. The reason for this is unclear. The Phase 1 LFs are predicted using all sources, using template redshifts when optical are unavailable. However even if we use the same conditions as D10 (using only optical redshifts and a corresponding correction factor) we still observe little change in our LF. As the disagreement seems to get worse with redshift it is possible that using an average template, even for $z < 0.5$ is not a valid option. However there is not enough information to.

The original D10 paper was only done on the SDP field. Subsequent to the paper being published there were some errors found in the catalogue used, such as several stars being left in and some minor flux boosting corrections were later made (Dye 2013, priv. comm.). These should not have had a huge effect on the data, mainly effecting the lowest redshift bins.

Table 4.1: Fit parameters for the 250 μm luminosity functions given in D10 (subscript Dye) fit with a double exponential and that estimated from the H-ATLAS Phase 1 sample (subscript 250). For D10 $\alpha_{Dye} = 1.53 \pm 0.28$ and $\sigma_{Dye} = 0.67 \pm 0.32$. Plots are shown in Figures 4.2 and 4.3.

Redshift	$\log(\phi^{\star}_{\rm Dye})$	$\log(L^{\star}_{\rm Dye})$	$\log(\phi^{\star}_{250})$	$\log(L^{\star}_{250})$
$0.0 < z < 0.1$	-2.18 $\pm$ 0.08	23.25 $\pm$ 0.95	-2.78 $\pm$ 0.03	24.68 $\pm$ 0.03
$0.1 < z < 0.2$	-2.02 $\pm$ 0.14	23.24 $\pm$ 0.11	-2.89 $\pm$ 0.02	24.81 $\pm$ 0.02
$0.2 < z < 0.3$	-1.08 $\pm$ 0.28	22.81 $\pm$ 0.17	-3.21 $\pm$ 0.08	25.05 $\pm$ 0.03
$0.3 < z < 0.4$	-0.47 $\pm$ 0.85	22.57 $\pm$ 0.47	-3.08 $\pm$ 0.06	25.16 $\pm$ 0.02
$0.4 < z < 0.5$	0.14 $\pm$ 0.61	22.38 $\pm$ 0.28	-3.40 $\pm$ 0.06	25.36 $\pm$ 0.02

V10 used a single fixed low redshift bin of $0.0 < z < 0.2$, instead opting to examine changes due to wavelength. As the LF progresses to higher wavelengths the peak luminosity gets lower. This is to be expected as these wavelengths will be intrinsically less

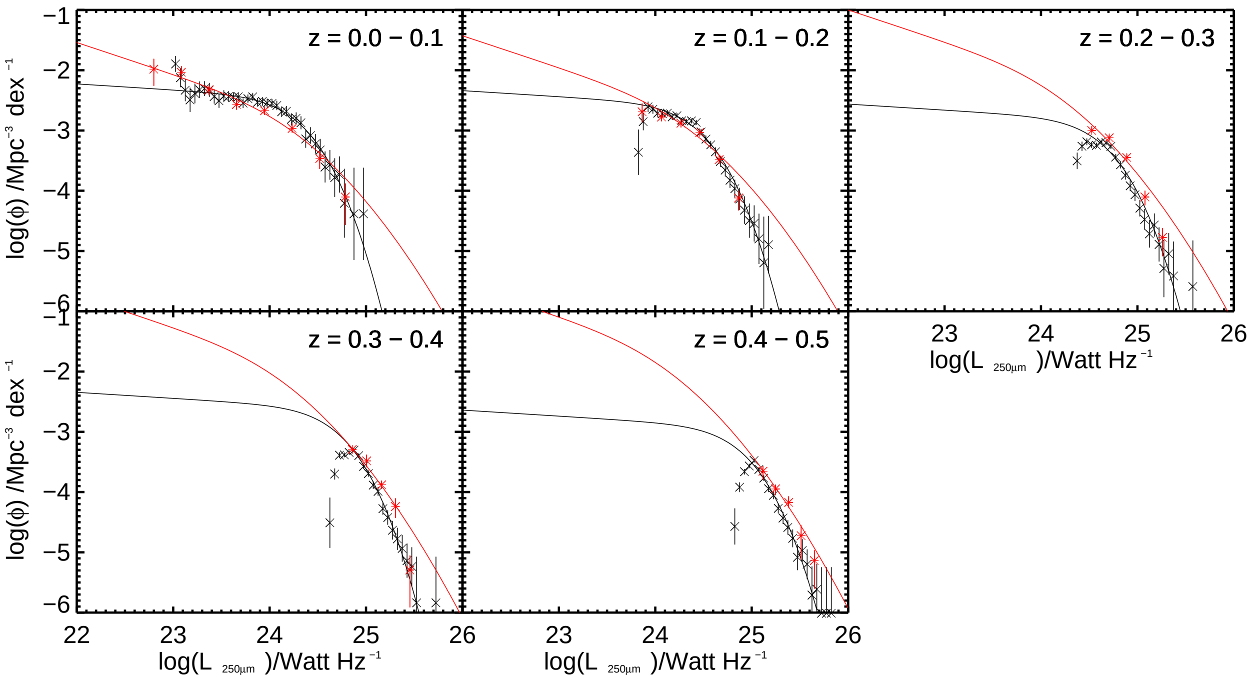

Figure 4.2: The LF at 250 μm obtained using the template. The sources were selected such that $S_{250} > 5\sigma$. The black points and fit line are from the $z_{\rm best}$ estimates and the red are those given in D10. Table 4.1 for fit parameters.

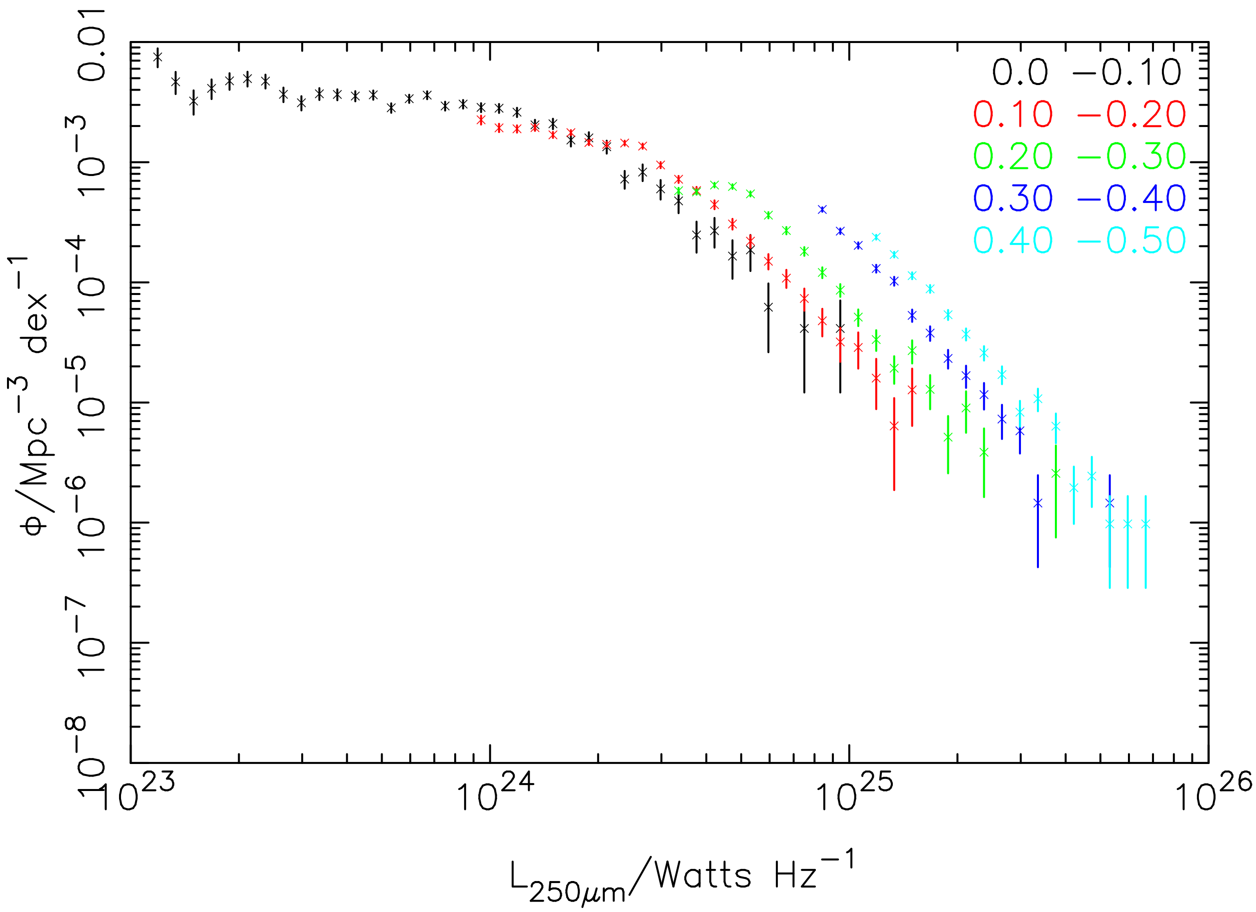

Figure 4.3: The LF at 250 μm obtained using $z_{\rm best}$ overlaid onto each other. Redshift bins are colour coded according to the key at the side. The sources were selected such that $S_{250} > 5\sigma$. See Table 4.1 for fit parameters.

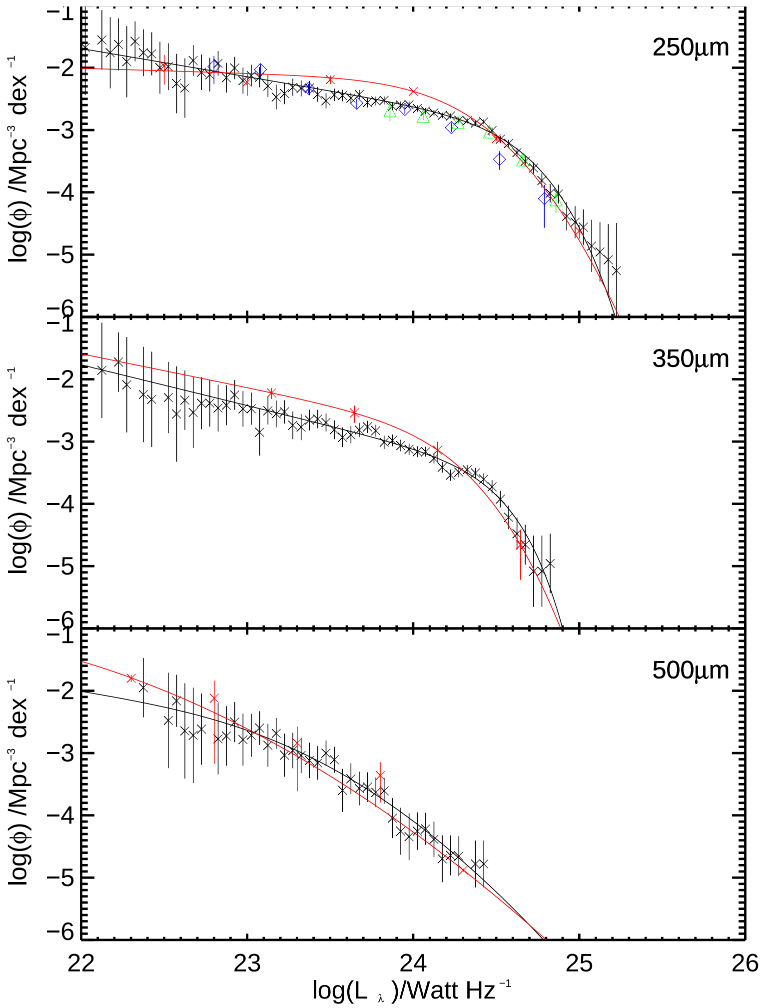

Figure 4.4: The LF at 250, 350 and 500 μm in the redshift range $0.0 < z < 0.2$. The black points are those from the template, the red from V10. The blue diamonds are D10 $0.0 < z < 0.1$ and the green triangles are $0.1 < z < 0.2$. The sources were selected such that $S_{250} > 5\sigma$.

bright past the peak of sub-mm emission. The template estimated LF at 500 μm appears to be less steep than that of the 250 and 350 μm selections. However the 250 μm selection used 9203 H-ATLAS sources while the 500 μm only had 336 sources meeting the criteria, meaning that the 500 μm LF is drawn from 3% of the sources than the 250 μm equivalent uses. Both my and V10 LFs match within error bars but V10 appears to estimate slightly higher at mid-luminosities for both 250 and 350 μm selections.

Lapi et al. (2011)

Lapi et al. (2011) (hereafter L11) used a single template to estimate the LF of H-ATLAS galaxies at a wavelength of 100 μm LF in the redshift range $1.2 < z < 4.0$. They used a

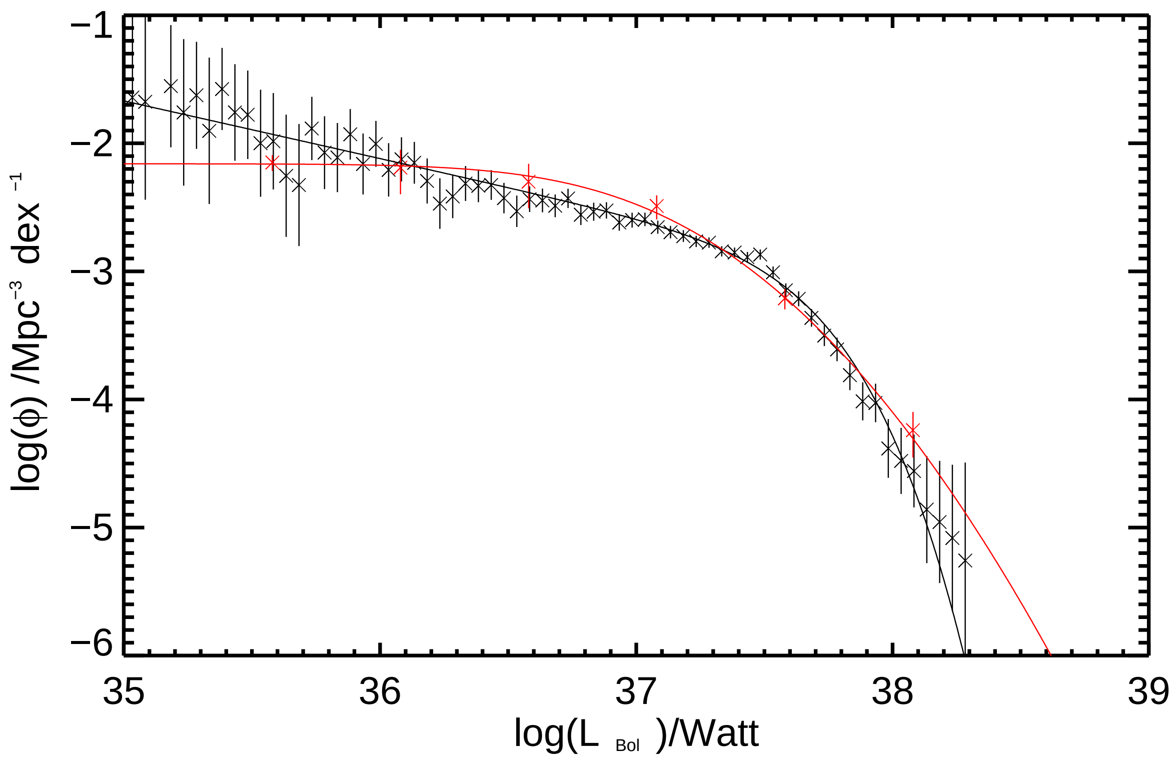

Figure 4.5: The bolometric luminosity function between $0.0 < z < 0.2$ obtained using the template as compared to that from V10. The black points are those estimated by the template from the H-ATLAS Phase 1 and the red points are taken from V10. The sources were selected such that $S_{250} > 5\sigma$. See Tables 4.2 and 4.5 for fit parameters.

Table 4.2: Fit parameters for the luminosity functions in the range $0.0 < z < 0.2$ given in V10 fit using a double exponential using the method described in 4.3. The bolometric parameters are taken from the literature. Plots are shown in Figure 4.5.

Wavelength	$\log(\phi^\star_\lambda)$	$\log(L^\star_\lambda)$	α_λ	σ_λ
250	-2.17 ± 0.04	24.0 ± 0.1	1.1 ± 0.1	0.31 ± 0.02
350	-2.8 ± 0.8	24.2 ± 1.0	1.5 ± 0.4	0.2 ± 0.1
500	-1.0 ± 0.8	21.0 ± 1.1	1.3 ± 0.3	0.9 ± 0.2
Bol	2.16	36.7	1.00	0.5

Table 4.3: Fit parameters for the H-ATLAS LF in the range $0.0 < z < 0.2$ fit with a double exponential using the method described in 4.3. Plots are shown in Figure 4.5.

Wavelength	$\log(\phi^\star_\lambda)$	$\log(L^\star_\lambda)$	α_λ	σ_λ
250	-2.99 ± 0.04	24.87 ± 0.04	1.45 ± 0.03	0.141 ± 0.008
350	-3.89 ± 0.18	25.25 ± 0.22	1.65 ± 0.06	0.049 ± 0.025
500	-2.20 ± 0.48	22.47 ± 0.51	1.42 ± 0.50	0.641 ± 0.097
Bol	-2.98 ± 0.04	37.91 ± 0.04	1.45 ± 0.03	0.145 ± 0.008

template SED to obtain the redshift and luminosity of all sources, much the same as I do, except that they used an SED from the galaxy SMM J2135-0102 ($z_{\rm SMM} \sim 2.$). L11 used only those sources without an optical counterpart, where as I use all sources. However at these high redshifts, optically observed sources make up less than 1% of the sample. A significant amount of evolution can be seen in the LF (see Figure 4.7).

There is very good agreement in the $1.2 < z < 2.4$ region, though the highest redshift bin differs considerably. In the $2.4 < z < 4$ bin our LF is considerably lower at mid luminosities but remains high to greater luminosities. The highest luminosity reading for L11 has a large error margin and could be said to agree within error margins. At lower luminosities, however, my estimates have a very wide and spread out turn over region. This is most likely caused by the wide redshift bin used here. The cumulative effect of incompleteness at all redshifts combines to 'drag down' the LF at lower luminosities.

Table 4.4: Fit parameters for the LFs given in Lapi et al. (2011) (subscript Lapi) and the comparative values found for the H-ATLAS sources (subscript 100). Number is the number of H-ATLAS sources meeting the criteria of that bin. $\alpha_{Lapi} = 1.37\pm$ and $\sigma_{Lapi} = 0.028\pm$ while $\alpha_{100} = 1.69 \pm 0.78$ and $\sigma_{100} = 0.183 \pm 0.007$. Plots are shown in Figures 4.6 and 4.7.

Redshift	Number	$\log(\phi^\star_{Lapi})$	$\log(L^\star_{Lapi})$	$\log(\phi^\star_{100})$	$\log(L^\star_{100})$
$1.2 < z < 1.6$	8927	-4.57 ± 0.03	27.56 ± 0.01	-3.81 ± 0.05	26.46 ± 0.02
$1.6 < z < 2.0$	8056	-4.52 ± 0.03	27.69 ± 0.01	-3.72 ± 0.08	26.60 ± 0.02
$2.0 < z < 2.4$	5335	-4.40 ± 0.03	27.79 ± 0.01	-3.78 ± 0.09	26.72 ± 0.02
$2.4 < z < 4.0$	4325	-4.44 ± 0.04	27.87 ± 0.01	-4.94 ± 0.11	27.07 ± 0.04

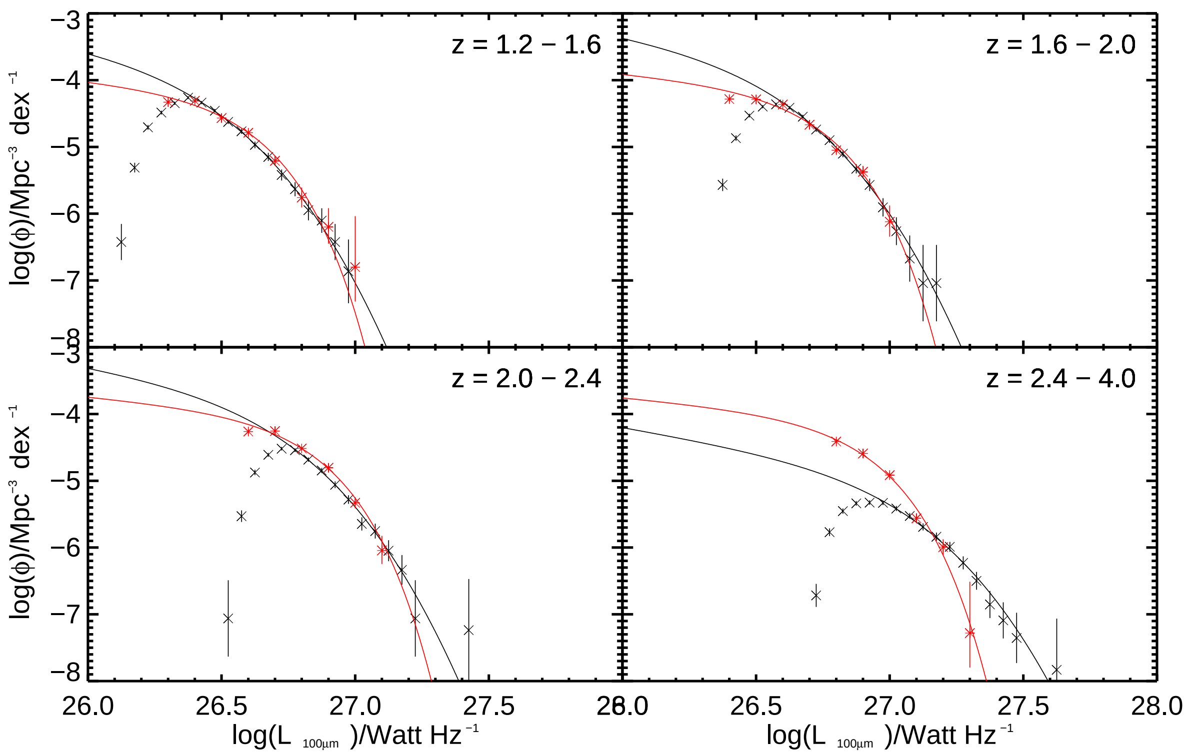

Figure 4.6: The LF at 100 μm obtained using $z_{\rm best}$ as compared to that from Lapi et al. (2011). The sources were selected such that $S_{250} > 5\sigma$. See Table 4.4 for fit parameters and Figure figure:Lapi100LFz for the overlaid LFs.

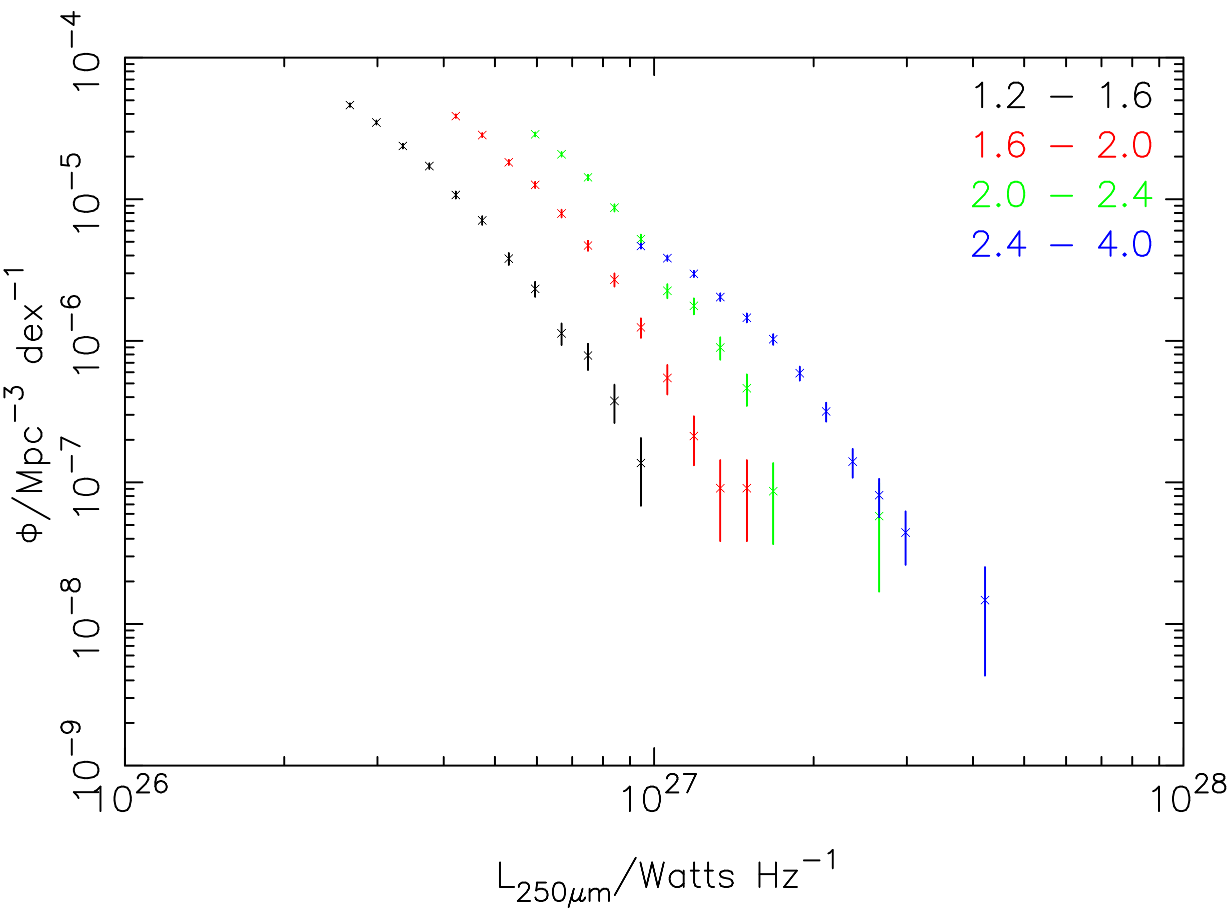

Figure 4.7: The LF at 100 μm obtained using z_{best} at multiple redshifts. The colour code at the side shows the redshift bins of each point. The sources were selected such that $S_{250} > 5\sigma$. See Table 4.4 for fit parameters.

Gruppioni et al. (2013)

Gruppioni et al. (2013) (hereafter G13) used a more complicated method to determine the sub-mm LF using several SEDs. Each of the sources was matched using the wealth of complimentary data to gain as much information of the galaxies SED as possible at a variety of different wavelengths. This was then used to characterise the galaxy's type in order to assign the template SED that best describes the source from a library of potential SEDs. The results for the Phase 1 data are shown in Figure 4.9 alongside those found in G13.

The dip at mid-luminosities seen in the lowest redshift bin for $z_{\rm best}$ is most likely due to the fact that at the high redshift end of the bin, a turn over would be observed in the LF but at the low redshift end this would not be present. The cumulative effect is the dip seen in the mid region. The full set of data points was used to fit the double exponential.

As in L11, G13 saw strong evolution in the LF up to a redshift of $z \sim 2$. Between $2 \lesssim z \lesssim 3$ there is still evolution, but it is remarkably less pronounced than at redshifts lower than 2 (see Figure 4.9). Beyond this it is difficult to draw conclusions as these high redshift bins were sparsely populated, however it does appear that there is a negative evolution of the LF at very high redshifts ($z > 3$), with the LF moving back towards lower luminosities. Similar decreases are seen in the space density of high luminosity AGNs at $z > 2.7 - 3$ (Brusa et al., 2009; Civano et al., 2011) and similar negative evolution is seen in the HerMES IR LF (Vacarri et. al. in prep.). This suggests that at $z > 3$ there is a drop off in star formation.

G13 used the PACS measurements to estimate the LF at $90\,\mu$m, being the mean restframe frequency of the $160\,\mu$m PACS band. Here I use the $250\,\mu$m band to estimate the $90\,\mu$m LF. This is quite a long wavelength shift in the lower redshift bands but at $z \sim 2$ the restframe wavelength of the $250\,\mu$m band is $\sim$$90\,\mu$m. As SPIRE has a much greater sensitivity than PACS does a greater number of sources meet the required signal to noise ratio. In order avoid using two different SEDs in the same bin the redshift cut off for using the low-z SED was moved to $z < 0.4$.

There appears to be good agreement between our results and that of G13. My LFs tend to extend to higher luminosities, whereas the deeper HerMES survey extends to lower luminosities. Most of our LFs turn over due to incompleteness before the knee predicted by G13, which means we are only looking at the high luminosity tail. This makes parameter fitting difficult and unreliable. For this reason I combined the two data sets in order to create the fits shown in blue on the diagram. I combined the data sets by taking all the data points used in G13 and the points estimated using the template. As mentioned in Section 4.2.3 only points with a luminosity greater than the luminosity with the peak value of Φ were considered.

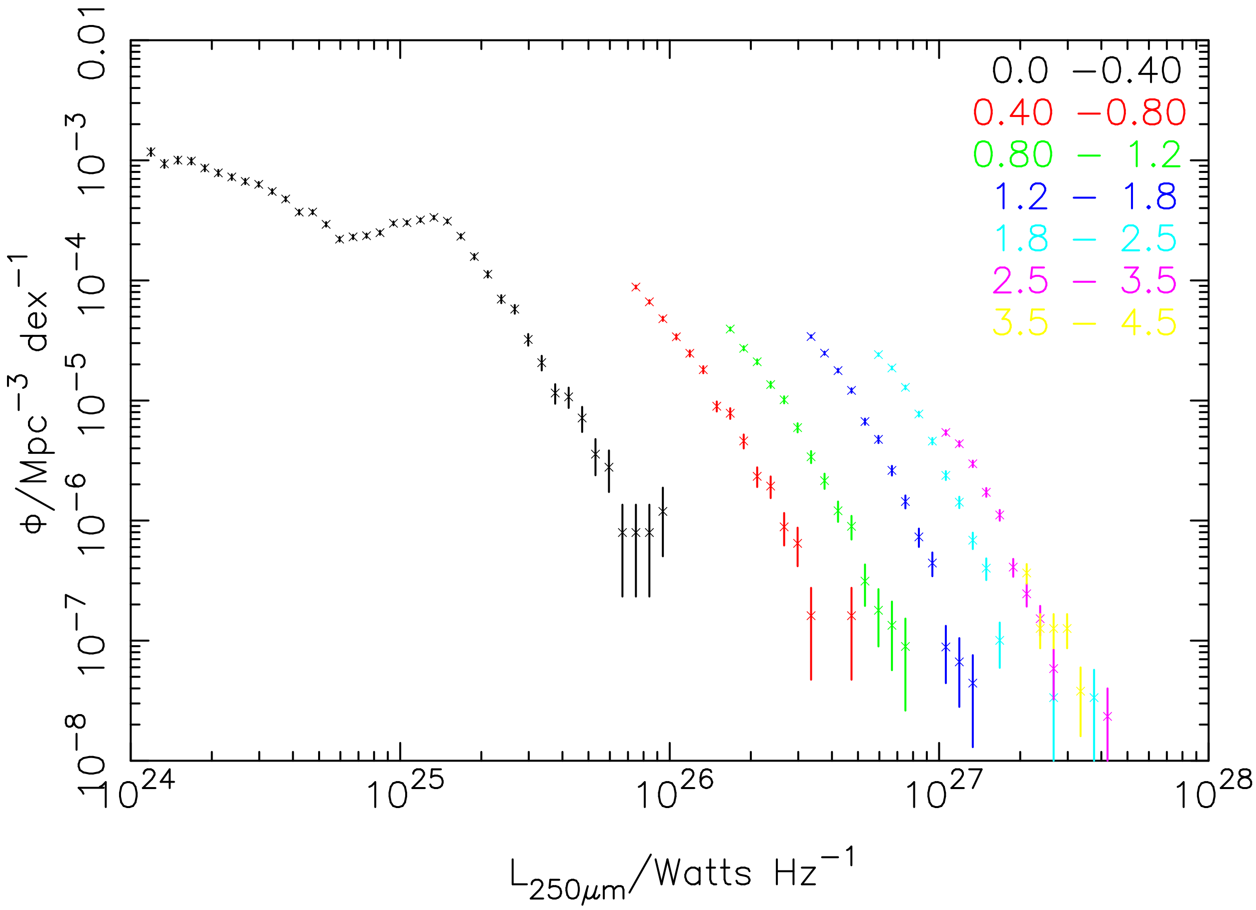

Figure 4.8: The LF at 90 μm obtained using the template as compared to that from Gruppioni et al. (2013). The colour code at the side shows the redshift bins of each point. The sources were selected such that $S_{250} > 5\sigma$. See Table 4.5 for fit parameters.

The only exception to this rule is the $0.0 < z < 0.4$ bin. The low luminosity tail of this bin fluctuates significantly and I only wished to use the high luminosity section from my fits. For this reason I only used those points where $\log(L) > 25.15$. As would be expected the combined fits match with G13 at low luminosities and with our points at high luminosities.

In the overlay plot we see what many other previous studies found: there is strong evolution out to a $z \sim 2$ at which point the evolution slows down and potentially reverses at $z > 3$. However neither the H-ATLAS survey nor that used by G13 observes enough sources at redshifts this high in order to be able to make a reasonable conclusion, though neither exclude this possibility.

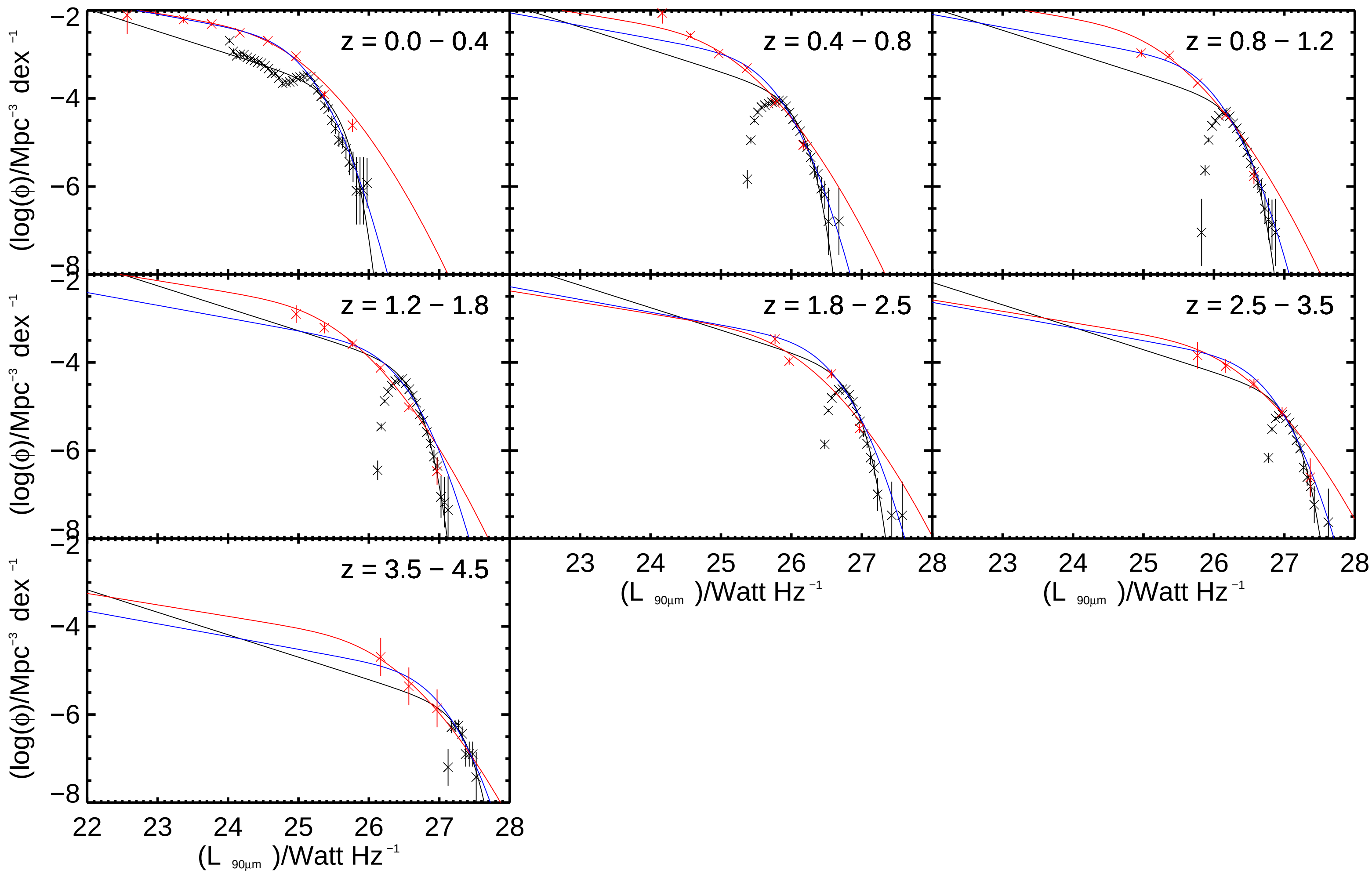

Figure 4.9: The LF at 90 μm. The black points are those from obtained using the template, the red are the LFs as given in G13 and the blue lines are double exponential fits to the combined data set. The sources were selected such that $S_{250} > 5\sigma$. See Table 4.5 for fit parameters and Figure 4.8 for an overlay of the LFs.

Table 4.5: Fit parameters for the 90 μm luminosity functions using $z_{\rm best}$ (subscript 90) and those from the LF values given in G13 (subscript Grup). I found that $\alpha_{\rm Grup} = 1.51 \pm 0.02$ and $\sigma_{\rm Grup} = 0.085 \pm 0.023$ while $\alpha_{90} = 1.29 \pm 0.04$ and $\sigma_{90} = 0.35 \pm 0.01$. Plots are shown in Figures 4.9 and 4.8.

Redshift	$\log(\phi^{\star}_{\rm Grup})$	$\log(L^{\star}_{\rm Grup})$	$\log(\phi^{\star}_{90})$	$\log(L^{\star}_{90})$
$0.0 < z < 0.4$	-3.98 ± 0.01	25.95 ± 0.01	-2.55 ± 0.02	24.60 ± 0.01
$0.4 < z < 0.8$	-4.16 ± 0.04	26.49 ± 0.01	-3.00 ± 0.02	25.25 ± 0.01
$0.8 < z < 1.2$	-4.38 ± 0.04	26.77 ± 0.01	-3.11 ± 0.02	25.50 ± 0.01
$1.2 < z < 1.8$	-4.31 ± 0.03	27.02 ± 0.01	-3.55 ± 0.03	25.93 ± 0.02
$1.8 < z < 2.5$	-4.42 ± 0.05	27.26 ± 0.01	-3.47 ± 0.05	26.10 ± 0.02
$2.5 < z < 3.5$	-4.98 ± 0.08	27.48 ± 0.02	-3.87 ± 0.10	26.28 ± 0.03
$3.5 < z < 4.5$	-6.1 ± 0.4	27.7 ± 0.1	-4.96 ± 0.31	26.52 ± 0.11

Changes due to wavelength

The LF has been studied at a variety of different wavelengths across the sub-mm region. When examining the behaviour of the LF with respect to wavelength (see Figure 4.10) it is apparent that the behaviour at a certain wavelength is related to where that wavelength is with respect to the peak of emission ($\sim 100\,\mu$m). As the observed wavelength moves to either side of this peak, the knee of the LF appears to move to lower and lower luminosities. This is expected as the SED drops off, meaning that sources are less intrinsically bright as the wavelength moves away from the peak of emission.

As the rest frame wavelength gets intrinsically dimmer it also means that sources are less likely to be detected This means that the low luminosity end of the LF will appear weaker at these wavelengths. The low luminosity section is not particularly well pinned down in these works, but it appears that there is little change with respect to wavelength as any changes are in the section that suffers from incompleteness.

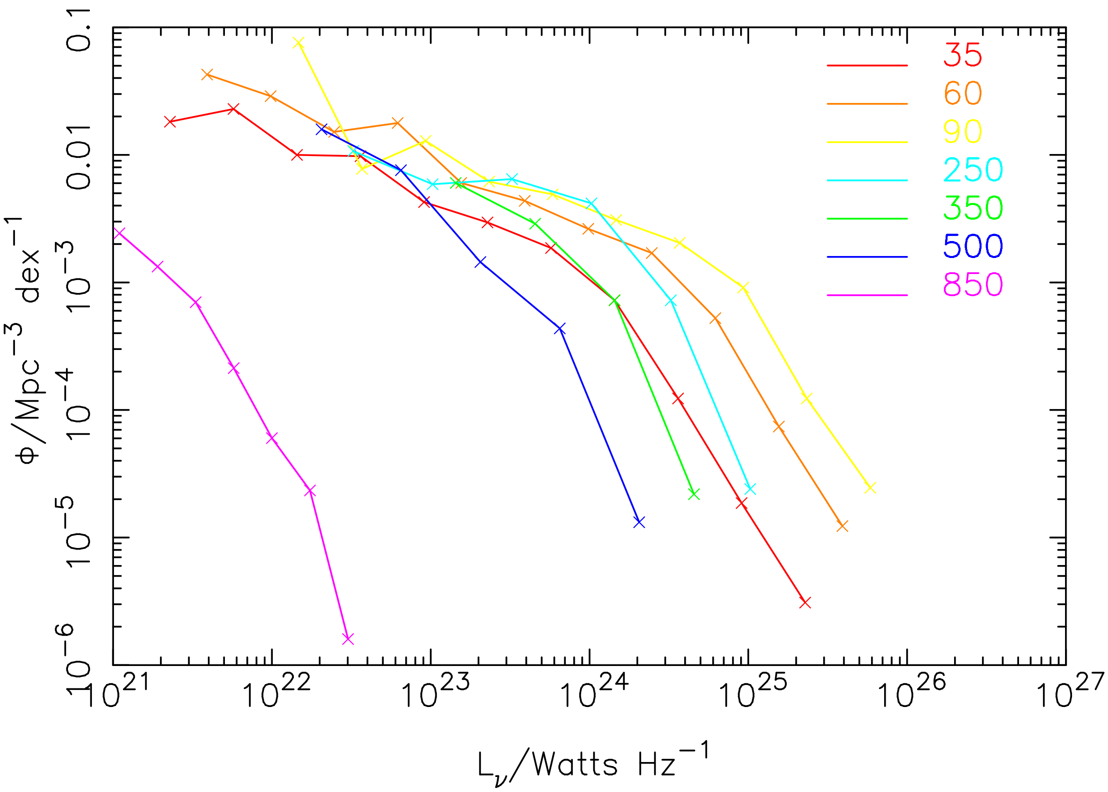

Figure 4.10: Changes in the LF according to wavelength. All of these are low redshift LFs (in the region of $0 < z < 0.4$. The 35 to 90 μm are from G13, 250 to 500 μm from Vaccari et al. (2010), 850 from Clements et al. (2010).

4.3.2 The H-ATLAS Luminosity Function

Figures 4.11, 4.12, 4.16 show the 250, 350 μm and bolometric LFs for all sources up to a redshift of 4.5. Beyond this point there were not enough sources to draw any meaningful conclusions. It was shown in the comparison with L10 a large redshift range over a bin can cause the turn over of the LF to become very spread out, making the information difficult to interoperate For this reason I set the limit of the bin size at $\Delta z = 0.5$. The 500 μm band was omitted as there were too few sources to create a meaningful LF.

As suggested with previous studies the LF seems to undergo evolution up to a redshift of $z > 3$. However at these redshifts the LF is restricted to the high luminosity end as these are the only source capable of being detected above the flux limit of the H-ATLAS survey. There are considerably fewer sources detected at redshifts this high and so drawing meaningful conclusions is difficult. It is possible that the highest redshift bin could show a 'turn back', where the LF moves back towards lower luminosities, indicating negative evolution but this is not clear due to the scarcity of points and large error bars.

The turn over seen in the template at low luminosities is due to incompleteness in the survey data, and the problems inherent to the accessible volume method and is not a real reflection of the LF. The method for calculating the accessible volume as laid down in Section 4.2.2 does not account for sources that are missed entirely by the flux survey. The flux cut of the survey means that it is the faintest sources, and so the least luminous, that will be effected by this incompleteness. As the volume is worked out from a theoretical value, rather than directly from the data, if sources are missing as they are too dim to be observed, this results in an artificial reduction of the luminosity function at that particular luminosity. Due to the distributions of redshifts across each redshift slice, the luminosity the cutoff effects is spread out, resulting the gradual turnover observed in the LFs.

The turn over mostly effected results from the low luminosity end, after the knee and so the template results are only really reliable for the high luminosity end. From the previous comparisons to the literature this seems to mostly effect the steepness of the slope both before and after the knee. While previous LFs had a smooth transition between the low and high luminosity sections of the LF, the template results appear to have a much sharper transition. α and σ are parametrised in the lowest redshift bin, where there is good coverage at all luminosities, meaning that they might not apply at higher redshifts. However they seem to create a good representation of the data.

From these results, however, we can see that the value of $L_\star$ decreases between 250 and 350 μm as expected and shown in other data. There is little change in the slope of the LF with regards to wavelength.

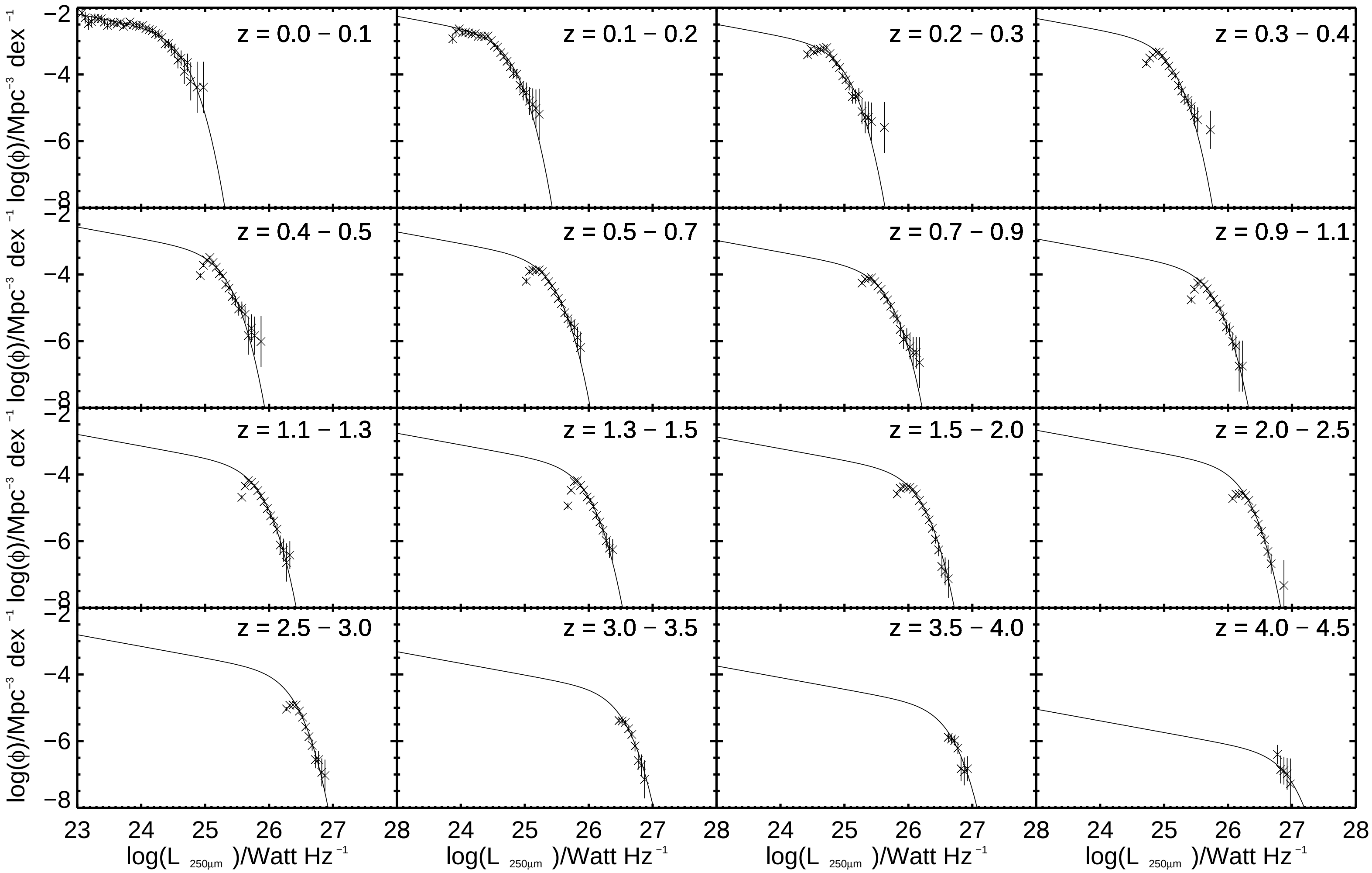

Figure 4.11: The LF at 250 μm obtained using $z_{\rm best}$. The sources were selected such that $S_{250} > 5\sigma$. See Table 4.6 for fit parameters and Figure 4.13 for the LFs overlaid.

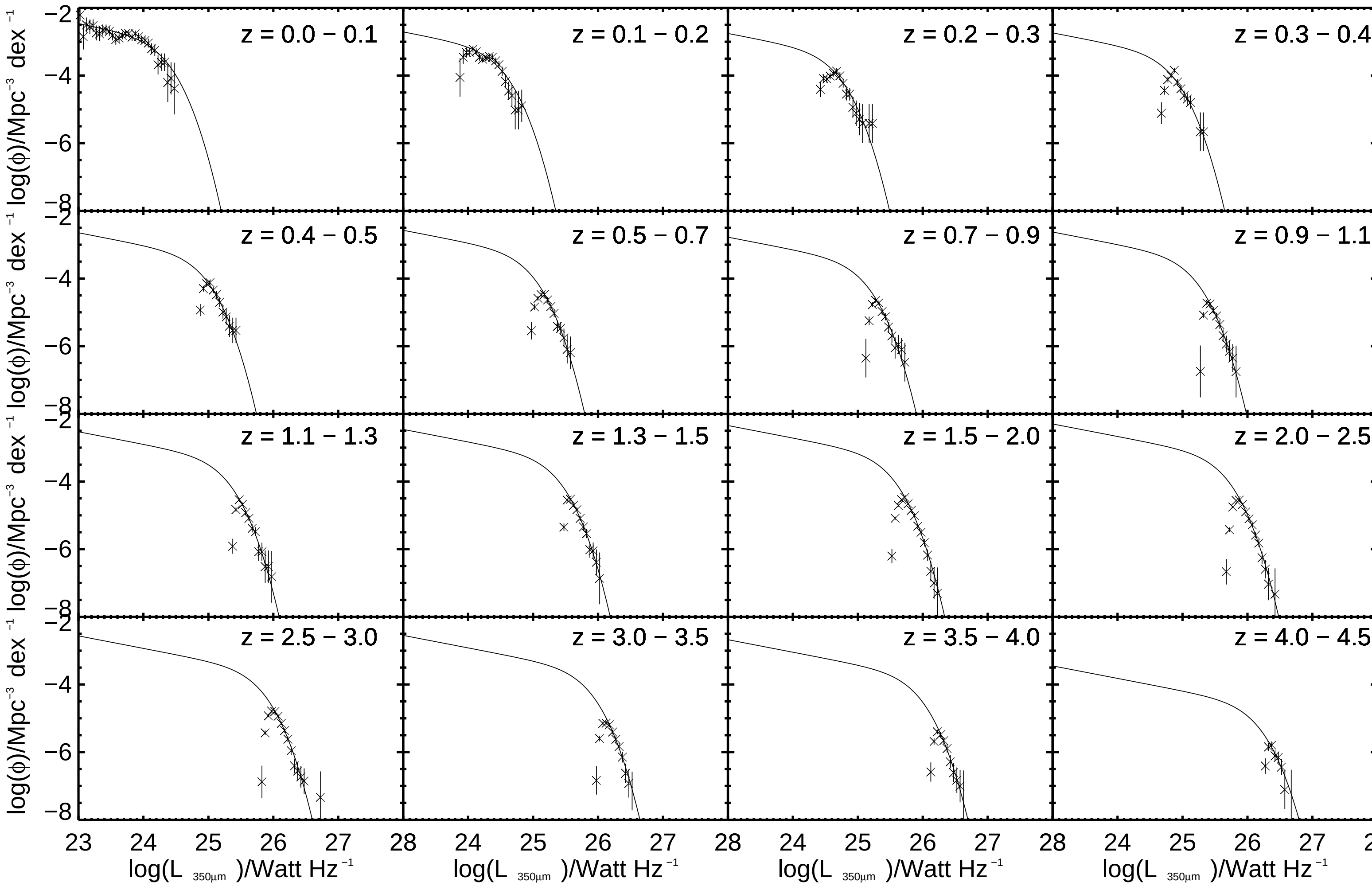

Figure 4.12: The LF at $350\,\mu$m obtained using $z_{\rm best}$. The sources were selected such that $S_{350} > 5\sigma$. See Table 4.6 for fit parameters and Figure 4.14 for the LFs overlaid.

Table 4.6: Fit parameters for the 250 μm LF fit with a double exponential using the method described in Section 4.3. Plots are shown in Figure 4.13.

Redshift	$\log(\phi^\star_{250})$	$\log(\mathrm{L}^\star_{250})$	α_{250}	σ_{250}
$0.0 < z < 0.1$	-2.78 $\pm$ 0.03	24.68 $\pm$ 0.03	1.35 $\pm$ 0.05	0.15 $\pm$ 0.02
$0.1 < z < 0.2$	-2.89 $\pm$ 0.02	24.81 $\pm$ 0.02	1.35	0.15
$0.2 < z < 0.3$	-3.21 $\pm$ 0.08	25.05 $\pm$ 0.03	1.35	0.15
$0.3 < z < 0.4$	-3.08 $\pm$ 0.06	25.16 $\pm$ 0.02	1.35	0.15
$0.4 < z < 0.5$	-3.40 $\pm$ 0.06	25.36 $\pm$ 0.02	1.35	0.15
$0.5 < z < 0.7$	-3.59 $\pm$ 0.06	25.47 $\pm$ 0.02	1.35	0.15
$0.7 < z < 0.9$	-3.92 $\pm$ 0.05	25.70 $\pm$ 0.02	1.35	0.15
$0.9 < z < 1.1$	-3.91 $\pm$ 0.06	25.80 $\pm$ 0.02	1.35	0.15
$1.1 < z < 1.3$	-3.81 $\pm$ 0.05	25.89 $\pm$ 0.02	1.35	0.15
$1.3 < z < 1.5$	-3.81 $\pm$ 0.06	26.00 $\pm$ 0.02	1.35	0.15
$1.5 < z < 2.0$	-4.00 $\pm$ 0.10	26.21 $\pm$ 0.03	1.35	0.15
$2.0 < z < 2.5$	-3.83 $\pm$ 0.14	26.29 $\pm$ 0.04	1.35	0.15
$2.5 < z < 3.0$	-4.00 $\pm$ 0.14	26.41 $\pm$ 0.03	1.35	0.15
$3.0 < z < 3.5$	-4.56 $\pm$ 0.32	26.56 $\pm$ 0.07	1.35	0.15
$3.5 < z < 4.0$	-5.06 $\pm$ 0.60	26.69 $\pm$ 0.19	1.35	0.15
$4.0 < z < 4.5$	-6.46 $\pm$ 2.42	27.03 $\pm$ 0.60	1.35	0.15

4.4 Bolometric Luminosity

The total bolometric luminosity is calculated by integrating the monochromatic luminosity function with respect to frequency such that

$$L_{\mathrm{bol}} = \int_{\nu_1}^{\nu_2} L_\nu d\nu. \tag{4.13}$$

The exact limits of this integration fluctuate between papers but are set most commonly to be between $\lambda_2 = 8\,\mu$m and $\lambda_1 = 1000\,\mu$m. However this would mean that the shortward end of the emission is extending into the mid-IR regime. The template created in Chapter 3 only accurately covers the sub-mm region. For this reason we will calculate the observed bolometric luminosity function in the range 60 μm - 1000 μm.

4.4.1 Model Bolometric Luminosity

A model estimate of the theoretical bolometric luminosity was made by Eales (2013, priv. comm., hereafter Eales 2013). This was done by first deriving the stellar mass function ($\phi(M_\star)$) using a double Schecter function (Pozzetti et al., 2010),

$$\phi(M)dM = e^{-\frac{M}{M_\star}} \left[\phi_1^\star \left(\frac{M}{M_\star} \right)^{\alpha_1} + \phi_2^\star \left(\frac{M}{M_\star} \right)^{\alpha_2} \right] \frac{dM}{M^\star}, \tag{4.14}$$

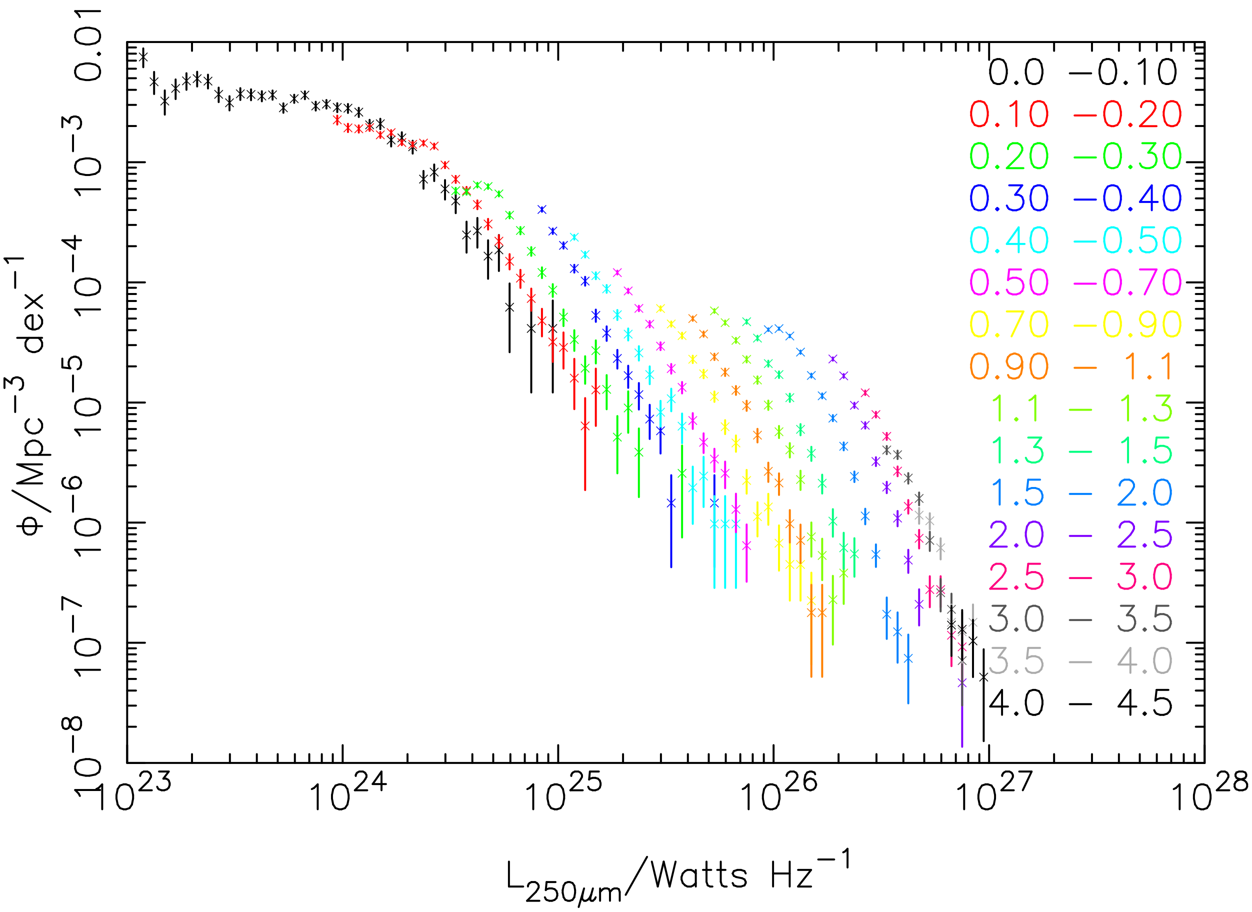

Figure 4.13: The LF at 250 μm obtained using $z_{\rm best}$. The colour code at the side shows the redshift bins of each point. The sources were selected such that $S_{250} > 5\sigma$. See Table 4.6 for fit parameters.

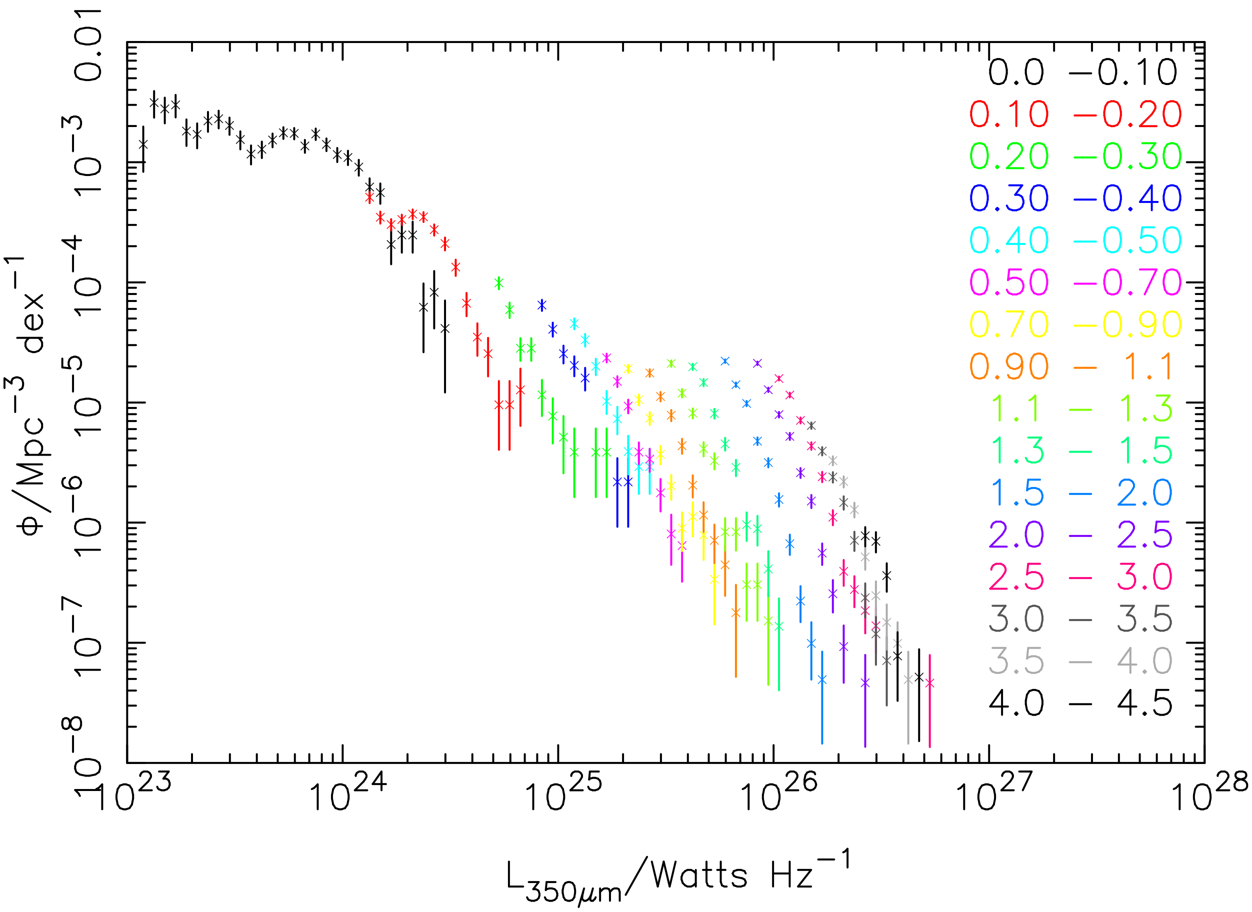

Figure 4.14: The LF at 350 μm obtained using z_{best}. The colour code at the side shows the redshift bins of each point. The sources were selected such that $S_{350} > 5\sigma$. See Table 4.7 for fit parameters.

Table 4.7: Fit parameters for the 350 μm LF fit with a double exponential using the method described in Section 4.3. Plots are shown in Figure 4.13.

Redshift	$\log(\phi^\star_{350})$	$\log(L^\star_{350})$	α_{350}	σ_{350}
$0.0 < z < 0.1$	-2.91 $\pm$ 0.05	24.21 $\pm$ 0.06	1.37 $\pm$ 0.09	0.22 $\pm$ 0.1
$0.1 < z < 0.2$	-3.23 $\pm$ 0.08	24.40 $\pm$ 0.05	1.37	0.22
$0.2 < z < 0.3$	-3.33 $\pm$ 0.26	24.56 $\pm$ 0.09	1.37	0.22
$0.3 < z < 0.4$	-3.38 $\pm$ 0.32	24.72 $\pm$ 0.10	1.37	0.22
$0.4 < z < 0.5$	-3.32 $\pm$ 0.28	24.81 $\pm$ 0.08	1.37	0.22
$0.5 < z < 0.7$	-3.26 $\pm$ 0.25	24.85 $\pm$ 0.06	1.37	0.22
$0.7 < z < 0.9$	-3.51 $\pm$ 0.26	24.99 $\pm$ 0.07	1.37	0.22
$0.9 < z < 1.1$	-3.39 $\pm$ 0.28	25.06 $\pm$ 0.06	1.37	0.22
$1.1 < z < 1.3$	-3.33 $\pm$ 0.20	25.16 $\pm$ 0.05	1.37	0.22
$1.3 < z < 1.5$	-3.29 $\pm$ 0.19	25.25 $\pm$ 0.04	1.37	0.22
$1.5 < z < 2.0$	-3.23 $\pm$ 0.12	25.39 $\pm$ 0.03	1.37	0.22
$2.0 < z < 2.5$	-3.24 $\pm$ 0.12	25.54 $\pm$ 0.03	1.37	0.22
$2.5 < z < 3.0$	-3.56 $\pm$ 0.15	25.70 $\pm$ 0.04	1.37	0.22
$3.0 < z < 3.5$	-3.56 $\pm$ 0.35	25.74 $\pm$ 0.08	1.37	0.22
$3.5 < z < 4.0$	-3.72 $\pm$ 0.43	25.81 $\pm$ 0.09	1.37	0.22
$4.0 < z < 4.5$	-4.57 $\pm$ 1.00	26.03 $\pm$ 0.31	1.37	0.22

where $\phi(M)dM$ is the number density of galaxies with a mass between M and $M + dM$, $M^\star$ is the characteristic stellar mass, α_1 and α_2 are slopes satisfying the criteria that $\alpha_2 < \alpha_1$, and $\phi^\star_1$ and $\phi^\star_2$ are normalisation constants.

The specific star formation (sSFR) is the star formation rate normalised by the stellar mass,

$$\mathrm{sSFR} = \frac{\mathrm{SFR}}{M_\star}. \tag{4.15}$$

In Peng et al. (2010) the sSFR is found to be

$$\mathrm{sSFR} = 2.5 \left(\frac{t}{3.5\mathrm{Gyr}}\right)^{-2.2} \left(\frac{M_\star}{10^{10} M_\odot}\right)^{-\beta} \mathrm{Gyr}^{-1}, \tag{4.16}$$

where t is cosmic time and $\beta = -0.1$. As β is so close to zero it is a good working hypothesis to say that at a given cosmic time the sSFR is constant.

Knowing the star formation rate it is a simple matter to convert to a bolometric luminosity as $\mathrm{SFR} = kL_{\mathrm{bol}}$ (Kennicutt, 1998).

4.4.2 The Bolometric Luminosity Function

The bolometric luminosity function for the H-ATLAS fields was compared to those values found in Gruppioni et al. (2013), Rodighiero et al. (2010), Huynh et al. (2007) and Floch et al. (2005) (hereafter G13, R10, H07, C05 and F05 respectively, see Figure 4.15) as well as compared to the model made by Eales 2013. An additional comparison to the LFs found at 250 and 350 μm in Section 4.3.2. All of the previously estimated LFs used SED templates and models derived from the local universe.

R10 and F05 derived the bolometric luminosity from the mid-IR with *Spitzer* rather than from the sub-mm. This may not be wise as in distant galaxies complex dust physics will have an effect on the PAH and silicate absorption features which fall in this region (H07). Changes in these features will have knock on effects when adjusting the SED for the galaxy, particularly as redshift moves the PAH features into the mid-IR bands. H07 observed at 70 μm, well beyond the range of this region. G13 meanwhile was created from Herschel wavelengths, and then integrating the best-fit SED for each source between 8 - 1000 μm.

Comparing to G13, R10 and F05 our results match well at low luminosities. However as the redshift goes up the observable portion of the LF moves towards the higher luminosity end and these observations pull away from ours. G13, R10 and F05 estimate LFs higher than the H-ATLAS values. Both G13 and R10 values are more in line with the H-ATLAS values than F05, and are more recent and precise. R10 takes L_{bol} to be between 8 μm and 1000 μm and this could cause the LF to move to the right as the their bolometric luminosity would be slightly higher than the H-ATLAS luminosities. R10 calculated the LF from the mid IR (24 μm) luminosity, biasing sources to the mid-IR, and used a source specific SED that was fit to the full range of multiwavelength data, both of which would cause discrepancies.

For lower redshifts ($0 < z < 2$) the model by Eales 2013 matches accurately to the H-ATLAS estimated luminosity function. However at higher redshifts the model over predicts ϕ and the estimated LF begins to pull away from the model. The mass function used to derive this bolometric LF was only well tested in the $0 < z < 2$ range (Conroy & Wechsler, 2009). As has been well established the evolution of the LF, and presumably by extension the mass function, slows down at $z > 2$. If the mass function used in the model does not account for this then it is expected that the model would over predict the LF at higher redshifts, which is what we see in Figure 4.16. This suggests that the slowing down we see is due to some real physical process and not due to a secondary effect of redshift or the bins being chosen. At high-L the model is consistently shown to under predict compared to both the template estimates and those taken from complimentary data. However the model is still on the cusp of the error measurements.

In Table 4.10 we see the fit parameters when a double exponential was applied to the Eales 2013 model, and the results are shown in blue on Figure 4.16. Comparing parameters for $\phi^{\star}_{Bol}$ and $L^{\star}_{Bol}$ obtained from the data it appears that it is $\phi^{\star}_{Bol}$ that is overestimated in Eales 2013. This would suggest that at these higher redshifts either the accessible volume is being overestimated or the number of galaxies is being underestimated for that particular redshift and luminosity bin. As the problem affects the highest redshift bins, it could be that even very luminous galaxies are still so far away that they fall below the detection limit.

However, from comparison by eye it appears that the double exponential does not appear to fit the model with a great degree of accuracy. For this reason I decided to repeat the analysis, allowing all the parameters to vary. As the model extends down to low luminosities there is not the same problem with lack of data as when considering the H-ATLAS data. When this was allowed, the fits matched exactly to the model, confirming that the model does fit the double exponential parametrisation. These values are given in Table 4.10.

When we do this it appears that both $\phi^{\star}_{Bol}$, $L^{\star}_{Bol}$ and α are consistently higher for the model than from the data values, but that σ is consistently lower. At the highest redshifts, however, it appears that both $\phi^{\star}_{Bol}$, $L^{\star}_{Bol}$ and σ match within errors, but that α is much higher for the model. This parameter is governed by the slope of the low luminosity end of the LF. The sources that contribute to the LF at these low luminosities are likely to be far too dim to be above the flux limit. It could therefore be possible that the discrepancy between the model and the data is simply a completeness issue.

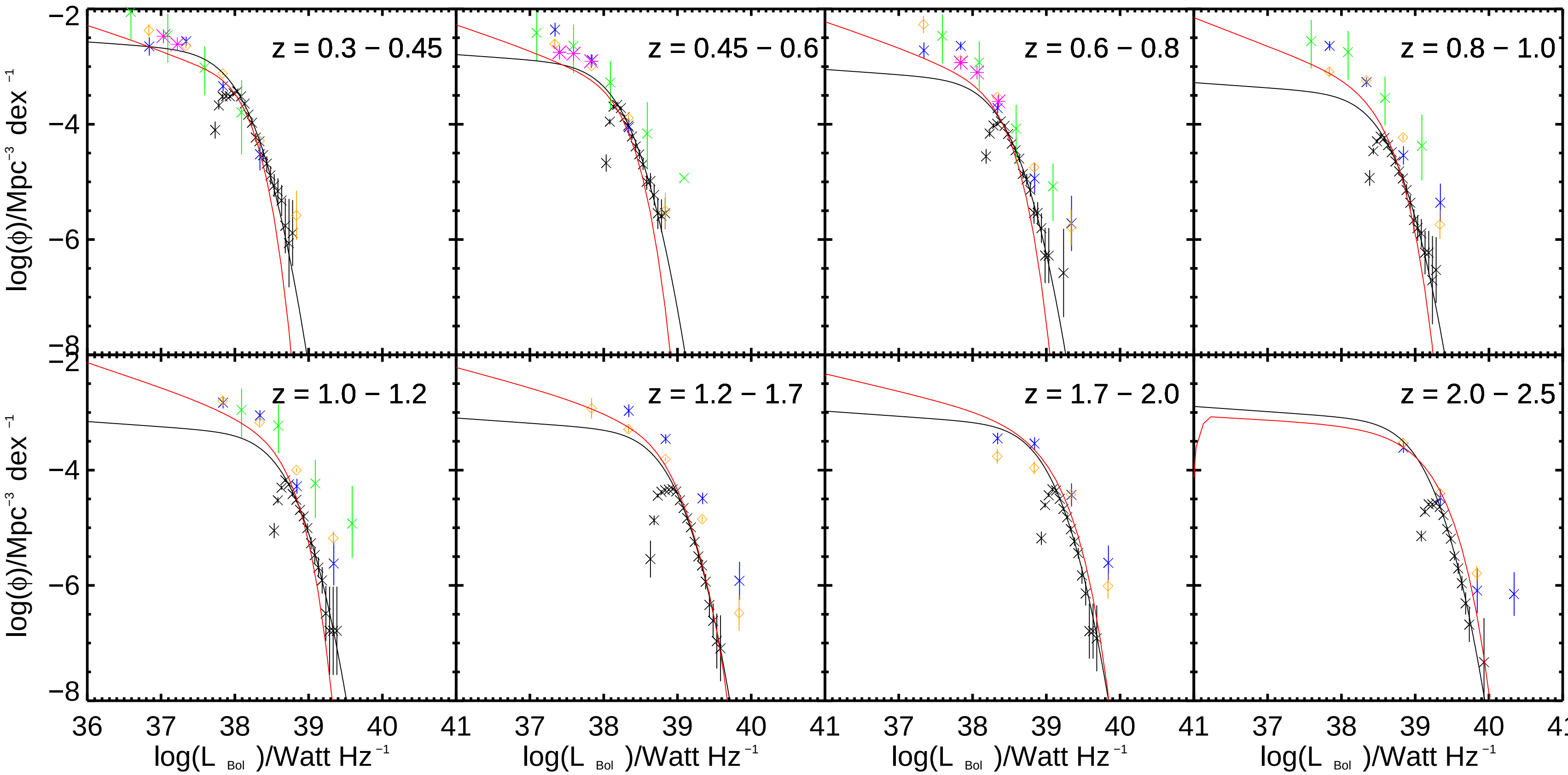

Figure 4.15: The bolometric LF obtained using $z_{\rm best}$ (black points) for the H-ATLAS field. For comparison with Gruppioni et al. (2013) (orange diamonds), Rodighiero et al. (2010) (blue crosses), Huynh et al. (2007) (magenta asterisks), Chapman et al. (2005) (cyan diamonds) Floch et al. (2005) (green crosses). The red line represents the LF derived by Eales 2013.

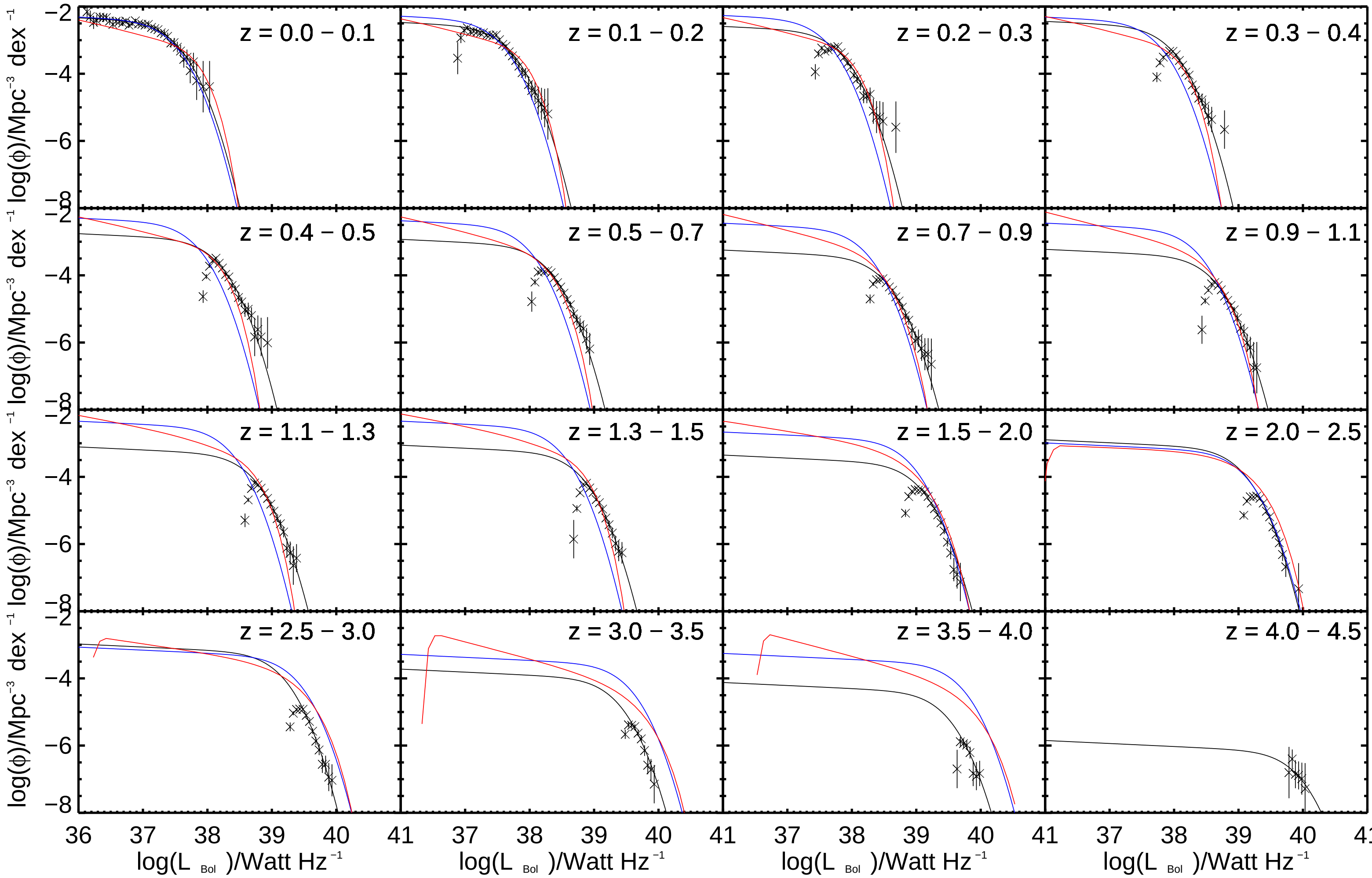

Figure 4.16: The bolometric LF obtained using z_{best}. The sources were selected such that $S_{250} > 5\sigma$. See Table 4.8 for fit parameters. The model produced by Eales 2013 is shown in red, while the blue line represents the fit produced from a double exponential with a fixed value of α and σ was applied to the Eales 2013 model (Table 4.10). The double exponentials where all fits are allowed to vary are not shown as they were identical to the model (Table 4.9).

Table 4.8: Fit parameters for the bolometric LF fit with a double exponential using the method described in 4.3. Plots are shown in Figure 4.16.

Redshift	$\log(\phi^{\star}_{Bol})$	$\log(L^{\star}_{Bol})$	α_{Bol}	σ_{Bol}
$0.0 < z < 0.1$	-2.45 ± 0.02	37.28 ± 0.03	1.09 ± 0.12	0.25 ± 0.03
$0.1 < z < 0.2$	-2.60 ± 0.03	37.44 ± 0.02	1.09	0.25
$0.2 < z < 0.3$	-2.73 ± 0.13	37.59 ± 0.05	1.09	0.25
$0.3 < z < 0.4$	-2.59 ± 0.08	37.71 ± 0.03	1.09	0.25
$0.4 < z < 0.5$	-2.93 ± 0.08	37.92 ± 0.03	1.09	0.25
$0.5 < z < 0.7$	-3.11 ± 0.11	38.03 ± 0.04	1.09	0.25
$0.7 < z < 0.9$	-3.45 ± 0.07	38.25 ± 0.03	1.09	0.25
$0.9 < z < 1.1$	-3.44 ± 0.08	38.36 ± 0.03	1.09	0.25
$1.1 < z < 1.3$	-3.33 ± 0.08	38.45 ± 0.03	1.09	0.25
$1.3 < z < 1.5$	-3.29 ± 0.09	38.54 ± 0.03	1.09	0.25
$1.5 < z < 2.0$	-3.60 ± 0.19	38.79 ± 0.05	1.09	0.25
$2.0 < z < 2.5$	-3.15 ± 0.26	38.81 ± 0.07	1.09	0.25
$2.5 < z < 3.0$	-3.24 ± 0.29	38.90 ± 0.07	1.09	0.25
$3.0 < z < 3.5$	-4.00 ± 0.60	39.10 ± 0.12	1.09	0.25
$3.5 < z < 4.0$	-4.41 ± 0.99	39.21 ± 0.27	1.09	0.25
$4.0 < z < 4.5$	-6.18 ± 2.63	39.67 ± 0.83	1.09	0.25

The investigation done here probes the high luminosity section of the LF to much higher redshifts than previous studies have done. However, this section of the LF is controlled by a few very bright sources with high star formation rates. Despite the phenomenal amount of star formation that these sources are going through, they are so small in number that they contribute little to the overall star formation rate of the universe.

4.5 Conclusions

We estimated the LF of the H-ATLAS Phase 1 field at sub-mm wavelengths for a variety of redshifts. Due to the flux limit of the survey there is an incompleteness effect that causes a turn over in the LF seen at low luminosities, a problem exaserbated by the problems with the accessible volume determination method. In comparison with Lapi et al. (2011) it was demonstrated that this turn over becomes more pronounced the bigger the redshift bin being examined. For this reason a maximum bins size of $\Delta z = 0.5$ was imposed to reduce this. This also meant that in most cases only the high luminosity section of the LFs produced had any validity. The exception to this rule was at very low redshifts where the LF extended across the full range of luminosity. However if the bin was too large the higher redshift contribution began to turn over and create a dip at mid-luminosities.

At all wavelengths strong evolution in the LF is observed out to a redshift of approxi-

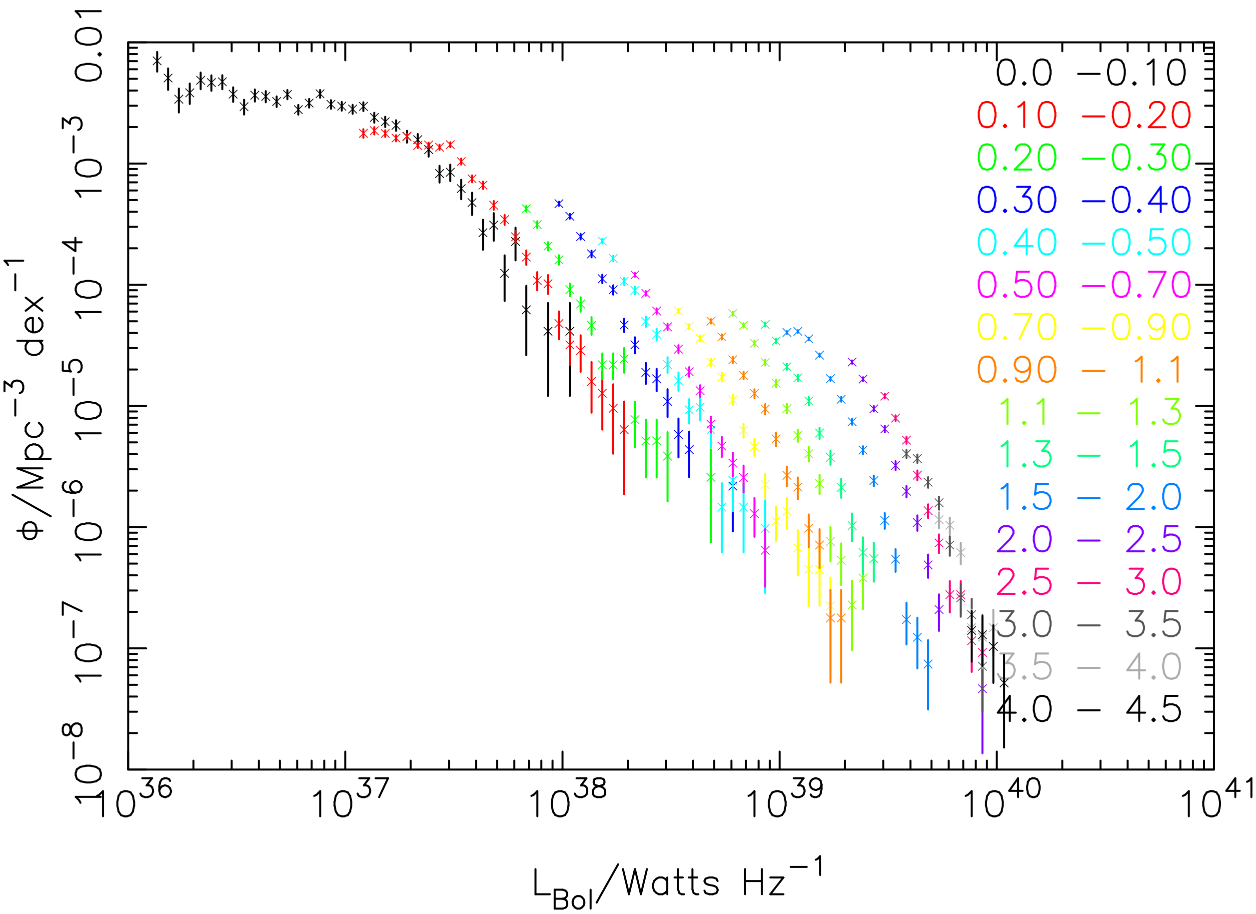

Figure 4.17: The bolometric LF obtained using the template redshifts. The colour code at the side shows the redshift bins of each point. The sources were selected such that $S_{250} > 5\sigma$.

Table 4.9: Fit parameters for the LF produced by Eales 2013, fit with a double exponential using the method described in 4.3 where α and σ are fixed values. The models are shown in Figure 4.16 in red.

Redshift	$\log(\phi^{\star}_{Bol})$	$\log(L^{\star}_{Bol})$	α_{Bol}	σ_{Bol}
$0.0 < z < 0.1$	-2.420 ± 0.002	37.2303 ± 0.0005	1.09	0.25
$0.1 < z < 0.2$	-2.402 ± 0.002	37.2993 ± 0.0005	1.09	0.25
$0.2 < z < 0.3$	-2.387 ± 0.002	37.3699 ± 0.0005	1.09	0.25
$0.3 < z < 0.4$	-2.448 ± 0.002	37.5103 ± 0.0006	1.09	0.25
$0.4 < z < 0.5$	-2.440 ± 0.002	37.5815 ± 0.0005	1.09	0.25
$0.5 < z < 0.7$	-2.531 ± 0.005	37.7258 ± 0.0007	1.09	0.25
$0.7 < z < 0.9$	-2.625 ± 0.007	37.9646 ± 0.0012	1.09	0.25
$0.9 < z < 1.1$	-2.636 ± 0.003	38.1106 ± 0.0008	1.09	0.25
$1.1 < z < 1.3$	-2.533 ± 0.002	38.0937 ± 0.0005	1.09	0.25
$1.3 < z < 1.5$	-2.542 ± 0.002	38.2192 ± 0.0005	1.09	0.25
$1.5 < z < 2.0$	-2.904 ± 0.002	38.6557 ± 0.0006	1.09	0.25
$2.0 < z < 2.5$	-3.245 ± 0.002	38.8385 ± 0.0006	1.09	0.25
$2.5 < z < 3.0$	-3.350 ± 0.002	39.1258 ± 0.0006	1.09	0.25
$3.0 < z < 3.5$	-3.579 ± 0.002	39.2884 ± 0.0007	1.09	0.25
$3.5 < z < 4.0$	-3.566 ± 0.002	39.4425 ± 0.0007	1.09	0.25

mately $z \sim 2$. At this point evolution was still seen but its advancement was considerably slowed until a redshift of ~ 3 where the evolution appeared to stop for the high luminosity LF. The results did not display any negative evolution at this point but the data points were too scarce to preclude this.

A simple model of the bolometric luminosity function produced by Steven Eales (2013) fit well with the data up to $z > 2$ where the model began to overpredict the LF. However the mass function used to create the model was only tested between $0 < z < 2$. As has already been stated, the evolution of the LF slows above this point and the model bolometric LF did not take this into account. Comparison between the model and the data showed that the discrepancy between the model and the data could also have been caused by a lack of data at high redshifts, especially of low luminosity sources.

Parametrisation of the LF proved difficult. In most cases α and σ were fit using the lowest redshift LF. This meant that they were fit to a different SED than is used for higher redshift bins and so these values might change at higher redshifts. However at higher redshifts there was not enough information to gain accurate fits. It is difficult to judge the accuracy of these parameters as the low luminosity region, governed by α, is only viewable at low redshifts. The high luminosity section does seem well parametrised in most cases.

Table 4.10: Fit parameters for the LF produced by Eales 2013, fit with a double exponential using the method described in 4.3 where α and σ are allowed to vary. The models are shown in Figure 4.16 in red.

Redshift	$\log(\phi^{\star}_{Bol})$	$\log(L^{\star}_{Bol})$	α_{Bol}	σ_{Bol}
$0.0 < z < 0.1$	-3.4097 ± 0.0099	38.2730 ± 0.0261	1.4393 ± 0.0003	0.0920 ± 0.0034
$0.1 < z < 0.2$	-3.4096 ± 0.0098	38.3535 ± 0.0078	1.4382 ± 0.0030	0.0920 ± 0.0009
$0.2 < z < 0.3$	-3.3780 ± 0.0191	38.4313 ± 0.0149	1.4262 ± 0.0054	0.0921 ± 0.0017
$0.3 < z < 0.4$	-3.3716 ± 0.0044	38.4717 ± 0.0023	1.4321 ± 0.0019	0.0991 ± 0.0003
$0.4 < z < 0.5$	-3.3907 ± 0.0074	38.5733 ± 0.0056	1.4364 ± 0.0025	0.0963 ± 0.0007
$0.5 < z < 0.7$	-3.6070 ± 0.0052	38.6799 ± 0.0028	1.5044 ± 0.0023	0.1064 ± 0.0004
$0.7 < z < 0.9$	-3.5200 ± 0.0048	38.6303 ± 0.0028	1.5110 ± 0.0022	0.1474 ± 0.0005
$0.9 < z < 1.1$	-3.5697 ± 0.0049	38.7915 ± 0.0033	1.5261 ± 0.0020	0.1443 ± 0.0005
$1.1 < z < 1.3$	-3.5901 ± 0.0084	39.1306 ± 0.0070	1.4670 ± 0.0024	0.0954 ± 0.0008
$1.3 < z < 1.5$	-3.5536 ± 0.0090	39.2103 ± 0.0074	1.4587 ± 0.0027	0.1001 ± 0.0009
$1.5 < z < 2.0$	-3.4690 ± 0.0042	39.0564 ± 0.0035	1.3932 ± 0.0018	0.1894 ± 0.0007
$2.0 < z < 2.5$	-3.9951 ± 0.0416	39.9211 ± 0.0430	1.3079 ± 0.0106	0.0796 ± 0.0051
$2.5 < z < 3.0$	-3.8650 ± 0.0054	39.5062 ± 0.0050	1.3630 ± 0.0022	0.1905 ± 0.0010
$3.0 < z < 3.5$	-4.4811 ± 0.0036	39.7700 ± 0.0016	1.5764 ± 0.0016	0.1869 ± 0.0003
$3.5 < z < 4.0$	-4.3125 ± 0.0054	39.7186 ± 0.0052	1.5522 ± 0.0020	0.2379 ± 0.0013

4.6 Further Work

Semi analytical models (SAMs) are a methodology where by the observational consequences of galaxy evolution are predicted by making assumptions about the astrophysical process at work behind them. While they work well at optical and near-IR wavelengths, they fail to properly be applied to sub-mm (Blain et al., 2002). This is mainly due to a lack of information. The main problem with these models stems from the high redshift population, which SAMs can only account for by either adding an extra population of more luminous galaxies (Guiderdoni et al., 1998) or by breaking away from the traditional initial mass function (Blain et al., 2002). By drawing on the data found here it might be possible to increase the effectiveness of these models by using them to better constrain the high redshift sub-mm region.

Chapter 5

Angular correlation function

I, a universe of atoms, an atom in the universe.

Richard P. Feynman

5.1 Introduction

Galaxies, as we see them on the sky, are a 2D projection of the universe. Having estimated redshifts for all of the galaxies in the H-ATLAS field means that it is possible to study the clustering properties and structure of the H-ATLAS field in a third dimension as well. Such information is vital for understanding the distribution of dark matter within the universe, as most theories accept that the distribution of galaxies follows the underlying dark matter distribution (Maddox et al., 2010; Cooray et al., 2010).

Simulations of dark matter show that it is organised into a cosmic web, with centres of high density connected by filaments, and separated by great voids. Theory states that galaxies formed within these dark matter halos, and so the luminous matter in the galaxy follows this distribution of dark matter. If we study how galaxies cluster with respect to redshift, we will begin to understand not only how galaxies are organised over great distances, but also how this has changed over time.

As I have estimated redshifts for every source in the field we know that we are looking at a complete sample free from observational bias associated with finding redshifts via a counterpart method. Completeness is important as removing sources due to observational constraints could preferentially remove sources of a given population. This could make structure less prominent, or mask it entirely. As the overall density of galaxies decreased the errors involved would also increase.

The most common and easiest way to examine how sources are distributed is using the two point angular-correlation function (ACF). Section 5.2 will explain the ACF and how it is parameterised. I will look at previous studies on the ACF of sub-mm galaxies

(SMGs) in Section 5.3, then calculate an estimate for the ACF of the H-ATLAS galaxies using the redshifts determined in Chapter 3. I will then compare to previous work in Section 5.3 and draw some conclusions about what this can tell us about the distribution of SMGs at Herschel wavelengths.

In this Chapter '$z_{\rm best}$' refers to those redshifts found in Chapter 3, where an optical redshift is used where a reliable optical counterpart has been found else the redshift generated from the template is used.

5.2 Two point angular-correlation function $w(\theta)$

In an astronomical field the angular separation between any two galaxies is given as θ. By studying the distribution of θ over an entire field we can determine how the galaxies in that field are organised. For instance, if there is a cluster within a field there will be more sources closer together than in field without a cluster. This will cause the number of close galaxy pairs in that field of sky to increase, meaning that there will be a greater number of galaxies with a close separation. Conversely there may be voids causing a deficit of sources with a small separation. In order to quantify this increase we use the angular correlation function $w(\theta)$. This is defined as

$$\delta P = \varsigma^2 \left[1 + w(\theta)\right] \delta\Omega_1 \delta\Omega_2. \tag{5.1}$$

where δP is the probability of finding an object in a field with surface density ς that lies in both of two solid angle elements $\delta\Omega_1$ and $\delta\Omega_2$ that are separated by θ (Wall & Jenkins, 2003).

In broad terms $w(\theta)$ is calculated by determining the angular separation distribution of a field and then comparing this to the distribution for the same field if it was populated instead by a random distribution of galaxies. To find the angular separation distribution for N_g galaxies in a given field it is necessary to go through every galaxy and find the angular separation, θ, between it and every other galaxy in the field. There are $\frac{1}{2}N_g(N_g - 1)$ unique galaxy pairs. These are then binned according to θ to gives the distribution $N_{gg}(\theta_i)$.

In order to make a comparison a field of random galaxies must be created. To account for different sensitivities and depths of field I had to create random sources such that they followed the overall surface density of the observed field. This helps to counteract false structure caused by the shape of the field and areas that are masked out within the field. First I created a set of sources that with uniformly distributed random positions over the field. To each of these I then assigned a random flux such that the total flux distribution followed the number counts given in Negrello et al. (2007). These fluxes were then compared to the noise value of the corresponding position in the noise map. If the random source was at least five times the noise then the source was included as a 'detection', if not then the source was thrown out. From here the same process of pair comparison that was taken to produce $N_{gg}(\theta_i)$ was undertaken with the random sources. The resulting distribution is $N_{rr}(\theta_i)$.

I created 10 fields of approximately 500 sources in each. I did this rather than using one field with 5000 sources as the time taken to process goes with n^2. Doing a number of small fields greatly increases the time efficiency of finding the angular distribution. These must then be summed across all the fields to find $N_{rr}(\theta_i)$, which is found by

$$N_{rr}(\theta_i) = \sum_{j=1}^{10} N_{rr_j}(\theta_i) \tag{5.2}$$

$$\tag{5.3}$$

where $N_{rr_j}(\theta_i)$ is the distribution of the j^{th} random field.

The accuracy of estimating $w(\theta)$ was found to be greatly improved (Landy & Szalay, 1993) by the inclusion of a direct comparison between the random and observed sources, rather than just looking at the distribution of the two separately. The addition of this estimator takes into account edge effects (Bernstein, 1994) where the shape of the field might cause an apparent clustering signal to appear. $N_{gr}(\theta_i)$ is therefore the angular distance distribution between every random source and every observed source. Again $N_{gr}(\theta_i)$ is the summation of the distribution from all ten random fields.

We then define the data pair count as $DD = N_{gg}(\theta_i)$. In order to find the equivalent pair count for the random sets it is necessary to normalise $N_{rr}(\theta_i)$ and $N_{gr}(\theta_i)$ so that they have the same number of pairings as DD.

In order to find the equivalent for the random sets we need to normalise them such that the total number of comparisons is the same as $N_{gg}(\theta_i)$. Normally this would be simple as the number of random-random comparisons would be $\frac{1}{2}N_r(N_r - 1)$ and the number of random-galaxy would be $N_r N_g$. However as I am using more than one random field this is not correct. Therefore we say that

$$RR = N_{rr}(\theta_i)\frac{N_g(N_g-1)}{\sum_{j=1}^{10} N_{r_j}(N_{r_j}-1)} \quad (5.4)$$

$$DR = N_{gr}(\theta_i)\frac{N_g(N_g-1)}{\sum_{j=1}^{10} N_{r_j}N_g} \quad (5.5)$$

where N_{r_j} is the number of sources in random field j.

Knowing DD, RR and DR we can now estimate $w(\theta)$ using the Landy & Szalay (1993) estimator:

$$w(\theta_i) = \frac{DD - 2DR + RR}{RR}. \quad (5.6)$$

While other estimators exist this was found to give a more reliable estimate at large separations (Landy & Szalay, 1993; Ratcliffe et al., 1998). If there is a cluster smaller angular scales will have a larger value of $w(\theta)$.

The angular correlation function provides a simple and straight forward way of quantifying clustering in a given sky field. However there are several drawbacks to the method. Errors are difficult to compute due to edge effects and the fact that the error of adjacent $\Delta\theta$ bins is correlated and the value of $w(\theta)$ at a given θ depends on the density fluctuations on all angular scales. This makes estimating the true error very difficult which makes parametrising the resulting points unreliable. This will be tackled in Section 5.2.1. A large scale structure will effect the profile of smaller scales and this method provides no prescription for disentangling the two (Wall & Jenkins, 2003).

There is an added complication in that H-ATLAS does not cover one continuous field. Phase 1 spans three separate GAMA fields and each of these had the value of $w(\theta)$ calculated separately before being stacked together by taking the weighted average of the three fields, given as

$$w(\theta_z) = \frac{\sum_{3,z} N_{k,z} w(\theta)_{k,z}}{\sum_{3,z} N_{k,z}}. \quad (5.7)$$

where $N_{k,z}$ is the number of sources in the kth field at a given redshift z. This meant that the more populous field carried more weight. However if a field had an erroneously high number of sources due to a higher noise level or similar this could potentially propagate into the values. When inspecting $w(\theta)$ for each of the three fields individually there did not appear to be a significant difference though, so this is unlikely.

In order to parameterise $w(\theta)$ we use a power law (Roche & Eales, 1999) of the form

$$w(\theta) = A\theta^{-\delta} - C \tag{5.8}$$

where C is an integral constraint such that

$$C = \frac{\sum N_{rr}(\theta)\theta^{-\delta}}{\sum N_{rr}(\theta)}. \tag{5.9}$$

A is an indicator of the amplitude of the clustering signal while δ indicates the slope of the distribution. This power law is usually fit in either a two-parameter form, where both A and δ are allowed to vary, or in a single parameter form where δ is fixed, usually at either 0.8 or 2. Both of these methods will be used in Section 5.4.

The ACF can be greatly affected by foreground interference, such as Galactic cirrus. Cirrus can sometimes be misinterpreted as a source and falsely put into the catalogue, however the source extraction methods took efforts to prevent this from happening (Rigby et al., 2011). What this method did not account for, however, was whether there are sources 'hidden' behind the cirrus that were not detected. While the former would create a falsely high concentration of sources in certain area, the latter would create an unnatural void, both of which would interfere with the results. The GAMA-09 field was noted for having a much higher level of cirrus than the other two fields however it was included in this analysis. Though I made no adjustments to account for any extra or missing sources, the effects these might have caused were accounted for in the 'bootstrapping' error calculation described in Section 5.2.1.

5.2.1 Estimating errors

Determining the errors for the angular correlation function is notoriously difficult (Bernstein, 1994). Initially I estimated the error margins on $w(\theta)$ from the Poisson noise based on the number of galaxy pairs being examined. However the true error is often larger than the Poisson noise (Roche & Eales, 1999) as the field shape, survey depth and surface density of the field all have an effect, as does the fact that the error on each bin is correlated (Wall & Jenkins, 2003). It also does not account for errors brought about by foreground objects that might interfere with analysis, making a certain area appear more or less populous than it truly is. For these reasons it is more accurate to apply a bootstrapping method to determine the error. This was done by selecting ten $2\,\mathrm{deg}^2$ subsections across the field. Only ten subsections were used due to time constraints, as calculating $w(\theta)$ was a timely process and repeating it ten times more so. The fields were only $2\,\mathrm{deg}^2$ in size, meaning that only $20\,\mathrm{deg}^2$ of the $\sim 50\,\mathrm{deg}^2$ field was covered, due to the irregular shape of the field making larger error fields difficult to fit into the field and more difficult to calculate. This was not ideal, but provided enough coverage to get a reasonable upper limit on the uncertainty.

To calculate the error one of these sections was blanked out from the survey before re-determining $w(\theta)$, repeating for all of the subsections. The scatter of these ten $w(\theta)$ was then taken to be the error after normalising by a factor of

$$\sqrt{N-1} \times \sqrt{\frac{N-1}{N}} \tag{5.10}$$

where N is the number of subsections that would be needed to cover the whole survey area. This normalises for the fact that a section of the field has been removed and so the fields are different sizes.

As with calculating $w(\theta)$ itself this had to be performed over all three of the GAMA fields and then a weighted average taken such that

$$\sigma_w(\theta_z) = \sqrt{\frac{\sum\limits_{3,z} \left[N_{k,z}\sigma_{k,z}\right]^2}{\left[\sum\limits_{3,z} N_{k,z}\right]^2}}. \tag{5.11}$$

Errors on fit parameters were also estimated using a bootstrap method. 5000 sets of random data points were created by using the real values of $w(\theta)$ and varying the points according to a Gaussian distribution where σ is the value given by the error bars. I then fitted Equation 5.8 to each of these, taking the standard deviation of the resulting parameters to be the error on these parameters.

This method of error analysis does not, however, account for the effects of errors in redshift. Errors in redshift would cause sources to appear in the wrong bin. If there is widely differing signals between bins, this effect could smear out the signal from one redshift bin into the adjacent bins. This is not accounted for in the error analysis.

5.3 Previous angular correlation functions

The angular correlation function shows how galaxies are organised within the universe. Studying the clustering properties of SMGs was important in the investigation as to whether they were indeed the high redshift progenitors to elliptical galaxies in the local universe. Studies of the local universe have found that early types are more clustered than late type galaxies (Guzzo et al., 1997; Marzke et al., 1998) and so if SMGs do evolve to become elliptical galaxies it would be expected that these were strongly clustered too.

As with much sub-mm astronomy, early investigations of the angular correlation function of sub-mm galaxies (Scott et al., 2002; Almaini et al., 2003; Webb et al., 2003; Blain et al., 2004) were been hampered by a lack of sources. A few small blind surveys did yield $w(\theta)$ but for a statistically valid study a large survey needed to be completed with many more sources. Despite these drawbacks strong clustering signals on arc minute scales was tentatively observed. Studies into the mid-IR (Gilli et al., 2007) found clustering at these wavelengths as well. Larger surveys still only detected a handful of sources (Scott et al., 2006; Weiß et al., 2009b). Examination of extremely red objects (Daddi et al., 2000) suggesting that there was a selection of highly clustered elliptical galaxies corroborated the idea that SMGs evolve to be elliptical galaxies in the local universe.

With the advent of large area blind surveys, such as those *Herschel* is capable of undertaking, it is now possible to probe the ACF with a large number of sources. However the ACF is a 2D representation of a 3D structure. If no account is taken of the differences in redshift of the sources then the very little clustering is observed (Cooray et al., 2010; Maddox et al., 2010; Magliocchetti et al., 2011; van Kampen et al., 2012).

Attempting to account for redshift by using either colour cuts (see Section 5.3.1) or by using redshifts from counterpart matching at various wavelengths, it appeared that there was a strong clustering signal of sub-mm galaxies but the signal was being washed out as they observed several clusters along a single line of sight (Maddox et al., 2010). van Kampen et al. (2012) looked at the ACF to a depth of $z < 0.3$, a range where the redshift distribution is nearly complete. The fit parameters are shown in Table 5.1. When all sources meeting the flux cut, regardless of their z, were used no clustering signal was seen. When split into finer redshift bins the signal was considerably stronger, showing the effect of this washing out.

Table 5.1: Clustering fit parameters for van Kampen et al. (2012) for both the single and two parameter fit models. Values of A greatly increases at low redshifts.

Slice	N	A [arcmin]	δ	$A_{0.8}$
all z	5363	0.006 ± 0.008	0.51 ± 0.09	0.04 ± 0.02
$z < 0.3$	724	0.28 ± 0.33	1.10 ± 0.39	0.20 ± 0.04
$0.05 < z < 0.10$	123	1.09 ± 0.97	0.80 ± 0.29	1.14 ± 0.38
$0.10 < z < 0.15$	137	2.45 ± 1.20	0.62 ± 0.15	1.99 ± 0.51
$0.15 < z < 0.20$	167	2.13 ± 0.62	0.95 ± 0.19	1.78 ± 0.31
$0.20 < z < 0.25$	136	0.59 ± 0.66	0.58 ± 0.19	1.20 ± 0.30
$0.25 < z < 0.30$	145	0.66 ± 0.86	1.05 ± 0.83	1.13 ± 0.26

In the lowest redshift bins there is little clustering. However these bins are the least populated and so a clear clustering signal is difficult to find. This may also be more of an effect due to luminosity limits as some models predict clustering over a particular luminosity threshold (Baugh et al., 2005; Lacey et al., 2010), rather than a redshift one. Higher redshift sources must be at a greater luminosity in order to be meet our flux limits and be detected. This means that not all models which predict clustering at low-z should necessarily be thrown out straight away.

Increasing the wavelength makes the signal less clear, potentially due to the increasing beam size (Cooray et al., 2010) or from a relative scarcity or sources.

Previously surveys relied on identification with a source at another wavelength to make a redshift determination meaning that there was only a reasonably complete sample of sources up to $z < 0.5$ so only the local universe was well studied. By using the method of redshift determination laid down in Chapter 3 we will be able to examine the ACF to high redshifts.

5.3.1 Maddox et al. (2010) and Cooray et. al (2010)

Maddox et al. (2010) (hereafter M10) created angular correlation functions from the Science Demonstration Phase (SDP) of the H-ATLAS survey, which was only 16 deg^2 in size. In Section 5.4 I will perform an in depth comparison to these ACFs (see Figures 5.8 and 5.14) to see how the data of the SDP compares to the Phase 1 data when no redshifts are taken into account.

As accurate distance and redshift measurements were not available for all sources, only those at low-z, they instead attempted to split the data using flux cuts. They created five different selections:

- $S_{250} > 33$ - all sources with a flux greater than 33 mJy in the 250 μm waveband. This is approximately equal to a 5σ detection according to the combined expected instrumental and confusion noise. This covered 90% of the SDP sources so will have sources at a variety of redshifts. Applying these cuts to the $z_{\rm best}$ distribution generates a mean redshift of $z = 1.1$.

- $S_{350} > 36$ - all sources with a flux greater than 36 mJy in the 350 μm waveband. Applying these cuts to the $z_{\rm best}$ distribution generates a mean redshift of $z = 1.7$.

- $S_{500} > 45$ - all sources with a flux greater than 45 mJy in the 500 μm waveband. This selection will contain a large number of high-z galaxies. Applying these cuts to the $z_{\rm best}$ distribution generates a mean redshift of $z = 2.4$.

- $S_{350} > 36 + 3\sigma$ - as $S_{350} > 36$ but with the additional stipulation that the flux measurements at 250 and 500 μm must also be greater than 3σ. Amblard et al.

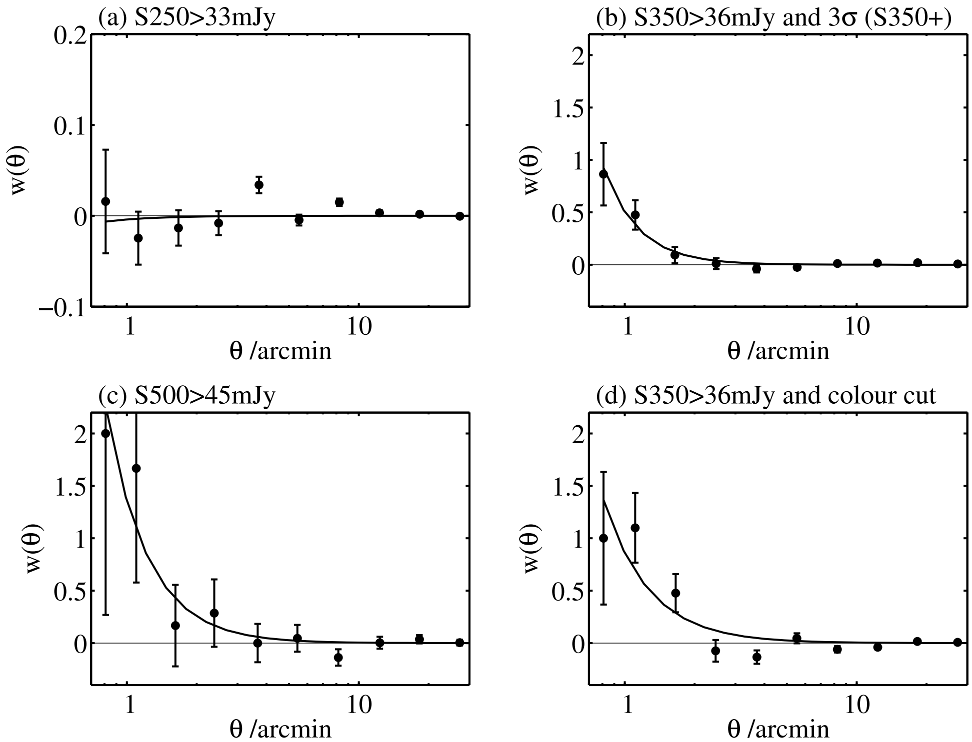

Figure 5.1: $w(\theta)$ from M10. The panels show the following selections - (a) $S_{250} > 33$mJy (A), (b) $S_{350} > 36$mJy with 3σ detection at 250 μm and 500 μm (B+), (c) $S_{500} > 45$mJy (C), and (d) $S_{350} > 36$mJy with 3σ and $S_{500}/S_{250} > 0.75$ colour selected sample (BCol). The error bars on the plots are estimated from the Poisson noise in the pair counts.

(2011) predicts that this additional flux cut would generate a distribution with a mean redshift of 2.2 ± 0.6, while applying them to the z_{best} distribution generates a mean redshift of $z = 2$.

- $S_{500}/S_{250} > 0.75$ - as $S_{350} > 36$ with a colour cut. Amblard et al. (2011) generates a mean redshift of 2.6 ± 0.3, which is in agreement with that found when the cut was applied to the z_{best} distribution.

From these selections $w(\theta)$ was worked out using the Landy & Szalay (1993) estimator. As with ours, M10 created random sources according to the noise maps. Their errors were taken from the Poisson error on the number counts and so are most likely underestimates.

The data was then fitted with a standard power law (Eqn 5.8). At first they allowed both A and δ to vary, then re-ran the procedure with a fixed $\delta = 0.8$ and $\delta = 2.0$. The results of all these fits are shown in Table 5.2. Fig 5.1 shows these points with the fits from the two parameter model shown.

Cooray et al. (2010) performed a very similar analysis to $S_{250} > 33$, $S_{350} > 36$ and $S_{500} > 45$ on two widest HerMES fields, but set the flux limit for all detections at 30mJy across all bands (see Figure 5.2). In addition, Cooray et al. (2010) also fit the

Table 5.2: Fit parameters for $w(\theta)$ in M10. N is the number of sources in each sample. A is the amplitude of $w(\theta = 1')$ and δ is the power-law slope. $A_{0.8}$ and $A_{2.0}$ are the amplitudes at $1'$ with the slopes fixed at 0.8 and 2.0 respectively. Values are provided from M10.

Sample	Symbol	N	A	δ	$A_{0.8}$	$A_{2.0}$
$S_{250} > 33$	A	6317	-0.01 $\pm$ 0.07	1.7 $\pm$ 0.2	-0.00	-0.01
$S_{350} > 36$	B	2754	0.20 $\pm$ 0.07	2.0 $\pm$ 0.2	0.11	0.20
$S_{500} > 45$	C	304	1.24 $\pm$ 1.6	2.4 $\pm$ 1.3	0.51	1.24
$S_{350} > 36 + 3\sigma$	B+	1633	0.50 $\pm$ 0.09	2.8 $\pm$ 0.5	0.21	0.50
$S_{500}/S_{250} > 0.75$	BCol	808	0.92 $\pm$ 0.3	2.1 $\pm$ 0.5	0.38	0.92

data using a halo model with both a 1 and 2 halo component. The 2-halo component captures the large scale clustering, while the 1-halo arises from having multiple sources in a dark matter halo. However, this Cooray et al. (2010) did not include any correction for cirrus emission, which may also reduce large scale structure, whereas in the H-ATLAS catalogues this was accounted for.

The found no difference in correlation between the two fields. Due to the lack of spectroscopic redshifts they used isothermal SEDs to approximate the relation between colour and redshift (See the description of Amblard et al. (2010) in Chapter 3 for more details on this method). Their results showed some evidence for clustering at arcminute angular scales, clearly at 250 μm and less so for longer wavelengths, most likely due to the increase in beam size.

5.3.2 Conclusions

All of the previous studies agree that when no redshift cut is put into place then there is minimal to zero clustering observed due to the fact we are looking along the whole line of sight, thus washing out any clustering signal that might exist. Increasing the redshift and changing the wavelength of the survey effects the number of sources available for study. The less sources there are available the more difficult it is to obtain an ACF.

When accounting for redshift then a strong clustering signal is observed at low redshifts. Due to incompleteness and a lack of data the angular correlation function has been unable to be studied in any real depth at high-z.

5.4 Determined angular correlation function

$w(\theta)$ was calculated according to the method laid down in 5.2 and then parameterised using a standard power law (Eqn 5.8). $w(\theta)$ was found for sources detected at 5σ in all three SPIRE wavebands using the redshifts obtained in Chapter 3, separating the sources

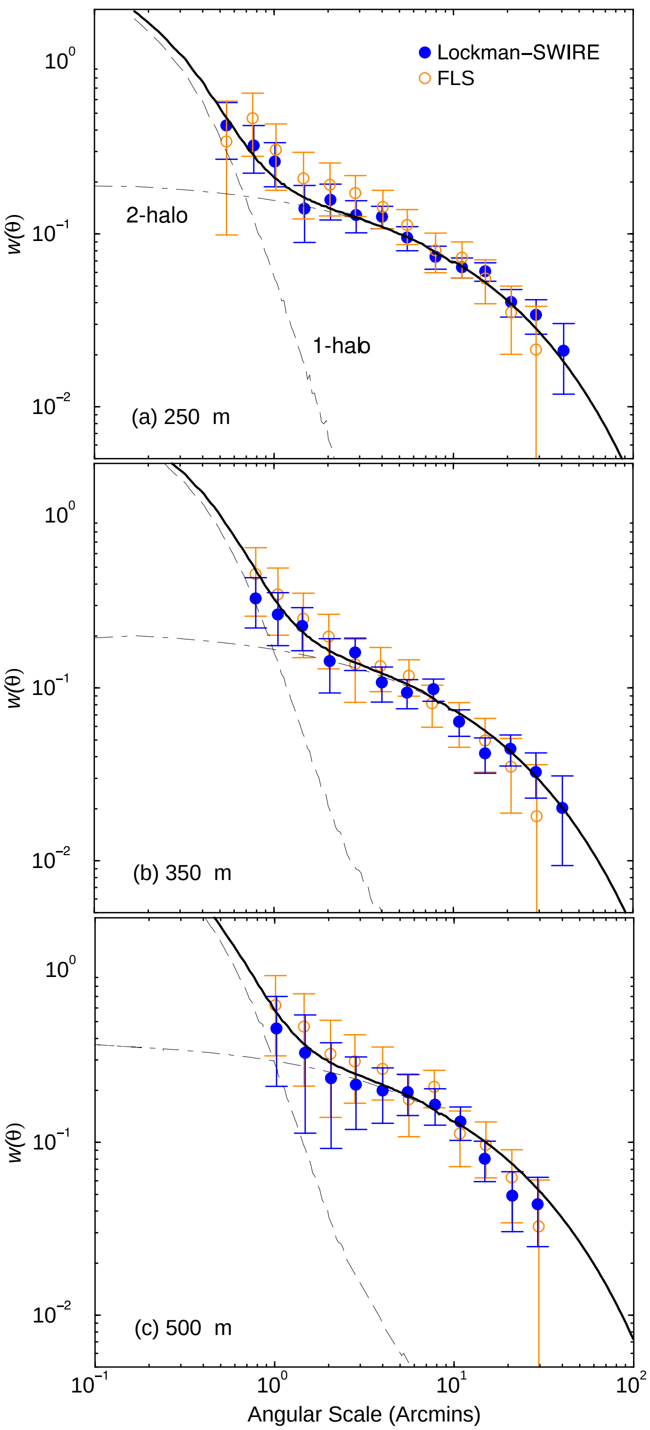

Figure 5.2: $w(\theta)$ from Cooray et al. (2010). The black line shows the fit determined from the halo model.

redshift	N	A[arcmin]	δ	$A_{0.8}$	$A_{2.0}$
$0.0 < z < 0.5$	23342	0.26 ± 0.04	0.95 ± 0.08	0.201 ± 0.008	0.35 ± 0.05
$0.5 < z < 1.0$	12960	0.19 ± 0.06	1.0 ± 0.2	0.135 ± 0.005	0.21 ± 0.08
$1.0 < z < 1.5$	12486	0.00 ± 0.05	3.0 ± 0.8	0.035 ± 0.001	0.00 ± 0.04
$1.5 < z < 2.0$	12183	0.11 ± 0.05	0.7 ± 0.2	0.149 ± 0.006	0.15 ± 0.10
$2.0 < z < 2.5$	7448	0.1 ± 0.1	0.6 ± 0.2	0.217 ± 0.008	0.4 ± 0.2
$2.5 < z < 3.0$	3138	0.6 ± 0.4	1.2 ± 0.5	0.27 ± 0.01	0.8 ± 0.4
$3.0 < z < 3.5$	912	0.1 ± 0.78	0.6 ± 1.0	0.168 ± 0.006	0.0 ± 0.8
$3.5 < z < 4.0$	233	0.0 ± 5.0	3.0 ± 1.0	0.0001 ± 0.0001	0.0 ± 5.0
$4.0 < z < 4.5$	42	0 ± 42	3.0 ± 1.0	0.0001 ± 0.0001	0 ± 39

Table 5.3: Fit parameters for the $S_{250} > 5\sigma$ selection using Poisson errors and $z_{\rm best}$. Plots are shown in Figure 5.3.

into redshift bins of $\Delta z = 0.5$. The redshifts used for the ACFs found here use optical redshifts where available and the template obtained redshift for those with no reliable optical counterpart ($z_{\rm best}$).

I performed a single and a two parameter fit, found by minimising the chi squared fit to the data. For the two parameter fit both δ and A were allowed to vary in the range $0.6 < \delta < 3.0$ and $10^{-4} < A < 10^2$. A single parameter fit was also done, once setting $\delta = 0.8$ and again with $\delta = 2.0$.

5.4.1 ACFs with Poissonian errors

At first I used the Poisson errors to estimate the uncertainty in $w(\theta)$. The Poisson error is based solely on the number of galaxies, both real and random, being used and takes no account of the fluctuations within the field, such as those due to cirrus. As the random sources are taken from the noise maps there is some consideration of these effects but the error is still usually vastly underestimated. The best fit redshifts are shown in Figs 5.3 - 5.5 with the best fit parameters listed in Tables 5.3 - 5.5.

Here we can see that the fits to the 500 μm selection have significantly larger error bars and uncertainties on the fit parameters than those at shorter wavelengths. However as the number of sources in each bin is very low this is to be expected. At all wavelengths the errors in the highest redshift bins are the largest, most likely due to the same reason. For the 250 μm selection we find strong clustering at low-z. This is surprising as in previous studies a redshift bin this coarse was found to cover up clustering signals at low redshifts. However at mid-z ($1.0 < z < 2.5$) the signal decreases, picking up again at $z > 2.5$ though it is difficult to tell much at these redshifts due to large error bars. This mid-z range is the most populated region and so it is possible that what we are seeing is a washing out of the signal rather than an actual lull in clustering.

redshift	N	A[arcmin]	δ	$A_{0.8}$	$A_{2.0}$
$0.0 < z < 0.5$	5004	0.5 ± 0.2	0.9 ± 0.3	0.35 ± 0.08	0.6 ± 0.2
$0.5 < z < 1.0$	2771	0.4 ± 0.3	1.7 ± 0.8	0.05 ± 0.10	0.4 ± 0.3
$1.0 < z < 1.5$	4315	0.2 ± 0.2	1.1 ± 0.7	0.12 ± 0.08	0.2 ± 0.2
$1.5 < z < 2.0$	7504	0.3 ± 0.1	1.0 ± 0.3	0.21 ± 0.05	0.4 ± 0.1
$2.0 < z < 2.5$	6862	0.5 ± 0.2	1.1 ± 0.3	0.30 ± 0.06	0.7 ± 0.2
$2.5 < z < 3.0$	3972	0.7 ± 0.3	1.4 ± 0.4	0.2 ± 0.1	0.8 ± 0.3
$3.0 < z < 3.5$	1723	1.9 ± 0.8	1.7 ± 0.5	0.3 ± 0.2	2.0 ± 0.8
$3.5 < z < 4.0$	733	0.9 ± 1.3	1.1 ± 0.9	0.5 ± 0.5	1 ± 1
$4.0 < z < 4.5$	263	9 ± 15	3.0 ± 1.0	0.0 ± 0.9	3 ± 8

Table 5.4: Fit parameters for the $S_{350} > 5\sigma$ selection using Poisson errors and $z_{\rm best}$. Plots are shown in Figure 5.4.

redshift	N	A[arcmin]	δ	$A_{0.8}$	$A_{2.0}$
$0.0 < z < 0.5$	650	2 ± 3	1.6 ± 0.8	0.3 ± 0.5	3 ± 3
$0.5 < z < 1.0$	178	0 ± 16	0.6 ± 1.1	0.4 ± 1.7	0 ± 12
$1.0 < z < 1.5$	128	0 ± 31	0.6 ± 1.1	1 ± 2	0 ± 32
$1.5 < z < 2.0$	569	2 ± 4	1.5 ± 0.8	0.2 ± 0.5	3 ± 4
$2.0 < z < 2.5$	1139	1 ± 1	1.0 ± 0.9	0.5 ± 0.3	2 ± 2
$2.5 < z < 3.0$	1192	2 ± 2	1.8 ± 0.7	0.1 ± 0.3	2 ± 1
$3.0 < z < 3.5$	718	0 ± 1	3 ± 1	0.1 ± 0.4	0 ± 1
$3.5 < z < 4.0$	444	0 ± 3	3 ± 1	0.1 ± 0.6	0 ± 3
$4.0 < z < 4.5$	213	0 ± 5	3 ± 1	0 ± 1	0 ± 5

Table 5.5: Fit parameters for the $S_{500} > 5\sigma$ selection using Poisson errors and $z_{\rm best}$. Plots are shown in Figure 5.5.

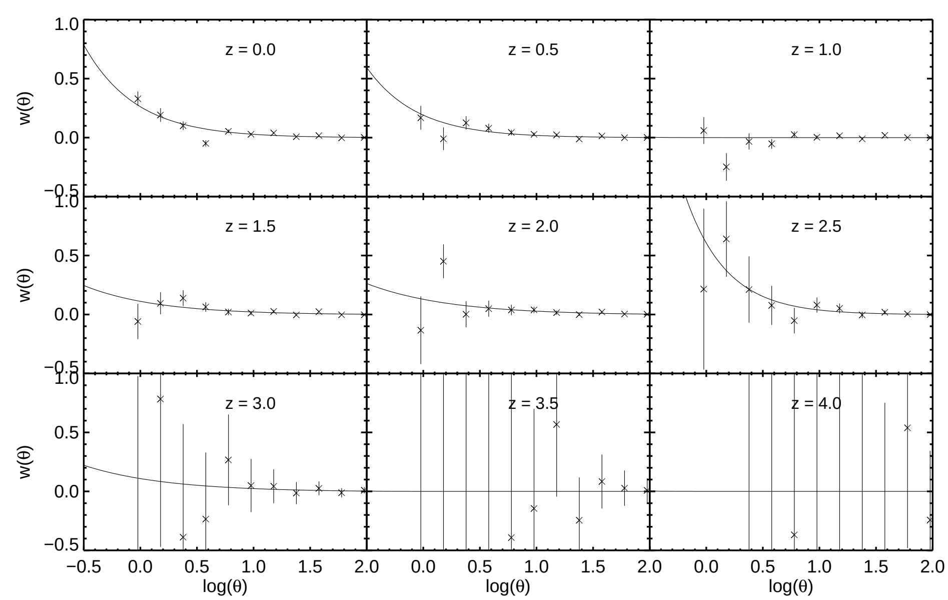

Figure 5.3: Plot of $w(\theta)$ for the $S_{250} > 5\sigma$ selection, separated out into $\Delta z = 0.5$ bins using $z_{\rm best}$ for redshift determination and Poisson errors. See Table 5.3 for fit parameters.

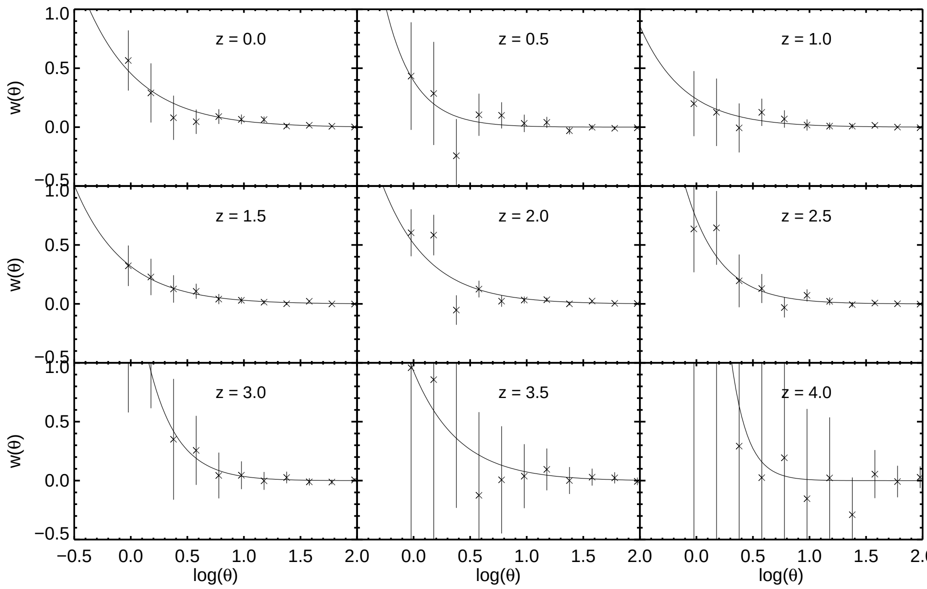

Figure 5.4: Plot of $w(\theta)$ for the $S_{350} > 5\sigma$ selection, separated out into $\Delta z = 0.5$ bins using z_{best} for redshift determination and Poisson errors. See Table 5.4 for fit parameters.

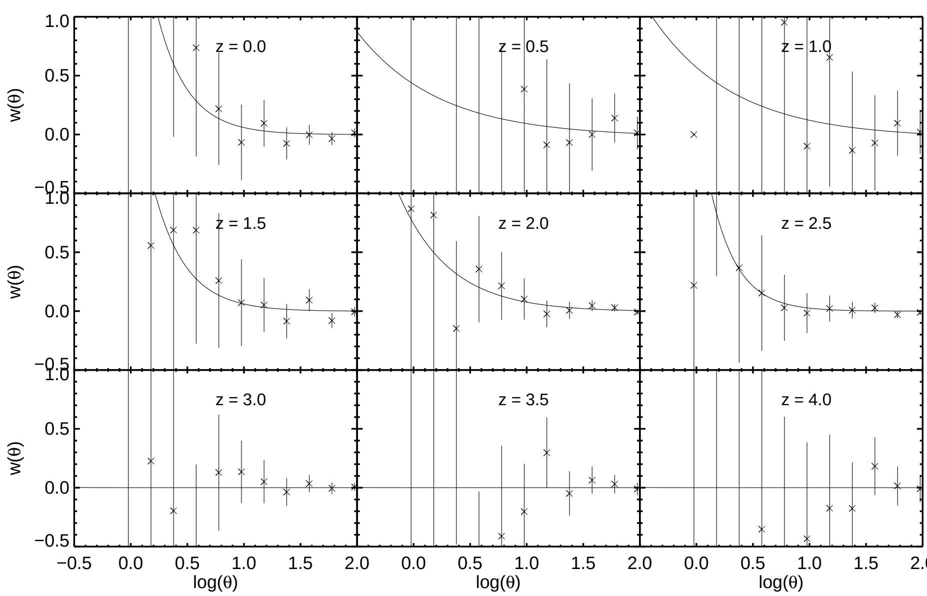

Figure 5.5: Plot of $w(\theta)$ for the $S_{500} > 5\sigma$ selection, separated out into $\Delta z = 0.5$ bins using z_{best} for redshift determination and Poisson errors. See Table 5.5 for fit parameters.

redshift	N	A[arcmin]	δ	$A_{0.8}$	$A_{2.0}$
$0.00 < z < 0.50$	23342	0.26 ± 0.04	0.95 ± 0.08	0.201 ± 0.008	0.35 ± 0.05
$0.00 < z < 0.05$	3401	1.7 ± 0.6	0.8 ± 0.1	1.6 ± 0.4	1.7 ± 1.0
$0.05 < z < 0.10$	2066	1.7 ± 0.4	0.74 ± 0.07	1.9 ± 0.2	2.3 ± 0.6
$0.10 < z < 0.15$	2698	1.6 ± 0.2	0.70 ± 0.05	2.0 ± 0.2	2.3 ± 0.5
$0.15 < z < 0.20$	2430	1.2 ± 0.3	0.66 ± 0.09	1.7 ± 0.2	2.3 ± 0.6
$0.20 < z < 0.25$	1840	0.9 ± 0.4	0.8 ± 0.1	1.0 ± 0.2	1.2 ± 0.7
$0.25 < z < 0.30$	2229	0.5 ± 0.4	1.0 ± 0.7	0.3 ± 0.2	0.6 ± 0.5
$0.30 < z < 0.35$	2334	0.9 ± 0.5	1.0 ± 0.3	0.5 ± 0.2	1.4 ± 0.6
$0.35 < z < 0.40$	2340	0.6 ± 0.6	1.0 ± 0.8	0.4 ± 0.1	1.1 ± 0.6
$0.40 < z < 0.45$	2086	0.1 ± 0.3	0.5 ± 0.8	0.3 ± 0.2	0.1 ± 0.4
$0.45 < z < 0.50$	1920	0.4 ± 0.5	1.1 ± 1.0	0.2 ± 0.2	0.6 ± 0.6

Table 5.6: Fit parameters for $S_{250} > 5\sigma$ using Poisson errors and $z_{\rm best}$ for low redshifts. For comparison values for the $0.00 < z < 0.50$ bin is shown as well. Plots are shown in Figure 5.6.

At 350 μm the clustering signal is strong at all redshifts. The same is true of the 500 μm selection, however this waveband has very large uncertainties due to the lack of sources observed.

It was found by van Kampen et al. (2012) that at low redshifts, coarse binning can hide potential clustering. Though this doesn't appear to be the case here as the $z < 0.5$ bin shows clear signs of clustering, I investigated further by separating the lowest redshift bin into further sub bins, $\Delta z = 0.05$ in size and then determined the ACF (see Tables 5.6 and 5.7). As with van Kampen et al. (2012) I find that the clustering signal for most of the sub-bins is higher than that of the total bin stated previously. This further demonstrates that some care needs to be taken with interpreting this data.

It should be noted that at these low redshifts I am predominately examining the SDSS redshifts, rather than those generated by the template. The results for 500 μm are excluded here as there were too few sources to make any meaningful conclusions.

For comparison the same method was applied to the cuts used by M10. My comparative ACFs generate considerably smaller error bars compared to M10, most likely due to the vastly increased survey size. As with M10 there is a small clustering signal seen for Selection A, with the amplitude increasing with estimated mean redshift. Results are shown in Figure 5.8 and Table 5.8 (the original data found in M10 are given in Figure 5.1 and Table 5.2).

redshift	N	A[arcmin]	δ	$A_{0.8}$	$A_{2.0}$
$0.00 < z < 0.50$	5004	0.5 ± 0.2	0.9 ± 0.3	0.35 ± 0.08	0.6 ± 0.2
$0.00 < z < 0.05$	533	6 ± 4	1.2 ± 0.4	1.9 ± 0.9	9 ± 5
$0.05 < z < 0.10$	767	1.8 ± 1.1	0.7 ± 0.2	2.6 ± 0.6	4 ± 2
$0.10 < z < 0.15$	692	2 ± 1	0.7 ± 0.2	2.7 ± 0.6	3 ± 2
$0.15 < z < 0.20$	486	1.1 ± 1.0	0.4 ± 0.6	2.5 ± 1.0	0.8 ± 1.9
$0.20 < z < 0.25$	340	1 ± 4	0.8 ± 1.0	1.4 ± 1.2	2 ± 4
$0.25 < z < 0.30$	396	2 ± 4	3.0 ± 0.9	0.0 ± 0.5	1 ± 3
$0.30 < z < 0.35$	425	0.2 ± 3.7	0.9 ± 1.2	0.2 ± 0.7	0 ± 3
$0.35 < z < 0.40$	493	0.2 ± 1.3	0.6 ± 1.1	0.3 ± 0.6	0.0 ± 1.3
$0.40 < z < 0.45$	458	0.4 ± 1.7	0.8 ± 1.2	0.5 ± 0.7	0.5 ± 1.8
$0.45 < z < 0.50$	414	0.0 ± 1.4	1.8 ± 1.3	0.0 ± 0.5	0.0 ± 1.5

Table 5.7: Fit parameters for $S_{350} > 5\sigma$ for low redshifts using Poisson errors and $z_{\rm best}$. For comparison values for the $0.00 < z < 0.50$ bin is shown as well. Plots are shown in Figure 5.7

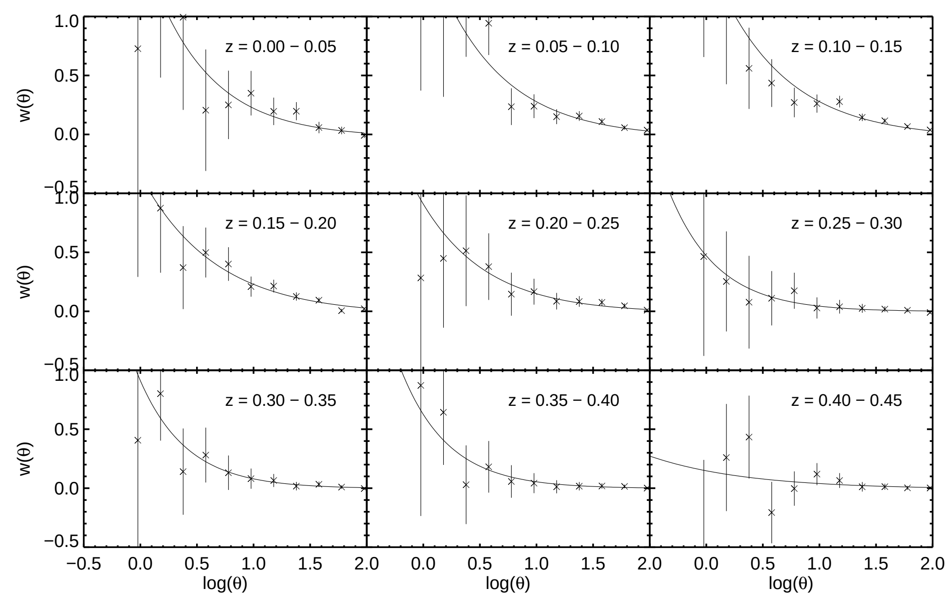

Figure 5.6: Plot of $w(\theta)$ for $S_{250} > 5\sigma$ selection at low-z, separated out into $\Delta z = 0.05$ bins using $z_{\rm best}$ for redshift determination and Poisson errors. See Table 5.6 for fit parameters.

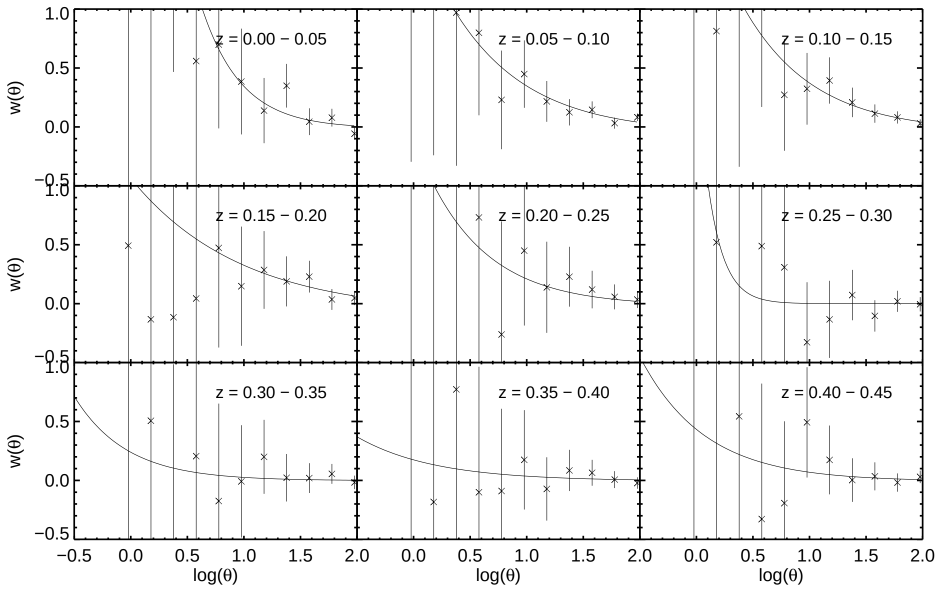

Figure 5.7: Plot of $w(\theta)$ for $S_{350} > 5\sigma$ selection at low-z, separated out into $\Delta z = 0.05$ bins using $z_{\rm best}$ for redshift determination and Poisson errors. See Table 5.7 for fit parameters.

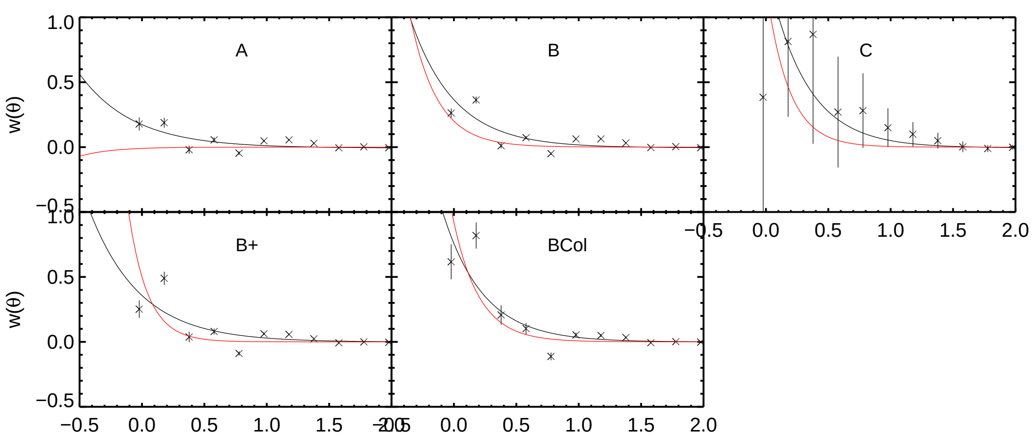

Figure 5.8: Plot of $w(\theta)$ for selections used in M10 using $z_{\rm best}$ and Poisson errors. The values and fit parameters found using the ACF derived in this work but with M10's cuts are shown in black (see Table 5.8 for fit parameters). The fit parameters from M10 are shown in red.

Table 5.8: As Table 5.2 with the Phase 1 sources using z_{best}. Error are from based on the Poissonian error. Plots shown in Figure 5.8.

Sample	N	A[arcmin]	δ	$A_{0.8}$	$A_{2.0}$
$S_{250} > 33$	71485	0.18 ± 0.05	1.0 ± 0.5	0.14 ± 0.02	0.25 ± 0.04
$S_{350} > 36$	40636	0.37 ± 0.02	1.23 ± 0.06	0.19 ± 0.01	0.43 ± 0.02
$S_{500} > 45$	7691	1.4 ± 0.4	1.4 ± 0.2	0.38 ± 0.09	2.0 ± 0.4
$S_{350} > 36 + 3\sigma$	21626	0.46 ± 0.05	1.5 ± 0.1	0.16 ± 0.02	0.49 ± 0.05
$S_{500}/S_{250} > 0.75$	11722	0.89 ± 0.09	1.5 ± 0.1	0.25 ± 0.04	0.95 ± 0.09

5.4.2 ACFs with Bootstrap Errors

I repeated the procedure for sources with the errors I obtained via a bootstrapping method. This led to much larger, but more realistic, error bars. In turn this resulted in larger errors on our fit parameters. The coarse selections, where $\Delta z = 0.5$, are shown in Figures 5.9 - 5.11 and the fit parameters given in Tables 5.9 - 5.11. The $\Delta z = 0.05$ bins are shown in Figures 5.12 - 5.13

redshift	N	A[arcmin]	δ	$A_{0.8}$	$A_{2.0}$
$0.0 < z < 0.5$	23342	0.3 ± 0.3	1.1 ± 1.0	0.2 ± 0.1	0.3 ± 0.3
$0.5 < z < 1.0$	12960	0.3 ± 0.3	1.1 ± 0.9	0.2 ± 0.2	0.2 ± 0.3
$1.0 < z < 1.5$	12486	0.0 ± 0.2	3 ± 1	0.0 ± 0.1	0.0 ± 0.3
$1.5 < z < 2.0$	12183	0.0 ± 0.3	0.6 ± 1.0	0.1 ± 0.1	0.2 ± 0.3
$2.0 < z < 2.5$	7448	0.1 ± 0.2	0.6 ± 1.0	0.2 ± 0.2	0.4 ± 0.4
$2.5 < z < 3.0$	3138	0.4 ± 0.3	1.0 ± 0.7	0.3 ± 0.2	0.5 ± 0.4
$3.0 < z < 3.5$	912	1.1 ± 0.6	1.4 ± 0.8	0.2 ± 0.3	0.0 ± 0.6
$3.5 < z < 4.0$	233	2 ± 3	3 ± 1	0.0 ± 0.3	0.0 ± 0.8
$4.0 < z < 4.5$	42	0.0 ± 0.6	3.0 ± 0.5	0.0 ± 0.0	0.0 ± 0.4

Table 5.9: Fit parameters for $S_{250} > 5\sigma$ using bootstrap errors and $z_{\rm best}$.Plots shown in Figure 5.9.

redshift	N	A[arcmin]	δ	$A_{0.8}$	$A_{2.0}$
$0.0 < z < 0.5$	5004	0.3 ± 0.3	0.8 ± 0.8	0.3 ± 0.2	0.6 ± 0.4
$0.5 < z < 1.0$	2771	0.4 ± 0.4	1.5 ± 0.9	0.1 ± 0.2	0.4 ± 0.4
$1.0 < z < 1.5$	4315	0.2 ± 0.3	0.9 ± 1.0	0.1 ± 0.2	0.3 ± 0.4
$1.5 < z < 2.0$	7504	0.3 ± 0.3	1.0 ± 0.9	0.2 ± 0.2	0.5 ± 0.3
$2.0 < z < 2.5$	6862	0.6 ± 0.3	1.4 ± 0.7	0.3 ± 0.2	0.7 ± 0.3
$2.5 < z < 3.0$	3972	0.8 ± 0.3	1.3 ± 0.6	0.4 ± 0.2	0.9 ± 0.4
$3.0 < z < 3.5$	1723	2.2 ± 0.9	1.8 ± 0.5	0.5 ± 0.3	2.5 ± 0.9
$3.5 < z < 4.0$	733	0.8 ± 0.9	1.3 ± 1.0	0.4 ± 0.4	1.0 ± 1.0
$4.0 < z < 4.5$	263	9 ± 6	3.0 ± 0.5	0.0 ± 0.3	6 ± 5

Table 5.10: Fit parameters for $S_{350} > 5\sigma$ using bootstrap errors and $z_{\rm best}$.Plots shown in Figure 5.10.

One effect that was much more important while using bootstrap errors rather than Poisson errors is 'bottoming out' in the fit procedure. δ was allowed to vary in the range $0.6 < \delta < 3.0$ and A in the range $10^{-5} < A < 10^{5}$. Due to the lack of sources in some bins there was a high scatter and large errors, resulting in the fitting procedure struggling to find a good fit to the data and settling on the extremes of the search field. This was particularly bad at high-z and increased with wavelength, where the number of sources is lower. This resulted in falsely high values of A or δ but upon inspecting the plot it is obvious that $w(\theta)$ is actually flat (within error bars).

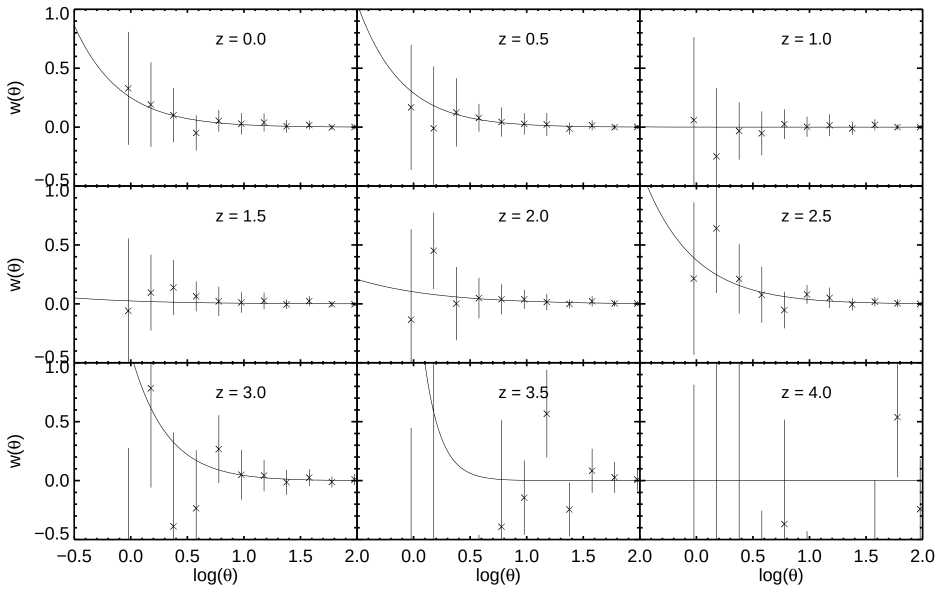

Figure 5.9: Plot of $w(\theta)$ for $S_{250} > 5\sigma$, separated out into $\Delta z = 0.5$ bins using $z_{\rm best}$ for redshift determination and bootstrap errors. See Table 5.9 for fit parameters.

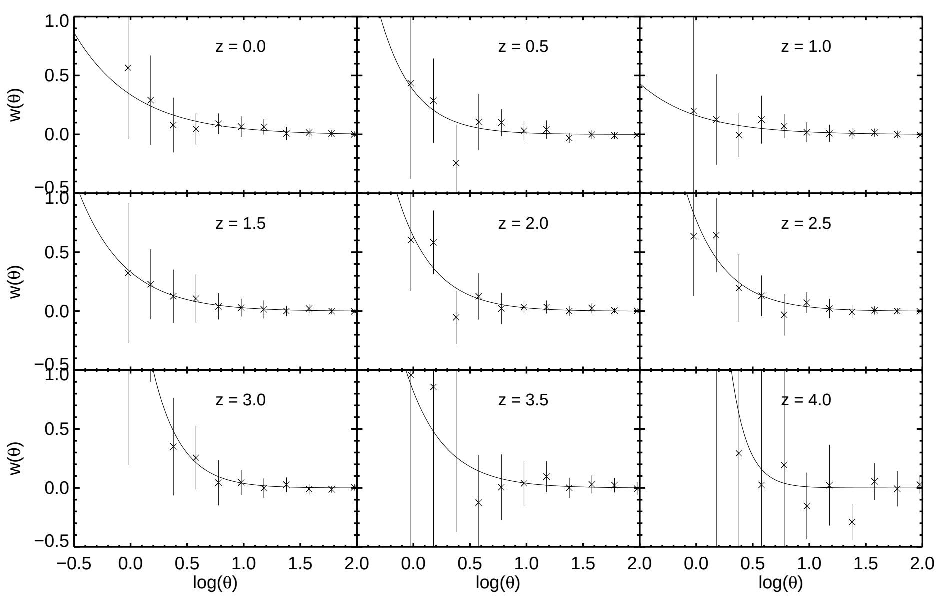

Figure 5.10: Plot of $w(\theta)$ for $S_{350} > 5\sigma$, separated out into $\Delta z = 0.5$ bins using $z_{\rm best}$ for redshift determination and bootstrap errors. See Table 5.10 for fit parameters.

redshift	N	A[arcmin]	δ	$A_{0.8}$	$A_{2.0}$
$0.0 < z < 0.5$	164	3 ± 2	1.7 ± 0.7	0.4 ± 0.5	3 ± 2
$0.5 < z < 1.0$	143	0.0 ± 0.6	3.0 ± 0.9	0.0 ± 0.3	0.0 ± 0.5
$1.0 < z < 1.5$	111	16 ± 20	3.0 ± 1.0	0.0 ± 0.7	0 ± 5
$1.5 < z < 2.0$	288	1.1 ± 1.0	1.2 ± 0.6	0.4 ± 0.4	1.2 ± 1.3
$2.0 < z < 2.5$	928	0.7 ± 1.0	1.0 ± 0.9	0.5 ± 0.4	1.2 ± 1.2
$2.5 < z < 3.0$	1448	1.0 ± 1.1	1.6 ± 0.7	0.2 ± 0.3	1.1 ± 1.1
$3.0 < z < 3.5$	1205	0.0 ± 1.0	3.0 ± 1.0	0.0 ± 0.3	0.0 ± 0.9
$3.5 < z < 4.0$	658	0.0 ± 1.5	3.0 ± 1.5	0.0 ± 0.4	0.0 ± 1.2
$4.0 < z < 4.5$	275	0.0 ± 1.8	3.0 ± 0.7	0.0 ± 0.2	0.0 ± 1.4

Table 5.11: Fit parameters for $S_{500} > 5\sigma$ using bootstrap errors and $z_{\rm best}$. Plots shown in Figure 5.11.

The same pattern of clustering is seen as with the Poisson errors. The 250 μm selection shows a lull in clustering at mid-z. 350 μm is strongly clustered at all redshifts, though clustering seems to get stronger as redshift increases. At 500 μm the error bars are so large that in most cases the fit parameters are not reliable.

As with the Poisson error ACFs when we split the $z < 0.5$ redshift bin into smaller sub-bins we see a much higher clustering signal and the M10 selections (Figure 5.14 and Table 5.14) agreed with the findings of that paper.

redshift	N	A[arcmin]	δ	$A_{0.8}$	$A_{2.0}$
$0.00 < z < 0.50$	23342	0.3 ± 0.3	1.1 ± 1.0	0.2 ± 0.1	0.3 ± 0.3
$0.00 < z < 0.05$	3401	1.5 ± 0.5	0.7 ± 0.2	1.7 ± 0.4	1.9 ± 0.8
$0.05 < z < 0.10$	2066	1.8 ± 0.5	0.8 ± 0.2	1.9 ± 0.3	2.9 ± 0.7
$0.10 < z < 0.15$	2698	1.2 ± 0.4	0.6 ± 0.2	1.5 ± 0.3	2.0 ± 0.6
$0.15 < z < 0.20$	2430	1.1 ± 0.4	0.6 ± 0.2	1.5 ± 0.3	1.9 ± 0.6
$0.20 < z < 0.25$	1840	0.7 ± 0.3	0.6 ± 0.3	0.8 ± 0.3	0.8 ± 0.5
$0.25 < z < 0.30$	2229	0.5 ± 0.3	0.9 ± 0.9	0.4 ± 0.2	0.5 ± 0.4
$0.30 < z < 0.35$	2334	0.7 ± 0.6	0.9 ± 0.7	0.6 ± 0.3	0.9 ± 0.7
$0.35 < z < 0.40$	2340	0.9 ± 0.6	1.3 ± 0.9	0.4 ± 0.2	1.1 ± 0.7
$0.40 < z < 0.45$	2086	0.1 ± 0.5	0.4 ± 1.2	0.3 ± 0.3	0.1 ± 0.6
$0.45 < z < 0.50$	1920	0.4 ± 0.4	1.0 ± 1.1	0.3 ± 0.2	0.4 ± 0.5

Table 5.12: Fit parameters for $S_{250} > 5\sigma$ for low redshifts using bootstrap errors and $z_{\rm best}$. Plots shown in Figure 5.12.

5.4.3 Comparison

The bootstrap errors are larger than the Poisson errors, generating greater uncertainties on the fit parameters. However the resulting fit parameters agree with each other within these uncertainty limits.

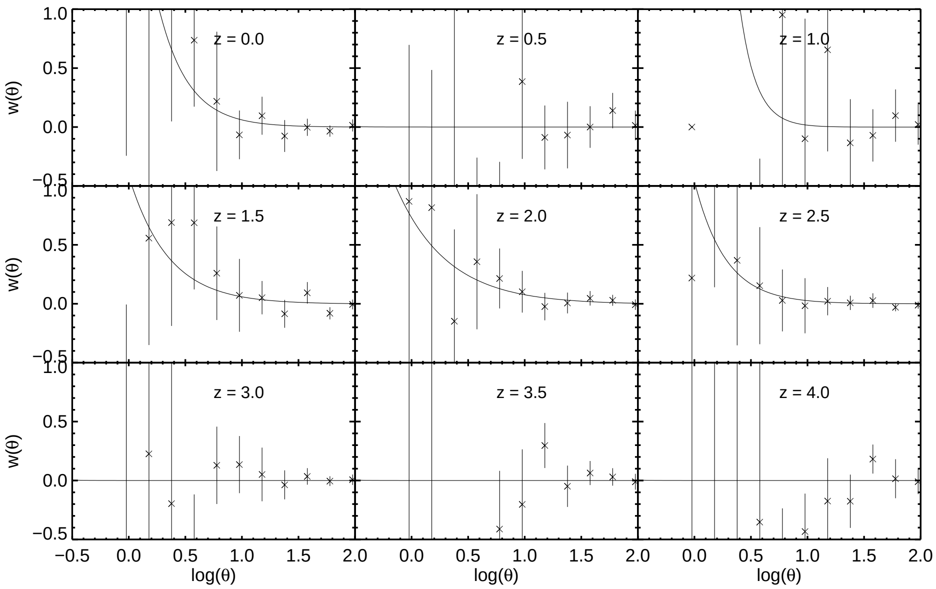

Figure 5.11: Plot of $w(\theta)$ for $S_{500} > 5\sigma$, separated out into $\Delta z = 0.5$ bins using $z_{\rm best}$ for redshift determination and bootstrap errors. See Table 5.11 for fit parameters.

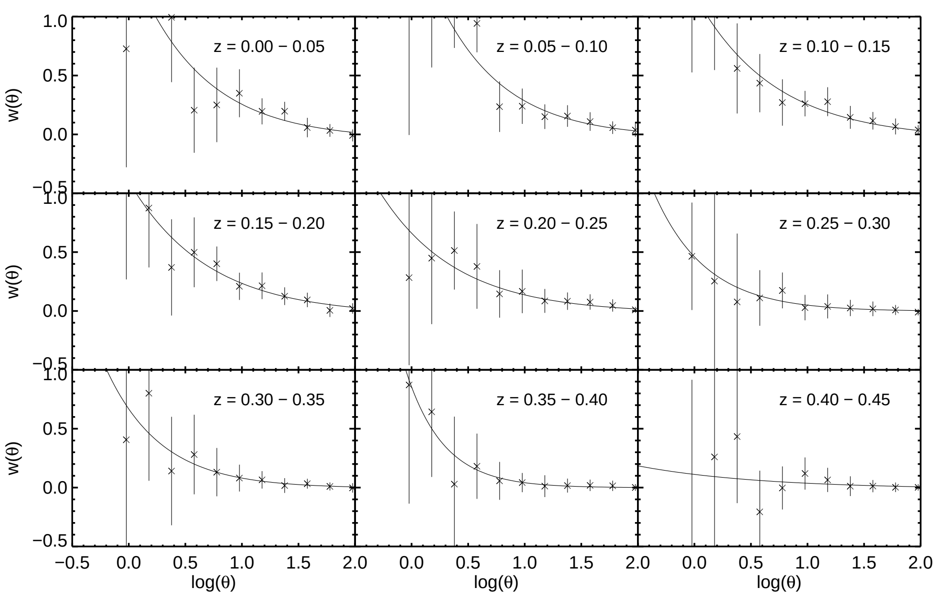

Figure 5.12: Plot of $w(\theta)$ for $S_{250} > 5\sigma$ selection at low-z, separated out into $\Delta z = 0.05$ bins using the best fit values for the redshift bins and bootstrap errors. See Table 5.12 for fit parameters.

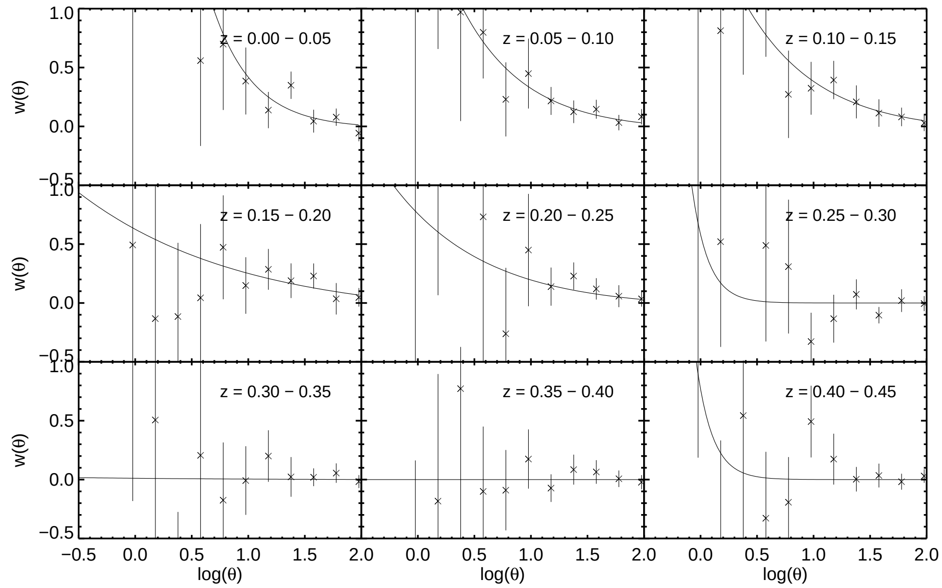

Figure 5.13: Plot of $w(\theta)$ for $S_{350} > 5\sigma$ selection at low-z, separated out into $\Delta z = 0.05$ bins using the best fit values for the redshift bins and bootstrap errors. See Table 5.13 for fit parameters.

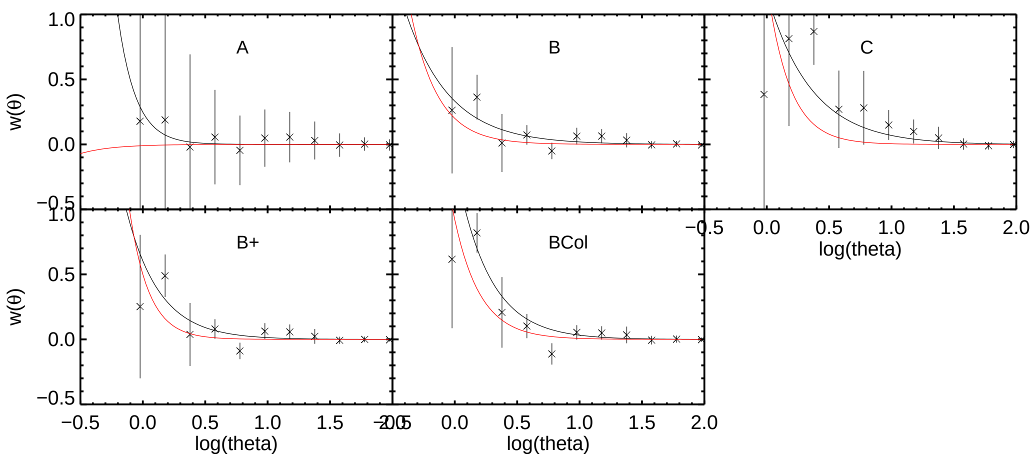

Figure 5.14: Plot of $w(\theta)$ for selections used in M10 using z_{best} and bootstrap errors. The values and fit parameters found using the ACF derived in this work but with M10's cuts are shown in black (see Table 5.14 for fit parameters). The fit parameters from M10 are shown in red

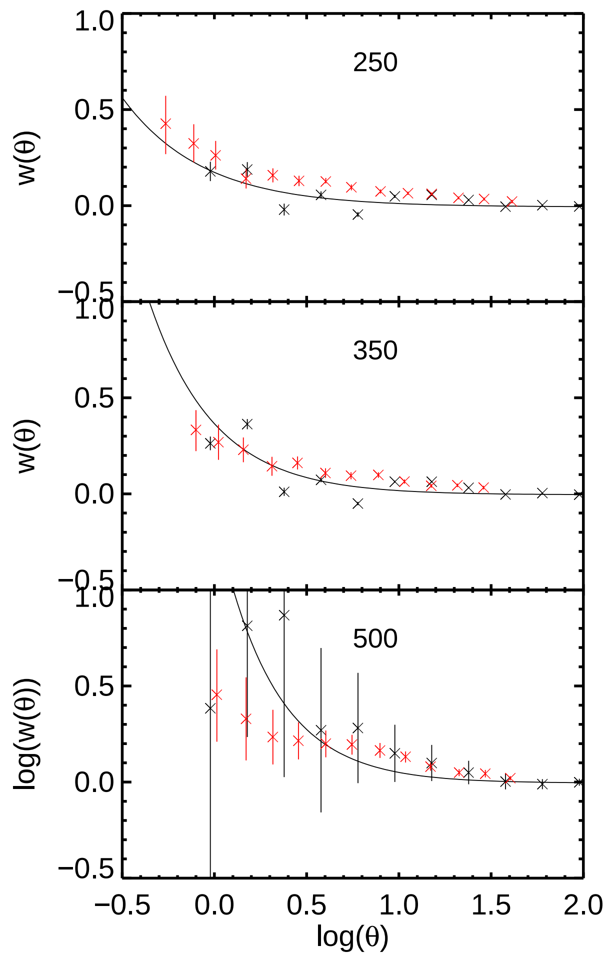

Figure 5.15: $S_{250} > 33$, $S_{350} > 36$ and $S_{500} > 45$ from 5.14 for comparison with Cooray et al. (2010) shown in red. The fit line corresponds to the fit of the data points in Figure 5.14.

redshift	N	A[arcmin]	δ	$A_{0.8}$	$A_{2.0}$
$0.00 < z < 0.50$	5004	0.3 ± 0.3	0.8 ± 0.8	0.3 ± 0.2	0.6 ± 0.4
$0.00 < z < 0.05$	533	7 ± 3	1.2 ± 0.3	2.9 ± 0.7	11 ± 3
$0.05 < z < 0.10$	767	2 ± 1	0.8 ± 0.3	2.2 ± 0.5	5 ± 2
$0.10 < z < 0.15$	692	2.0 ± 0.9	0.7 ± 0.2	2.5 ± 0.6	4 ± 2
$0.15 < z < 0.20$	486	0.7 ± 0.4	0.3 ± 0.9	1.3 ± 0.6	0.5 ± 1.0
$0.20 < z < 0.25$	340	0.8 ± 1.3	0.5 ± 0.8	1.4 ± 0.7	1.7 ± 1.8
$0.25 < z < 0.30$	396	0.6 ± 1.6	3.0 ± 0.4	0.0 ± 0.1	0.0 ± 0.8
$0.30 < z < 0.35$	425	0 ± 2	0.3 ± 1.4	0.0 ± 0.3	0.2 ± 1.1
$0.35 < z < 0.40$	493	0.0 ± 0.2	0.0 ± 1.3	0.0 ± 0.2	0.0 ± 0.2
$0.40 < z < 0.45$	458	0.8 ± 0.6	3 ± 1	0.4 ± 0.4	0.7 ± 0.6
$0.45 < z < 0.50$	414	0.0 ± 0.4	0 ± 1	0.0 ± 0.3	0.0 ± 0.4

Table 5.13: Fit parameters for $S_{350} > 5\sigma$ for low redshifts using bootstrap errors and z_{best}. Plots shown in Figure 5.13.

Table 5.14: As Table 5.2 with cuts applied to all Phase 1 sources using z_{best}. Error bars are from the bootstrap errors on the pair counts. Plots shown in Figure 5.14.

Sample	N	A[arcmin]	δ	$A_{0.8}$	$A_{2.0}$
$S_{250} > 33$	71485	0.2 ± 0.6	3.0 ± 1.0	0.1 ± 0.3	0.2 ± 0.6
$S_{350} > 36$	40636	0.3 ± 0.3	1.2 ± 0.9	0.2 ± 0.1	0.5 ± 0.3
$S_{500} > 45$	7691	1.2 ± 0.6	1.2 ± 0.4	0.6 ± 0.3	1.5 ± 0.7
$S_{350} > 36 + 3\sigma$	21626	0.6 ± 0.3	1.6 ± 0.7	0.3 ± 0.1	0.7 ± 0.3
$S_{500}/S_{250} > 0.75$	11722	1.4 ± 0.3	1.6 ± 0.3	0.6 ± 0.1	1.6 ± 0.3

Sources detected at 250 μm appear to have weaker clustering than those detected at 350 and 500 μm, even when redshift is accounted for. Our valid values of δ mostly fall in the $0.8 < \delta < 2.0$ range, with the exception of those fits where the procedure bottomed out and gave a false fit. This is in agreement with previous works.

In Figure 5.14 the fits found in M10 are compared to the results obtained by applying the same parameters to the data set. The two data sets appear consistent when you take into account the large errors, more accurately predicted by the bootstrap method. Though the fit lines between the two data sets differ consistently, these discrepancies are well within the margin of error. The only large difference between the two is in the A data set, however this is bar far the least well constrained due to the huge number of sources, meaning that there is little redshift constraint on this selection.

When comparing Cooray et al. (2010) with Figure 5.15 it appears that the 250 μm ACF is slightly flatter in their work. This would indicate that Cooray et al. (2010) had a higher amplitude for this data set. However at 350 μm it is the Cooray et al. (2010) values that appears to be flatter and lower in amplitude. At both of these wavelengths the Cooray et al. (2010) ACFs have a higher amplitude over the mid-angular separations in the $log(\theta) = 0.0 - 1.5$ range. In this area the values from this thesis have a significant amount of scatter but the Cooray et al. (2010) values still appear to be higher than even the maximum of this scatter. At short separations the fit line produced for the thesis values are within the error margin of the Cooray et al. (2010) values, though only just. It should be noted that this section of the fit is not very well characterised, as only a few points with larger errors constrain it.

At 500 μm the error bars on the values calculated within this thesis are far too large to make any meaningful comparison, though the Cooray et al. (2010) values do lie within the error margin. the descrepancies between these two data sets, and the difference between Cooray et al. (2010) and the values found in this thesis, arises from the fact that Cooray et al. (2010) did not account for any background cirrus.

5.5 Discussion

Our results found evidence of clustering at most redshifts. Both the 350 and 500 μm selections have an increase in clustering with increasing redshift. At 250 μm the clustering signal increases up to $z < 1.0$ then flattens of significantly, picking up again when $z \gtrsim 2.0$. These redshifts are the peak of the redshift distribution for 250 μm and so these are the redshifts with the greatest number of sources. It is likely that this redshift bin suffers from the same problems of creating a redshift bin to cover $0.0 < z < 0.5$ in that any signal gets washed out by the huge number of sources, all piling on top of each other. It is also likely to be the bin that is worst effected by errors in the redshift as sources are falsely placed into this bin, further dulling any signal.

Clustering appears to become stronger with wavelength and increase with redshifts. This could be as when selecting at 500 μm we are selecting a particular subset of particullarly dusty galaxies, so we are detecting the clustering of this particular subset rather than several galaxy types, as might be the case with 250 μm.

At the highest redshifts both varieties of error bars are so large that any clustering is likely hidden. Between the two error regimes we see little difference in the actual values produced but the errors in the fit parameters varies greatly. The bootstrap method generated much larger error bars than those found using the Poissonian technique. This could indicate that there are large fluctuations in the field, but this is difficult to be certain of as the bootstrap errors were found over only 40% of the region.

5.6 Conclusions

I calculated the total angular correlation function across all three GAMA fields of the H-ATLAS Phase 1 survey. I found that at 250 μm there is a clustering signal at low and high-z but a lull at mid-z. 350 μm and 500 μm are much more strongly clustered than the 250 μm selection. Clustering increases with wavelength and redshift. Without redshift cuts it is difficult to see any sign of clustering at all. The size of the redshift bins could also cause the signal to be washed out by several clusters overlaid on top of each other. Results were marred by large error bars thought this did not appear to have much of an effect on the resulting values, only on their uncertainties.

Chapter 6

Conclusions

Sometimes it seems the universe wants to be noticed.

John Green

6.1 Overview

The aim of this Thesis was to use H-ATLAS to investigate the high redshift sub-mm Universe. Firstly, I selected a sample of forty sources to study in detail before using these to create a method of redshift determination. I then applied this method to the whole the H-ATLAS Phase 1 field. From here I investigated the large scale structure of the universe, looking at the luminosity and clustering properties of these sources with respect their their redshift.

6.2 The Template

To determine the redshift of all sources in the H-ATLAS field I generated a template from a selection of high redshift ($z > 0.5$) sources. The selection consisted of 25 sources with a spectroscopically determined redshift in the range $0.5 < z < 1$ along with another 15 sources with a redshift of $z > 1$ determined by CO observations. In comparison with other H-ATLAS galaxies and samples of high redshift dusty galaxies, these sources appeared to be representative of the survey in terms of their colours and temperatures.

There were however several sources of potential bias with this selection. These sources were chosen to be bright to ensure a high signal to noise ratio but this biased towards exceptionally bright sources. However several of these sources are known to be lensed meaning that they are not intrinsically bright but have simply been magnified. Though most of the foreground lens galaxies are large ellipticals that are relatively free of dust, there is still a chance that there may be some contamination of the sub-mm fluxes of the background source by the lens. Sources chosen for CO follow up were selected as they were either potential lenses, lay at high redshift or were interesting in some other respect. This means that the CO sources may not be typical of the rest of the high redshift sources. There is also an additional bias in that many sources pursued for CO follow up were not observed to have CO lines, so this selection may be biased towards galaxies with high enough temperatures to excite the CO into observable states. Despite these drawbacks the sample seemed representative of the survey as a whole.

Using the SPIRE fluxes for all sources and the PACS fluxes for the 25 optically selected sources (where available) I created a template based on a two temperature SED. To do this I adjusted the fluxes to their rest frame wavelength and fit an SED allowing the dust temperatures and mass ratio to vary, while setting the dust emissivity index to the previously established value of $\beta = 2$ and normalising the fluxes to account for differences in brightness. This led to a template with $T_w = 47$, $T_c = 24$ and $a = 30$.

This was then used to estimate redshifts for all of the sources with SPIRE fluxes. In order to gauge the resulting uncertainty the spectroscopic redshifts of the sample were compared to the redshifts estimated by the template leading to and uncertainty of $\Delta z/(1+z) = 0.03$ with an rms of 0.26. It was apparent that while the template seemed to be effective with high redshift sources, at low redshifts the template was not a valid redshift determination method. To combat this I decided that any source with an optical ID would use the redshift from that optical ID and not from the template. The template was not intended to be used as a method of determining individual redshifts but as a statistical tool as on average the template gives a good representation of the survey.

6.3 Large Scale Universe

As I now had a complete set of sub-mm fluxes and redshifts I performed a basic investigation into the large scale structure of the universe by estimating the luminosity and angular correlation functions of the Phase 1 fields. As every source had a redshift determined for every source in the Phase 1 fields, either through ID matching or from the template, the sample was complete with respect to redshift, and so this did not have to be considered.

The luminosity function (LF) was effected by incompleteness, however, due to the flux cut of the survey. This meant that at as redshift increased, sources needed to be more and more luminous in order to be detected, meaning that only the high luminosity section of the function could be examined. The exception to this was at low redshifts where there was a full enough sample to span the entire luminosity range. Strong evolution of the luminosity function was seen up to $z \sim 2$, after which the LF still evolved but with an increasingly slowed rate up until $z \sim 3$ where it appeared to stop entirely. There was no evidence of negative evolution beyond this point.

The LF was also compared to a simple model created by Steve Eales. This corresponded well up to a redshift of $z \sim 2$ but above this point the two deviated. The mass function used to generate this model had only been tested to this redshift, however, and as this is the point at which the evolution drops off it makes sense that this simple model would disagree.

The angular correlation function (ACF) is a way of parameterising the clustering of the universe. When redshift is not taken into account there is simply too much of space being looked at for clustering to be apparent. Clusters that exist at a certain redshift are hidden by the clusters that exist at all other redshifts. However when I examined the field taking into account my determined redshifts there was clear evidence of clustering. Uncertainties were difficult to consider as simple Poissonian errors determined from number counts were insufficient to describe all sources of uncertainty, so a bootstraping method was used to estimate the error.

A clustering signal was observed for high and low-z sources in the 250 μm waveband but at mid-z this clustering lulled. 350 and 500 μm were strongly clustered but suffered from a low number of sources in many bins, particularly at the highest redshifts. Clustering appeared to increase with wavelength and redshift however as wavelength and redshift increased the number of sources in each bin decreased making errors large and the results uncertain. To really examine the clustering properties in these ranges many more sources are needed.

6.4 Future Work

This work only considered Phase 1 of the full H-ATLAS survey which is approximately a quarter of the whole survey. H-ATLAS has now been completed and the data in the process of being reduced. Once the full survey is available it will be possible to apply the techniques used here to the whole survey area. One of the main problems with investigating the ACF was lack of sources and so with the full survey it will be possible to probe the ACF to higher redshifts.

It would also be possible to add more high redshift sources when creating the template. 15 CO sources were used to create the template as there were no other reliable measurements available. Increasing the fraction of high redshift sources to create a better template would help to pin down the short wavelength end of the template. Several sources have already had CO follow up at the time of writing, with several more targeted for follow up observations.

It may also be possible to improve the fit for low redshift sources by introducing data from surveys at different wavelengths. The intention of this thesis was to create a template based solely on the H-ATLAS observations but by introducing other surveys it might be possible to determine the Rayleigh-Jeans tail and improve the template's viability for low redshift objects.

The luminosity function was shown to have good agreement with a simple model at $z < 2$. By using more complex models which account for the drop off of evolution and other effects it would be possible to test cosomological models more stringently. In this work no attempt was made to relate the angular correlation function to models and simulations of clustering in the universe so by doing this it would be possible to learn more about the structure of the early Universe.

6.5 Concluding remarks

Though Herschel is dead its legacy lives on. The data it produced will be a valuable resource to astronomers investigating the dusty universe for years to come. The method of redshift determination was intended to be used as a statistical tool for more than just the H-ATLAS survey it could be applied to other fields and surveys in order to examine the dusty universe at high redshift that we are still only just beginning to uncover.

Appendix A

Luminosity Functions

This chapter contains the values of the luminosity functions shown in Chapter 4. The Figure to which they correspond is given in the caption.

Table A.1: LF for $0.1 < z < 0.2$ at $250\,\mu$m where $\alpha = 1.35 \pm 0.05$ and $\sigma = 0.15 \pm 0.02$. See Figures 4.2, 4.3, 4.11 and 4.13.

$\log(\phi_{250})$	$\log(L_{250})$	$\log(\phi_{250})$	$\log(L_{250})$
23.825	-3.54 ± 0.48	24.575	-3.18 ± 0.06
23.875	-2.93 ± 0.16	24.625	-3.34 ± 0.07
23.925	-2.71 ± 0.10	24.675	-3.46 ± 0.08
23.975	-2.63 ± 0.07	24.725	-3.60 ± 0.10
24.025	-2.75 ± 0.07	24.775	-3.77 ± 0.12
24.075	-2.73 ± 0.06	24.825	-3.97 ± 0.15
24.125	-2.75 ± 0.05	24.875	-3.99 ± 0.16
24.175	-2.79 ± 0.05	24.925	-4.32 ± 0.23
24.225	-2.78 ± 0.04	24.975	-4.50 ± 0.28
24.275	-2.85 ± 0.04	25.025	-4.54 ± 0.30
24.325	-2.85 ± 0.04	25.075	-4.80 ± 0.42
24.375	-2.87 ± 0.04	25.125	-4.89 ± 0.48
24.425	-2.84 ± 0.04	25.175	-5.02 ± 0.57
24.475	-2.98 ± 0.05	25.225	-5.20 ± 0.77
24.525	-3.13 ± 0.06		

Table A.2: LF for $0.0 < z < 0.1$ at $250\,\mu$m where $\alpha = 1.35 \pm 0.05$ and $\sigma = 0.15 \pm 0.02$. See Figures 4.2, 4.3, 4.11 and 4.13.

$\log(\phi_{250})$	$\log(L_{250})$	$\log(\phi_{250})$	$\log(L_{250})$
22.025	-1.41 ± 0.48	23.525	-2.44 ± 0.10
22.125	-1.56 ± 0.48	23.575	-2.45 ± 0.09
22.175	-1.77 ± 0.57	23.625	-2.49 ± 0.09
22.225	-1.62 ± 0.42	23.675	-2.43 ± 0.08
22.275	-1.91 ± 0.57	23.725	-2.55 ± 0.08
22.325	-1.56 ± 0.32	23.775	-2.50 ± 0.07
22.375	-1.76 ± 0.38	23.825	-2.42 ± 0.06
22.425	-1.77 ± 0.35	23.875	-2.51 ± 0.07
22.475	-2.00 ± 0.42	23.925	-2.53 ± 0.07
22.525	-1.99 ± 0.38	23.975	-2.55 ± 0.07
22.575	-2.24 ± 0.48	24.025	-2.53 ± 0.07
22.625	-2.32 ± 0.48	24.075	-2.62 ± 0.08
22.675	-1.89 ± 0.25	24.125	-2.66 ± 0.08
22.725	-2.08 ± 0.28	24.175	-2.68 ± 0.09
22.775	-2.11 ± 0.27	24.225	-2.78 ± 0.10
22.825	-1.93 ± 0.20	24.275	-2.80 ± 0.10
22.875	-2.16 ± 0.24	24.325	-2.89 ± 0.11
22.925	-2.00 ± 0.18	24.375	-3.08 ± 0.14
22.975	-2.21 ± 0.21	24.425	-3.07 ± 0.14
23.025	-2.12 ± 0.17	24.475	-3.21 ± 0.16
23.075	-2.15 ± 0.16	24.525	-3.32 ± 0.18
23.125	-2.30 ± 0.18	24.575	-3.57 ± 0.25
23.175	-2.47 ± 0.20	24.625	-3.51 ± 0.23
23.225	-2.42 ± 0.17	24.675	-3.91 ± 0.38
23.275	-2.31 ± 0.14	24.725	-3.64 ± 0.27
23.325	-2.33 ± 0.13	24.775	-4.21 ± 0.57
23.375	-2.33 ± 0.12	24.875	-4.38 ± 0.77
23.425	-2.43 ± 0.12	24.975	-4.38 ± 0.77
23.475	-2.53 ± 0.12		

Table A.3: LF for $0.2 < z < 0.3$ at $250\,\mu$m where $\alpha = 1.35 \pm 0.05$ and $\sigma = 0.15 \pm 0.02$. See Figures 4.2, 4.3, 4.11 and 4.13.

$\log(\phi_{250})$	$\log(L_{250})$	$\log(\phi_{250})$	$\log(L_{250})$
24.375	-3.94 ± 0.23	24.975	-4.04 ± 0.10
24.425	-3.41 ± 0.09	25.025	-4.16 ± 0.12
24.475	-3.23 ± 0.06	25.075	-4.33 ± 0.15
24.525	-3.33 ± 0.06	25.125	-4.66 ± 0.21
24.575	-3.29 ± 0.05	25.175	-4.66 ± 0.21
24.625	-3.25 ± 0.04	25.225	-4.61 ± 0.20
24.675	-3.21 ± 0.04	25.275	-5.11 ± 0.38
24.725	-3.19 ± 0.04	25.325	-5.29 ± 0.48
24.775	-3.37 ± 0.05	25.375	-5.29 ± 0.48
24.825	-3.50 ± 0.06	25.425	-5.41 ± 0.57
24.875	-3.68 ± 0.07	25.625	-5.59 ± 0.77
24.925	-3.79 ± 0.08		

Table A.4: LF for $0.3 < z < 0.4$ at $250\,\mu$m where $\alpha = 1.35 \pm 0.05$ and $\sigma = 0.15 \pm 0.02$. See Figures 4.2, 4.3, 4.11 and 4.13.

$\log(\phi_{250})$	$\log(L_{250})$	$\log(\phi_{250})$	$\log(L_{250})$
24.675	-4.10 ± 0.15	25.175	-4.04 ± 0.08
24.725	-3.67 ± 0.07	25.225	-4.33 ± 0.11
24.775	-3.51 ± 0.05	25.275	-4.49 ± 0.13
24.825	-3.42 ± 0.04	25.325	-4.72 ± 0.17
24.875	-3.33 ± 0.03	25.375	-4.78 ± 0.18
24.925	-3.33 ± 0.03	25.425	-4.96 ± 0.23
24.975	-3.43 ± 0.04	25.475	-5.24 ± 0.32
25.025	-3.60 ± 0.05	25.525	-5.36 ± 0.38
25.075	-3.75 ± 0.06	25.725	-5.66 ± 0.57
25.125	-3.95 ± 0.07		

Table A.5: LF for $0.4 < z < 0.5$ at $250\,\mu$m where $\alpha = 1.35 \pm 0.05$ and $\sigma = 0.15 \pm 0.02$. See Figures 4.2, 4.3, 4.11 and 4.13.

$\log(\phi_{250})$	$\log(L_{250})$	$\log(\phi_{250})$	$\log(L_{250})$
24.875	-4.63 ± 0.19	25.375	-4.41 ± 0.10
24.925	-4.04 ± 0.07	25.425	-4.66 ± 0.13
24.975	-3.73 ± 0.04	25.475	-4.79 ± 0.15
25.025	-3.57 ± 0.04	25.525	-5.03 ± 0.20
25.075	-3.49 ± 0.03	25.575	-5.01 ± 0.20
25.125	-3.64 ± 0.04	25.625	-5.20 ± 0.25
25.175	-3.78 ± 0.05	25.675	-5.83 ± 0.57
25.225	-3.97 ± 0.06	25.725	-5.61 ± 0.42
25.275	-4.05 ± 0.06	25.775	-5.83 ± 0.57
25.325	-4.30 ± 0.09	25.875	-6.01 ± 0.77

Table A.6: LF for $1.2 < z < 1.6$ at $100\,\mu$m where $\alpha = 1.69 \pm 0.8$ and $\sigma = 0.183 \pm 0.006$. See Figures 4.6 and 4.7.

$\log(\phi_{100})$	$\log(L_{100})$	$\log(\phi_{100})$	$\log(L_{100})$
26.125	-6.42 ± 0.27	26.575	-4.77 ± 0.04
26.175	-5.31 ± 0.07	26.625	-4.97 ± 0.05
26.225	-4.71 ± 0.04	26.675	-5.15 ± 0.06
26.275	-4.49 ± 0.03	26.725	-5.42 ± 0.08
26.325	-4.35 ± 0.02	26.775	-5.63 ± 0.11
26.375	-4.26 ± 0.02	26.825	-5.95 ± 0.15
26.425	-4.34 ± 0.02	26.875	-6.10 ± 0.18
26.475	-4.46 ± 0.03	26.925	-6.42 ± 0.27
26.525	-4.62 ± 0.03	26.975	-6.86 ± 0.48

Table A.7: LF for $1.6 < z < 2.0$ at $100\,\mu$m where $\alpha = 1.69 \pm 0.8$ and $\sigma = 0.183 \pm 0.006$. See Figures 4.6 and 4.7.

$\log(\phi_{100})$	$\log(L_{100})$	$\log(\phi_{100})$	$\log(L_{100})$
26.375	-5.57 ± 0.09	26.825	-5.10 ± 0.05
26.425	-4.87 ± 0.04	26.875	-5.33 ± 0.07
26.475	-4.53 ± 0.03	26.925	-5.57 ± 0.09
26.525	-4.40 ± 0.02	26.975	-5.90 ± 0.14
26.575	-4.36 ± 0.02	27.025	-6.26 ± 0.21
26.625	-4.41 ± 0.02	27.075	-6.67 ± 0.35
26.675	-4.55 ± 0.03	27.125	-7.04 ± 0.57
26.725	-4.74 ± 0.04	27.175	-7.04 ± 0.57
26.775	-4.90 ± 0.04		

Table A.8: LF for $2.0 < z < 2.4$ at $100\,\mu$m where $\alpha = 1.69 \pm 0.8$ and $\sigma = 0.183 \pm 0.006$. See Figures 4.6 and 4.7.

$\log(\phi_{100})$	$\log(L_{100})$	$\log(\phi_{100})$	$\log(L_{100})$
26.525	-7.06 ± 0.57	26.925	-5.06 ± 0.05
26.575	-5.53 ± 0.09	26.975	-5.28 ± 0.06
26.625	-4.88 ± 0.04	27.025	-5.65 ± 0.10
26.675	-4.61 ± 0.03	27.075	-5.75 ± 0.11
26.725	-4.52 ± 0.03	27.125	-6.05 ± 0.16
26.775	-4.54 ± 0.03	27.175	-6.33 ± 0.22
26.825	-4.68 ± 0.03	27.225	-7.06 ± 0.57
26.875	-4.85 ± 0.04	27.425	-7.24 ± 0.77

Table A.9: LF for $2.4 < z < 4.0$ at $100\,\mu$m where $\alpha = 1.69 \pm 0.8$ and $\sigma = 0.183 \pm 0.006$. See Figures 4.6 and 4.7.

$\log(\phi_{100})$	$\log(L_{100})$	$\log(\phi_{100})$	$\log(L_{100})$
26.725	-6.72 ± 0.17	27.175	-5.84 ± 0.06
26.775	-5.77 ± 0.06	27.225	-5.99 ± 0.07
26.825	-5.45 ± 0.04	27.275	-6.23 ± 0.10
26.875	-5.34 ± 0.03	27.325	-6.50 ± 0.13
26.925	-5.33 ± 0.03	27.375	-6.85 ± 0.20
26.975	-5.33 ± 0.03	27.425	-7.09 ± 0.27
27.025	-5.42 ± 0.04	27.475	-7.35 ± 0.38
27.075	-5.53 ± 0.04	27.625	-7.83 ± 0.77
27.125	-5.69 ± 0.05		

Table A.10: LF for $0.0 < z < 0.4$ at $90\,\mu$m where $\alpha = 1.51 \pm 0.02$ and $\sigma = 0.085 \pm 0.02$. See Figure 4.8 and 4.9.

$\log(\phi_{90})$	$\log(L_{90})$	$\log(\phi_{90})$	$\log(L_{90})$
24.025	-2.69 ± 0.05	25.025	-3.52 ± 0.03
24.075	-2.93 ± 0.06	25.075	-3.50 ± 0.03
24.125	-3.03 ± 0.07	25.125	-3.48 ± 0.03
24.175	-3.00 ± 0.06	25.175	-3.51 ± 0.03
24.225	-3.01 ± 0.05	25.225	-3.63 ± 0.04
24.275	-3.06 ± 0.05	25.275	-3.80 ± 0.04
24.325	-3.10 ± 0.05	25.325	-3.95 ± 0.05
24.375	-3.14 ± 0.05	25.375	-4.16 ± 0.07
24.425	-3.18 ± 0.04	25.425	-4.24 ± 0.07
24.475	-3.20 ± 0.04	25.475	-4.49 ± 0.10
24.525	-3.26 ± 0.04	25.525	-4.68 ± 0.12
24.575	-3.32 ± 0.04	25.575	-4.94 ± 0.16
24.625	-3.43 ± 0.04	25.625	-4.97 ± 0.17
24.675	-3.43 ± 0.04	25.675	-5.15 ± 0.21
24.725	-3.53 ± 0.04	25.725	-5.45 ± 0.30
24.775	-3.66 ± 0.04	25.775	-5.56 ± 0.35
24.825	-3.64 ± 0.04	25.825	-6.10 ± 0.77
24.875	-3.63 ± 0.04	25.875	-6.10 ± 0.77
24.925	-3.60 ± 0.03	25.925	-6.10 ± 0.77
24.975	-3.52 ± 0.03	25.975	-5.92 ± 0.57

Table A.11: LF for $0.4 < z < 0.8$ at $90\,\mu$m where $\alpha = 1.51 \pm 0.02$ and $\sigma = 0.085 \pm 0.02$. See Figure 4.8 and 4.9.

$\log(\phi_{90})$	$\log(L_{90})$	$\log(\phi_{90})$	$\log(L_{90})$
25.375	-5.84 ± 0.21	26.025	-4.47 ± 0.04
25.425	-4.95 ± 0.07	26.075	-4.61 ± 0.05
25.475	-4.50 ± 0.04	26.125	-4.74 ± 0.06
25.525	-4.32 ± 0.04	26.175	-5.05 ± 0.08
25.575	-4.20 ± 0.03	26.225	-5.11 ± 0.09
25.625	-4.16 ± 0.03	26.275	-5.34 ± 0.12
25.675	-4.12 ± 0.03	26.325	-5.63 ± 0.16
25.725	-4.09 ± 0.03	26.375	-5.71 ± 0.18
25.775	-4.05 ± 0.03	26.425	-6.05 ± 0.27
25.825	-4.04 ± 0.03	26.475	-6.19 ± 0.32
25.875	-4.06 ± 0.03	26.525	-6.79 ± 0.77
25.925	-4.18 ± 0.03	26.675	-6.79 ± 0.77
25.975	-4.32 ± 0.04		

Table A.12: LF for $0.8 < z < 1.2$ at $90\,\mu$m where $\alpha = 1.51 \pm 0.02$ and $\sigma = 0.085 \pm 0.02$. See Figure 4.8 and 4.9.

$\log(\phi_{90})$	$\log(L_{90})$	$\log(\phi_{90})$	$\log(L_{90})$
25.825	-7.05 ± 0.77	26.375	-4.87 ± 0.05
25.875	-5.63 ± 0.12	26.425	-4.99 ± 0.06
25.925	-4.94 ± 0.05	26.475	-5.23 ± 0.08
25.975	-4.62 ± 0.04	26.525	-5.47 ± 0.10
26.025	-4.51 ± 0.03	26.575	-5.67 ± 0.13
26.075	-4.40 ± 0.03	26.625	-5.92 ± 0.17
26.125	-4.32 ± 0.03	26.675	-6.05 ± 0.20
26.175	-4.30 ± 0.03	26.725	-6.50 ± 0.35
26.225	-4.40 ± 0.03	26.775	-6.75 ± 0.48
26.275	-4.56 ± 0.04	26.825	-6.87 ± 0.57
26.325	-4.68 ± 0.04	26.875	-7.05 ± 0.77

Table A.13: LF for $1.2 < z < 1.8$ at $90\,\mu$m where $\alpha = 1.51 \pm 0.02$ and $\sigma = 0.085 \pm 0.02$. See Figure 4.8 and 4.9.

$\log(\phi_{90})$	$\log(L_{90})$	$\log(\phi_{90})$	$\log(L_{90})$
26.125	-6.45 ± 0.22	26.675	-4.92 ± 0.04
26.175	-5.46 ± 0.07	26.725	-5.18 ± 0.05
26.225	-4.88 ± 0.04	26.775	-5.32 ± 0.06
26.275	-4.67 ± 0.03	26.825	-5.58 ± 0.08
26.325	-4.53 ± 0.02	26.875	-5.84 ± 0.11
26.375	-4.42 ± 0.02	26.925	-6.14 ± 0.15
26.425	-4.40 ± 0.02	26.975	-6.35 ± 0.20
26.475	-4.38 ± 0.02	27.025	-7.05 ± 0.48
26.525	-4.47 ± 0.02	27.075	-7.18 ± 0.57
26.575	-4.61 ± 0.03	27.125	-7.35 ± 0.77
26.625	-4.75 ± 0.03		

Table A.14: LF for $1.8 < z < 2.5$ at $90\,\mu$m where $\alpha = 1.51 \pm 0.02$ and $\sigma = 0.085 \pm 0.02$. See Figure 4.8 and 4.9.

$\log(\phi_{90})$	$\log(L_{90})$	$\log(\phi_{90})$	$\log(L_{90})$
26.475	-5.86 ± 0.10	26.925	-5.11 ± 0.04
26.525	-5.09 ± 0.04	26.975	-5.34 ± 0.05
26.575	-4.81 ± 0.03	27.025	-5.62 ± 0.07
26.625	-4.68 ± 0.02	27.075	-5.85 ± 0.09
26.675	-4.63 ± 0.02	27.125	-6.16 ± 0.14
26.725	-4.61 ± 0.02	27.175	-6.40 ± 0.18
26.775	-4.62 ± 0.02	27.225	-7.00 ± 0.38
26.825	-4.73 ± 0.03	27.425	-7.48 ± 0.77
26.875	-4.89 ± 0.03	27.575	-7.48 ± 0.77

Table A.15: LF for $2.5 < z < 3.5$ at $90\,\mu$m where $\alpha = 1.51 \pm 0.02$ and $\sigma = 0.085 \pm 0.02$. See Figure 4.8 and 4.9.

$\log(\phi_{90})$	$\log(L_{90})$	$\log(\phi_{90})$	$\log(L_{90})$
26.775	-6.17 ± 0.11	27.175	-5.76 ± 0.07
26.825	-5.52 ± 0.05	27.225	-5.95 ± 0.09
26.875	-5.27 ± 0.04	27.275	-6.39 ± 0.15
26.925	-5.22 ± 0.04	27.325	-6.61 ± 0.19
26.975	-5.18 ± 0.04	27.375	-6.82 ± 0.25
27.025	-5.27 ± 0.04	27.425	-7.23 ± 0.42
27.075	-5.36 ± 0.05	27.625	-7.63 ± 0.77
27.125	-5.53 ± 0.05		

Table A.16: LF for $3.5 < z < 4.5$ at $90\,\mu$m where $\alpha = 1.51 \pm 0.02$ and $\sigma = 0.085 \pm 0.02$. See Figure 4.8 and 4.9.

$\log(\phi_{90})$	$\log(L_{90})$	$\log(\phi_{90})$	$\log(L_{90})$
27.125	-7.20 ± 0.42	27.375	-6.90 ± 0.28
27.175	-6.29 ± 0.14	27.425	-6.90 ± 0.28
27.225	-6.26 ± 0.13	27.475	-6.90 ± 0.28
27.275	-6.25 ± 0.13	27.525	-7.42 ± 0.57
27.325	-6.44 ± 0.16		

Table A.17: LF for $0.5 < z < 0.7$ at $250\,\mu$m where $\alpha = 1.35 \pm 0.05$ and $\sigma = 0.15 \pm 0.02$. See Figures 4.11 and 4.13.

$\log(\phi_{250})$	$\log(L_{250})$	$\log(\phi_{250})$	$\log(L_{250})$
24.975	-4.78 ± 0.30	25.475	-4.53 ± 0.06
25.025	-4.20 ± 0.09	25.525	-4.72 ± 0.08
25.075	-3.91 ± 0.05	25.575	-4.87 ± 0.10
25.125	-3.87 ± 0.04	25.625	-5.15 ± 0.13
25.175	-3.89 ± 0.03	25.675	-5.33 ± 0.16
25.225	-3.86 ± 0.03	25.725	-5.47 ± 0.19
25.275	-3.92 ± 0.03	25.775	-5.59 ± 0.22
25.325	-4.07 ± 0.04	25.825	-5.89 ± 0.32
25.375	-4.22 ± 0.04	25.875	-6.19 ± 0.48
25.425	-4.35 ± 0.05		±

Table A.18: LF for $0.7 < z < 0.9$ at $250\,\mu$m where $\alpha = 1.35 \pm 0.05$ and $\sigma = 0.15 \pm 0.02$. See Figures 4.11 and 4.13.

$\log(\phi_{250})$	$\log(L_{250})$	$\log(\phi_{250})$	$\log(L_{250})$
25.225	-4.70 ± 0.13	25.725	-4.95 ± 0.09
25.275	-4.26 ± 0.05	25.775	-5.20 ± 0.12
25.325	-4.13 ± 0.04	25.825	-5.34 ± 0.14
25.375	-4.13 ± 0.03	25.875	-5.65 ± 0.20
25.425	-4.10 ± 0.03	25.925	-5.95 ± 0.28
25.475	-4.22 ± 0.04	25.975	-5.87 ± 0.26
25.525	-4.35 ± 0.04	26.025	-6.17 ± 0.38
25.575	-4.44 ± 0.05	26.075	-6.35 ± 0.48
25.625	-4.64 ± 0.06	26.125	-6.35 ± 0.48
25.675	-4.76 ± 0.07	26.175	-6.65 ± 0.77

Table A.19: LF for $0.9 < z < 1.1$ at $250\,\mu$m where $\alpha = 1.35 \pm 0.05$ and $\sigma = 0.15 \pm 0.02$. See Figures 4.11 and 4.13.

$\log(\phi_{250})$	$\log(L_{250})$	$\log(\phi_{250})$	$\log(L_{250})$
25.375	-5.62 ± 0.42	25.825	-4.90 ± 0.07
25.425	-4.76 ± 0.09	25.875	-5.03 ± 0.08
25.475	-4.45 ± 0.05	25.925	-5.27 ± 0.11
25.525	-4.26 ± 0.03	25.975	-5.57 ± 0.16
25.575	-4.21 ± 0.03	26.025	-5.67 ± 0.18
25.625	-4.30 ± 0.04	26.075	-6.01 ± 0.27
25.675	-4.43 ± 0.04	26.125	-6.15 ± 0.32
25.725	-4.62 ± 0.05	26.175	-6.75 ± 0.77
25.775	-4.75 ± 0.06	26.225	-6.75 ± 0.77

Table A.20: LF for $1.1 < z < 1.3$ at $250\,\mu$m where $\alpha = 1.35 \pm 0.05$ and $\sigma = 0.15 \pm 0.02$. See Figures 4.11 and 4.13.

$\log(\phi_{250})$	$\log(L_{250})$	$\log(\phi_{250})$	$\log(L_{250})$
25.525	-5.29 ± 0.20	25.975	-5.02 ± 0.08
25.575	-4.69 ± 0.06	26.025	-5.24 ± 0.10
25.625	-4.35 ± 0.04	26.075	-5.39 ± 0.12
25.675	-4.18 ± 0.03	26.125	-5.64 ± 0.16
25.725	-4.24 ± 0.03	26.175	-6.12 ± 0.28
25.775	-4.34 ± 0.04	26.225	-6.27 ± 0.35
25.825	-4.48 ± 0.04	26.275	-6.64 ± 0.57
25.875	-4.64 ± 0.05	26.325	-6.42 ± 0.42
25.925	-4.81 ± 0.06		±

Table A.21: LF for $1.3 < z < 1.5$ at $250\,\mu$m where $\alpha = 1.35 \pm 0.05$ and $\sigma = 0.15 \pm 0.02$. See Figures 4.11 and 4.13.

$\log(\phi_{250})$	$\log(L_{250})$	$\log(\phi_{250})$	$\log(L_{250})$
25.625	-5.85 ± 0.57	26.025	-4.77 ± 0.06
25.675	-4.94 ± 0.09	26.075	-4.96 ± 0.07
25.725	-4.48 ± 0.04	26.125	-5.22 ± 0.09
25.775	-4.22 ± 0.03	26.175	-5.42 ± 0.12
25.825	-4.19 ± 0.03	26.225	-5.67 ± 0.16
25.875	-4.33 ± 0.03	26.275	-5.99 ± 0.23
25.925	-4.46 ± 0.04	26.325	-6.21 ± 0.30
25.975	-4.68 ± 0.05	26.375	-6.26 ± 0.32

Table A.22: LF for $1.5 < z < 2.0$ at $250\,\mu$m where $\alpha = 1.35 \pm 0.05$ and $\sigma = 0.15 \pm 0.02$. See Figures 4.11 and 4.13.

$\log(\phi_{250})$	$\log(L_{250})$	$\log(\phi_{250})$	$\log(L_{250})$
25.775	-5.08 ± 0.11	26.225	-4.94 ± 0.04
25.825	-4.59 ± 0.04	26.275	-5.13 ± 0.05
25.875	-4.42 ± 0.03	26.325	-5.36 ± 0.07
25.925	-4.38 ± 0.02	26.375	-5.62 ± 0.09
25.975	-4.39 ± 0.02	26.425	-5.94 ± 0.13
26.025	-4.39 ± 0.02	26.475	-6.26 ± 0.19
26.075	-4.45 ± 0.02	26.525	-6.76 ± 0.35
26.125	-4.58 ± 0.03	26.575	-6.91 ± 0.42
26.175	-4.78 ± 0.03	26.625	-7.13 ± 0.57

Table A.23: LF for $2.0 < z < 2.5$ at $250\,\mu$m where $\alpha = 1.35 \pm 0.05$ and $\sigma = 0.15 \pm 0.02$. See Figures 4.11 and 4.13.

$\log(\phi_{250})$	$\log(L_{250})$	$\log(\phi_{250})$	$\log(L_{250})$
26.025	-5.14 ± 0.09	26.425	-5.19 ± 0.05
26.075	-4.72 ± 0.04	26.475	-5.49 ± 0.07
26.125	-4.59 ± 0.03	26.525	-5.70 ± 0.09
26.175	-4.59 ± 0.03	26.575	-5.96 ± 0.13
26.225	-4.57 ± 0.03	26.625	-6.31 ± 0.19
26.275	-4.64 ± 0.03	26.675	-6.68 ± 0.30
26.325	-4.78 ± 0.03	26.875	-7.33 ± 0.77
26.375	-5.02 ± 0.04		±

Table A.24: LF for $2.5 < z < 3.0$ at $250\,\mu$m where $\alpha = 1.35 \pm 0.05$ and $\sigma = 0.15 \pm 0.02$. See Figures 4.11 and 4.13.

$\log(\phi_{250})$	$\log(L_{250})$	$\log(\phi_{250})$	$\log(L_{250})$
26.225	-5.44 ± 0.13	26.575	-5.57 ± 0.08
26.275	-5.04 ± 0.06	26.625	-5.86 ± 0.11
26.325	-4.93 ± 0.04	26.675	-6.13 ± 0.16
26.375	-4.91 ± 0.04	26.725	-6.56 ± 0.26
26.425	-4.92 ± 0.04	26.775	-6.56 ± 0.26
26.475	-5.10 ± 0.05	26.825	-6.94 ± 0.42
26.525	-5.28 ± 0.06	26.875	-7.03 ± 0.48

Table A.25: LF for $3.0 < z < 3.5$ at $250\,\mu$m where $\alpha = 1.35 \pm 0.05$ and $\sigma = 0.15 \pm 0.02$. See Figures 4.11 and 4.13.

$\log(\phi_{250})$	$\log(L_{250})$	$\log(\phi_{250})$	$\log(L_{250})$
26.425	-5.66 ± 0.14	26.675	-5.80 ± 0.11
26.475	-5.38 ± 0.08	26.725	-6.15 ± 0.16
26.525	-5.39 ± 0.07	26.775	-6.58 ± 0.27
26.575	-5.43 ± 0.07	26.825	-6.72 ± 0.32
26.625	-5.63 ± 0.09	26.875	-7.15 ± 0.57

Table A.26: LF for $3.5 < z < 4.0$ at $250\,\mu$m where $\alpha = 1.35 \pm 0.05$ and $\sigma = 0.15 \pm 0.02$. See Figures 4.11 and 4.13.

$\log(\phi_{250})$	$\log(L_{250})$	$\log(\phi_{250})$	$\log(L_{250})$
26.575	-6.70 ± 0.57	26.775	-6.21 ± 0.18
26.625	-5.89 ± 0.15	26.825	-6.83 ± 0.38
26.675	-5.94 ± 0.13	26.875	-6.91 ± 0.42
26.725	-5.98 ± 0.14	26.925	-6.83 ± 0.38

Table A.27: LF for $4.0 < z < 4.5$ at $250\,\mu$m where $\alpha = 1.35 \pm 0.05$ and $\sigma = 0.15 \pm 0.02$. See Figures 4.11 and 4.13.

$\log(\phi_{250})$	$\log(L_{250})$	$\log(\phi_{250})$	$\log(L_{250})$
26.725	-6.80 ± 0.77	26.875	-6.89 ± 0.42
26.775	-6.40 ± 0.28	26.925	-6.98 ± 0.48
26.825	-6.85 ± 0.42	26.975	-7.29 ± 0.77

Table A.28: LF for $0.0 < z < 0.1$ at $350\,\mu$m where $\alpha = 1.37 \pm 0.09$ and $\sigma = 0.22 \pm 0.1$. See Figures 4.12 and 4.14.

$\log(\phi_{350})$	$\log(L_{350})$	$\log(\phi_{350})$	$\log(L_{250})$
23.025	-2.21 ± 0.19	23.775	-2.76 ± 0.10
23.075	-2.85 ± 0.38	23.825	-2.86 ± 0.11
23.125	-2.50 ± 0.22	23.875	-2.77 ± 0.10
23.175	-2.56 ± 0.21	23.925	-2.85 ± 0.11
23.225	-2.52 ± 0.19	23.975	-2.94 ± 0.12
23.275	-2.74 ± 0.22	24.025	-2.96 ± 0.12
23.325	-2.77 ± 0.21	24.075	-3.04 ± 0.13
23.375	-2.66 ± 0.17	24.125	-3.21 ± 0.16
23.425	-2.64 ± 0.15	24.175	-3.25 ± 0.17
23.475	-2.69 ± 0.14	24.225	-3.68 ± 0.28
23.525	-2.81 ± 0.15	24.275	-3.61 ± 0.26
23.575	-2.93 ± 0.16	24.325	-3.61 ± 0.26
23.625	-2.89 ± 0.14	24.375	-4.21 ± 0.57
23.675	-2.82 ± 0.11	24.425	-4.08 ± 0.48
23.725	-2.76 ± 0.10	24.475	-4.38 ± 0.77

Table A.29: LF for $0.1 < z < 0.2$ at $350\,\mu$m where $\alpha = 1.37 \pm 0.09$ and $\sigma = 0.22 \pm 0.1$. See Figures 4.12 and 4.14.

log(ϕ_{350})	log(L$_{350}$)	log(ϕ_{350})	log(L$_{250}$)
23.875	-4.05 ± 0.57	24.375	-3.46 ± 0.08
23.925	-3.46 ± 0.21	24.425	-3.56 ± 0.09
23.975	-3.32 ± 0.15	24.475	-3.68 ± 0.11
24.025	-3.31 ± 0.13	24.525	-3.87 ± 0.14
24.075	-3.22 ± 0.10	24.575	-4.17 ± 0.19
24.125	-3.29 ± 0.09	24.625	-4.46 ± 0.27
24.175	-3.46 ± 0.10	24.675	-4.59 ± 0.32
24.225	-3.52 ± 0.10	24.725	-5.02 ± 0.57
24.275	-3.48 ± 0.09	24.775	-5.02 ± 0.57
24.325	-3.43 ± 0.08	24.825	-4.89 ± 0.48

Table A.30: LF for $0.2 < z < 0.3$ at $350\,\mu$m where $\alpha = 1.37 \pm 0.09$ and $\sigma = 0.22 \pm 0.1$. See Figures 4.12 and 4.14.

log(ϕ_{350})	log(L$_{350}$)	log(ϕ_{350})	log(L$_{250}$)
24.425	-4.41 ± 0.23	24.825	-4.55 ± 0.19
24.475	-4.09 ± 0.13	24.875	-4.55 ± 0.19
24.525	-4.10 ± 0.11	24.925	-4.94 ± 0.30
24.575	-4.02 ± 0.10	24.975	-5.11 ± 0.38
24.625	-3.94 ± 0.09	25.025	-5.29 ± 0.48
24.675	-3.87 ± 0.09	25.075	-5.41 ± 0.57
24.725	-4.00 ± 0.10	25.175	-5.41 ± 0.57
24.775	-4.23 ± 0.13	25.225	-5.41 ± 0.57

Table A.31: LF for $0.3 < z < 0.4$ at $350\,\mu$m where $\alpha = 1.37 \pm 0.09$ and $\sigma = 0.22 \pm 0.1$. See Figures 4.12 and 4.14.

log(ϕ_{350})	log(L$_{350}$)	log(ϕ_{350})	log(L$_{250}$)
24.675	-5.11 ± 0.32	24.975	-4.39 ± 0.12
24.725	-4.44 ± 0.12	25.025	-4.59 ± 0.15
24.775	-4.12 ± 0.09	25.075	-4.69 ± 0.17
24.825	-4.00 ± 0.07	25.125	-4.80 ± 0.19
24.875	-3.84 ± 0.06	25.275	-5.66 ± 0.57
24.925	-4.19 ± 0.09	25.325	-5.66 ± 0.57

Table A.32: LF for $0.4 < z < 0.5$ at $350\,\mu$m where $\alpha = 1.37 \pm 0.09$ and $\sigma = 0.22 \pm 0.1$. See Figures 4.12 and 4.14.

$\log(\phi_{350})$	$\log(L_{350})$	$\log(\phi_{350})$	$\log(L_{250})$
24.875	-4.93 ± 0.18	25.175	-4.70 ± 0.14
24.925	-4.30 ± 0.09	25.225	-4.99 ± 0.19
24.975	-4.16 ± 0.07	25.275	-5.14 ± 0.23
25.025	-4.12 ± 0.07	25.325	-5.41 ± 0.32
25.075	-4.34 ± 0.09	25.375	-5.53 ± 0.38
25.125	-4.48 ± 0.11	25.425	-5.53 ± 0.38

Table A.33: LF for $0.5 < z < 0.7$ at $350\,\mu$m where $\alpha = 1.37 \pm 0.09$ and $\sigma = 0.22 \pm 0.1$. See Figures 4.12 and 4.14.

$\log(\phi_{350})$	$\log(L_{350})$	$\log(\phi_{350})$	$\log(L_{250})$
24.975	-5.54 ± 0.26	25.325	-5.03 ± 0.11
25.025	-4.84 ± 0.09	25.375	-5.41 ± 0.18
25.075	-4.59 ± 0.07	25.425	-5.47 ± 0.19
25.125	-4.48 ± 0.06	25.475	-5.75 ± 0.27
25.175	-4.47 ± 0.06	25.525	-6.09 ± 0.42
25.225	-4.63 ± 0.07	25.575	-6.19 ± 0.48
25.275	-4.82 ± 0.09		

Table A.34: LF for $0.7 < z < 0.9$ at $350\,\mu$m where $\alpha = 1.37 \pm 0.09$ and $\sigma = 0.22 \pm 0.1$. See Figures 4.12 and 4.14.

$\log(\phi_{350})$	$\log(L_{350})$	$\log(\phi_{350})$	$\log(L_{250})$
25.125	-6.35 ± 0.57	25.475	-5.43 ± 0.15
25.175	-5.25 ± 0.12	25.525	-5.69 ± 0.21
25.225	-4.77 ± 0.07	25.575	-6.05 ± 0.32
25.275	-4.65 ± 0.06	25.625	-5.95 ± 0.28
25.325	-4.72 ± 0.07	25.675	-6.10 ± 0.35
25.375	-4.98 ± 0.09	25.725	-6.47 ± 0.57
25.425	-5.13 ± 0.11		

Table A.35: LF for $0.9 < z < 1.1$ at $350\,\mu$m where $\alpha = 1.37 \pm 0.09$ and $\sigma = 0.22 \pm 0.1$. See Figures 4.12 and 4.14.

$\log(\phi_{350})$	$\log(L_{350})$	$\log(\phi_{350})$	$\log(L_{250})$
25.275	-6.75 ± 0.77	25.575	-5.36 ± 0.12
25.325	-5.08 ± 0.09	25.625	-5.69 ± 0.18
25.375	-4.73 ± 0.06	25.675	-5.94 ± 0.25
25.425	-4.75 ± 0.06	25.725	-6.15 ± 0.32
25.475	-4.95 ± 0.08	25.775	-6.35 ± 0.42
25.525	-5.11 ± 0.09	25.825	-6.75 ± 0.77

Table A.36: LF for $1.1 < z < 1.3$ at $350\,\mu$m where $\alpha = 1.37 \pm 0.09$ and $\sigma = 0.22 \pm 0.1$. See Figures 4.12 and 4.14.

$\log(\phi_{350})$	$\log(L_{350})$	$\log(\phi_{350})$	$\log(L_{250})$
25.375	-5.91 ± 0.22	25.725	-5.48 ± 0.13
25.425	-4.83 ± 0.06	25.775	-6.08 ± 0.27
25.475	-4.54 ± 0.04	25.825	-6.08 ± 0.27
25.525	-4.68 ± 0.05	25.875	-6.52 ± 0.48
25.575	-4.92 ± 0.07	25.925	-6.52 ± 0.48
25.625	-5.09 ± 0.08	25.975	-6.82 ± 0.77
25.675	-5.39 ± 0.12		

Table A.37: LF for $1.3 < z < 1.5$ at $350\,\mu$m where $\alpha = 1.37 \pm 0.09$ and $\sigma = 0.22 \pm 0.1$. See Figures 4.12 and 4.14.

$\log(\phi_{350})$	$\log(L_{350})$	$\log(\phi_{350})$	$\log(L_{250})$
25.475	-5.35 ± 0.11	25.775	-5.34 ± 0.11
25.525	-4.55 ± 0.04	25.825	-5.54 ± 0.14
25.575	-4.52 ± 0.04	25.875	-6.02 ± 0.24
25.625	-4.70 ± 0.05	25.925	-6.05 ± 0.25
25.675	-4.83 ± 0.06	25.975	-6.39 ± 0.38
25.725	-5.09 ± 0.08	26.025	-6.86 ± 0.77

Table A.38: LF for $1.5 < z < 2.0$ at $350\,\mu$m where $\alpha = 1.37 \pm 0.09$ and $\sigma = 0.22 \pm 0.1$. See Figures 4.12 and 4.14.

$\log(\phi_{350})$	$\log(L_{350})$	$\log(\phi_{350})$	$\log(L_{250})$
25.525	-6.20 ± 0.21	25.925	-5.32 ± 0.06
25.575	-5.09 ± 0.05	25.975	-5.50 ± 0.08
25.625	-4.71 ± 0.03	26.025	-5.81 ± 0.11
25.675	-4.54 ± 0.03	26.075	-6.18 ± 0.17
25.725	-4.47 ± 0.02	26.125	-6.65 ± 0.30
25.775	-4.66 ± 0.03	26.175	-7.00 ± 0.48
25.825	-4.85 ± 0.04	26.225	-7.31 ± 0.77
25.875	-5.01 ± 0.04		

Table A.39: LF for $2.0 < z < 2.5$ at $350\,\mu$m where $\alpha = 1.37 \pm 0.09$ and $\sigma = 0.22 \pm 0.1$. See Figures 4.12 and 4.14.

$\log(\phi_{350})$	$\log(L_{350})$	$\log(\phi_{350})$	$\log(L_{250})$
25.675	-6.67 ± 0.38	26.075	-5.28 ± 0.06
25.725	-5.43 ± 0.07	26.125	-5.58 ± 0.08
25.775	-4.75 ± 0.03	26.175	-5.82 ± 0.11
25.825	-4.56 ± 0.03	26.225	-6.25 ± 0.18
25.875	-4.55 ± 0.02	26.275	-6.59 ± 0.27
25.925	-4.67 ± 0.03	26.325	-7.03 ± 0.48
25.975	-4.89 ± 0.04	26.425	-7.33 ± 0.77
26.025	-5.10 ± 0.05		

Table A.40: LF for $2.5 < z < 3.0$ at $350\,\mu$m where $\alpha = 1.37 \pm 0.09$ and $\sigma = 0.22 \pm 0.1$. See Figures 4.12 and 4.14.

$\log(\phi_{350})$	$\log(L_{350})$	$\log(\phi_{350})$	$\log(L_{250})$
25.525	-6.20 ± 0.21	25.925	-5.32 ± 0.06
25.575	-5.09 ± 0.05	25.975	-5.50 ± 0.08
25.625	-4.71 ± 0.03	26.025	-5.81 ± 0.11
25.675	-4.54 ± 0.03	26.075	-6.18 ± 0.17
25.725	-4.47 ± 0.02	26.125	-6.65 ± 0.30
25.775	-4.66 ± 0.03	26.175	-7.00 ± 0.48
25.825	-4.85 ± 0.04	26.225	-7.31 ± 0.77
25.875	-5.01 ± 0.04		

Table A.41: LF for $3.0 < z < 3.5$ at $350\,\mu$m where $\alpha = 1.37 \pm 0.09$ and $\sigma = 0.22 \pm 0.1$. See Figures 4.12 and 4.14.

$\log(\phi_{350})$	$\log(L_{350})$	$\log(\phi_{350})$	$\log(L_{250})$
25.975	-6.84 ± 0.42	26.275	-5.62 ± 0.09
26.025	-5.60 ± 0.08	26.325	-5.83 ± 0.11
26.075	-5.15 ± 0.05	26.375	-6.15 ± 0.16
26.125	-5.14 ± 0.05	26.425	-6.62 ± 0.28
26.175	-5.19 ± 0.05	26.475	-6.93 ± 0.42
26.225	-5.40 ± 0.07	26.525	-7.15 ± 0.57

Table A.42: LF for $3.5 < z < 4.0$ at $350\,\mu$m where $\alpha = 1.37 \pm 0.09$ and $\sigma = 0.22 \pm 0.1$. See Figures 4.12 and 4.14.

$\log(\phi_{350})$	$\log(L_{350})$	$\log(\phi_{350})$	$\log(L_{250})$
26.125	-6.59 ± 0.28	26.425	-6.29 ± 0.19
26.175	-5.68 ± 0.10	26.475	-6.61 ± 0.28
26.225	-5.40 ± 0.07	26.525	-6.83 ± 0.38
26.275	-5.48 ± 0.08	26.575	-7.01 ± 0.48
26.325	-5.66 ± 0.09	26.625	-7.31 ± 0.77
26.375	-5.89 ± 0.12		

Table A.43: LF for $4.0 < z < 4.5$ at $350\,\mu$m where $\alpha = 1.37 \pm 0.09$ and $\sigma = 0.22 \pm 0.1$. See Figures 4.12 and 4.14.

$\log(\phi_{350})$	$\log(L_{350})$	$\log(\phi_{350})$	$\log(L_{250})$
26.275	-6.41 ± 0.23	26.475	-6.16 ± 0.17
26.325	-5.85 ± 0.12	26.525	-6.44 ± 0.24
26.375	-5.79 ± 0.11	26.575	-7.11 ± 0.57
26.425	-6.11 ± 0.16	26.675	-7.29 ± 0.77

Table A.44: Bolometric LF for $0.0 < z < 0.1$ where $\alpha = 1.09 \pm 0.12$ and $\sigma = 0.25 \pm 0.03$. See Figures 4.17 and 4.18.

$\log(\phi_{Bol})$	$\log(L_{Bol})$	$\log(\phi_{Bol})$	$\log(L_{Bol})$
36.084	-1.90 ± 0.13	37.034	-2.55 ± 0.07
36.134	-2.15 ± 0.16	37.084	-2.53 ± 0.07
36.184	-2.30 ± 0.18	37.134	-2.62 ± 0.08
36.234	-2.47 ± 0.20	37.184	-2.66 ± 0.08
36.284	-2.42 ± 0.17	37.234	-2.68 ± 0.09
36.334	-2.31 ± 0.14	37.284	-2.78 ± 0.10
36.384	-2.33 ± 0.13	37.334	-2.80 ± 0.10
36.434	-2.33 ± 0.12	37.384	-2.89 ± 0.11
36.484	-2.43 ± 0.12	37.434	-3.08 ± 0.14
36.534	-2.53 ± 0.12	37.484	-3.07 ± 0.14
36.584	-2.44 ± 0.10	37.534	-3.21 ± 0.16
36.634	-2.45 ± 0.09	37.584	-3.32 ± 0.18
36.684	-2.49 ± 0.09	37.634	-3.57 ± 0.25
36.734	-2.43 ± 0.08	37.684	-3.51 ± 0.23
36.784	-2.55 ± 0.08	37.734	-3.91 ± 0.38
36.834	-2.50 ± 0.07	37.784	-3.64 ± 0.27
36.884	-2.42 ± 0.06	37.834	-4.21 ± 0.57
36.934	-2.51 ± 0.07	37.934	-4.38 ± 0.77
36.984	-2.53 ± 0.07	38.034	-4.38 ± 0.77

Table A.45: Bolometric LF for $0.1 < z < 0.2$ where $\alpha = 1.09 \pm 0.12$ and $\sigma = 0.25 \pm 0.03$. See Figures 4.17 and 4.18.

$\log(\phi_{Bol})$	$\log(L_{Bol})$	$\log(\phi_{Bol})$	$\log(L_{Bol})$
36.884	-3.54 ± 0.48	37.634	-3.18 ± 0.06
36.934	-2.93 ± 0.16	37.684	-3.34 ± 0.07
36.984	-2.71 ± 0.10	37.734	-3.46 ± 0.08
37.034	-2.63 ± 0.07	37.784	-3.60 ± 0.10
37.084	-2.75 ± 0.07	37.834	-3.77 ± 0.12
37.134	-2.73 ± 0.06	37.884	-3.97 ± 0.15
37.184	-2.75 ± 0.05	37.934	-3.99 ± 0.16
37.234	-2.79 ± 0.05	37.984	-4.32 ± 0.23
37.284	-2.78 ± 0.04	38.034	-4.50 ± 0.28
37.334	-2.85 ± 0.04	38.084	-4.54 ± 0.30
37.384	-2.85 ± 0.04	38.134	-4.80 ± 0.42
37.434	-2.87 ± 0.04	38.184	-4.89 ± 0.48
37.484	-2.84 ± 0.04	38.234	-5.02 ± 0.57
37.534	-2.98 ± 0.05	38.284	-5.20 ± 0.77
37.584	-3.13 ± 0.06		

Table A.46: Bolometric LF for $0.2 < z < 0.3$ where $\alpha = 1.09 \pm 0.12$ and $\sigma = 0.25 \pm 0.03$. See Figures 4.17 and 4.18.

$\log(\phi_{Bol})$	$\log(L_{Bol})$	$\log(\phi_{Bol})$	$\log(L_{Bol})$
37.434	-3.94 ± 0.23	38.034	-4.04 ± 0.10
37.484	-3.41 ± 0.09	38.084	-4.16 ± 0.12
37.534	-3.23 ± 0.06	38.134	-4.33 ± 0.15
37.584	-3.33 ± 0.06	38.184	-4.66 ± 0.21
37.634	-3.29 ± 0.05	38.234	-4.66 ± 0.21
37.684	-3.25 ± 0.04	38.284	-4.61 ± 0.20
37.734	-3.21 ± 0.04	38.334	-5.11 ± 0.38
37.784	-3.19 ± 0.04	38.384	-5.29 ± 0.48
37.834	-3.37 ± 0.05	38.434	-5.29 ± 0.48
37.884	-3.50 ± 0.06	38.484	-5.41 ± 0.57
37.934	-3.68 ± 0.07	38.684	-5.59 ± 0.77
37.984	-3.79 ± 0.08		

Table A.47: Bolometric LF for $0.3 < z < 0.4$ where $\alpha = 1.09 \pm 0.12$ and $\sigma = 0.25 \pm 0.03$. See Figures 4.17 and 4.18.

$\log(\phi_{Bol})$	$\log(L_{Bol})$	$\log(\phi_{Bol})$	$\log(L_{Bol})$
37.734	-4.10 ± 0.15	38.234	-4.04 ± 0.08
37.784	-3.67 ± 0.07	38.284	-4.33 ± 0.11
37.834	-3.51 ± 0.05	38.334	-4.49 ± 0.13
37.884	-3.42 ± 0.04	38.384	-4.72 ± 0.17
37.934	-3.33 ± 0.03	38.434	-4.78 ± 0.18
37.984	-3.33 ± 0.03	38.484	-4.96 ± 0.23
38.034	-3.44 ± 0.04	38.534	-5.24 ± 0.32
38.084	-3.60 ± 0.05	38.584	-5.36 ± 0.38
38.134	-3.75 ± 0.06	38.784	-5.66 ± 0.57
38.184	-3.95 ± 0.07		

Table A.48: Bolometric LF for $0.4 < z < 0.5$ where $\alpha = 1.09 \pm 0.12$ and $\sigma = 0.25 \pm 0.03$. See Figures 4.17 and 4.18.

$\log(\phi_{Bol})$	$\log(L_{Bol})$	$\log(\phi_{Bol})$	$\log(L_{Bol})$
37.934	-4.63 ± 0.19	38.434	-4.41 ± 0.10
37.984	-4.04 ± 0.07	38.484	-4.66 ± 0.13
38.034	-3.73 ± 0.04	38.534	-4.79 ± 0.15
38.084	-3.57 ± 0.04	38.584	-5.03 ± 0.20
38.134	-3.49 ± 0.03	38.634	-5.01 ± 0.20
38.184	-3.64 ± 0.04	38.684	-5.20 ± 0.25
38.234	-3.78 ± 0.05	38.734	-5.83 ± 0.57
38.284	-3.97 ± 0.06	38.784	-5.61 ± 0.42
38.334	-4.05 ± 0.06	38.834	-5.83 ± 0.57
38.384	-4.30 ± 0.09	38.934	-6.01 ± 0.77

Table A.49: Bolometric LF for $0.5 < z < 0.7$ where $\alpha = 1.09 \pm 0.12$ and $\sigma = 0.25 \pm 0.03$. See Figures 4.17 and 4.18.

$\log(\phi_{Bol})$	$\log(L_{Bol})$	$\log(\phi_{Bol})$	$\log(L_{Bol})$
38.034	-4.78 ± 0.30	38.534	-4.53 ± 0.06
38.084	-4.20 ± 0.09	38.584	-4.72 ± 0.08
38.134	-3.91 ± 0.05	38.634	-4.87 ± 0.10
38.184	-3.87 ± 0.04	38.684	-5.15 ± 0.13
38.234	-3.89 ± 0.03	38.734	-5.33 ± 0.16
38.284	-3.86 ± 0.03	38.784	-5.47 ± 0.19
38.334	-3.92 ± 0.03	38.834	-5.59 ± 0.22
38.384	-4.07 ± 0.04	38.884	-5.89 ± 0.32
38.434	-4.22 ± 0.04	38.934	-6.19 ± 0.48
38.484	-4.35 ± 0.05		

Table A.50: Bolometric LF for $0.7 < z < 0.9$ where $\alpha = 1.09 \pm 0.12$ and $\sigma = 0.25 \pm 0.03$. See Figures 4.17 and 4.18.

$\log(\phi_{Bol})$	$\log(L_{Bol})$	$\log(\phi_{Bol})$	$\log(L_{Bol})$
38.284	-4.70 ± 0.13	38.784	-4.95 ± 0.09
38.334	-4.26 ± 0.05	38.834	-5.20 ± 0.12
38.384	-4.13 ± 0.04	38.884	-5.34 ± 0.14
38.434	-4.13 ± 0.03	38.934	-5.65 ± 0.20
38.484	-4.10 ± 0.03	38.984	-5.95 ± 0.28
38.534	-4.22 ± 0.04	39.034	-5.87 ± 0.26
38.584	-4.35 ± 0.04	39.084	-6.17 ± 0.38
38.634	-4.44 ± 0.05	39.134	-6.35 ± 0.48
38.684	-4.64 ± 0.06	39.184	-6.35 ± 0.48
38.734	-4.76 ± 0.07	39.234	-6.65 ± 0.77

Table A.51: Bolometric LF for $0.9 < z < 1.1$ where $\alpha = 1.09 \pm 0.12$ and $\sigma = 0.25 \pm 0.03$. See Figures 4.17 and 4.18.

$\log(\phi_{Bol})$	$\log(L_{Bol})$	$\log(\phi_{Bol})$	$\log(L_{Bol})$
38.434	-5.62 ± 0.42	38.884	-4.90 ± 0.07
38.484	-4.76 ± 0.09	38.934	-5.03 ± 0.08
38.534	-4.45 ± 0.05	38.984	-5.27 ± 0.11
38.584	-4.26 ± 0.03	39.034	-5.57 ± 0.16
38.634	-4.21 ± 0.03	39.084	-5.67 ± 0.18
38.684	-4.30 ± 0.04	39.134	-6.01 ± 0.27
38.734	-4.43 ± 0.04	39.184	-6.15 ± 0.32
38.784	-4.62 ± 0.05	39.234	-6.75 ± 0.77
38.834	-4.75 ± 0.06	39.284	-6.75 ± 0.77

Table A.52: Bolometric LF for $1.1 < z < 1.3$ where $\alpha = 1.09 \pm 0.12$ and $\sigma = 0.25 \pm 0.03$. See Figures 4.17 and 4.18.

$\log(\phi_{Bol})$	$\log(L_{Bol})$	$\log(\phi_{Bol})$	$\log(L_{Bol})$
38.584	-5.29 ± 0.20	39.034	-5.02 ± 0.08
38.634	-4.69 ± 0.06	39.084	-5.24 ± 0.10
38.684	-4.35 ± 0.04	39.134	-5.39 ± 0.12
38.734	-4.18 ± 0.03	39.184	-5.64 ± 0.16
38.784	-4.24 ± 0.03	39.234	-6.12 ± 0.28
38.834	-4.34 ± 0.04	39.284	-6.27 ± 0.35
38.884	-4.48 ± 0.04	39.334	-6.64 ± 0.57
38.934	-4.64 ± 0.05	39.384	-6.42 ± 0.42
38.984	-4.81 ± 0.06		

Table A.53: Bolometric LF for $1.3 < z < 1.5$ where $\alpha = 1.09 \pm 0.12$ and $\sigma = 0.25 \pm 0.03$. See Figures 4.17 and 4.18.

$\log(\phi_{Bol})$	$\log(L_{Bol})$	$\log(\phi_{Bol})$	$\log(L_{Bol})$
38.684	-5.85 ± 0.57	39.084	-4.77 ± 0.06
38.734	-4.94 ± 0.09	39.134	-4.96 ± 0.07
38.784	-4.48 ± 0.04	39.184	-5.22 ± 0.09
38.834	-4.22 ± 0.03	39.234	-5.42 ± 0.12
38.884	-4.19 ± 0.03	39.284	-5.67 ± 0.16
38.934	-4.33 ± 0.03	39.334	-5.99 ± 0.23
38.984	-4.46 ± 0.04	39.384	-6.21 ± 0.30
39.034	-4.68 ± 0.05	39.434	-6.26 ± 0.32

Table A.54: Bolometric LF for $1.5 < z < 2.0$ where $\alpha = 1.09 \pm 0.12$ and $\sigma = 0.25 \pm 0.03$. See Figures 4.17 and 4.18.

$\log(\phi_{Bol})$	$\log(L_{Bol})$	$\log(\phi_{Bol})$	$\log(L_{Bol})$
38.834	-5.08 ± 0.11	39.284	-4.94 ± 0.04
38.884	-4.59 ± 0.04	39.334	-5.13 ± 0.05
38.934	-4.42 ± 0.03	39.384	-5.36 ± 0.07
38.984	-4.38 ± 0.02	39.434	-5.62 ± 0.09
39.034	-4.39 ± 0.02	39.484	-5.94 ± 0.13
39.084	-4.39 ± 0.02	39.534	-6.26 ± 0.19
39.134	-4.45 ± 0.02	39.584	-6.76 ± 0.35
39.184	-4.58 ± 0.03	39.634	-6.91 ± 0.42
39.234	-4.78 ± 0.03	39.684	-7.13 ± 0.57

Table A.55: Bolometric LF for $2.0 < z < 2.5$ where $\alpha = 1.09 \pm 0.12$ and $\sigma = 0.25 \pm 0.03$. See Figures 4.17 and 4.18.

$\log(\phi_{Bol})$	$\log(L_{Bol})$	$\log(\phi_{Bol})$	$\log(L_{Bol})$
39.084	-5.14 ± 0.09	39.484	-5.19 ± 0.05
39.134	-4.72 ± 0.04	39.534	-5.49 ± 0.07
39.184	-4.59 ± 0.03	39.584	-5.70 ± 0.09
39.234	-4.59 ± 0.03	39.634	-5.96 ± 0.13
39.284	-4.57 ± 0.03	39.684	-6.31 ± 0.19
39.334	-4.64 ± 0.03	39.734	-6.68 ± 0.30
39.384	-4.78 ± 0.03	39.934	-7.33 ± 0.77
39.434	-5.02 ± 0.04		

Table A.56: Bolometric LF for $2.5 < z < 3.0$ where $\alpha = 1.09 \pm 0.12$ and $\sigma = 0.25 \pm 0.03$. See Figures 4.17 and 4.18.

$\log(\phi_{Bol})$	$\log(L_{Bol})$	$\log(\phi_{Bol})$	$\log(L_{Bol})$
39.284	-5.44 ± 0.13	39.634	-5.57 ± 0.08
39.334	-5.04 ± 0.06	39.684	-5.86 ± 0.11
39.384	-4.93 ± 0.04	39.734	-6.13 ± 0.16
39.434	-4.91 ± 0.04	39.784	-6.56 ± 0.26
39.484	-4.92 ± 0.04	39.834	-6.56 ± 0.26
39.534	-5.10 ± 0.05	39.884	-6.94 ± 0.42
39.584	-5.28 ± 0.06	39.934	-7.03 ± 0.48

Table A.57: Bolometric LF for $3.0 < z < 3.5$ where $\alpha = 1.09 \pm 0.12$ and $\sigma = 0.25 \pm 0.03$. See Figures 4.17 and 4.18.

$\log(\phi_{Bol})$	$\log(L_{Bol})$	$\log(\phi_{Bol})$	$\log(L_{Bol})$
39.484	-5.66 ± 0.14	39.734	-5.80 ± 0.11
39.534	-5.38 ± 0.08	39.784	-6.15 ± 0.16
39.584	-5.39 ± 0.07	39.834	-6.58 ± 0.27
39.634	-5.43 ± 0.07	39.884	-6.72 ± 0.32
39.684	-5.63 ± 0.09	39.934	-7.15 ± 0.57

Table A.58: Bolometric LF for $3.5 < z < 4.0$ where $\alpha = 1.09 \pm 0.12$ and $\sigma = 0.25 \pm 0.03$. See Figures 4.17 and 4.18.

$\log(\phi_{Bol})$	$\log(L_{Bol})$	$\log(\phi_{Bol})$	$\log(L_{Bol})$
39.634	-6.70 ± 0.57	39.834	-6.21 ± 0.18
39.684	-5.89 ± 0.15	39.884	-6.83 ± 0.38
39.734	-5.94 ± 0.13	39.934	-6.91 ± 0.42
39.784	-5.98 ± 0.14	39.984	-6.83 ± 0.38

Table A.59: Bolometric LF for $4.0 < z < 4.5$ where $\alpha = 1.09 \pm 0.12$ and $\sigma = 0.25 \pm 0.03$. See Figures 4.17 and 4.18.

$\log(\phi_{Bol})$	$\log(L_{Bol})$	$\log(\phi_{Bol})$	$\log(L_{Bol})$
39.784	-6.80 ± 0.77	39.934	-6.89 ± 0.42
39.834	-6.40 ± 0.28	39.984	-6.98 ± 0.48
39.884	-6.85 ± 0.42	40.034	-7.29 ± 0.77

Bibliography

Almaini, O., Scott, S. E., Dunlop, J. S., et al. 2003, MNRAS, 338, 303

Amblard, A., Cooray, A., Serra, P., et al. 2010, A&A, 518, L9

—. 2011, Nature, 470, 510

Avni, Y. 1976, ApJ, 210, 642

Avni, Y., & Bahcall, J. N. 1980, ApJ, 235, 694

Barger, A. J., Cowie, L. L., Sanders, D. B., et al. 1998, Nature, 394, 248

Barnes, J. E., & Hernquist, L. E. 1991, ApJL, 370, L65

Baugh, C. M., Lacey, C. G., Frenk, C. S., et al. 2005, MNRAS, 356, 1191

Bernstein, G. M. 1994, ApJ, 424, 569

Bertoldi, F., Carilli, C. L., Menten, K. M., et al. 2000, A&A, 360, 92

Blain, A. W. 1996, MNRAS, 283, 1340

Blain, A. W., Barnard, V. E., & Chapman, S. C. 2003, MNRAS, 338, 733

Blain, A. W., Chapman, S. C., Smail, I., & Ivison, R. 2004, ApJ, 611, 725

Blain, A. W., Kneib, J.-P., Ivison, R. J., & Smail, I. 1999, ApJL, 512, L87

Blain, A. W., & Longair, M. S. 1996, MNRAS, 279, 847

Blain, A. W., Smail, I., Ivison, R. J., & Kneib, J.-P.and Frayer, D. T. 2002, PR, 369, 111

Blandford, R. D., Kochanek, C. S., Kovner, I., & Narayan, R. 1989, Science, 245, 824

Bond, N. A., Benford, D. J., Gardner, J. P., et al. 2012, ApJL, 750, L18

Brusa, M., Comastri, A., Gilli, R., et al. 2009, ApJ, 693, 8

Cannon, R., Drinkwater, M., Edge, A., et al. 2006, MNRAS, 372, 425

Carilli, C. L., Daddi, E., Riechers, D., et al. 2010, ApJ, 714, 1407

Casey, C. M., Berta, S., Béthermin, M., et al. 2012, ApJ, 761, 140

Chapman, S. C., Blain, A. W., Smail, I., & Ivison, R. J. 2005, ApJ, 622, 772

Chary, R., & Elbaz, D. 2001, ApJ, 556, 562

Civano, F., Brusa, M., Comastri, A., et al. 2011, ApJ, 741, 91

Clements, D. L., Dunne, L., & Eales, S. 2010, MNRAS, 403, 274

Collaboration, H.-A. 2010, private communication

Colless, M., Dalton, G., Maddox, S., et al. 2001, MNRAS, 328, 1039

Conroy, C., & Wechsler, R. H. 2009, ApJ, 696, 620

Cooray, A., Amblard, A., Wang, L., et al. 2010, A&A, 518, L22

Cooray, A. R. 1999, ApJ, 524, 504

Cooray, A. R., & Huterer, D. 1999, ApJL, 513, L95

Coppin, K., Halpern, M., Scott, D., et al. 2008, MNRAS, 384, 1597

Coppin, K., Chapin, E. L., Mortier, A. M. J., et al. 2006, Mon. Not. R. Astron. Soc., 372, 1621

Cox, P., Krips, M., Neri, R., et al. 2011, ApJ, 740, 63

Croom, S. M., Richards, G. T., Shanks, T., et al. 2009, MNRAS, 399, 1755

Daddi, E., Cimatti, A., Pozzetti, L., et al. 2000, A&A, 361, 535

Davies, J. I., Bianchi, S., Cortese, L., et al. 2012, MNRAS, 419, 3505

Devereux, N. A., & Young, J. S. 1990, ApJ, 359, 42

Devlin, M. J., Ade, P. A. R., Aretxaga, I., et al. 2009, Nature, 458, 737

Dole, H., Lagache, G., Puget, J.-L., et al. 2006, A&A, 451, 417

Driver, S. P., Hill, D. T., Kelvin, L. S., et al. 2011, MNRAS, 413, 971

Dunlop, J. S., Ade, P. A. R., Bock, J. J., et al. 2010, MNRAS, 408, 2022

Dunne, L., Clements, D. L., & Eales, S. A. 2000, MNRAS, 319, 813

Dunne, L., Eales, S., Edmunds, M., et al. 2000, MNRAS, 315, 115

Dunne, L., & Eales, S. A. 2001, MNRAS, 327, 697

Dunne, L., Gomez, H. L., da Cunha, E., et al. 2011, MNRAS, 417, 1510

Dye, S., Dunne, L., Eales, S., Smith, D. J. B., & Amblard, A. 2010, Astronomy and Astrophysics, 518, L10

Dyson, F. W., Watson, F., & Eddington, A. S. 1920, Philosophical Transactions of the Royal Society of London, 220, 291

Eales, S., Lilly, S., Gear, W., et al. 1999, ApJ, 515, 518

Eales, S., Chapin, E. L., Devlin, M. J., et al. 2009, ApJ, 707, 1779

Eales, S., Dunne, L., Clements, D., et al. 2010, PASP, 122, 499

Eales, S., Smith, M. W. L., Auld, R., et al. 2012, ApJ, 761, 168

Einstein, A. 1936, Science, 84, 506

Elbaz, D., Cesarsky, C. J., Chanial, P., et al. 2002, A&A, 384, 848

Farrah, D., Afonso, J., Efstathiou, A., et al. 2003, MNRAS, 343, 585

Fixsen, D. J., Dwek, E., Mather, J. C., Bennett, C. L., & Shafer, R. A. 1998, ApJ, 508, 123

Fleuren, S., Sutherland, W., Dunne, L., et al. 2012, MNRAS, 423, 2407

Floch, E. L., Papovich, C., Dole, H., et al. 2005, The Astrophysical Journal, 632, 169

Fox, M. J., Efstathiou, A., Rowan-Robinson, M., et al. 2002, MNRAS, 331, 839

Franceschini, A., Aussel, H., Cesarsky, C. J., Elbaz, D., & Fadda, D. 2001, A&A, 378, 1

Frayer, D. T., Harris, A. I., Baker, A. J., et al. 2011, ApJL, 726, L22

Fu, H. 2010, gemini Observatory Proposal

Fu, H., Jullo, E., Cooray, A., et al. 2012, ApJ, 753, 134

Fukugita, M., & Peebles, P. J. E. 1993, ArXiv Astrophysics e-prints

Fukugita, M., & Turner, E. L. 1991, MNRAS, 253, 99

Galametz, M., Kennicutt, R. C., Albrecht, M., et al. 2012, MNRAS, 425, 763

Gilli, R., Daddi, E., Chary, R., et al. 2007, A&A, 475, 83

Gispert, R., Lagache, G., & Puget, J. L. 2000, A&A, 360, 1

Gomez, H. L., Krause, O., Barlow, M. J., et al. 2012, ApJ, 760, 96

González-Nuevo, J., Lapi, A., Fleuren, S., et al. 2012, ApJ, 749, 65

Goto, T., Arnouts, S., Inami, H., et al. 2011, MNRAS, 410, 573

Griffin, M. J., Abergel, A., Abreu, A., et al. 2010, A&A, 518, L3+

Groves, B., Dopita, M. A., Sutherland, R. S., et al. 2008, ApJS, 176, 438

Gruppioni, C., Pozzi, F., Rodighiero, G., et al. 2013, ArXiv e-prints

Guiderdoni, B., Hivon, E., Bouchet, F. R., & Maffei, B. 1998, MNRAS, 295, 877

Guzzo, L., Strauss, M. A., Fisher, K. B., Giovanelli, R., & Haynes, M. P. 1997, ApJ, 489, 37

Harris, A. I., Baker, A. J., Zonak, S. G., et al. 2010, ApJ, 723, 1139

Harris, A. I., Baker, A. J., Frayer, D. T., et al. 2012, ApJ, 752, 152

Holland, W. S., Robson, E. I., Gear, W. K., et al. 1999, MNRAS, 303, 659

Hubble, E. P. 1925, ApJ, 62, 409

Hughes, D. H., Serjeant, S., Dunlop, J., et al. 1998, Nature, 394, 241

Huynh, M. T., Frayer, D. T., Mobasher, B., et al. 2007, ApJL, 667, L9

Ivison, R. J., Papadopoulos, P. P., Smail, I., et al. 2011, MNRAS, 412, 1913

Jones, A. P. 2002, in EAS Publications Series, Vol. 4, EAS Publications Series, ed. M. Giard, J. P. Bernard, A. Klotz, & I. Ristorcelli, 37–37

Jones, D. H., Read, M. A., Saunders, W., et al. 2009, MNRAS, 399, 683

Keller, S. C., Schmidt, B. P., Bessell, M. S., et al. 2007, PASA, 24, 1

Kennicutt, Jr., R. C. 1998, ARAA, 36, 189

Kessler, M. F., Steinz, J. A., Anderegg, M. E., et al. 1996, A&A, 315, L27

Lacey, C. G., Baugh, C. M., Frenk, C. S., et al. 2010, MNRAS, 405, 2

Lagache, G., Dole, H., Puget, J.-L., et al. 2004, ApJS, 154, 112

Landy, S. D., & Szalay, A. S. 1993, ApJ, 412, 64

Lapi, A., González-Nuevo, J., Fan, L., et al. 2011, ApJ, 742, 24

Lawrence, A., Warren, S. J., Almaini, O., Edge, A. C., & Hambly, N. C. 2007, MNRAS, 379, 1599

Lupu, R. E., Scott, K. S., Aguirre, J. E., et al. 2012, ApJ, 757, 135

Maddox, S. J., Dunne, L., Rigby, E., et al. 2010, A&A, 518, L11+

Magliocchetti, M., Santini, P., Rodighiero, G., et al. 2011, MNRAS, 416, 1105

Magnelli, B., Elbaz, D., Chary, R. R., et al. 2009, A&A, 496, 57

—. 2011, A&A, 528, A35

Martin, D. C., Fanson, J., Schiminovich, D., et al. 2005, ApJL, 619, L1

Marzke, R. O., da Costa, L. N., Pellegrini, P. S., Willmer, C. N. A., & Geller, M. J. 1998, ApJ, 503, 617

Mauch, T., Klöckner, H.-R., Rawlings, S., et al. 2013, ArXiv e-prints

Mitchell-Wynne, K., Cooray, A., Gong, Y., et al. 2012, ApJ, 753, 23

Negrello, M., Perrotta, F., González-Nuevo, J., et al. 2007, MNRAS, 377, 1557

Negrello, M., Hopwood, R., De Zotti, G., et al. 2010, Science, 330, 800

Neugebauer, G., Beichman, C. A., Soifer, B. T., et al. 1984, Science, 224, 14

Page, M. J., & Carrera, F. J. 2000, MNRAS, 311, 433

Pascale, E., Auld, R., Dariush, A., et al. 2011, MNRAS, 415, 911

Peng, Y.-j., Lilly, S. J., Kovač, K., et al. 2010, ApJ, 721, 193

Perrotta, F., Baccigalupi, C., Bartelmann, M., De Zotti, G., & Granato, G. L. 2002, MNRAS, 329, 445

Perrotta, F., Magliocchetti, M., Baccigalupi, C., et al. 2003, MNRAS, 338, 623

Pilbratt, G. L., Riedinger, J. R., Passvogel, T., et al. 2010, A&A, 518, L1+

Poglitsch, A., Waelkens, C., Geis, N., et al. 2010, A&A, 518, L2+

Pozzetti, L., Bolzonella, M., Zucca, E., et al. 2010, A&A, 523, A13

Press, W. H., & Schechter, P. 1974, ApJ, 187, 425

Puget, J.-L., Abergel, A., Bernard, J.-P., et al. 1996, A&A, 308, L5

Ratcliffe, A., Shanks, T., Parker, Q. A., & Fong, R. 1998, MNRAS, 296, 173

Riechers, D. A., Hodge, J., Walter, F., Carilli, C. L., & Bertoldi, F. 2011, ApJL, 739, L31

Rigby, E. E., Maddox, S. J., Dunne, L., et al. 2011, MNRAS, 415, 2336

Roche, N., & Eales, S. A. 1999, MNRAS, 307, 703

Rodighiero, G., Vaccari, M., Franceschini, A., et al. 2010, A&A, 515, A8

Salpeter, E. E. 1974, ApJ, 193, 585

Sanders, D. B., Mazzarella, J. M., Kim, D.-C., Surace, J. A., & Soifer, B. T. 2003, ApJ, 126, 1607

Sanders, D. B., & Mirabel, I. F. 1996, ARAA, 34, 749

Sanders, D. B., Soifer, B. T., Elias, J. H., et al. 1988, ApJ, 325, 74

Sargent, M. T., Béthermin, M., Daddi, E., & Elbaz, D. 2012, ApJL, 747, L31

Saunders, W., Rowan-Robinson, M., Lawrence, A., et al. 1990, MNRAS, 242, 318

Schechter, P. 1976, ApJ, 203, 297

Schneider, N., Urban, J., & Baron, P. 2009, Planetary and Space Science, 57, 1419

Scott, S. E., Dunlop, J. S., & Serjeant, S. 2006, MNRAS, 370, 1057

Scott, S. E., Fox, M. J., Dunlop, J. S., et al. 2002, MNRAS, 331, 817

Smail, I., Ivison, R. J., & Blain, A. W. 1997, ApJL, 490, L5

Smail, I., Ivison, R. J., Blain, A. W., & Kneib, J.-P. 2002, MNRAS, 331, 495

Smith, D. J. B., Dunne, L., Maddox, S. J., et al. 2011, MNRAS, 1229

Smith, D. J. B., Dunne, L., da Cunha, E., et al. 2012, MNRAS, 427, 703

Smolčić, V., Schinnerer, E., Zamorani, G., et al. 2009, ApJ, 690, 610

Soifer, B. T., & Neugebauer, G. 1991, ApJ, 101, 354

Stefanon, M., & Marchesini, D. 2013, MNRAS, 429, 881

Strazzullo, V., Pannella, M., Owen, F. N., et al. 2010, ApJ, 714, 1305

Tully, R. B., & Fisher, J. R. 1977, A&A, 54, 661

Turner, E. L. 1990, ApJL, 365, L43

Vaccari, M., Marchetti, L., Franceschini, A., et al. 2010, A&A, 518, L20

van Kampen, E., Smith, D. J. B., Maddox, S., et al. 2012, MNRAS, 426, 3455

Vlahakis, C., Dunne, L., & Eales, S. 2005, MNRAS, 364, 1253

Wall, J. V., & Jenkins, C. R. 2003, Practical Statistics for Astronomers (Cambridge Press)

Walsh, D., Carswell, R. F., & Weymann, R. J. 1979, Nature, 279, 381

Warren, S. J., Cross, N. J. G., Dye, S., et al. 2007, ArXiv Astrophysics e-prints

Webb, T. M., Eales, S., Foucaud, S., et al. 2003, ApJ, 582, 6

Weiß, A., Kovács, A., Coppin, K., et al. 2009a, Astrophys. J., 707, 1201

—. 2009b, ApJ, 707, 1201

Werner, M. W., Roellig, T. L., Low, F. J., et al. 2004, ApJS, 154, 1

Whittet, D. C. B., ed. 2003, Dust in the galactic environment

Wright, G. S., Joseph, R. D., & Meikle, W. P. S. 1984, Nature, 309, 430

Wright, T. 1750, London: H. Chappelle

Yang, M., Greve, T. R., Dowell, C. D., & Borys, C. 2007, ApJ, 660, 1198

Yin, J., Hou, J. L., Prantzos, N., et al. 2009, A&A, 505, 497

York, D. G., Adelman, J., Anderson, Jr., J. E., et al. 2000, ApJ, 120, 1579

Younger, J. D., Fazio, G. G., Huang, J.-S., et al. 2007, The Astrophysical Journal, 671, 1531